

**Disentangled Ultra-High Molecular Weight Polyethylene and its  
Nanocomposites: Relaxation Dynamics, Entanglement Formation and  
Anisotropic Properties due to Orientation**

**by**

**Stavros X. Drakopoulos**

**A Doctoral Thesis submitted in partial fulfilment of the requirements  
for the award of Doctor of Philosophy of Loughborough University**

**September 2019**

**© by Stavros X. Drakopoulos 2019**

**Loughborough University**

**School of Aeronautical, Automotive, Chemical and Materials Engineering**

**Department of Materials**



*Disentangled Ultra-High Molecular Weight Polyethylene and its  
Nanocomposites: Relaxation Dynamics, Entanglement Formation and  
Anisotropic Properties due to Orientation*

A DOCTORAL THESIS

Postgraduate Student (Research)

Mr Stavros X. Drakopoulos

Supervisors

Dr Sara Ronca

Dr Ignacio Martin-Fabiani

Dr Simon Martin

Date

30 September 2019

## ABSTRACT

In the present doctoral research, the chain relaxations and dynamics present in linear disentangled ultra-high molecular weight polyethylene (both pure and as a composite) were investigated and presented. Considering its disentangled character, the relaxation dynamics and the formation of entanglements were primarily analysed. Additionally, the presence of fillers and the effect of uniaxial orientation were also studied. With respect to the chain relaxation analysis, torsional rheology and broadband dielectric spectroscopy were employed to identify the disentangled amorphous phase in comparison with fully entangled samples. The rheological results gave significantly different relaxation behaviour for the disentangled sample, affecting all the mechanical processes namely  $\alpha_c$ -,  $\beta$ - and  $\gamma$ -relaxations, with the latter exhibiting a non-Arrhenius temperature dependence, indicative of the dynamic glass-to-rubber transition. This indication would support previous studies that would locate the glass transition temperature of linear polyethylene around  $-100^\circ\text{C}$ . The dielectric analysis was only possible in the presence of  $\text{Al}_2\text{O}_3$  catalytic ashes and expanded further the relaxation investigation by showing two types of interfacial polarization attributed to the disentangled and entangled amorphous phases. A common relaxation map combining rheological and dielectric data was constructed. In addition to the observation that disentangled ultra-high molecular weight polyethylene is metastable in the melt state, evidence that entanglements can form in the solid state by means of dielectric spectroscopy are presented. A new model is proposed to analyse the effect and a critical activation temperature was calculated to be around  $60^\circ\text{C}$ .

Considering that disentangled ultra-high molecular weight polyethylene can be solid state processed due to its disentangled character, uniaxially oriented tapes in the presence of various fillers were prepared and analysed for draw ratios up to 150 times. An in-depth structural analysis was performed by means of Raman spectroscopy, visible/near infrared spectrophotometry, small-angle and wide-angle X-ray scattering and the potential application of oriented disentangled ultra-high molecular weight polyethylene nanocomposites as dielectric materials for capacitor applications was investigated. With orientation, the recovery efficiency was found to increase significantly (up to 30 times) indicating that disentangled ultra-high molecular weight polyethylene could be successfully used as capacitor material. The thermal conductivity was found to increase up to 15 times along the orientation axis, which is a paramount property to dissipate heat in capacitor materials. The formation of entanglements was also investigated in uniaxially oriented samples and was found to affect both the interfacial polarization response and the dc conduction.

## LIST OF SYMBOLS

### Latin characters

$A$	Area
$b$	Shift factor in time-temperature superposition
$C$	Capacitance
$d$	Diameter
$D$	VFTH parameter
$D_e$	Electric displacement
$DR$	Draw ratio
$E$	Electric field
$E_A$	Activation energy
$E_D$	Entanglement formation energy
$f$	Frequency
$f_{M,max}$	Frequency maximum modulus loss peak position
$f_{\varepsilon,max}$	Frequency maximum permittivity loss peak position
$g_N$	Numerical factor
$I$	Light scattering intensity
$I_c$	Charge current
$I_d$	Discharge current
$G_N^0$	Plateau modulus
$G^*$	Complex mechanical modulus
$G'$	Real part of mechanical modulus
$G''$	Imaginary part of mechanical modulus
$G_s$	Static value of mechanical modulus
$G_\infty$	Mechanical modulus at infinite frequency
$G_N$	Normalized relaxation strength parameter
$k_B$	Boltzmann constant
$l$	Thickness
$L$	Length in real space
$M_e$	Molecular weight between entanglements
$M_n$	Number average molecular weight
$M_w$	Weight average molecular weight

$M^*$	Complex electric modulus
$M'$	Real part of electric modulus
$M''$	Imaginary part of electric modulus
$M_s$	Static value of electric modulus
$M_\infty$	Electric modulus at infinite frequency
$MWD$	Molecular weight distribution
$n$	Number of frequency sweeps
$n_{eff}$	Coefficient of recovery efficiency
$P$	Pressure
$P_0$	Ideal glass-to-rubber transition pressure
$P_D$	Entanglement formation power
$Q$	Electric charge
$q$	Momentum transfer vector
$R$	Ideal gas constant
$R_g$	Radius of gyration
$T$	Temperature
$T_M$	Measurement temperature
$T_V$	Vogel temperature
$T_{dielectric}$	Temperature loss peak position in the dielectric spectra
$T_{mechanical}$	Temperature loss peak position in the mechanical spectra
$\tan\delta$	Loss tangent
$T_m$	Melting temperature
$T_{ref}$	Reference temperature
$T_g$	Glass-to-rubber transition temperature
$t$	Absolute time
$t_0$	Time duration of one frequency sweep
$U_e$	Electrical energy density
$V$	Voltage
$X_c$	Crystallinity
$Z^*$	Complex impedance
$Z'$	Real part of impedance
$Z''$	Imaginary part of impedance

Greek characters

$\alpha$	Cole-Cole parameter
$\beta$	Cole-Cole parameter
$\gamma$	Davidson-Cole parameter
$\Delta H_m$	Melting enthalpy
$\Delta H_m^c$	Melting enthalpy of a 100% crystalline sample
$\varepsilon^*$	Complex dielectric permittivity
$\varepsilon'$	Real part of dielectric permittivity
$\varepsilon''$	Imaginary part of dielectric permittivity
$\varepsilon''_{der}$	Logarithmic derivative of dielectric permittivity
$\varepsilon_s$	Static value of dielectric permittivity
$\varepsilon_\infty$	Dielectric permittivity at infinite frequency
$\varepsilon_0$	Dielectric constant of vacuum
$\eta^*$	Complex viscosity
$\eta_0$	Zero shear viscosity
$2\theta$	Scattering angle
$\lambda$	Wavelength
$\mu$	Linear absorption coefficient
$\rho$	Density of a material
$\sigma^*$	Complex electrical conductivity
$\sigma'$	Real part of electrical conductivity
$\sigma''$	Imaginary part of electrical conductivity
$\sigma_{dc}$	Direct current electrical conductivity
$\sigma_{dc}^0$	Plateau value of Ohmic conduction
$\tau$	Relaxation time
$\tau_D$	Debye relaxation time
$\tau_{CC}$	Cole-Cole relaxation time
$\tau_{DC}$	Davidson-Cole relaxation time
$\tau_{HN}$	Havriliak-Negami relaxation time
$\tau_0$	Pre-exponential factor of relaxation time
$\omega$	Angular frequency
$\omega_{max}$	Angular frequency maximum loss peak position

## LIST OF FIGURES

Figure 1.1. Crystalline structures of thickness  $\zeta$  of regularly folded chains (left) and irregular folded chains (right). The graph was taken from P.J. Flory (1962).

Figure 1.2. A 2D (top) and 3D (bottom) representation of a crystalline (orthorhombic) polyethylene chain. The images were obtained from Alsaygh et al., (2014).

Figure 1.3. The two most intense diffraction peaks of polyethylene's orthorhombic crystal phase (left) with their corresponding cell planes (right) The graph was taken from L.M. Lozano-Sánchez et al., (2018).

Figure 1.4. The monoclinic (top) and hexagonal (bottom) crystal cells of linear polyethylene, including the cell dimensions. The image was obtained from G.-R. Nejabat (2018).

Figure 1.5. The surface morphology of (a) a pristine disentangled UHMWPE sample and (b) a commercial fully entangled UHMWPE sample, as obtained by means of SEM. The pictures were obtained from A. Pandey *et al.*, (2011).

Figure 1.6. Schematic representation of the crystal morphology for (a) nascent disentangled crystals, (b) nascent commercial crystals and (c) crystals after melting. The black lines correspond to one polyethylene chain while the red ones correspond to more chains. The graph were taken from A. Pandey *et al.*, (2011).

Figure 1.7. Schematic representation of polymer entanglements in a polymer chain of molecular weight  $M$  and average molecular weight between entanglements  $M_e$ . The graph was taken from D.T. Turner (1977).

Figure 1.8. The zero shear viscosity,  $\eta_0$ , as a function of molecular weight for polyethylene. The graph is taken from J.T. Padding and W.J. Briels (2002).

Figure 1.9. The real part of mechanical modulus as a function of time at 160°C of (a) a disentangled UHMWPE sample (black points) and an entangled UHMWPE sample (red points) of similar molecular weights; (b) two initially disentangled UHMWPE samples of molar masses  $2.0 \cdot 10^6$  g/mol ( $\blacktriangle$ ) and  $5.3 \cdot 10^6$  g/mol ( $\blacksquare$ ) g/mol. The graphs were obtained from K. Liu *et al.*, (2016) and S. Talebi *et al.*, (2010) respectively.

Figure 1.10. The comparison between the four basic dielectric formalisms (imaginary parts of: dielectric permittivity  $\varepsilon''$  (black), electric modulus  $M''$  (red) and impedance  $Z''$  (blue), the real part of electrical conductivity  $\sigma_{ac}$  (green)) as a function of frequency in an ideal system consisting of two basic phenomena, a Debye dipolar relaxation and dc conductivity.

Figure 1.11. The dielectric permittivity loss as a function of frequency of a single relaxation process varying (a) the parameter  $\beta$  and (b) the parameter  $\gamma$ . For  $\beta = \gamma = 1$  the *Debye* behaviour is observed.

Figure 1.12. (a) The real and imaginary parts of mechanical modulus as a function of angular frequency of a fictional relaxation in the temperature range of 280 to 400 K and in (b) the master curve (open symbols) according to the *TTS* principle is presented. The relaxation follows the Havriliak-Negami function model with parameters:  $G_s = 10^4$  Pa,  $G_\infty = 10^0$  Pa and  $\beta = \gamma = 0.50$ . The angular frequency loss peak positions  $\omega_{max}$  were set to follow the Arrhenius equation (Equation (1.7)) where  $\omega_{max} = \frac{1}{\tau}$ , with an activation energy  $E_A = 1$  eV, as shown within the inset. The shift factor  $b$  in accordance with Equation (1.11) also followed the same Arrhenius equation. In this case, the  $T_{ref} = 340$  K.

Figure 3.1. First heating thermographs of all the specimens under study including the untreated UHMWPE powders (disentangled and commercial).

Figure 3.2. The imaginary part of modulus ( $G''$ ) as a function of temperature varying frequency for (a) PE\_C\_160, (b) PE\_D\_160 and (c) PE\_D\_125 samples. (The lines serve as guides for the eyes only.)

Figure 3.3. Temperature dependence of the real part of modulus ( $G'$ ) and the loss tangent ( $\tan\delta$ ) for all the samples under study at 39.8 Hz.



Figure 3.4. Cole-Cole representation of the data at 39.8 Hz for the (a) PE\_C\_160, (b) PE\_D\_160 and (c) PE\_D\_125 samples. The lines follow Equation (3.4) and the corresponding parameters can be found in Table 3.2.

Figure 3.5. The normalized relaxation strength,  $G_N$ , of the recorded relaxations as a function of crystallinity fraction,  $X_c$ , for the samples under study. The values presented are the average of the  $G_N$  as calculated for each relaxation from the  $10^{-2}$  Hz,  $10^{-1}$  Hz,  $10^0$  Hz,  $10^1$  Hz and  $10^2$  Hz Cole-Cole plots and the errors correspond to the uncertainty calculations. (The lines serve as guide for the eye only.)

Figure 3.6. Arrhenius plot of the recorded relaxations for all the samples under study.

Figure 3.7. (a) The real and (b) imaginary parts of dielectric permittivity as a function of frequency at 160°C for the studied samples.

Figure 3.8. The imaginary parts of (a) dielectric permittivity and (b) electric modulus both as a function of frequency and temperature for the PE\_4.2\_AIO sample.

Figure 3.9. The imaginary part of electric modulus as a function of frequency for PE\_4.2\_AIO at Top to bottom: (a) 50 – 100°C and (b) 110 – 160°C with a step of 10°C. The points represent the experimental data while the interpolating lines are obtained from the computational model. The lines are: —  $\beta_1$ -relaxation, —  $\beta_2$ -relaxation, —  $\alpha_c$ -relaxation, — MWS-IP<sub>1</sub>, — MWS-IP<sub>2</sub> and — conductivity relaxation.

Figure 3.10. The log-log representation of the imaginary part of dielectric permittivity as a function of angular frequency at 160°C for sample PE\_4.2\_AIO. The fitting line has a slope equal to -1 and from the intercept the dc conduction can be approximately calculated as  $\sim 3.3 \cdot 10^{-12}$  S/m, following the relation:  $\log \varepsilon''_{dc} = \log \left( \frac{\sigma_{dc}}{\varepsilon_0} \right) - \log \omega$ .

Figure 3.11. Arrhenius plot for the maximum loss positions as a function of the reciprocal temperature for all observed relaxation processes in PE\_4.2\_AIO. The activation energy for each process is given as well.

Figure 3.12. Arrhenius plot comparing the dielectric data (solid symbols) as obtained from the PE\_4.2\_AIO sample and the rheological (mechanical) data (open symbols) of the PE\_D\_125 sample.

Figure 3.13. The real part of electric modulus as a function of time at 100 and 10 Hz. Inset the real part of mechanical shear modulus as a function of time at 1 and 10 Hz. All for the PE\_4.2\_AIO sample at 160°C.

Figure 3.14. The imaginary part of electric modulus as a function of frequency varying time at 160°C for PE\_4.2\_AIO. The arrow shows the shift towards lower frequencies caused by the progressive entanglement formation. The points represent the experimental data while the lines represent the superposition of the computational models. Inset shows the loss peak position of the MWS-IP<sub>1</sub> with the progression of time where the values of the entanglement formation power and energy are indicated.

Figure 3.15. (a) The maximum loss positions as a function of time for the MWS-IP<sub>1</sub> in PE\_4.2\_AIO at different temperatures where the entanglement formation energy ( $E_D$ ) is indicated for each temperature ( $R^2 > 0.98$  in all cases); (b) the values of the entanglement formation energy ( $E_D$ ) as a function of temperature, as calculated by Equation (3.12). The point at 140°C deviates from the linear behaviour, due to the melting of crystals, and it has not been included in the fitting line.

Figure 3.16. The imaginary part of dielectric permittivity as a function of frequency varying time at 160°C for samples with different molecular weight: (a) PE\_5.6\_AIO, (b) PE\_4.2\_AIO and (c) PE\_2.4\_AIO.

Figure 4.1. The WAXS profile of DR1 (unoriented) dis-UHMWPE/gold nanocomposite indicating the amorphous halos and the crystalline peaks.

Figure 4.2. (a) WAXS profiles of gold/UHMWPE nanocomposite films where the intensity is normalized with the (200) reflection. (b) Crystallinity as calculated by WAXS (left axis) and intensity ratio of the (200) and (110) reflections (right axis) versus draw ratio. The dotted line is a guide for the eye to show when the peak inversion of the reflections takes place.

Figure 4.3. SAXS profile of gold/UHMWPE nanocomposite films normalized by the thickness for all samples under study including the DR1 in the absence of Au nanoparticles. In (a) the Guinier plot fitted with the Guinier law according to Equation (4.1) as an inset, (b) Lorentz-correction and (c) the log-log representations of the data.

Figure 4.4. Raman spectra as a function of wavenumber at room temperature varying the draw ratio for dis-UHMWPE/gold nanocomposite films at (a) 1500 to 1000  $\text{cm}^{-1}$  and (b) 1500 to 1400  $\text{cm}^{-1}$  including the Lorentzian fitting (only for DR1 and DR5 to avoid confusion). The green arrows indicate the variation in intensity of each peak with orientation.

Figure 4.5. (a) Vis/NIR absorbance and (b) linear absorption coefficient both as a function of wavelength at room temperature varying the draw ratio for ds-UHMWPE/gold nanocomposite films.

Figure 4.6. Measured thermal conductivity for partially drawn gold/UHMWPE nanocomposite films (DR4 and DR5) versus the angle with respect to the stretching direction at 30°C. The presented data were provided from our collaborators in CalTech.

Figure 4.7. (a) The real part of dielectric permittivity and (b) capacitance of gold/UHMWPE nanocomposite films as a function of frequency at 30°C varying the stretching draw ratio.

Figure 4.8. The charge-discharge dc currents gold/UHMWPE nanocomposite films as a function of time for different drawing ratios at: (a) 100V, (b) 300V and (c) 500V.

Figure 4.9. Recovered energy density values of gold/UHMWPE nanocomposite films as a function of time varying the draw ratio for: (a) 100V, (b) 300V and (c) 500V. The inset represents the coefficient of energy recovery efficiency after 30 seconds of discharge.

Figure 4.10. Coefficient of recovery efficiency as a function of time for the samples under study at: (a) 100 V, (b) 300 V and (c) 500 V.

Figure 4.11. The real part of dielectric permittivity as a function of frequency varying the time for the samples under study: (a) DR1, (b) DR2 and (c) DR3. As an inset the corresponding imaginary part of dielectric permittivity is presented.

Figure 4.12. The logarithmic derivative of dielectric permittivity as a function of frequency (following Equation (4.11)) varying time for the samples under study: (a) DR1, (b) DR2 and (c) DR3. As an inset the log-log fittings of the imaginary part minus the logarithmic derivative of dielectric permittivity as a function of frequency (following Equation (4.12)) are presented with a fixed slope of -1.

Figure 4.13. The calculated estimation of the dc conductivity for the samples under study as a function of time. The lines serve as guides for the eye only.

Figure 4.14. The real part of electric modulus for the samples under study as a function of time. As an inset, a normalized representation of the same data is provided with a common fitting as a superposition of extended time ( $t + t_0$ ) and draw ratio with DR3 being the reference sample ( $t_0 = 0$  s). The  $t_0$  parameter for samples DR1 and DR2 was calculated to be 520.5 s and 347.0 s respectively. The lines correspond to fittings follow Equation (4.13) and the parameters are presented at Table 4.4.

Figure 4.15. 2D WAXS patterns of oriented UHMWPE/gold nanocomposites at (a) DR72.5 and (b) DR150 with corresponding crystallinities  $X_c$  to be 84.8% and 86.3% respectively.

Figure 4.16. 2D SAXS patterns of UHMWPE/gold nanocomposites at (a) DR72.5 and (b) DR150. After integration, the (c) Guinier plot of the SAXS patterns are also given, fitted with the Guinier law. The diameters of the gold nanoparticles as obtained by the Guinier law for spherical nanoparticles are presented within the graph.

Figure 4.17. Raman spectra as a function of wavenumber for UHMWPE/gold composites at high drawing ratios.

Figure 4.18. Vis/NIR absorbance of the UHMWPE/gold nanocomposites as a function of wavelength. For clarity, blue and green lines are employed to show the corresponding peaks.

Figure 4.19. 2D WAXS patterns. (L – R): DR2.5, DR5.0, DR7.5, DR72.5 and DR150 draw ratios of dis-UHMWPE containing: (top) ZnO nanoparticles and (bottom)  $\beta$ -carotene.

Figure 4.20. Calculated crystallinities as obtained from the integrated WAXS patterns for the different fillers as a function of draw ratio, indicating an increase with uniaxial orientation.

## LIST OF TABLES

Table 1.1. Melting peak and average crystallinity of PE types.

Table 2.1.  $M_w$ ,  $M_n$  and polydispersity of the samples. When applicable, the theoretical  $Al_2O_3$  concentration was calculated based on the assumption that all the MAO added as co-catalyst does react during quenching to form  $Al_2O_3$ , so it is in fact the maximum amount that can be realistically found in the sample.

Table 3.1. First and second heating runs of all the samples under study.

Table 3.2. The  $G_\infty$ ,  $G_\infty - G_s$ ,  $G_N$ ,  $\beta$  and  $\gamma$  Havriliak-Negami parameters for the fittings at 39.8 Hz.

Table 3.3. Arrhenius and VFTH fitting parameters of the corresponding relaxations.

Table 4.1. Relative Raman intensities as a function of uniaxial plastic deformation with respect to the  $1063\text{ cm}^{-1}$  peak.

Table 4.2. Fitting parameters from the Raman spectra according to Equation (4.3).

Table 4.3. Coefficient of recovery efficiency at 30 seconds varying the voltage for the samples under study.

Table 4.4. Fitting parameters for the real part of electric modulus as a function of time, according to Equation (4.13) employing two modes. The fitted superimposed data in the inset of Figure 4.14 are also included.

## INDEX PAGE

Introduction .....	pp. 17 – 18
1. Literature Review .....	pp. 19 – 48
1. Polyethylene’s crystalline structure .....	pp. 23 – 28
2. Polymer chain entanglements .....	pp. 28 – 33
3. Relaxation dynamics .....	pp. 33 – 42
1. Dielectric relaxation .....	pp. 33 – 38
2. Mechanical relaxation .....	pp. 38 – 42
4. Orientation through plastic deformation .....	pp. 42 – 45
5. Electrical energy storage in dielectric materials .....	pp. 45 – 48
2. Experimental .....	pp. 49 – 55
1. Chemical synthesis of dis-UHMWPE .....	pp. 49
2. Specimen processing .....	pp. 50 – 52
3. Characterization techniques .....	pp. 52 – 55
3. Dis-UHMWPE chain dynamics .....	pp. 56 – 87
1. Relaxation dynamics .....	pp. 56 – 79
1. Torsional rheology .....	pp. 56 – 68
2. Broadband dielectric spectroscopy .....	pp. 68 – 78
3. Comparison .....	pp. 78 – 79
2. Entanglement dynamics .....	pp. 79 – 86
1. Connection between electric modulus & mechanical shear modulus .....	pp. 79 – 84
2. The molecular weight effect .....	pp. 84 – 86
3. Conclusions .....	pp. 86 – 87
4. Uniaxial plastic deformation in the presence of fillers .....	pp.
1. Metallic filler: Au nanoparticles at low draw ratios .....	pp. 88 – 116
1. Structural information & optical absorption .....	pp. 88 – 98

2.	Thermal Conductivity .....	pp. 98 – 99
3.	Electrical energy storage & recovery .....	pp. 99 – 108
4.	Entanglements formation .....	pp. 108 – 116
2.	Metallic filler: Au nanoparticles at high draw ratios .....	pp. 116 – 121
3.	Ceramic or organic fillers: ZnO nanoparticles or $\beta$ -carotene .....	pp. 121 – 124
4.	Conclusions .....	pp. 124 – 125
5.	Conclusions & future work .....	pp. 126 – 130
1.	Concluding remarks .....	pp. 126 – 129
2.	Future work .....	pp. 129 – 130
6.	Acknowledgements .....	pp. 130 – 131
7.	Publications and Conferences .....	pp. 132 – 134
8.	Short Curriculum Vitae .....	pp. 135
9.	References .....	pp. 136 – 163

*"Τό γάρ άπειρον ουδέν άλλο ή ύλη έστιν ού δύναται  
δ' ή ύλη είναι ενέργεια, αν μή τό ποιούν ύποκέηται"*

*"Because infinity is nothing but matter;  
matter cannot be energy unless there is a cause"*

Flavius Aetius (391 AD – 454 AD) on Anaximander's (610 BC – 546 BC) Theory of Infinity.



## Introduction

The word "polymer" is a composite word that derives from the Greek words "πολύ" and "μέρη" and translates in to something that consists of many parts. Hermann Staudinger was the first to identify polymers as macromolecules of repeating units, initiating the era of Polymer Chemistry. For his work, Hermann Staudinger was awarded the 1953 Nobel Prize in Chemistry and changed modern society irreversibly. Since then, the scientific and industrial interest towards polymers has advanced in such extent, that various areas of expertise need to join forces, from Chemistry, Physics and Materials Science to Chemical, Mechanical, Electrical, Pharmaceutical and Materials Engineering, all with a common goal, to understand and appreciate polymer properties and utilize them for the progress of society. Hence, understanding the chemical and physical properties of polymeric materials, researchers can invent new ways to employ and advance them. Among all the different classes of polymers, polyethylene (PE) is the most commercially important, ranging from low-cost everyday products like pipes and cable insulation to high-end applications like artificial hips and high-strength parts for the aerospace industry.

When the molecular weight exceeds  $10^6$  g/mol and the chains are linear (no branches) then the resulting polyethylene grade is called ultra-high molecular weight polyethylene (UHMWPE). It has been possible to synthesize ultra-high molecular weight polyethylene that is less entangled and at temperatures above the melting ( $> 140^\circ\text{C}$ ) it is metastable due to the formation of entanglements. This disentangled ultra-high molecular weight polyethylene exhibits very interesting physical properties and possesses the ability to be solid state processed to maintain some of its disentangled character. More information on the literature about disentangled ultra-high molecular weight polyethylene and its solid-state processing can be found in Chapters 1 and 2 respectively.

In the present doctoral research, the physical properties of disentangled ultra-high molecular weight polyethylene and its nanocomposites are investigated. The main objectives of this work can be summarized in the five questions below:

- (1) What is the role of the disentangled amorphous phase upon the mechanical and dielectric relaxation dynamics in a broad range of temperatures and frequencies?
- (2) Is the solid state metastable like the melt state?
- (3) How does uniaxial orientation affect the physical properties?
- (4) How does uniaxial orientation affect the formation of entanglements?

(5) What is the role of nanofillers in the resulting physical properties with or without uniaxial orientation?

Chapter 3 section 1.1 of the present dissertation provides the mechanical relaxation dynamics of disentangled ultra-high molecular weight polyethylene compared to a fully entangled UHMWPE sample while the dielectric relaxations are examined in Chapter 3 section 1.2; the comparison between the two techniques in terms of relaxation dynamics is given in Chapter 3 section 1.3 (Question 1). Chapter 3 section 2 provides experimental evidence that entanglements are forming also in the solid state, as examined by dielectric spectroscopy, above a critical temperature (Question 2). The effect that uniaxial orientation has upon the structure, the thermal conductivity and the dielectric properties was investigated in Chapter 4 section 1 (Question 3). With dielectric spectroscopy it was possible to study the formation of entanglements as a function of orientation, and how it affects the dc conductivity of the system (Question 4). Finally, the presence of nanofillers and how they affect the physical properties was thoroughly examined in most of Chapter 3 and all the Chapter 4 (Question 5).

## 1. Literature Review

Polyethylene is an alkane ( $-\text{CH}_2-\text{CH}_2-$ ) with a degree of polymerization ranging from 100 to over 250,000 resulting in molecular weights that exceed 10,000,000 g/mol. There are several types of polyethylene materials, depending on their molecular weight and branching degrees [1]. Low density polyethylene (LDPE) is a common type of industrial polyethylene used for cable applications and is characterized by a substantial concentration of branches that hinder its ability to crystallise, hence resulting into low crystallinity values [2–5]. Cross-linked polyethylene (XLPE) can also find use in electrical insulation applications since they exhibit high breakdown strengths [6]. High density polyethylene (HDPE) contains a low branching concentration and therefore is mostly linear. Naturally, due to its linear chains, HDPE has a high degree of crystallinity and hence is most resistant to radiation [7]. Ultra-high molecular weight polyethylene (UHMWPE) differs from HDPE in the average chain length, where it exhibits 10 to 100 times higher degree of polymerization, resulting in average molecular weights above  $10^6$  g/mol [8,9]. In the Table 1.1 presented below, thermal information for these materials as reported in the literature is shown.

Table 1.1. Melting peak and average crystallinity of PE types [10,11].

Polymer	Melting peak (°C)	Crystallinity (%)
LDPE	114.1	43.8
HDPE	132.1	74.3
UHMWPE	137.2	56.9

The molecular characteristics of plain polyethylene after uniaxial orientation were firstly studied during the 50s and 60s by the group of Richard S. Stein in Amherst, Massachusetts. They observed that upon stretching, both the crystalline and amorphous polymer chains were oriented, thus, affecting the optical properties [12,13]. They draw a connection between the structural information (spherulitic dimensions) and the resulting optical and thermal properties [13–15]. In the same university, during the late 70s, the group of Roger S. Porter achieved higher stretching orientations than ever before (over 30 times the initial length), after processing HDPE in the solid state below the  $T_m$  [16]. They also discovered that oriented samples possessed enhanced mechanical properties such as high tensile modulus and strength due to the increase and orientation of the crystalline phase and also due to the

preferential movement of defects along the stretching axis [17–19]. The increase in crystallinity induced by orientation was observed by their group by means of wide-angle X-ray scattering and the fibril orientation was characterized by means of small-angle X-ray scattering respectively [20,21]. The mechanical properties of the oriented tapes of HDPE were highly affected by molecular weight (enhanced as  $M_w$  increased) and were found to be unaffected by the molecular weight distribution [18].

Several fillers have been employed over the years to modify and reinforce the properties of polyethylene to satisfy several applications. Even from the early 70s, polyethylene was considered a great candidate for orthopaedic applications such as joint replacement [22]. For such applications, fillers like carbon fibres and graphite have been employed to achieve better mechanical properties [23–25]. Alternative composites for bone replacement and green applications were reinforced with hydroxyapatite and wood fibres respectively [26,27]. To enhance the electrical and thermal conduction properties, metal particles were found useful due to their significantly higher conductivities than the fully insulating polyethylene [28,29]. Electrically speaking, the insulating character of polyethylene has attracted the interest of the polymer physics community, not solely because of the application as mentioned earlier, but for the dynamics as well. As it will be discussed later on, polyethylene is an ultra-low loss material and suitable fillers are needed as dielectric probes in order to determine its dielectric relaxation processes [30–33].

Industrially speaking, polyethylene is the most important and commercialized polymer and it covers over a third of the total plastic production worldwide [34]. A relatively narrower market share is occupied by UHMWPE, the linear highly crystalline analogue with an average molecular weight exceeding  $10^6$  g/mol, used especially for high-end applications, like the biomedical sector [9,35,36]. As mentioned earlier, due to UHMWPE's very high molecular weight and linear character, each chain is very long, resulting into a highly entangled melt state. As a result, UHMWPE is difficult to process with conventional thermoplastic methods due to the extremely high viscosity of this highly entangled melt [9,37,38]. These techniques traditionally include extrusion, injection moulding and film blowing at temperatures considerably higher than the melting (usually at temperatures over  $190^\circ\text{C}$ ) [39–41]. To prepare UHMWPE fibres, another processing technique is employed, known as gel-spinning, where a reduction of entanglement is realized through the use of dilute solutions (less than 10% w/w of polymer) of UHMWPE in suitable solvents like decalin [42] and paraffin oil [43]; the resulting fibres have been found to exhibit very high tensile strength (8 GPa) comparing to the pristine UHMWPE (0.04 GPa) [43], but very high

amounts of solvents need to be used and recycled in this process. The aforementioned high amounts of solvents are employed to decrease the entanglement density and achieve better drawability and to reduce the melting point. In order to overcome this issue, the realisation of ultra-high molecular weight polyethylene with a reduced number of entanglements i.e. disentangled (dis-UHMWPE) has been made by means of both pre- and post-synthesis methods [44–47]. Dis-UHMWPE presents significantly improved processability when compared with entangled UHMWPE. However, chain reptation in the melt results in the formation of entanglements, progressively increasing the viscosity of the polymer (the molecule is confined within a virtual tube of a thickness determined by entanglements from neighbouring molecules and exhibits snake-like movement, i.e. reptation). Hence, molten dis-UHMWPE should be considered a material in a non-equilibrium state, where the kinetics of entanglement formation are governed by several factors such as temperature, molecular weight, initial number of entanglements and presence of fillers. Rheology has proved to be an effective method to follow the formation of entanglements in the melt, both in the presence or absence of fillers [48–50]. It has been reported that the value of the real part of mechanical shear modulus,  $G'$ , of dis-UHMWPE approaches that of entangled UHMWPE once the equilibrium, fully-entangled state is reached [49–51]. Rheological studies have also allowed to determine molecular weights and their distributions of such polymers [49,50,52]. However, one major limitation of the dynamic rheological analysis is the upper frequency limit since most rheometers can reach up to 100 Hz, although the use of piezoelectric resonators can extend the frequency range [53]. This limitation is crucial in the study of processes with very short relaxation times where higher frequencies (or lower temperatures) are required that otherwise might be outside the experimentally observed window of frequencies, like sub-relaxations of various polymers including polyethylene. To overcome this issue of limited frequencies, broadband dielectric relaxation spectroscopy (BDRS) is a powerful experimental technique to investigate the interaction of electromagnetic waves with matter in the frequency range of  $10^{-6}$  to  $10^{12}$  Hz. Combining the broad frequency range with temperature variations, *BDRS* can identify different processes in polymers and polymer composites such as polarization and conductivity phenomena, molecular dipolar fluctuations, thermal transitions, charge transport and interfacial polarization [54,55]. The properties of pure UHMWPE have not been thoroughly investigated from a dielectric relaxation point of view, although some research articles have used BDRS to analyse the electrical properties of UHMWPE based nanocomposites intended for capacitor applications [11,56–59]. Dielectric and mechanical dynamic analysis can be employed in parallel to analyse the relaxation

behaviour of polymeric materials, although in some cases, processes arising from the same phenomena might appear at different relaxation times [60].

Considering the aforementioned unique properties of dis-UHMWPE, it has attracted the interest of several research groups around the globe where a few notable examples are going to be briefly discussed from the last 5 years (since 2014) in order to relate the present doctoral work with the interests of the community. The mechanisms underlying the formation of entanglements still bother the researchers working with dis-UHMWPE. With tensile tests conducted above melting (to avoid the contribution of the crystalline part), the effect of sintering time (0.25, 2 and 20 hours) and sintering temperature (150°C, 200°C and 250°C) were investigated varying the molecular weight (0.6 – 10.5 Mg/mol) [61]. It was observed that the diffusion of chain segments depends strongly on the molecular weight and thus the entanglements formation is affected (hindered) as the molecular weight increases. In parallel, findings indicated that the variation in sintering temperature affects more the entanglement density (a quantity related with the reciprocal average molecular weight between entanglements) than variation in the sintering time; the significance of temperature upon the formation of entanglements indicates that is an energy dependent process (an energetic barrier needs to be exceeded) [62]. The molecular weight dependence agrees with melt rheology experiments conducted from our group which are discussed in section 2 of the present chapter. A discussion about the entanglements formation energy barrier is provided in Chapter 3 section 2 from a relaxation dynamics point of view. Considering the lower viscosity of dis-UHMWPE due to lower entanglement density, it was found that it can be melt injection moulded; the injection moulding technique was observed to induce and orient the crystalline structure, enhancing thus the resulting mechanical properties [63]. Understanding the formation of entanglements mechanism and the parameters that affect it, is useful in improving the miscibility of dis-UHMWPE with other polymers. The extremely long chains of UHMWPE contribute into its great mechanical properties (high impact strength and wear resistance) making it a great candidate as a reinforcement in polymer-polymer composites and blends. Another polyethylene grade of particular industrial interest is HDPE, making it ideal as a host matrix to UHMWPE because of its common characteristics i.e. linear chains and high values of crystallinity. However, melt rheology experiments have indicated poor dissolution of fully entangled UHMWPE with HDPE due to high melt viscosity values (the zero-shear melt viscosity of UHMWPE is  $\sim 10^7$  times higher than HDPE) and thus a low self-diffusion coefficient; the use of dis-UHMWPE resulted into good dissolution with the HDPE matrix, according to the lower mechanical loss values ( $\tan\delta =$

$G''/G'$ ), and exhibited considerable strain hardening at low dis-UHMWPE concentrations (1%) [64]. It was confirmed via small amplitude oscillatory shear measurements that at least 50% of the dis-UHMWPE chains were fully dissolved in the HDPE matrix due to the higher mobility of the disentangled chains [65]. At higher dis-UHMWPE concentrations (10%) the observed tensile strength of the resulted blend was almost doubly increased (from 45.7 MPa to 83.1 MPa) [66]. Efforts to produce more uniform UHMWPE/HDPE blends by *in situ* polymerization techniques have also indicated that the low entanglement density of dis-UHMWPE is paramount for good interconnection between the two polymers [67]. The addition of fillers to reinforce dis-UHMWPE has also been investigated in the recent literature, also in comparison with the chain dynamics, like in the case of polyoctahedral silsesquioxanes (POSS) that retarded the polymerization due to electron transfer to the catalyst and increased the entanglement density, the thermal stability and the hydrophilicity [68]. The increased entanglement density was observed by means of melt rheology and was attributed to the high surface of the nanoparticles and their strong interaction with the UHMWPE chains. The thermal stability was improved in the order of  $\sim 20^{\circ}\text{C}$ , according to a thermogravimetric analysis investigation and the contact angle of dis-UHMWPE/POSS film with ultrapure water decreased from  $84^{\circ}$  to  $75^{\circ}$ . In addition, it affected the lamellae thickness quantitatively (since POSS was incorporated in the polymer chains) and slightly increased the crystallinity by 3%, both studied by means of differential scanning calorimetry [69]. In another case, the mechanical properties and the ability of dis-UHMWPE to be solid-state processed were found to enhance in the presence of graphene oxide nanosheets that affected the polymerization process resulting into an even lower entanglement density [70]. According to the authors, the presence of graphene oxide allowed the polymerization of a few chains on top of the nanosheets and increased the average distance between the chains, contributing to a decreased entanglement density. As it can be observed from the research efforts of other researchers, the main focus of dis-UHMWPE related research concentrated on the entanglement density and how it can affect the resulting properties, which is the ultimate goal of the present doctoral dissertation.

The past decade progress and innovation towards the scientific (chemistry and physics) and engineering (processing) characteristics of dis-UHMWPE have been also explored specifically by our group based in the Department of Materials in Loughborough University. The aforementioned advancements have been published in peer review journals and are the literature basis for the present doctoral work. The aim of this work is to advance further some scientific topics regarding dis-UHMWPE and therefore is based on the published know-how

that concerns the physical properties of the specific polymer. In the following literature review, a specific mention is going to be stated when addressing characteristics of dis-UHMWPE that were investigated from our group.

### 1.1. Polyethylene's crystalline structure

A semi-crystalline polymer can be considered as a mixture of crystalline and amorphous regions present in the same macromolecular chain [71]. The presence of these two phases and their interaction, are definitive for the resulting physical properties of a polymeric material.

The realistic arrangement at which the linear polymer chains crystallize, can be found between two extreme conditions that are presented in Figure 1.1 below. In one case, each chain crystallizes to the maximum possible extent producing a regularly folded arrangement while in the other case, a completely random sequence of the location of the chain within the crystal results into less crystals per chain length and crystalline defects [72]. It is also obvious from the graph that in the latter case, the amorphous loops are entangled and of variable length.

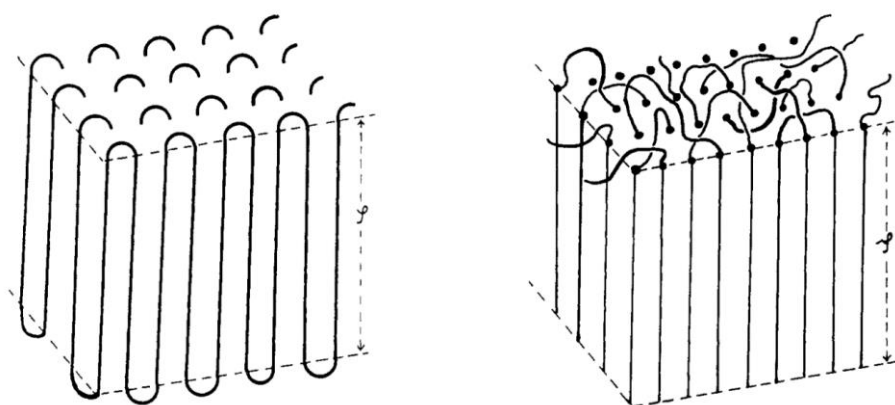


Figure 1.1. Crystalline structures of thickness  $\zeta$  of regularly folded chains (left) and irregularly folded chains (right). The graph was taken from P.J. Flory (1962) [72].

The crystalline structure of polyethylene has caught the interest of scientists since the 1930s with C.W. Bunn's revolutionary work proving the crystalline structure of polyethylene exceeding 130 carbon atoms, to be orthorhombic, via X-ray scattering [73]. It was previously realized that the positions of the atoms participating in a crystal are aligned in a plane zig-zag way, as it can be appreciated in Figure 1.2 below [74]. The dimensions of the linear polyethylene's orthorhombic cell at 23°C are:  $\mathbf{a} = 7.4069 \text{ \AA}$ ,  $\mathbf{b} = 4.9491 \text{ \AA}$  and  $\mathbf{c} = 2.55117 \text{ \AA}$  (where  $\mathbf{a}$ ,  $\mathbf{b}$  and  $\mathbf{c}$  can be found in Figure 1.2 respectively, with  $\mathbf{c}$  being along the chain) and produce a crystal density of  $0.9962 \text{ g/cm}^3$  [75]



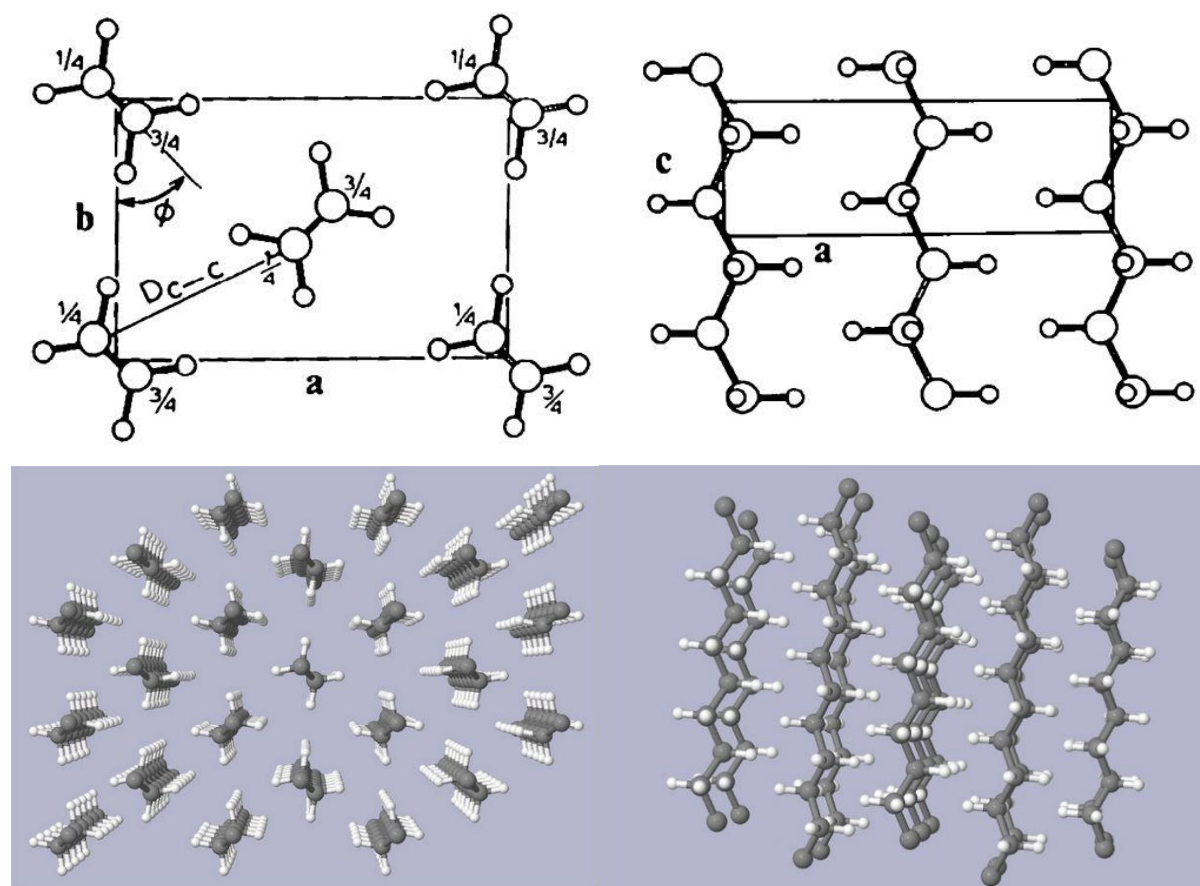


Figure 1.2. A 2D (top) and 3D (bottom) representation of a crystalline (orthorhombic) polyethylene chain. The images were obtained from Alsaygh et al., (2014) [76].

The orthorhombic crystal phase possesses anisotropic mechanical properties where the mechanical modulus is 3.2 GPa, 3.9 GPa and 216 GPa in the **a**, **b** and **c** direction respectively [77–79]. This anisotropy is a result of the pronounced difference in the attractive bond forces between the atoms along the chain and perpendicular to it. When the crystalline structures are randomly distributed within a polyethylene sample, macroscopically the material is isotropic. The (110) and (200) crystallographic planes of the orthorhombic polyethylene crystal are given in Figure 1.3 below. According to the Wulff-Bragg condition (Bragg’s law), a relation between the distance between atoms in the crystal lattice,  $d$ , the scattering angle,  $2\theta$ , and the wavelength of the beam,  $\lambda$ , can exist as seen below with  $n$  a positive integer:

$$d = \frac{n\lambda}{2\sin\theta} \quad (1.1a)$$

However, since the scattering angle is wavelength dependent and various research groups around the globe might employ X-ray beams of different wavelength, the momentum transfer vector,  $q = 4\pi \sin \theta/\lambda$ , was introduced as seen below:

$$d = \frac{2n\pi}{q} \quad (1.1b)$$

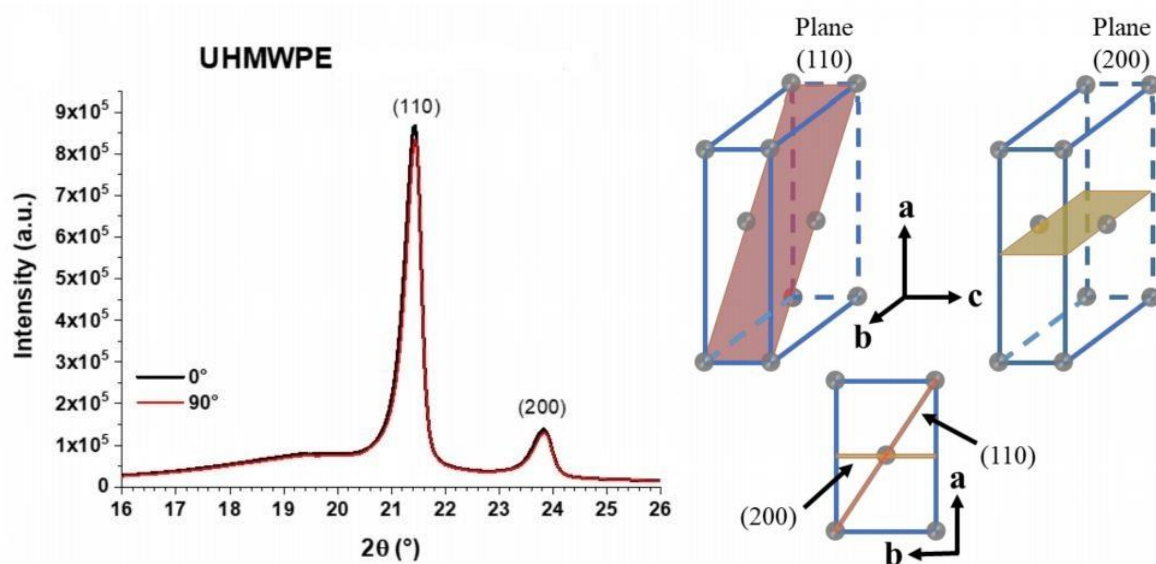


Figure 1.3. The two most intense diffraction peaks of polyethylene’s orthorhombic crystal phase (left) with their corresponding cell planes (right) The graph was taken from L.M. Lozano-Sánchez et al., (2018) [80].

Two additional crystalline phases have also been discovered; the less stable monoclinic phase (Figure 1.4 top) present in samples after mechanical stress and the high-pressure (300 MPa) hexagonal phase (Figure 1.4 bottom). The hexagonal phase has been found via wide-angle X-ray scattering to form at temperatures close to the melting, a transition that can also be achieved after irradiating the polyethylene samples with  $\gamma$ -rays at 40°C – 45°C [81–83]. In specific thermodynamic conditions (250°C and 330 MPa) three phases of polyethylene can co-exist (triple point) namely orthorhombic, hexagonal and melt states [84,85].

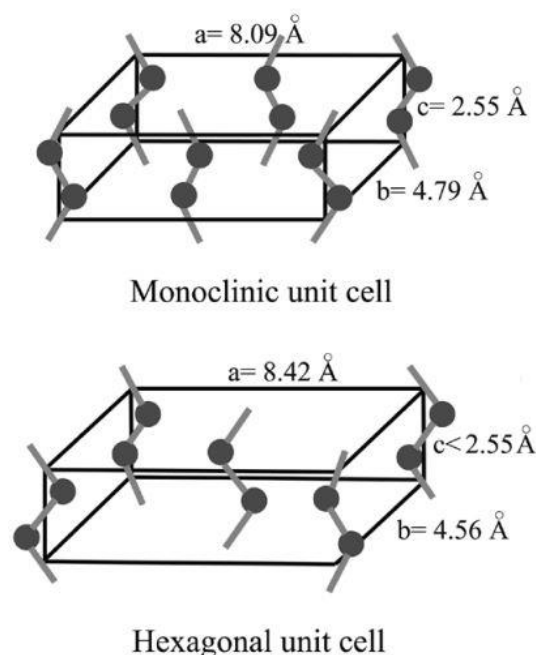


Figure 1.4. The monoclinic (top) and hexagonal (bottom) crystal cells of linear polyethylene, including the cell dimensions. The image was obtained from G.-R. Nejabat (2018) [86].

Although the crystalline structures of disentangled and fully entangled commercial UHMWPE samples are the same (including the lamellae thickness of around 20 nm), significant differences in the crystal size and morphology have been observed, as investigated in previous works from our group. The lateral dimensions of a dis-UHMWPE crystal are significantly larger (over  $1 \mu\text{m}$  against  $0.3 \mu\text{m}$  [46]) comparing to those of a commercial sample, attributed to the chemical synthesis conditions (discussed in Chapter 2 section 1); during the synthesis of a commercial sample, the relatively small distance between the active sites and their high density, are favouring the formation of more but smaller crystals [87,88]. The low concentration of the single-site catalyst employed for the polymerization of dis-UHMWPE is responsible for the formation of large crystals consisting of single chains, as the active sites of the catalyst are considerably far away from each other (in a molecular scale) [89]. The aforementioned concept can be simply observed by means of Scanning Electron Microscopy (SEM) as presented in Figure 1.5 below, with the dis-UHMWPE sample (Figure 1.5a) exhibiting a ‘flower’ morphology with each pedal corresponding to a crystalline unit [90].

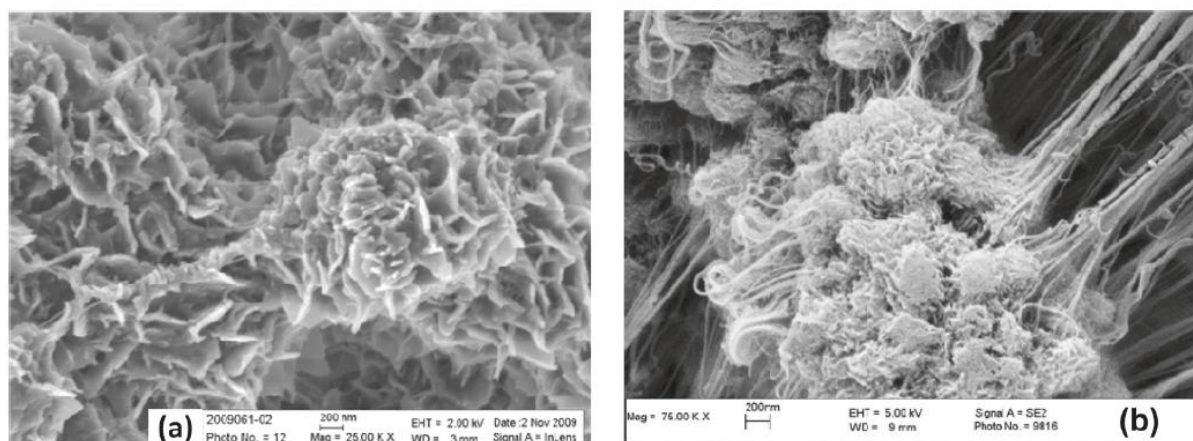


Figure 1.5. The surface morphology of (a) a pristine disentangled UHMWPE sample and (b) a commercial fully entangled UHMWPE sample, as obtained by means of SEM. The pictures were obtained from A. Pandey *et al.*, (2011) [90].

In addition to the differences in lateral dimensions, the crystals originating from dis-UHMWPE, after the sample is removed from the reactor (nascent), consist mostly of a single chain, as explained previously. Because of this, the chain is regularly folded when re-entering the crystal in a tight form, as presented below in Figure 1.6a. The crystals of a commercial fully entangled sample are shared between different polymer chains, with entanglements on the crystal surface contributing into less folded structures (Figure 1.6b). Finally, regardless of the entanglement density, after melt processing the pristine crystalline structure is destroyed, resulting into crystals consisting of several chains and highly entangled loops (Figure 1.6c) [90]. The aforementioned concepts for dis-UHMWPE have been investigated thoroughly in the literature by means of thermal analysis [89,91,92].

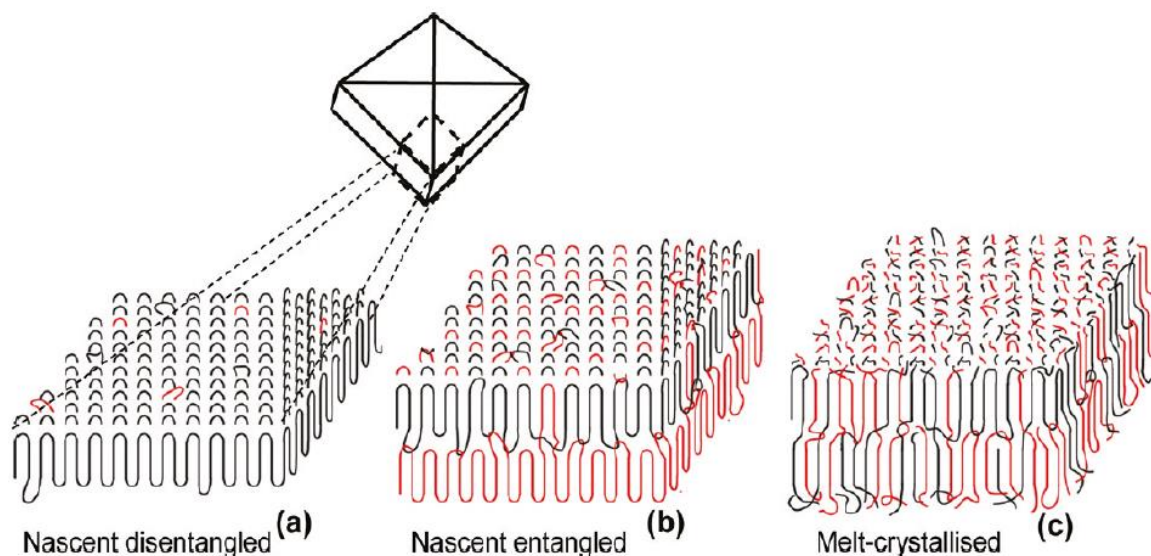


Figure 1.6. Schematic representation of the UHMWPE crystal morphology for (a) nascent disentangled crystals, (b) nascent commercial crystals and (c) crystals after melting. The black lines correspond to one specific polyethylene chain while the red lines correspond to additional chains. The graphs were taken from A. Pandey *et al.*, (2011) [90].

The structure can also be investigated by means of neutron scattering and Raman spectroscopy and the crystallinity concentration can also be estimated by means of differential scanning calorimetry [93–95]. Discussion about the crystal morphology and size is further given in Chapter 3 section 1.1 in parallel with torsional rheology and DSC experimental results. The crystallographic characteristics of dis-UHMWPE varying the draw ratio have been investigated in Chapter 4 sections 1.1, 2 and 3 where an increase in crystallinity is observable from relatively low draw ratios up to high draw ratios and no phase change (from orthorhombic to monoclinic) was observed.

## 1.2. Polymer chain entanglements

For decades the dynamic properties of concentrated polymer solutions and melts were not well understood above a critical molecular weight, until Nobel laureate Pierre-Gilles de Gennes' (1932 – 2007) tube theory of entangled systems [96]. The chain dynamics are governed by the presence of topological constraints caused by neighbouring chains, namely entanglements, as seen in Figure 1.7 below. These entanglements restrict the diffusion of the chains into a snake-like motion (reptation) along an imaginary tube [97]. The effect of entanglements on the chain dynamics can be considered as cross-links of finite (temporary)

life-time [98,99]. This parallel with cross-links has been reinforced by experimental observation of an increasing elevation of the glass-to-rubber transition temperature with increasing molecular weight [100]. Since the 60s, it was already apparent that only above a critical molecular weight this effect is observable in either polymer solution or bulk conditions, with the molecular weight between entanglements,  $M_e$ , to be characteristic for each amorphous polymer system [101]. Figure 1.8 shows that viscosity increases in a non-linear way with the molecular weight that is attributed to the formation of entanglements after a critical molar mass. At molecular weights lower than this critical molecular weight, the chain dynamics follow the Rouse theory, neglecting thus all the hydrodynamic interactions between monomers [102].

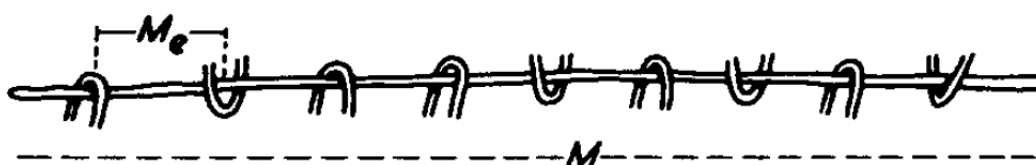


Figure 1.7. Schematic representation of polymer entanglements in a polymer chain of molecular weight  $M$  and average molecular weight between entanglements  $M_e$ . The graph was taken from D.T. Turner (1977) [100].

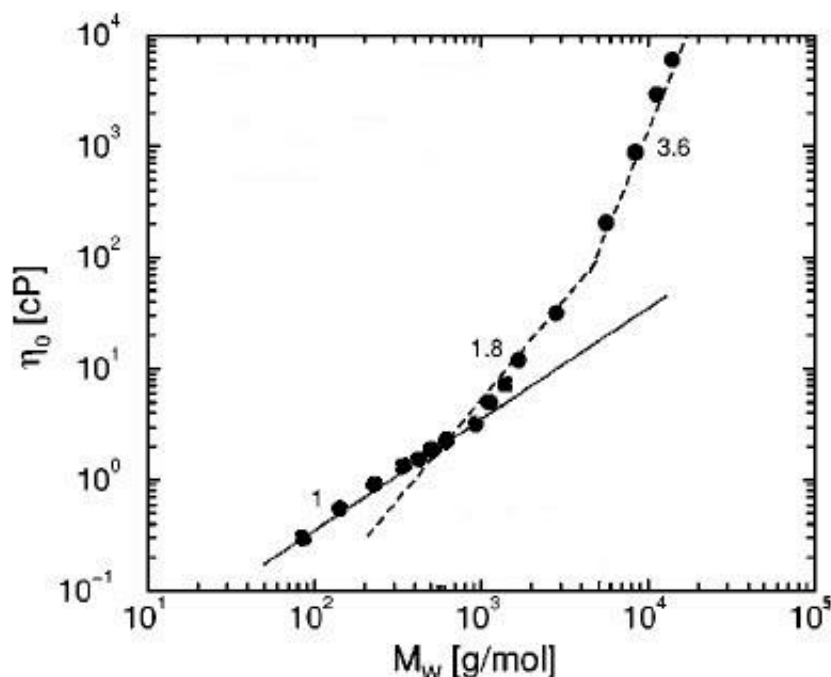


Figure 1.8. The zero shear viscosity,  $\eta_0$ , as a function of molecular weight for polyethylene. The graph is taken from J.T. Padding and W.J. Briels (2002) [103].

By employing a homogeneous catalyst during the polymerization of UHMWPE, it is possible to form disentangled high molecular weight polymers at room temperature; the low temperature is paramount to crystallize the polymer chains so fast so they form (almost) monomolecular crystals i.e. crystalline structures that are consisted of only one/few polymer chains [46]. Consequent to melting, the disentangled polymer molten chains are thermodynamically out of equilibrium, thus entanglements start to form, affecting the mechanical properties by building up the elastic modulus [104]. This effect can be appreciated graphically for one disentangled and one entangled sample (Figure 1.9a) and two samples of different molecular weight (Figure 1.9b), according to Equation (1.2) which connects the average molecular weight between entanglements,  $\langle M_e \rangle$ , with the elastic modulus in conditions of thermodynamic equilibrium, as explained below [105]:

$$G_N^0 = \frac{g_N \rho R T}{\langle M_e \rangle} \quad (1.2)$$

where  $G_N^0$  is the plateau modulus at thermodynamic equilibrium state,  $g_N$  is a numerical factor,  $\rho$  is the physical density of the material at the absolute temperature  $T$ ,  $R$  is the gas constant and  $M_e$  is the molecular weight between entanglements and it is inversely proportional to the entanglement density.



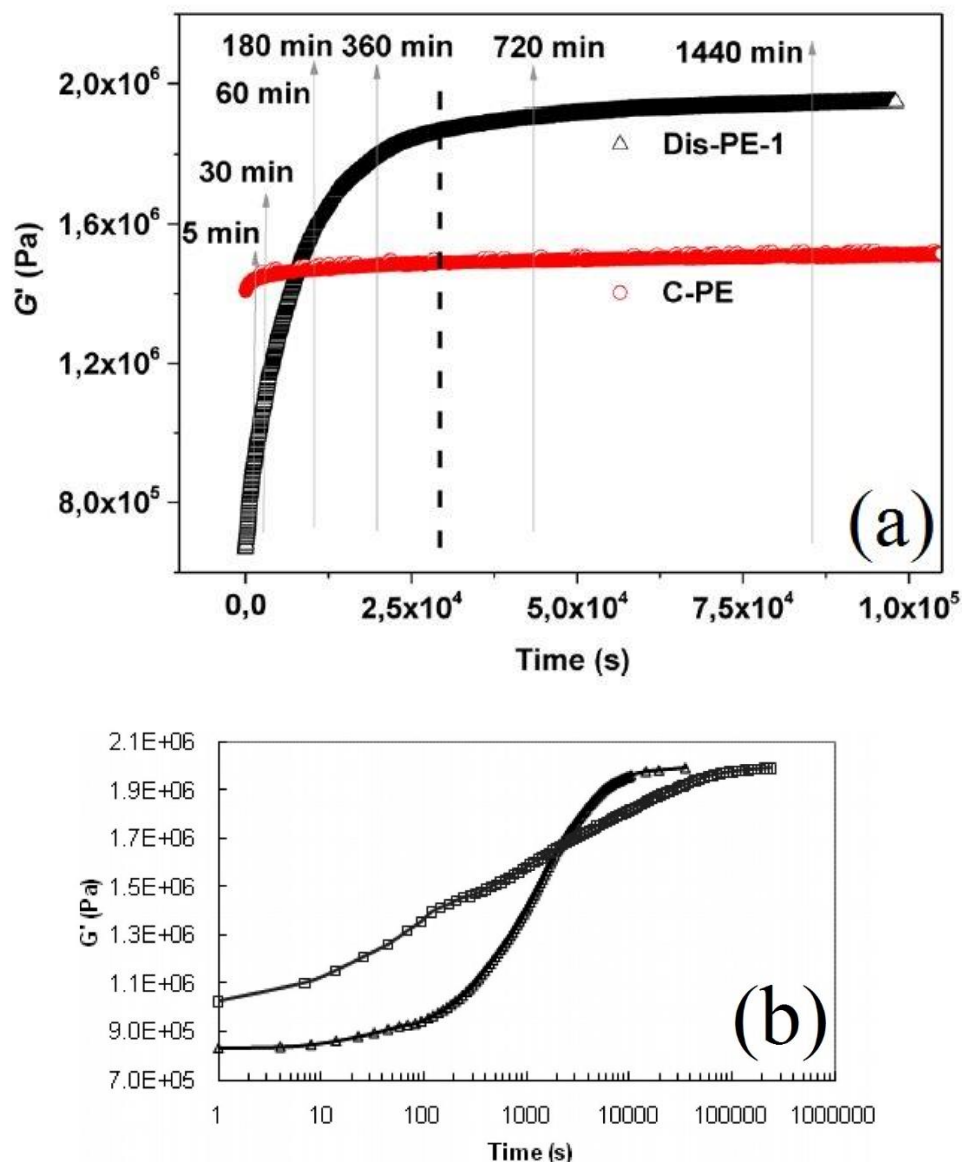


Figure 1.9. The real part of mechanical modulus as a function of time at  $160^\circ\text{C}$  of (a) a disentangled UHMWPE sample (black points) and an entangled UHMWPE sample (red points) of similar molecular weights; (b) two initially disentangled UHMWPE samples of molar masses  $2.0 \times 10^6$  g/mol ( $\blacktriangle$ ) and  $5.3 \times 10^6$  g/mol ( $\blacksquare$ ) g/mol. The graphs were obtained from K. Liu *et al.*, (2016) [49] and S. Talebi *et al.*, (2010) [104] respectively.

As it can be appreciated from Figure 1.9a, the mechanical properties of a disentangled UHMWPE sample as expressed by means of the real part of mechanical shear modulus,  $G'$ , are time dependent where the  $G'$  values increase until a plateau value that indicates the fully entangled equilibrium state. On the other hand, the fully entangled sample exhibits a very narrow variation in the  $G'$  values and it reaches the plateau at a significantly shorter time indicating that the material was at equilibrium [49]. The short increase in the beginning



corresponds to the formation of entanglements of the just molten crystals. The effect of molecular weight of dis-UHMWPE sample is presented in Figure 1.9b where the timescale of the entanglements' formation is different for each sample, with the higher molecular weight samples requiring more time to reach the fully-entangled equilibrium. This is due to the fact that the internal friction that hinders the movement of a particular chain increases with molecular weight. In addition, when the formation of entanglements is followed via melt plate-plate rheology, an initial rapid increase of the real part of mechanical modulus can be observed, followed by a second slower increase, until equilibrium is reached. Thus, according to Liu et al. (2016), the curve can be divided into two regions, with the first drastic change to be considered as the chain explosion, i.e. formation of entanglements in the disentangled amorphous phase that in the solid state consisted of the pristine crystalline domains. The slower change is due to chain reptation and further entanglements as shown with both rheological experiments and the rate at which the low temperature endothermic peak (associated with crystalline structures formed in the entangled amorphous phase) increases with the annealing time [49]. The comparison between a disentangled UHMWPE sample and a commercial fully entangled one, and the molecular weight effect on disentangled UHMWPE samples, have been investigated in our group.

As explicitly shown in Equation (1.2), the lower the average molecular weight between entanglements, the higher the mechanical modulus and thus the viscosity of polyethylene, with samples exceeding  $10^6$  g/mol to be very challenging to melt process with conventional methods. Since disentangled samples are characterized by higher crystallinities and considerably less entangled amorphous regions, they are capable of being processed even in the solid state, close to the melting temperature and produce highly oriented (uniaxially or biaxially) tapes [48]. As mentioned previously, Equation (1.2) applies in conditions of thermodynamic equilibrium; hence, it is not correct to use the equation in a reverse engineering way and calculate the average molecular weight between entanglements,  $\langle M_e \rangle$  from a build-up graph (like the data presented in Figure 1.9) and thus calculate the exact value of the entanglement density. In order to have thermodynamic equilibrium, the physical density,  $\rho$ , of the material needs to be constant at a specific temperature; with the formation of entanglements the physical density increases constantly over time since the amorphous disentangled polymer chains entangle. In addition, it is unknown whether the numerical factor,  $g_N$ , is time-dependent at non-equilibrium conditions and also the measurement requires the application of strain that is concentrated in the weak points of the melt [61] making thus the calculation with Equation (1.2) only an estimation [106]. Furthermore, in the

disentangled non-equilibrium state, disentanglement and entanglement of the chains due to reptation occur simultaneously with the rate of entanglement formation exceeding the rate of disentanglement; the two rates become identical once equilibrium is achieved [62].

As explained previously, until recently it was assumed that the formation of entanglements initiates upon melting [104]. However, part of the aims of this doctoral thesis was to provide sufficient experimental evidence that entanglements may form at lower temperatures in the disentangled amorphous phase. In order to investigate this, a complementary technique to melt plate-plate rheology was employed so experiments in the solid state could be performed. This is explained in Chapter 3 section 2 and for oriented samples in Chapter 4 section 1.4 with the use of dielectric spectroscopy. Not only it was experimentally observed that entanglements are forming at temperatures as low as 80°C (~60°C below the melting) but also the entanglements activation temperature was calculated to be 58°C via a model that we have proposed [107].

### 1.3. Relaxation Dynamics

#### 1.3.1. Dielectric Relaxation

The interaction of electromagnetic waves with molecular systems at frequencies between  $10^{-6}$  and  $10^{12}$  Hz induces relaxation and electrical conductivity phenomena arising from the reorientation of molecular dipoles and the translational motions of electrons or ions respectively [108]. Combining the broad frequency range with temperature variations, BDS can identify different processes in polymers and polymer composites such as polarization and conductivity phenomena, molecular dipolar fluctuations, thermal transitions, charge transport and interfacial polarization [54,55]. Nobel laureate Peter Debye (1884 – 1966) established the dielectric relaxation for dipolar liquids and solids, which is the dispersion of the real part of dielectric permittivity  $\epsilon'$  and the imaginary part of dielectric permittivity  $\epsilon''$  at the frequency domain [109–111]. Historically, four basic schools emerged within the field of dielectrics, utilizing different formalisms to analyse similar data. The "dielectric" school mainly uses the complex dielectric permittivity [ $\epsilon^*(\omega) = \epsilon'(\omega) - i\epsilon''(\omega)$ ], the "semiconductor" school uses the ac conductivity [ $\sigma^*(\omega) = \sigma'(\omega) + i\sigma''(\omega)$ ], the "ionic" school prefers the complex electric modulus [ $M^*(\omega) = M'(\omega) + iM''(\omega)$ ] and finally the "electrochemistry" school presents the data using the complex impedance [ $Z^*(\omega) = Z'(\omega) - iZ''(\omega)$ ] [112]. All different formalisms are equally important and each of them can be proven more useful than others at times, depending on the materials' molecular characteristics and experimental environment [113]. A

comparison between the four basic dielectric formalisms can be appreciated in Figure 1.10 below.

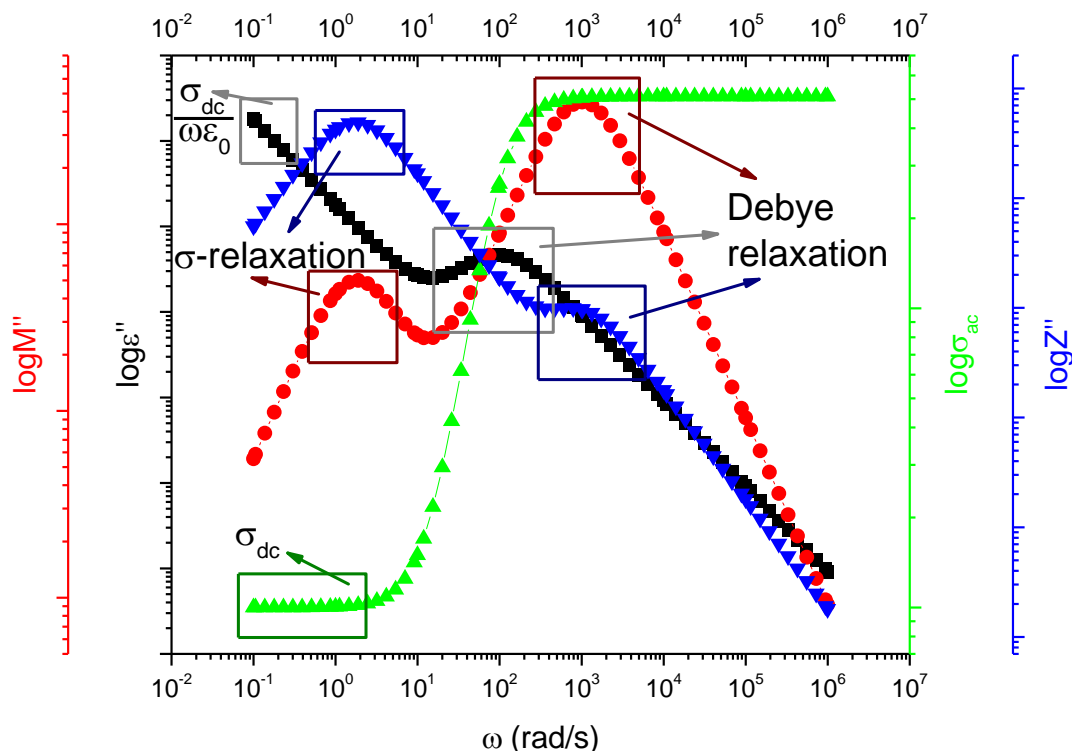


Figure 1.10. The comparison between the four basic dielectric formalisms (imaginary parts of: dielectric permittivity  $\epsilon''$  (black), electric modulus  $M''$  (red) and impedance  $Z''$  (blue), the real part of electrical conductivity  $\sigma_{ac}$  (green)) as a function of frequency in an ideal system consisting of two basic phenomena, a Debye dipolar relaxation and dc conductivity.

In Figure 1.10, the four basic dielectric formalisms are presented as a function of frequency for an ideal system consisting of a Debye dipolar relaxation and dc conductivity. In this representation, it is illustrated that the different formalisms discussed carry the same dielectric information. The Debye dipolar relaxation is presented as a peak in  $\epsilon''$ ,  $M''$  and  $Z''$  while the dc (Ohmic) conductivity can be interpreted as a line independent of frequency in the  $\sigma_{ac}$  representation, as a line with a slope of -1 in the  $\log \epsilon''$  vs  $\log \omega$  representation and as a peak (conductivity relaxation) in the  $M''$  and  $Z''$  representations respectively. Another useful piece of information that can be extracted from Figure 1.10 is that the frequency loss peak position of the Debye dipolar relaxation, as observed in loss permittivity, shifts to higher frequencies in the loss modulus and loss impedance formalisms and thus should be treated

with care during the temperature dependence of the dielectric relaxation processes. Additionally, the conductivity relaxation as observed in loss modulus and loss impedance, exhibits a Debye-like peak.

To study strongly heterogeneous systems (like polymer nanocomposites) the application of complex electric modulus has been proven beneficial and advantageous comparing to the classically used complex dielectric permittivity [114–116]. This is partially due to the fact that the complex electric modulus formalism minimizes the presence of electrode polarization, a parasitic effect that is due to the sample's conductivity and masks the material's true dielectric behaviour, and also the contribution of dc conductivity which transforms into a peak as explained previously [54,112,117]. The dielectric behaviour of these heterogeneous systems is heavily dominated by an additional capacitance that derives from polarization effects of the interface between the constituents that form the heterogeneous system [118]. This effect can be present in semicrystalline polymers with the amorphous regions of the polymer chains to be considered as the continuous matrix phase, and with the rigid crystallites in the role of the inclusion [119,120] or polymer nanocomposites [114]. Of great importance to the values of interfacial polarization is the conductivity and permittivity difference between the constituents, hence the use of highly conductive fillers into insulating polymer matrices (for example metallic fillers or graphene) [121–125] or reinforcing materials with very high dielectric constants (for example BaTiO<sub>3</sub> particles) [126–129]. In addition, the size of the particles plays a paramount role in the interface area between the particles and the polymer matrix giving scientific and technological rise to nanocomposites [130].

As mentioned earlier, the dielectric relaxation characterized by a single relaxation time was first discussed by Peter Debye in 1927 but its applicability was confined only in diluted polar gases and liquids, also presented in Figure 1.10 [131]. The complex dielectric permittivity coming from the Debye model can be appreciated in Equation (1.3) below:

$$\varepsilon^*(\omega) = \varepsilon_\infty + \frac{\varepsilon_s - \varepsilon_\infty}{1 + i\omega\tau_D} \quad (1.3)$$

where the  $\varepsilon_\infty = \lim_{\omega \rightarrow \infty} \varepsilon^*(\omega)$ ,  $\varepsilon_s = \lim_{\omega \rightarrow 0} \varepsilon^*(\omega)$  and  $\tau_D$  is the *Debye* relaxation time. Since the *Debye function model* was proven inapplicable for solid dielectrics, in 1941 K. S. Cole and R. H. Cole introduced the parameters  $\beta = 1 - \alpha$  ( $0 < \alpha, \beta < 1$ ) to be indicative of the symmetrical distribution (broadening) of relaxation times [132]. The symmetrical broadness of the peak associated with the parameter  $\beta$  can be appreciated in Figure 1.11a. The *Cole-Cole function model* is depicted in Equation (1.4):

$$\varepsilon^*(\omega) = \varepsilon_\infty + \frac{\varepsilon_s - \varepsilon_\infty}{1 + (i\omega\tau_{CC})^\beta} \quad (1.4)$$

were the  $\tau_{CC}$  is the *Cole-Cole* relaxation time. The *Cole-Cole function model* described accurately some liquid and solid materials but there was still a gap in the description of many other dielectrics and so in 1950, D. W. Davidson and R. H. Cole introduced the new parameter  $\gamma$  ( $0 < \gamma < 1$ ) to account for an asymmetrical distribution (broadening) of relaxation times which can be appreciated in Figure 1.11b respectively [133]. The *Davidson-Cole function model* follows Equation (1.5) as seen below:

$$\varepsilon^*(\omega) = \varepsilon_\infty + \frac{\varepsilon_s - \varepsilon_\infty}{(1 + i\omega\tau_{DC})^\gamma} \quad (1.5)$$

were the  $\tau_{DC}$  is the *Davidson-Cole* relaxation time.

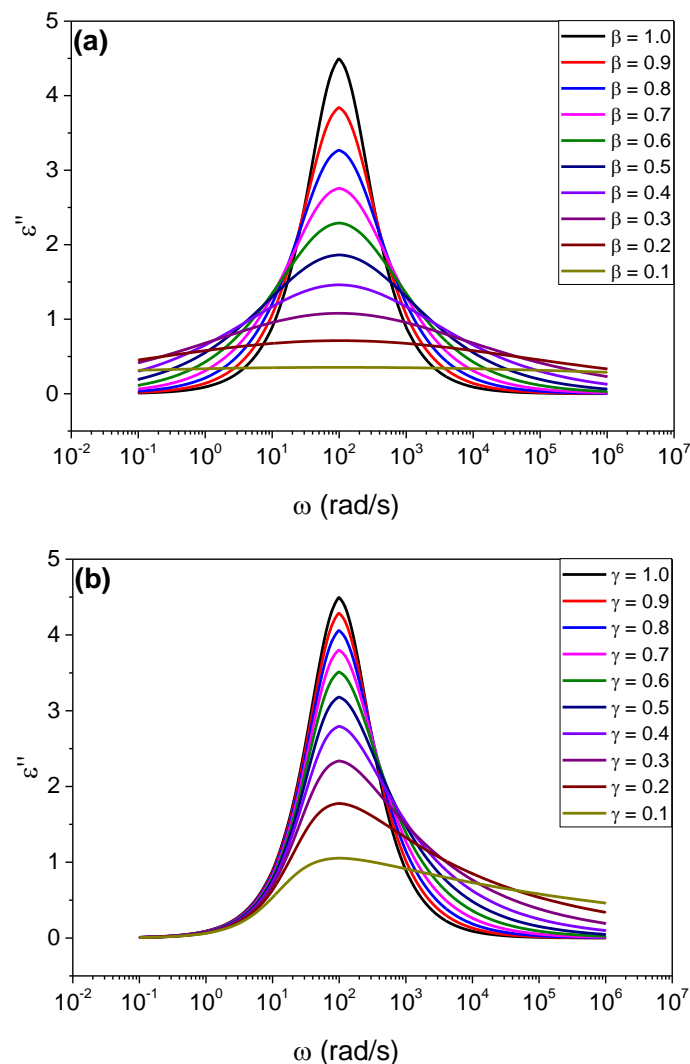


Figure 1.11. The dielectric permittivity loss as a function of frequency of a single relaxation process varying (a) the parameter  $\beta$  and (b) the parameter  $\gamma$ . For  $\beta = \gamma = 1$  the *Debye* behaviour is observed.

To generalize the *Cole-Cole* and *Davidson-Cole* function models, S. Havriliak and S. Negami in 1967 introduced their own function model combining the two parameters, as it can be seen in Equation (1.6) [134]:

$$\varepsilon^*(\omega) = \varepsilon_\infty + \frac{\varepsilon_s - \varepsilon_\infty}{(1 + (i\omega\tau_{HN})^\beta)^\gamma} \quad (1.6)$$

where the  $\tau_{HN}$  is the *Havriliak-Negami* relaxation time.

At different thermodynamic conditions (temperature, pressure), the relaxation time of a dielectric process is affected significantly [54]. Generally, when the temperature increases, the relaxation time decreases due to the increasing mobility of the dipoles, which can align faster with the applied electric field [55]. However, this might not always be the case, especially during melting transitions or close to the thermal degradation of a material [135]. The temperature dependence of the relaxation time is a paramount property of each relaxation process and when the  $\ln(\tau)$  vs  $T^{-1}$  has a linear behaviour, then the activation energy of the relaxation can be calculated by means of the *Arrhenius equation* as seen below:

$$\tau = \tau_0 e^{\frac{E_A}{k_B T}} \quad (1.7)$$

where the  $\tau_0$  is a pre-exponential factor,  $E_A$  is the activation energy of the process,  $k_B$  is the Boltzmann constant and  $T$  is the absolute temperature. When the  $\ln(\tau)$  vs  $T^{-1}$  is not linear then a common way to model this non-linear behaviour, is by employing the *Vogel-Fulcher-Tammann-Hesse (VFTH) equation*. Most notably, the dynamic glass-to-rubber relaxation process in the case of amorphous and semi-crystalline polymers follows the *VFTH equation* which can be seen in Equation (1.8):

$$\tau = \tau_0 e^{\frac{DT_V}{T-T_V}} \quad (1.8)$$

where  $T_V$  is the ideal glass-to-rubber transition temperature and  $D$  is a dimensional parameter that can be related with the steepness (fragility) of the relaxation and how much it deviates from the Arrhenius behaviour [136,137]. A thermodynamically equal *VFTH equation* can be obtained by the variation of pressure at constant temperature as seen below [138–141]:

$$\tau = \tau_s e^{\frac{DP}{P_0 - P}} \quad (1.9)$$

where  $\tau_s$  is the dynamic glass-to-rubber (segmental) relaxation process relaxation time at atmospheric pressure at a given temperature and  $P_0$  corresponds to the pressure of the ideal glass-to-rubber transition.

The dielectric spectrum of PE is known to exhibit three main processes. Since polyethylene is a non-polar material, the study of its dielectric relaxations is challenging. However, carbonyl or chlorine dipoles are often attached to polyethylene chains to render

them dielectrically active, thus altering the chemical structure and the chain dynamics [142]. The  $\alpha$ -process is related to molecular fluctuations in the crystalline part (namely  $\alpha_c$ -process). This nomenclature is contrary to the convention used for most polymers where the  $\alpha$  relaxation is associated with chain dynamics in the amorphous region. The  $\beta$ -process is assigned to the dynamic glass-to-rubber relaxation process of the amorphous segments [143–146], and the  $\gamma$ -process is related with mobile parts of the amorphous chains in the vicinity of the crystalline lamellae. The argument that the dynamic glass-to-rubber transition process is the  $\beta$ -relaxation is based on experimental observation of TiO<sub>2</sub>/LDPE samples that exhibited a VFTH temperature dependence [143] and also higher dielectric relaxation strength of less crystalline samples [147]. Often two, or even three types of  $\gamma$ -processes are observed but their assignment to specific molecular processes is not fully clear yet [54,148–150].

The relaxation dynamics of dis-UHMWPE by means of dielectric spectroscopy have been analysed and presented in Chapter 3 section 1.2 in the presence of Al<sub>2</sub>O<sub>3</sub> catalytic ashes as dielectric probes. The presence of the disentangled amorphous phase exhibits different mobility with the applied electric field affecting thus the interfacial properties of the system as observed for the first time in our analysis.

### 1.3.2. Mechanical Relaxation

It is possible to monitor relaxation processes observable with *Broadband Dielectric Relaxation Spectroscopy* (BDRS) with other dynamic techniques, such as *Dynamic Mechanical Analysis* (DMA) and *Nuclear Magnetic Resonance* (NMR). These relaxation processes might have the same physical origin depending from the polymer's structural, chemical and physical properties and can be observable at the same or similar temperature and frequency ranges so that the techniques can work in parallel and offer more information on the relaxation map of each sample [60,151].

The mechanical behaviour of a polymer can be described by two basic limiting behaviours; the elastic behaviour of a solid which can be associated with  $G_\infty$  and the viscous behaviour of a liquid  $G_s$ . As it can be deduced by Equation (1.10), polymers are viscoelastic materials and *DMA* is often used to study the dynamic transition from the elastic behaviour to the viscous one [152]. To obtain a frequency-dependent mechanical response in *DMA*, an oscillating strain is applied to the sample and the magnitude and phase angle stress are monitored. Similar relaxation models as in *BDRS* are employed in the form of the complex mechanical modulus [ $G^*(\omega) = G'(\omega) + iG''(\omega)$ ] or complex viscosity [ $\eta^*(\omega) = \frac{G^*(\omega)}{i\omega}$ ] to

analyse the shape factors, relaxation times and characteristics of mechanical relaxations. The real part of mechanical modulus strictly describes the energy storage while the imaginary part of mechanical modulus describes the energy loss of the specimen, in accordance with the *BDRS* analysis of the real and imaginary parts of dielectric permittivity and electrical modulus [108,152]. The direct equivalent of the *Debye function model* for *DMA* is the *Maxwell model* describing a relaxation process of a single relaxation time [60]. In Equation (1.10) below the *Havriliak-Negami function model* can be seen in the form of mechanical modulus [134]:

$$G^*(\omega) = G_\infty - \frac{G_\infty - G_s}{(1 + (i\omega\tau_{HN})^\beta)^\gamma} \quad (1.10)$$

where the  $G_\infty = \lim_{\omega \rightarrow \infty} G^*(\omega)$ ,  $G_s = \lim_{\omega \rightarrow 0} G^*(\omega)$  and  $\tau_{HN}$  is the *Havriliak-Negami* relaxation time.

The same relaxation dynamics equations like the Arrhenius law and the VFTH equation as presented in Equations (1.7) and (1.8) respectively, are also employed in the case of dynamic mechanical analysis to monitor the time-temperature dependency of the relaxation times but also for the temperature-dependency of the values of the zero shear viscosity, in equivalence with the dc conductivity [153,154]. In addition, when *BDRS* and *DMA* are directly compared, it is important to use the equivalent formalisms for such comparisons, hence the complex dielectric permittivity with the complex mechanical compliance and the complex electric modulus with the complex mechanical modulus since there are further frequency loss peak position shifts due to the use of a different formalism [60].

Polyethylene is known to exhibit three main mechanical relaxations, although they can be of different origin comparing to *BDRS*, when the polyethylene used in the latter is rendered dielectrically active via oxidizing the chains [142]. The mechanisms behind the  $\alpha$ -process is unanimously supported by *DMA* experiments to be attributed to fluctuations of the crystalline structure ( $\alpha_c$ -process) [155]. However, in contrast to dielectric experiments, for *DMA* it has been proven by Mansfield and Boyd that the temperature loss peak position at a common frequency of similar polyethylene samples exhibits a difference of 20 – 30°C ( $T_{\text{dielectric}} < T_{\text{mechanical}}$ ) due to an additional contribution arising from amorphous fractions that transfer the mechanical strain to the crystal [144]. Often, mechanical experiments show that the  $\alpha_c$ -process peak is also broader comparing to dielectric experiments, possibly because it is consisting of two dispersions (corresponding to this additional contribution of amorphous fractions as mentioned earlier) [156].



It should be noted that the glass-to-rubber transition temperature (and hence the relaxation which corresponds to the dynamic glass-to-rubber process) is still topic of dispute between researchers. Several people over the years have proposed that either the  $\beta$ -process [157,158] or the  $\gamma$ -process [159,160] are the dynamic glass-to-rubber transition process. Some have even proposed that polyethylene has two  $T_g$ , corresponding to both the  $\gamma$ - and the  $\beta$ -processes [161,162]. The notion that the  $\beta$ -process is the dynamic glass-to-rubber transition process has been supported by the fact that in semicrystalline polymers, the  $\beta$ -process appears to be broadened comparing with amorphous samples and considerably less prominent than the  $\alpha_c$ -process [157]. On the other hand, the school that considers the  $\gamma$ -process to be the dynamic glass-to-rubber transition process base their argument on the enhancement of the peak maximum with the crystallinity decrease, hence attribute the process to the amorphous segmental relaxation.

The time-temperature superposition principle (TTS) is a useful technique to analyse dynamic data (dielectric or mechanical) when the frequency and temperature range is limited [163]. It is useful when the values of the real part of the storage modulus at one temperature and frequency state are the same at a different temperature and frequency state [164]. The effect of *TTS* can be appreciated in Figure 1.12b where the effect of temperature in one mechanical relaxation process over a fixed frequency range is translated in one master-curve (open symbols) of a broader frequency range at the reference temperature.

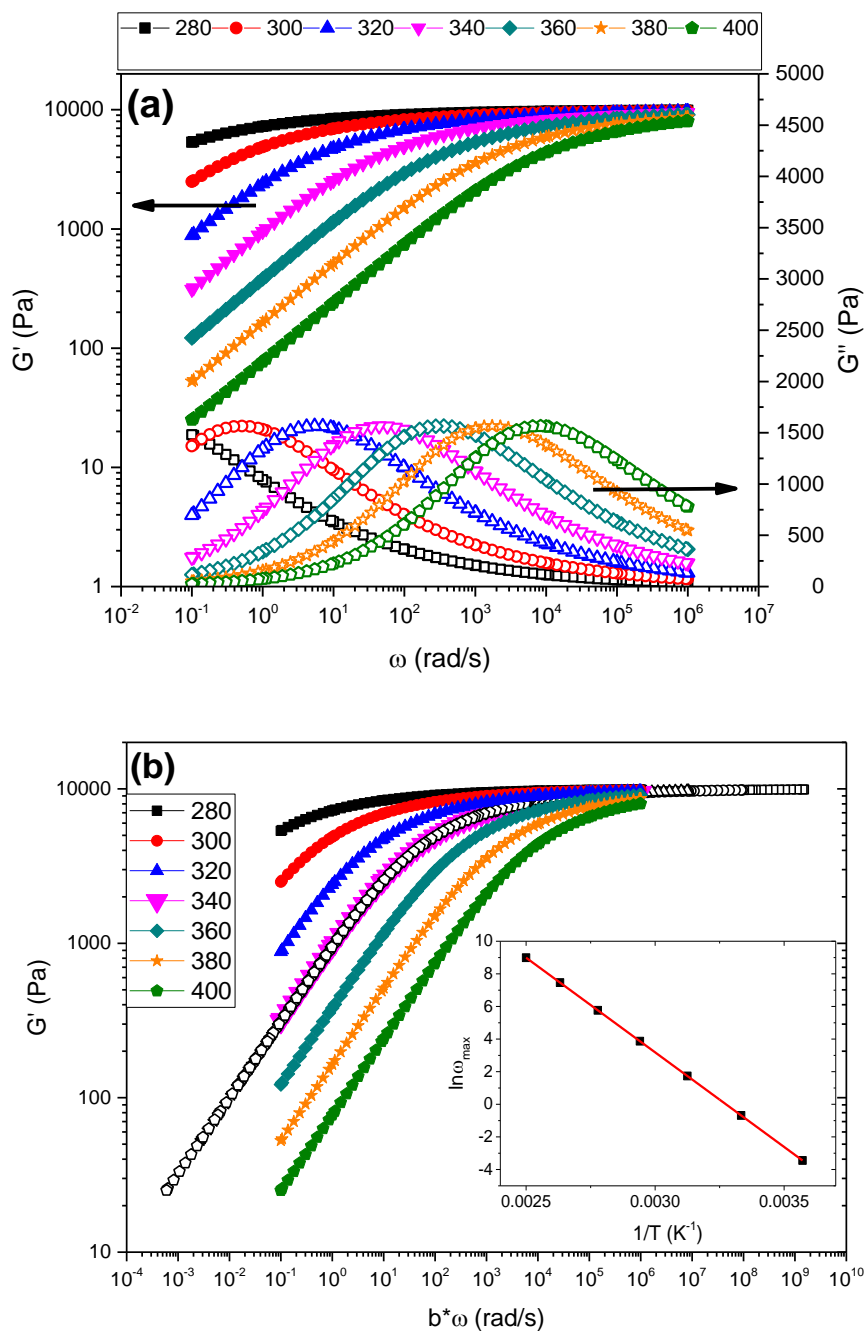


Figure 1.12. (a) The real and imaginary parts of mechanical modulus as a function of angular frequency of a fictional relaxation in the temperature range of 280 to 400 K and in (b) the master curve (open symbols) according to the *TTS* principle is presented. The relaxation follows the Havriliak-Negami function model with parameters:  $G_s = 10^4 Pa$ ,  $G_\infty = 10^0 Pa$  and  $\beta = \gamma = 0.50$ . The angular frequency loss peak positions  $\omega_{max}$  were set to follow the Arrhenius equation (Equation (1.7)) where  $\omega_{max} = \frac{1}{\tau}$ , with an activation energy  $E_A = 1 eV$ , as shown within the inset. The shift factor  $b$  in accordance with Equation (1.11) also followed the same Arrhenius equation. In this case, the  $T_{ref} = 340 K$ .

In order to have a successful *TTS* of the dynamic data, a reference temperature  $T_{ref}$  is set and the resulting master curve will present the data of a temperature range as if a broader frequency was accessible but only at this  $T_{ref}$ . To achieve this, a shift factor  $b$  is required to be employed which alters the frequency position of data at a temperature different than the reference temperature  $T_{ref}$  to fit the one of the  $T_{ref}$ . This shift factor  $b$  can be calculated with the Arrhenius equation as such:

$$b = \frac{\tau|_T}{\tau|_{T_{ref}}} = \frac{\tau_0 e^{\frac{E_A}{k_B T}}}{\tau_0 e^{\frac{E_A}{k_B T_{ref}}}} = e^{\frac{E_A(T_{ref}-T)}{k_B T_{ref} T}} \quad (1.11)$$

Other equations like the Vogel-Fulcher-Tammann-Hesse and the Williams-Landel-Ferry can be employed instead; the applicability of either is connected to the temperature dependency of the relaxation process [165]. The application of the *TTS* principle in systems with more than one relaxation processes is very challenging, especially when the strength of the relaxations ( $G_s - G_\infty$ ) is temperature-dependent and they are characterized by different activation energies and shape factors or even different relaxation dynamics models [163].

The relaxation dynamics of dis-UHMWPE by means of torsional rheology have been analysed and presented in Chapter 3 section 1.1 varying the processing conditions. The disentangled sample processed in the solid-state exhibited a completely different mechanical relaxation behaviour than the melt-processed one, jointly attributed to the disentangled amorphous phase and the pristine crystalline structure. A complete mechanical relaxation map was also constructed with indications that the  $\gamma$ -relaxation is the dynamic glass to rubber transition of linear polyethylene.

#### 1.4. Orientation through Plastic Deformation

The investigation of the anisotropic properties and structural characteristics induced by mechanical deformation in polymers and polyethylene in particular has interested scientists and engineers as early as the 50s and the 60s [13,166,167]. This interest arose from the industrial need towards light-weight, high-modulus polymer fibres for polymer-polymer composite applications [168–170], and extended in the direction of polymer physics and crystallography [171–173]. The contribution of the crystalline and the amorphous parts of oriented polyethylene upon the structural and optical properties gave food for thought towards understanding the chain dynamics with stretching [166]. Advancements in this direction arose in the 70s and 80s from the cold-drawing of polyethylene, resulting into the existence of three basic stages following the increase of the draw ratio: **(I)** plastic

deformation of the spherulitic structure, (II) the transformation of the elongated spherulite to a fibril structure and (III) the plastic deformation of the fibre [174]. The fibres are highly aligned in the direction of the orientation and are physically connected with each other through chain bridges in interfibrillar or intrafibrillar ways [175].

From the beginning, the oriented amorphous phase was understood as an intermediate state between ordered and disordered segments of the polymer chains, affecting the birefringence and infrared dichroism properties of the oriented crystals [166]. This molecular feature gave rise to decades of research around the anisotropic optical properties of oriented polyethylene modified with optically interesting inclusions, introducing photoluminescence capabilities to oriented polyethylene systems [176–178]. In order to produce highly dichroic films, the addition of photoluminescent dichroic dyes in small quantities to polymers followed by orientation has proven to be efficient. However, in order to achieve the orientation of the dyes during tensile stretching, the dyes must have a high molecular aspect ratio, a transition dipole moment that coincides with the orientation ratio direction and a melting temperature relatively close to the stretching temperature [178]. The key parameters that affect the most the efficiency of these oriented polymer-dichroic dye composite systems as stated by *Pucci et al.* are [179]:

- i. The dispersibility of the dye in the host polymer matrix.
- ii. The presence of rigid rod-like absorbing core in the dye.
- iii. High molar absorption which is usually related to a high dipole moment.

In addition, according to *Weder et al.* there are other important parameters for a researcher to take into account when planning the experimental procedure and materials design [177]:

- i. The molecular weight of the dye.
- ii. The structure of the side chains of both the polymer matrix and the organic dye.
- iii. The composition of the blend system.
- iv. The draw ratio of the blends.

When discussing about the molecular weight of the conjugated dyes, *Weder et al.* underlined the importance of it in comparison with the maximum orientability of larger molecules. In addition, the nature of the dyes' side chains was found to negatively influence the orientability at high draw ratios. This is presumed to be the result of the interaction of linear side chains with the matrix, obstructing the alignment with the applied force. It was also proven by them that the dichroic ratio and the draw ratio of the systems have a linear relationship; the higher the draw ratio, the more enhanced are the expected anisotropic optical characteristics. The most prominent applications of such materials are as polarizers and/or

Light-Emitting Devices (LED) which could contribute in brighter and more efficient Liquid-Crystal Displays (LCD) [177].

Metallic nanoparticles were also employed as fillers, targeting to dichroic and plasmon resonance absorption phenomena, again for optical properties. For example, the optical absorption anisotropy induced by uniaxial stretching of UHMWPE samples in the presence of metallic (usually Au and Ag) nanoparticles has been of interest since the 1990s [180–183]. The application of uniaxial plastic deformation could generate structural anisotropy in the continuous matrix (polymer) and also an alignment in the modifying fillers (metallic nanoparticles), thus affecting the optical characteristics (dichroism) as a function of measuring angle compared to the stretching orientation [183]. This results in different wavelength maxima positions as a function of the measuring angle, varying the plastic deformation [181]. The tunability of the optical properties relies on the nature, shape, dimensions, concentration and polydispersity of the nanofillers [180]. Additionally, due to the hydrophobic character of UHMWPE, the evolution of such systems results in durable polarizers for humid environments increasing the applicability of these composites [176].

Another interesting property that can be modified in UHMWPE through orientation is its thermal conductivity. In dielectric solids (non-conductive materials), the heat transfer is achieved mainly by wave-like elastic vibrations of the atomic lattices, the phonons [184]. In crystalline materials, the thermal conductivity underlying mechanisms are strongly affected by defects and boundaries that alter the elastic properties of the medium and hence are points of phonon scattering [185]. Polymers can be either amorphous or semi-crystalline with various degrees of crystallinity, giving thermal conductivity a strong temperature and order dependence [175]. In addition to the degree of crystallinity, the polydispersity and the size of the crystalline structures is also paramount due to the acoustic mismatch at the interfaces between the amorphous and the crystalline domains, thus enhancing the scattering phenomena [186]. The aforementioned polymer characteristics affect significantly the thermal conductivity of a sample by altering the phonon mean free path which is the average length that a phonon travels within the crystal between two scattering events. In a perfect crystal (with no dislocation defects), the phonon mean free paths are shortened only by crystal grain boundaries and other phonons.

With orientation, the crystallized chains are lined up along the direction of stretching, decreasing the thermal resistance [175]. Past studies have shown that the plastic deformation increases significantly the thermal conductivity of UHMWPE samples in the direction of orientation, resulting into metallic-like thermal conductivities [48,187]. A molecular weight

dependency was also found and attributed to the crystal size and number of chain ends that work as defects in the alignment of the crystals [187]. An important contribution to the thermal conductivity values exists from the chain bridges connecting different fibril structures and conducting heat between them by allowing the phonon propagation [175,188]. Studies towards the investigation of thermal conductivity with uniaxial or biaxial orientation, have been conducted by our group.

Uniaxially oriented samples of dis-UHMWPE in the presence of fillers of different nature (metallic, ceramic and organic) have been investigated and discussed in Chapter 4. An in-depth structural analysis by various techniques has been performed in addition to the thermal and electrical properties of the samples.

### **1.5. Electrical Energy Storage in Dielectric Materials**

The demanding societal and economic needs for a diverse energy portfolio, as described above, have recently driven fast progress in electrical energy storage materials and devices [189–194]. These devices find applications in modern electronics and electrical applications such as stationary power systems for hybrid and electrical vehicles and high frequency inverters for solar panels [195–197]. Upon the application of an electric field, the atomic and molecular charges in the material move from their equilibrium positions inducing polarization [54,198]. In linear dielectric materials, where the polarization is proportional to the applied electric field, the energy stored per unit volume increases when permittivity increases [199,200]. Therefore, an ideal electrical energy storage material would exhibit high permittivity, high electric breakdown field (the maximum electric field that the material can withstand without failing) and low energy losses due to the reorientation of the dipoles [201,202]. Insulating materials used as dielectric mediums to store capacitive electrical energy find application in many modern electronic systems, ranging from electronic devices to hybrid electric cars [193]. For such applications, a specific combination of properties is required including [199,201–203]: (i) High values of dielectric permittivity, which is a measure of the ability of the material to store energy; (ii) low dielectric loss ( $\tan\delta$ ) values, to maximize efficiency; (iii) low electrical conductivity, in order to reduce leakage currents; and (iv) high dielectric breakdown strength so higher electrical fields can be physically endured by the dielectric medium.

The use of polymers for electrical energy storage would offer advantages in terms of mechanical, lightweight, processing and insulating properties [196,204–206]. Although polymers exhibit high breakdown strength, polymers suffer from low values of dielectric

permittivity, decreasing their ability to store energy [207]. On the other hand, ceramic materials exhibit very high values of dielectric permittivity but low breakdown strengths [208]. Nanofillers of various shapes and electrical characteristics (dielectric permittivity and electric conductivity) have been introduced to enhance the dielectric properties of polymers [205,209,210]. The addition of high-permittivity, non-conductive ceramic nanofillers in polymers has been reported to enhance voltage endurance and their breakdown strength [211–214].

In heterogeneous dielectric nanomaterials, understanding the role of interface/interphase properties and the possibility to tailor them at will are scientific challenges with enormous technological applications [215,216]. The crystallinity and crystal morphology also affect the dielectric properties by enhancing interfacial polarization phenomena [217] and increase the dielectric breakdown strength due to higher resistance to electrical treeing (current propagation to failure) [218]. The observed increase in breakdown strength is correlated with crystal orientation, as the crystallites provide higher potential barriers for electrical treeing [219]. Towards this direction, biaxial orientation of semi-crystalline polymers, like polypropylene, have found use in thin dielectric membranes for film capacitors in electrical energy storage power system applications [220,221].

Apart from the orientation of the polymer chains and crystallites, orienting the fillers has also shown to affect the electrical breakdown strength, by optimizing the electric field distribution inside the nanocomposites and changing the breakdown tree inception and propagation across the dielectric medium. Hence, the orientation of fillers has been found to also enhance the dielectric behaviour of such polymer composites [203]. In nanocomposites where the electrical characteristics of the filler (permittivity and conductivity) are vastly different from that of the matrix, the dielectric properties are dominated by interfacial phenomena [114,128,222–224]. These interfacial phenomena are caused by physical and/or chemical interactions between polymer-nanoparticle or nanoparticle-nanoparticle interactions [127,225]. However, the smaller the dimensions of the nanoparticles, the higher is their surface area, which leads to a much higher tendency to aggregate in order to decrease their surface energy [226]. For this reason, surface treatment and functionalization by chemical means is often employed to reduce the aggregation [191,227–229]. Different materials have been employed as nanofillers for polymer energy nanocomposites, such as ceramic particles with ferroelectric properties like BaTiO<sub>3</sub> [196,230], 2D nanomaterials like boron nitride [231,232] and various carbon allotropes [233,234]. Some of the most common polymer for such applications are epoxy resins [235] and polyvinylidene fluoride [236]. Gold

nanostructures have been employed to increase electrical conductivity and hence increase the charge flow and energy recovery speed [237,238].

The energy density  $U_e$  of a dielectric material can be calculated as:

$$U_e = \int E dD_e \quad (1.12)$$

where  $E$  is the applied electric field and  $D_e$  is the electric displacement. For linear dielectrics, Equation (1.12) can be simplified to:

$$U_e = \frac{1}{2} D_e E = \frac{1}{2} \varepsilon' \varepsilon_0 E^2 \quad (1.13)$$

where  $\varepsilon_0$  is the dielectric permittivity of vacuum space ( $\varepsilon_0 = 8.85 \cdot 10^{-12}$  F/m) [195].

The addition of electrically conducting fillers within an insulating polymer matrix can be harnessed to tailor the electrical and electromagnetic properties for electromagnetic interference shielding applications and conductive adhesives in microelectronics [239]. Due to the vastly different electrical conductivities between the constituents of such system, the direct current conductivity is strongly dependent on the conducting filler concentration, thus leading to two basic charge transport mechanisms:

(i) At low filler concentrations, the mean distance between conducting fillers is sufficiently high and so the electrical properties of the composite are dominated by the insulating matrix. In such cases, the charge carriers (at most cases electrons, ions and holes) hop to a nearby state that can be quantum-mechanically described with higher or lower energetic jumps of the potential barrier, the latter through quantum tunnelling [124].

(ii) At concentrations at or higher than the percolation threshold, the conducting fillers are in contact hence, the charge carriers can move with low resistance (current flow), exhibiting the behaviour of a conductor [240]. This can also be determined by the temperature dependence of electrical conductivity; in dielectric materials, conductivity increases with temperature (due to higher mobility of charge carriers) while in conductors, conductivity decreases with temperature (due to polaron scattering effects) [241].

The movement of the conductive fillers' charge carriers can cause a dipolar response from the insulating polymer matrix and the corresponding interphase as well, leading to a Maxwell-Wagner-Sillars interfacial polarization, increasing thus, the capacitive storage ability of the resulting composite [114]. To achieve better interfacial characteristics (between the matrix and the filler) towards dielectric (and thermomechanical) properties, the process of surface modification has been extensively applied in the past decade. This modification



affects the polarizability of the polyolefin matrix by introducing polar groups and also enhances the hydrophobicity, both resulting into better-performing insulation materials [242].

Polyethylene is traditionally employed as an insulating material for cable manufacturing, due to its extremely weak conductivity and high dielectric breakdown strength. The two are interconnected, as the dielectric breakdown strength is dependent on electrical conductivity; the use of high permittivity or high conductivity particles will enhance or decrease the dielectric breakdown strength, respectively. To effectively improve the material's characteristics for insulation properties, the use of high permittivity, high thermal conductivity fillers is paramount also to enhance heat dissipation [243]. Moreover, the presence of agglomerates forming a percolating network can highly improve the thermal conductivity of the nanocomposite but decrease the dielectric breakdown strength. The tendency of polymers to build up heat, as a result of their generally low thermal conductivities (for amorphous polymers they range from 0.1 to 1.0  $\text{Wm}^{-1}\text{K}^{-1}$  [175,244–246]) is a limiting factor for their use in electrical applications. In polyethylene/montmorillonite composites, *Li et al.* observed that the inclusion of aligned fillers results in an enhancement of the dielectric breakdown response that adds up to that provided by the oriented polymer crystals [247]. The application of tensile stretching to fabricate highly oriented tapes results in improved values in terms of mechanical and thermal properties and reaching metallic-like thermal conductivities in dis-UHMWPE [48,187,248]. The combination of high thermal conductivity, electrical insulation, and light weight would then make oriented dis-UHMWPE an ideal candidate for a matrix material in an electric energy storage composite.

Nanocomposites of uniaxially oriented dis-UHMWPE in the presence of gold nanoparticles were tested as dielectric materials to store and recover electrical energy varying the draw ratio, as presented in Chapter 4 section 1.3. It was observed that the recovery efficiency and electrical energy density generally increased with orientation, attributed to the separation of nanoparticle aggregated increasing thus the contribution from interfacial polarization.

## 2. Experimental

### 2.1. Chemical Synthesis of dis-UHMWPE

Innovations and research towards the chemical synthesis of dis-UHMWPE is not a subject of the present doctoral thesis, although in-house prepared samples were employed for the experiments. As such, details of the polymerization experiments can be found in the literature [48,249,250]. A single-site homogeneous catalyst activated by methylaluminoxane (MAO) was employed with toluene as the solvent for the reactions [249]. Toluene was used due to its relatively high dielectric constant that leads to the formation of a solvent-separated catalyst/cocatalyst ion pair instead of a contact ion pair, thus ensuring higher catalytic activity. A wall-mounted, 10 L jacketed Pyrex reactor equipped with a double plane propeller blade mechanical stirrer, a temperature probe, a gas inlet/outlet, and a rubber septum for catalyst injection were all employed for the chemical reaction. The reactor was kept overnight at 125°C, and then the temperature was brought to room temperature while the vessel was purged with three cycles of vacuum/nitrogen. The required amount of toluene (5 L) was transferred under a nitrogen gas stream into the vessel, and the temperature was set to the desired value (10°C) by means of a thermostat. When the desired temperature was reached, the stream of gas was switched from nitrogen to ethylene. Ethylene uptake was controlled by means of a Buchi press flow gas controller bpc 6002. When the solution was saturated with ethylene at the desired partial pressure (1 bar ethylene), MAO (50 mL) was added, followed by a solution of the catalyst (50 mg) in toluene + MAO to start the polymerization. The reaction was carried on for the required time under vigorous stirring and constant feed of ethylene and then quenched either in methanol or acidified methanol (CH<sub>3</sub>OH/HCl 95/5 v/v). The polymer was filtered out, washed with additional methanol, and oven-dried under vacuum at 40°C for one night [48]. Quenching the polymerization reaction with methanol results in the presence of traces of catalytic ashes of aluminium oxide (Al<sub>2</sub>O<sub>3</sub>) derived from MAO (10% w/w solution in toluene, Albermarle) co-catalyst used. As the amount of MAO is kept constant for all polymerizations, the content of Al<sub>2</sub>O<sub>3</sub> is lower for longer polymerization times, where more polymer is produced. When acidified methanol is employed instead, the formation of Al<sub>2</sub>O<sub>3</sub> can be avoided completely. The aforementioned procedure is considered standard for the chemical synthesis of dis-UHMWPE followed by our research group, resulting into polymers with well reported characteristics regarding their disentangled character.

## 2.2 Specimen Processing

The samples listed in Table 2.1 and investigated in this thesis are divided in four main categories:

- (i) two plain UHMWPE samples which are indicated as PE\_ $x$ \_T, where  $x$  is either *C* (commercial) or *D* (disentangled), and the T represents the moulding temperature;
- (ii) four dis-UHMWPE samples which are indicated as PE\_ $M_w$ \_AIO of three different molecular weights,  $M_w$  (in  $10^6$  g/mol), and different Al<sub>2</sub>O<sub>3</sub> (AIO) catalytic ashes concentrations;
- (iii) dis-UHMWPE/gold nanocomposites of constant filler concentration (1% w/w) and different draw ratios (DR) from 1 (unoriented) up to 5;
- (iv) dis-UHMWPE nanocomposites modified with either ZnO nanoparticles or  $\beta$ -carotene molecules with a constant filler concentration (0.035% w/w) and different DR (2.5, 5.0, 7.5, 72.5 and 150).

The samples that have no indication of AIO were treated with acidified methanol as explained previously and contain only traces of TiO<sub>2</sub> catalytic ashes which are in the range of 0.0005% w/w to 0.005% w/w if treated with acidified methanol or not respectively [250]. Information on the processing conditions of each category of samples can be found below:

- (i) The specimens were obtained by compression moulding of the UHMWPE powders in a hydraulic hot press under an applied load of 5 tonnes for 5 minutes, 10 tonnes for 10 minutes and 20 tonnes for 5 minutes. During cooling, between 1 and 5 tonnes were applied to achieve permanent deformation. The disentangled sample (PE\_*D*) was processed at 125°C (solid-state) and 160°C (melt-state) while the commercial sample was only melt-processed. The sintering at 125°C (below the UHMWPE melting temperature of ~135-140°C) allows to maintain the material's crystalline structure and partial disentangled character.
- (ii) The synthesized dis-UHMWPE samples in powder form were taken from the reactor at different times, resulting in three molecular weights as presented in Table 2.1 alongside the theoretical amount of Al<sub>2</sub>O<sub>3</sub> catalytic ashes. All the dis-UHMWPE specimens were obtained by the same compression moulding procedure described previously at 125°C to maintain the disentangled character.
- (iii) To prepare dis-UHMWPE nanocomposites modified with dodecanethiol functionalized gold (Au) nanoparticles, dis-UHMWPE in powder form was

suspended in acetone ( $C_3H_6O$ ) and toluene ( $C_7H_8$ ) solutions of nanoparticles were added under magnetic stirring. The UHMWPE powder (as obtained from the in-house reactor) was suspended in acetone and left in the fume hood under magnetic stirring for approximately an hour. The dodecanethiol functionalized Au nanoparticles (2 – 5 nm in diameter purchased by Sigma-Aldrich) in toluene (2% w/v) were used as received. Finally, the two solutions were mixed together under magnetic stirring for few hours and then the solvent evaporated under a fume hood overnight. Complete removal of residual solvent was achieved by heating the composites to  $50^\circ C$  in a vacuum oven for 6 hours. As investigated in similar systems, this temperature is below the activation temperature of the formation of entanglements ( $58^\circ C$ ), as discussed in more details in Chapter 3 section 2 [107]. The resulting powder was compression-moulded according to the procedure described above at  $125^\circ C$ . Unstretched samples were compression-moulded in the form of two cylindrical discs of 25 mm in diameter and 1.1 mm in thickness. Samples intended for stretching were compression-moulded as square films of 50 mm x 60 mm with an initial thickness of 1.9 mm. The square samples were submitted to uniaxial deformation to reach drawing ratios (DR) from 1 to 5 via a twin-roll mill at  $125^\circ C$  at 0.2 rpm. For the DR over 5, tensile stretching was required, employing a Hounsfield tensometer at  $125^\circ C$  and 50 mm/min.

- (iv) The dis-UHMWPE nanocomposites modified with either ZnO nanoparticles (< 100 nm in diameter) or  $\beta$ -carotene (Figure 2.1) were prepared following the suspension procedure presented above. Both fillers were obtained in powder form from Sigma-Aldrich and were suspended in acetone before use. For the DR over 7.5, tensile stretching was required, following the same protocol mentioned previously for dis-UHMWPE/gold nanocomposites.

Table 2.1.  $M_w$ ,  $M_n$  and polydispersity of the samples. When applicable, the theoretical  $Al_2O_3$  concentration was calculated based on the assumption that all the MAO added as co-catalyst does react during quenching to form  $Al_2O_3$ , so it is in fact the maximum amount that can be realistically found in the sample.

Presented in Chapter(s)	Sample Name	$M_w$ (* $10^6$ g/mol)	$M_n$ (* $10^6$ g/mol)	$MWD$	$Al_2O_3$ (% w/w)
3 sections 1.1 and 1.3	PE_C	4.0	0.5	8.0	-
	PE_D	6.0	1.9	3.2	-
3 sections 1.2, 1.3 and 2	PE_5.6	5.6	1.7	3.3	-
	PE_5.6_AIO	5.6	1.7	3.3	1.7
	PE_4.2_AIO	4.2	1.6	2.6	2.6
	PE_2.4_AIO	2.4	1.0	2.4	4.8
4 section 1	DR1 – DR5, DR72.5, DR150 (gold)	5.6	1.7	3.3	-
4 section 3	DR2.5, DR5.0, DR7.5, DR72.5, DR150 (ZnO or $\beta$ -carotene)	5.6	1.7	3.3	-

### 2.3 Characterization techniques

Several characterization techniques have been employed to investigate the physical properties of dis-UHMWPE and its nanocomposites. Here they are listed in alphabetical order, including their location and the experimental details.

1. Broadband dielectric relaxation spectroscopy (Department of Materials Science, University of Patras). The electrical behaviour of the samples (Chapter 3 sections 1.2 and 1.3) was investigated by means of BDRS employing an Alpha-N Frequency Response Analyzer, where the voltage amplitude of the applied field was kept constant at 1 V and frequency varied from  $10^0$  Hz to  $0.429 \cdot 10^6$  Hz employing a two-parallel gold-plated electrode capacitor. The distance between the electrodes was constant and equal to the thickness of the specimen (the employed dielectric set up ensured the application of a homogeneous electric field). The temperature was controlled employing a Novotherm system where the isothermal scans were performed in a temperature range of 50 to 160°C, in steps of 10°C. The dielectric test cell used was a two parallel gold-plated electrode capacitor BDS-1200, all supplied by

Novocontrol Technologies (Hundsagen, Germany). For the analysis related to the formation of entanglements of Al<sub>2</sub>O<sub>3</sub> containing dis-UHMWPE samples (Chapter 3 section 2), a different protocol was employed with 21 consecutive frequency sweep cycles with a total duration of approximately 1 hour, isothermally. To analyze the temperature dependence of the entanglement formation, more tests were performed at different temperatures using a new specimen for each temperature. The temperatures selected for these experiments were 80, 100, 120, 140 and 160°C. The specimens were analyzed again for 21 frequency sweep cycles in the same frequency range as described above. The gold containing dis-UHMWPE samples (Chapter 4 section 1.3) were tested at 30°C at a frequency range of 10<sup>-2</sup> to 10<sup>2</sup> Hz with an applied voltage amplitude of 3 V. The higher voltage amplitude comparing to the Al<sub>2</sub>O<sub>3</sub> containing samples was chosen to decrease the experimental error due to the highly insulating character of polyethylene (the gold nanoparticles cannot work as dielectric probes because they are not dielectric materials). The formation of entanglements was tested also for the gold containing dis-UHMWPE samples (Chapter 4 section 1.4) at 160°C and 10<sup>0</sup> Hz to 10<sup>4</sup> Hz in for 21 consecutive frequency sweep cycles (~ 1 hour).

2. Differential scanning calorimetry (Department of Materials, Loughborough University). A TA Instruments Q-2000 DSC was employed to study the thermal behaviour of the samples. A protocol of three consecutive thermal cycles (heating – cooling – heating) from 50°C to 160°C at a rate of 10°C/minute was used. High precision TZero pans with lids were used and nitrogen was continuously purged at 50 mL/min during the experiments. The melting temperature,  $T_m$ , and the melting enthalpy,  $\Delta H_m$ , of the first and second heating scans were measured. The corresponding results are presented in Chapter 3 section 1.1.
3. Direct current analyser (Department of Materials Science, University of Patras). The experiments were carried out using a 4339B High-Resistance Meter, DC provided by Agilent Technologies (Santa Clara, California, USA) for the gold containing dis-UHMWPE samples (Chapter 4 section 1.3). An automatic measurement process is included in the experimental apparatus to record the charging and discharging electric current. A two parallel-plate electrodes apparatus was used with the sample lying in between throughout the experiment. Three different voltages were applied: 100, 300 and 500 V at a charging time of 60 seconds. It should be noted that before every experimental measurement, a discharge and short-circuit procedure was performed to avoid the accumulation of charges. To calculate the stored and recovered energy, the

capacitance was recorded from dielectric measurements at the lowest measured frequency (0.01 Hz), when the dielectric permittivity is closer to the dielectric constant of the material [251].

4. Raman spectroscopy (Department of Physics, Loughborough University). The Raman spectra of the gold-containing dis-UHMWPE samples (Chapter 4 section 1.1) were analysed in the wavenumber range of 1500 to 1000  $\text{cm}^{-1}$  at room temperature employing a laser beam at 633 nm. The Raman system used was a LabRAM HR provided by Horiba Jobin-Yvon (France).
5. Rheology (Department of Materials, Loughborough University). The mechanical relaxation response of the plain UHMWPE samples (Chapter 3 section 1.1) was studied by means of torsional rheology. The experiments were performed on a TA Instruments ARES-G2, using rectangular bars of  $\sim 2$  mm in thickness  $\sim 12$  mm in width and  $\sim 45$  mm in length as suggested by Dessi et al. for viscoelastic solids [252]. The frequency sweeps were performed between  $10^{-2}$  Hz and  $10^2$  Hz in a temperature range of  $-130^\circ\text{C}$  to  $130^\circ\text{C}$  with a  $5^\circ\text{C}$  step. The strain was kept constant at 0.001 % throughout the whole temperature range, as it was determined that it is well within the linear viscoelastic regime (LVR) in the strain range of 0.0001% to 0.01% at  $-130^\circ\text{C}$  and 1.59 Hz (10 rad/s). Oscillatory time sweep experiments were conducted at  $160^\circ\text{C}$  by means of melt plate-plate rheology employing a TA Instruments ARES-G2 at 1 and 10 Hz at 0.5% strain located in the linear viscoelastic region for almost 100 hours ( $\sim 350,000$  seconds).
6. Small angle X-ray scattering (Department of Macromolecular Physics, Instituto de Estructura de la Materia). Small-angle X-ray scattering (SAXS) experiments of gold containing dis-UHMWPE samples (Chapter 4 section 1.1) were carried out on a Bruker AXS Nanostar small-angle X-ray scattering instrument. The instrument uses Cu  $K\alpha$  radiation (1.54 Å) produced in a sealed tube. The scattered X-rays are detected on a two-dimensional multiwire area detector (Hi-star, Bruker) and can be converted to one-dimensional scattering by radial averaging and represented as a function of momentum transfer vector  $q$  according to Equation (1.12) presented previously. The sample to detector distance was 106 cm. The scattered intensity was corrected with the transmission of the samples calculated considering the absorption of the sample. A glassy carbon standard was used for this purpose.
7. Transient grating spectroscopy (Division of Engineering and Applied Science, California Institute of Technology). The thermal conductivities of the gold containing

dis-UHMWPE samples (Chapter 4 section 1.2) were measured using transient grating spectroscopy at 30°C, following the fundamental concepts that can be found in the literature [248,253,254]. Briefly, a pair of pump pulses (wavelength 515 nm, pulse duration  $\sim 1.0$  ns, pulse energy  $\sim 13$   $\mu$ J, repetition rate 200 Hz) was focused onto the sample to create a spatially periodic heating profile that yields transient thermal grating (grating period  $\sim 10.7$   $\mu$ m). A pair of continuous wave laser beams (wavelength 532 nm, average power  $\sim 27$  mW, chopped at 3.4% duty cycle to minimize steady heating) diffracts from the thermal grating, monitoring its relaxation.

8. Visible/near infrared spectrophotometry (Centre for Renewable Energy Systems Technology, Loughborough University). The absorption of the gold containing dis-UHMWPE samples (Chapter 4 section 1.1) was investigated in the visible wavelength range of 400 to 750 nm and at the near infra-red wavelength of 950 to 1800 nm at room temperature. The apparatus employed was a Cary 5000 UV-Vis-NIR spectrophotometer from Agilent Technologies (Santa Clara, California, United States).
9. Wide angle X-ray scattering (Department of Macromolecular Physics, Instituto de Estructura de la Materia). Wide Angle X-ray scattering (WAXS) experiments of gold containing dis-UHMWPE samples (Chapter 4 section 1.1) were carried out in a diffractometer Policristal X'Pert Pro PANalytical working in a  $\theta$ - $2\theta$  configuration using the Cu K $\alpha$  wavelength. The WAXS measurements presented in Chapter 4 section 2 were performed in a Pilatus 100K mounted at an angle of 36° to the beam direction at a distance of 162 mm using a Xenocs Xeuss 2.0 with a microfocus Cu Ka source collimated with scatter-less slits, performed at the University of Warwick X-ray facility.



### 3. Dis-UHMWPE chain dynamics

In the current chapter, the chain dynamics of dis-UHMWPE by means of torsional rheology and broadband dielectric relaxation spectroscopy are investigated in a broad temperature and frequency range. The target of this chapter is to understand the uniqueness of dis-UHMWPE in respect of the disentangled amorphous phase and how this phase affects the relaxation and entanglement dynamics.

#### 3.1. Relaxation dynamics

##### 3.1.1. Torsional rheology

As discussed in more detail in Chapter 1 section 1.2, polyethylene's glass-to-rubber transition temperature,  $T_g$ , (and hence which relaxation corresponds to the dynamic glass-to-rubber process) has been an issue for decades and is still matter of debate. In this chapter, an investigation on the relaxation dynamics of UHMWPE is presented to clarify this issue employing torsional rheology in a broad temperature and frequency range. The higher chain mobility of disentangled amorphous compared to fully entangled amorphous was expected to alter the chain dynamics and thus the relaxation behaviour of the dis-UHMWPE. To identify these different relaxation properties, solid-state processed dis-UHMWPE is compared with melt processed dis-UHMWPE and commercial (fully entangled) UHMWPE. Three relaxation processes were observed in all the samples, namely  $\alpha_c$ -,  $\beta$ - and  $\gamma$ -relaxations, as expected for linear polyethylene, and their physical properties are discussed below.

In Figure 3.1. the thermographs corresponding to the first heating cycle of all the specimens under study, including the untreated powders, are presented. The crystallinity,  $X_c$ , obtained from both heating cycles is also presented in Table 3.1 and was calculated according to Equation (3.1) considering the melting enthalpy of a fully crystalline polyethylene sample,  $\Delta H_m^c$ , to be 293 J/g [95]:

$$X_c = \frac{\Delta H_m}{\Delta H_m^c} \quad (3.1)$$

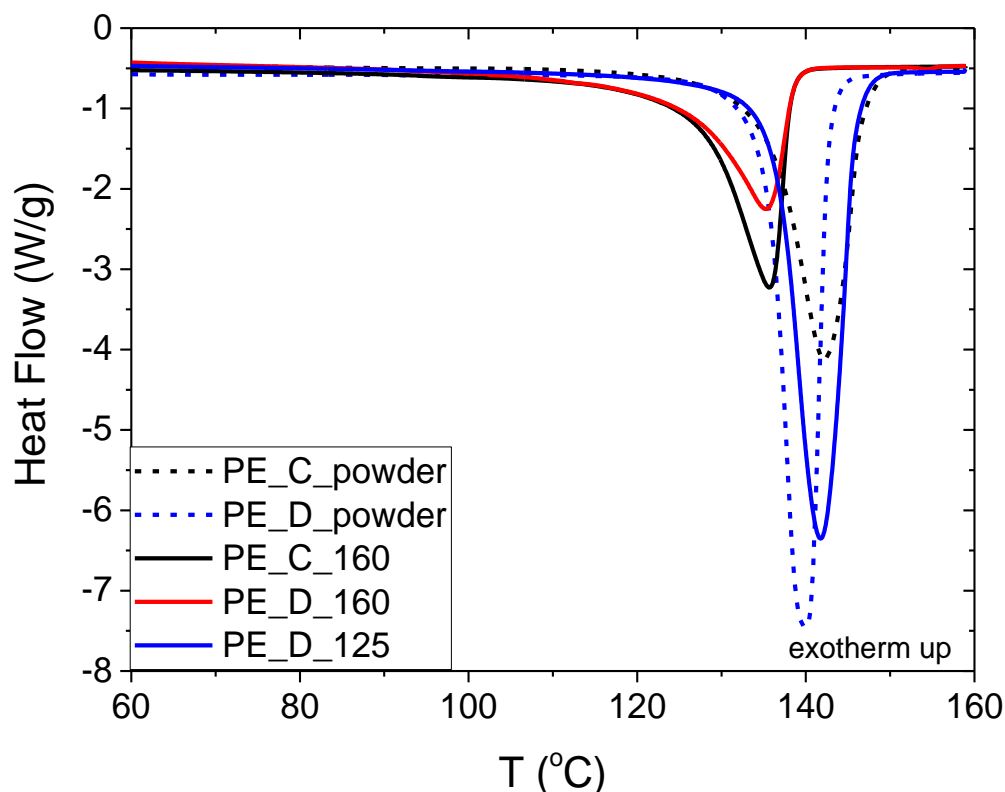


Figure 3.1. First heating thermographs of all the specimens under study including the untreated UHMWPE powders (disentangled and commercial).

Table 3.1. First and second heating runs of all the samples under study.

Sample	Compression moulding temperature (°C)	First heating run			Second heating run		
		$T_m$ (°C)	$\Delta H_m$ (J/g)	$X_c$ (%)	$T_m$ (°C)	$\Delta H_m$ (J/g)	$X_c$ (%)
PE_C_powder	-	142.3	186.7	63.7	134.5	137.9	47.1
PE_D_powder		139.9	231.9	79.1	133.7	109.2	37.3
PE_C_160	160	135.6	132.1	45.1	134.0	133.8	45.7
PE_D_160		135.4	107.8	36.8	135.1	109.3	37.3
PE_D_125	125	141.8	244.5	83.4	134.1	107.9	36.8

An endotherm peak can be observed between 135°C to 145°C for all samples, due to the melting of crystallites. As it can be noted from Table 3.1, the disentangled powder sample has a considerably higher crystallinity (79%) than the commercial one (64%) and it shows a more dramatic decrease during the second heating, most likely related to the higher molecular weight and lower polydispersity of the disentangled material. After melt-processing both

powders show a crystallinity decrease, again, more pronounced for the disentangled sample (37%, compared to 45% of the commercial), showing how the re-crystallisation from the melt (either in a DSC pan, or in a mould) is considerably hampered by the re-entanglement process [91]. However, for the solid-state processed disentangled material, a small increase in crystallinity is observed (from 79% to 83%), that could be attributed to additional solid-state crystallization induced by pressure at 125°C, close to the recrystallization temperature [255]. This is further confirmed by the fact that the solid-state processed sample exhibits a melting temperature slightly higher than the powder, indicating thicker crystals generated during the compression. The commercial sample, as described in previous papers, cannot be solid-state processed in coherent specimens [48].

Generally, the temperature position of the melting peak is associated with the crystallite thickness through the Gibbs-Thomson equation; according to Wunderlich, for polyethylene this equation reads as  $T_m = 414.2*(1 - 0.627/L)$  with  $L$  being the crystal thickness in nm [256], and  $T_m$  the melting temperature in Kelvin. By substituting the value of ~140 °C, that is 413.15 K, the value found for UHMWPE would be close to a 250 nm thickness, while SEM images of as-synthesised material only show thickness in the range of 20 nm. The reason for the aforementioned discrepancy is that one chain re-enters the same crystal many times, thus raising the required amount of energy for the melting transition, simulating a thicker crystal [91,257,258]. However, this situation ceases to exist after the first melting of the sample [89].

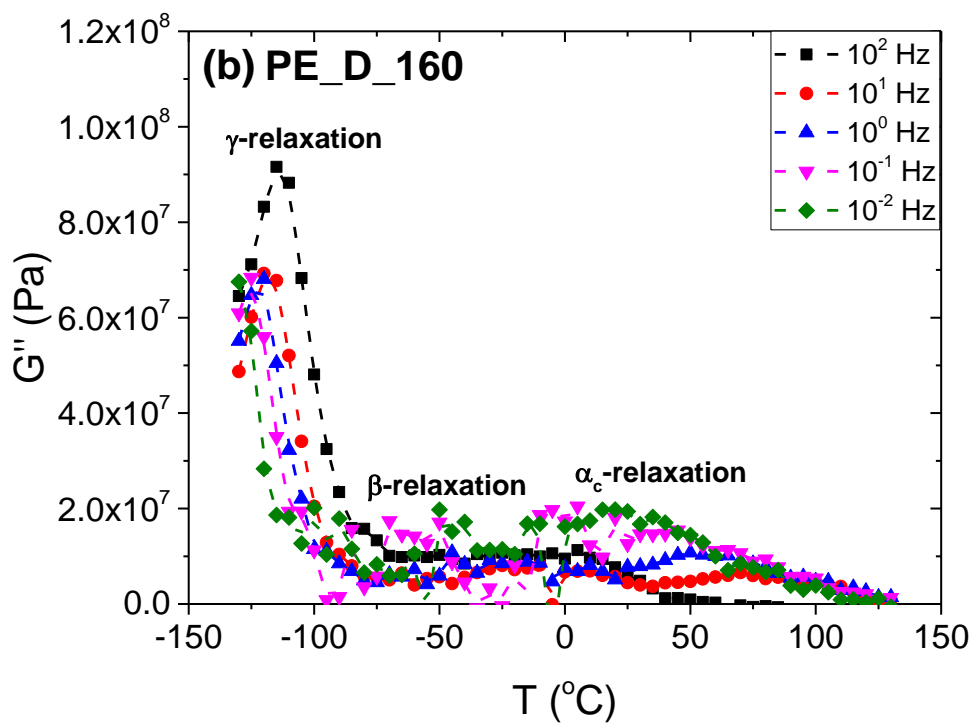
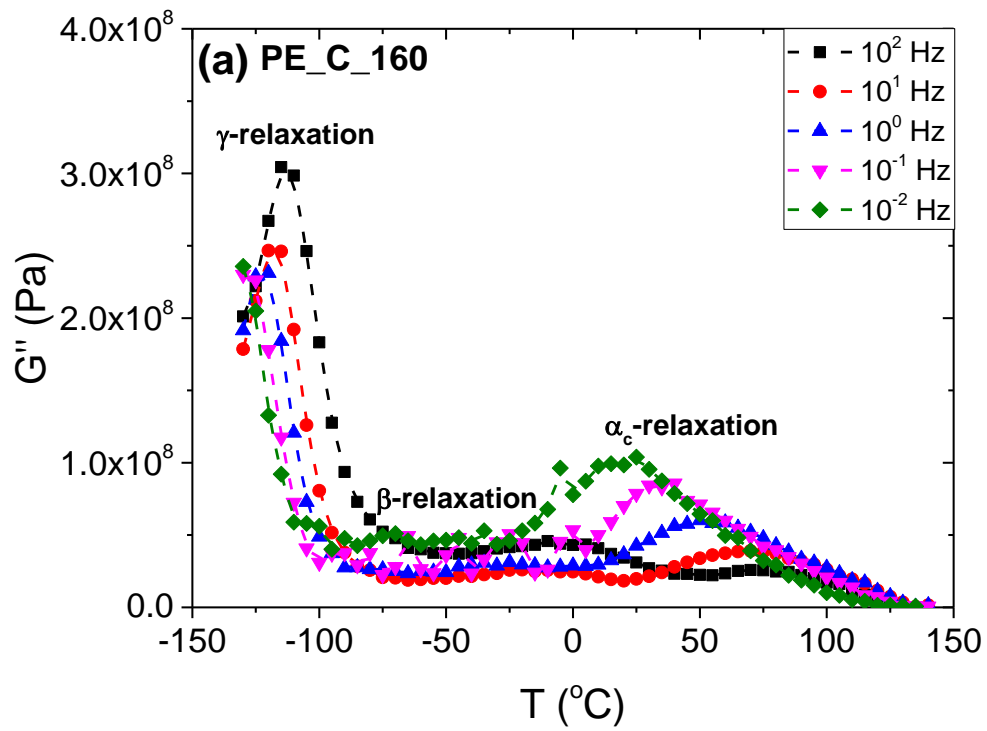
In the rheological analysis, the complex mechanical modulus  $G^*$  and loss tangent  $\tan\delta$  formalisms are going to be employed according to Equations (3.2) and (3.3) as seen below:

$$G^*(\omega, T) = G'(\omega, T) + iG''(\omega, T) \quad (3.2)$$

$$\tan\delta(\omega, T) = \frac{G''(\omega, T)}{G'(\omega, T)} \quad (3.3)$$

where the  $G'$  and  $G''$  are the real and imaginary parts of the complex mechanical modulus respectively.

In Figure 3.2, the imaginary part of modulus,  $G''$ , as a function of temperature varying the frequency is shown. The melt-processed samples PE\_C\_160 and PE\_D\_160 are presented in 3.2a and 3.2b respectively and exhibit a very similar behaviour. The strongest process in terms of relaxation strength appears to be the  $\gamma$ -relaxation, with a relatively narrow relaxation time distribution. A completely different picture is observed for the solid-state processed disentangled sample PE\_D\_125, in Figure 3.2c. Here the highest relaxation strength is observed for the  $\alpha_c$ -relaxation due to the considerably enhanced crystallinity.



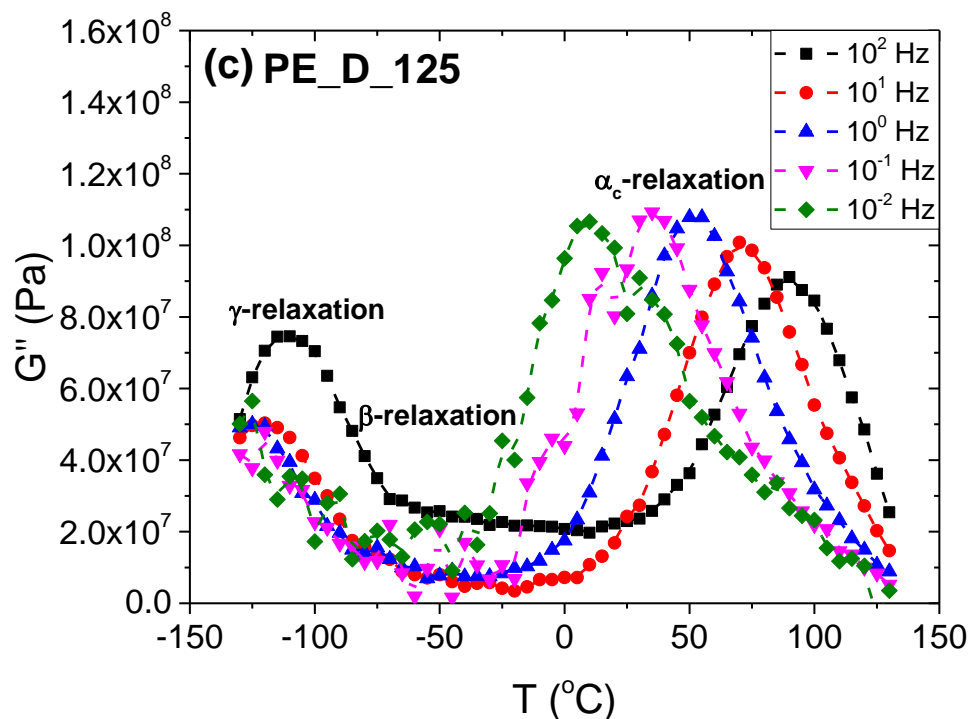


Figure 3.2. The imaginary part of modulus ( $G''$ ) as a function of temperature varying frequency for (a) PE\_C\_160, (b) PE\_D\_160 and (c) PE\_D\_125 samples. (The lines serve as guides for the eyes only.)

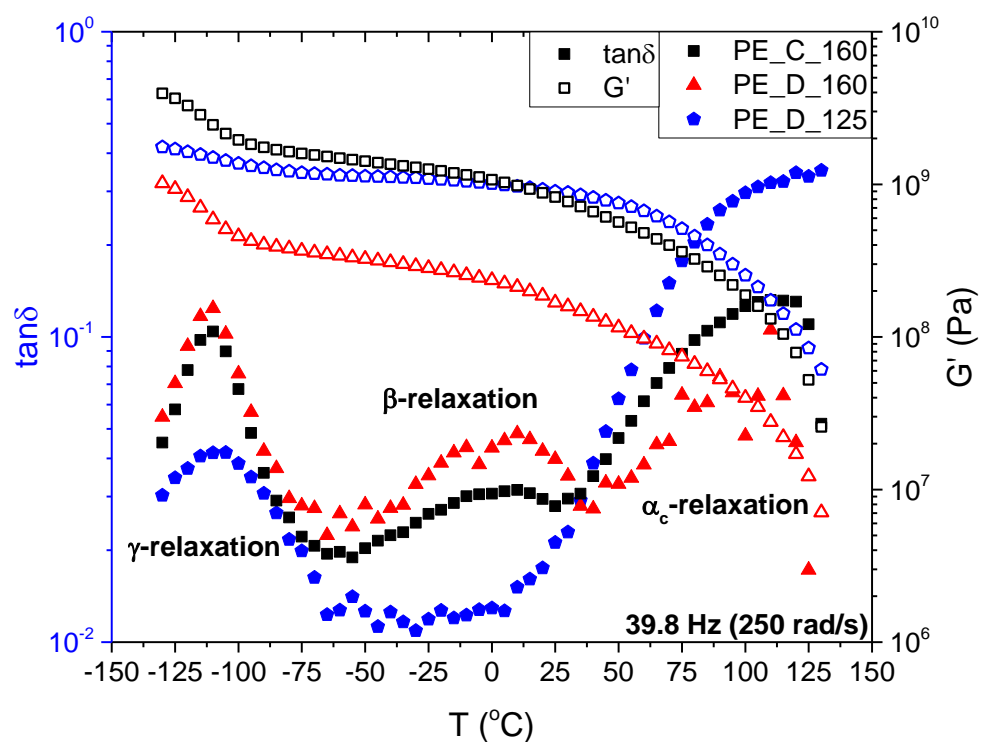


Figure 3.3. Temperature dependence of the real part of modulus ( $G'$ ) and the loss tangent ( $\tan\delta$ ) for all the samples under study at 39.8 Hz.

In Figure 3.3, the values of the real part of modulus and the corresponding loss tangent at 39.8 Hz are presented as a function of temperature for all the samples under study. This frequency was chosen because it was found to be the optimum to clearly observe all the relaxation processes. For the melt processed samples (PE\_C\_160 and PE\_D\_160) we observed an intense  $\gamma$ -relaxation peak at  $-110^\circ\text{C}$  and a well-defined broad  $\beta$ -relaxation located at around  $0^\circ\text{C}$ . On the other hand, the solid-state processed disentangled sample PE\_D\_125 exhibits a broader  $\gamma$ -relaxation (and hence a broader distribution of relaxation times) compared to the other samples, and a very weak  $\beta$ -relaxation, almost undetectable. In the high temperature end, the melting transition is partially shadowing the  $\alpha_c$ -relaxation, so its peak is not clearly observed in  $\tan\delta$ .

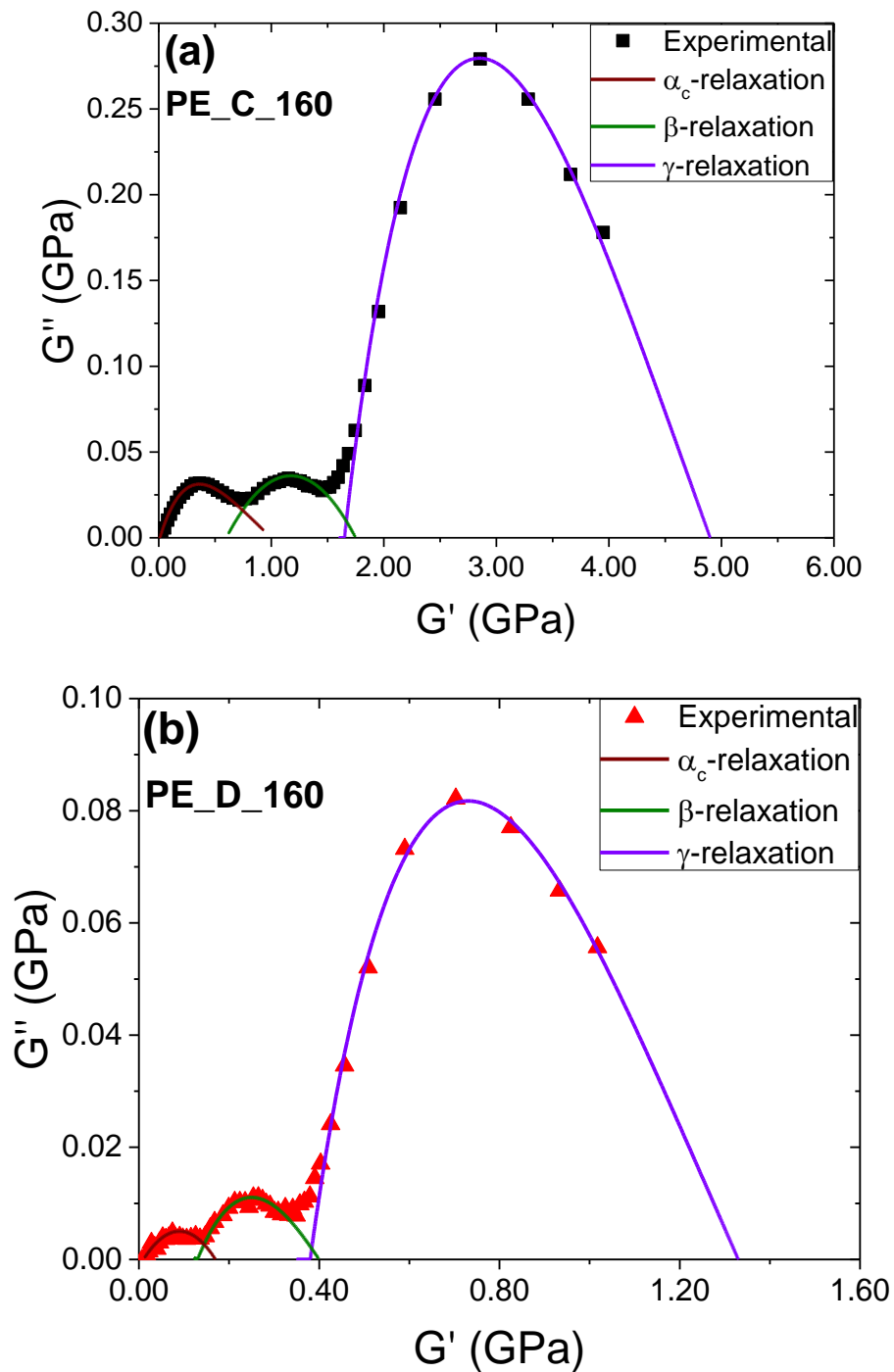
An alternative representation of the rheological data is given in Figure 3.4, plotting the imaginary part versus the real part of modulus, also known as Cole-Cole plot [132]. With this representation, the relaxation strength of each recorded process can be appreciated and evaluated. For this analysis the experimental data at 39.8 Hz as a function of temperature were selected (for the reasons explained previously), and fitted with the Havriliak-Negami frequency-dependent function model according to Equation (1.10), of which analytical form can be seen below in Equation (3.4) [134]:

$$G'(\omega) = G_\infty - \frac{(G_\infty - G_s) \cos \left\{ \arctan \left[ \frac{\sin \left( \frac{\beta\pi}{2} \right)}{(\omega\tau)^{-\beta} + \cos \left( \frac{\beta\pi}{2} \right)} \right] \gamma \right\}}{\left[ 1 + 2(\omega\tau)^\beta \cos \left( \frac{\beta\pi}{2} \right) + (\omega\tau)^{2\beta} \right]^{\frac{\gamma}{2}}} \quad (3.4a)$$

$$G''(\omega) = \frac{(G_\infty - G_s) \sin \left\{ \arctan \left[ \frac{\sin \left( \frac{\beta\pi}{2} \right)}{(\omega\tau)^{-\beta} + \cos \left( \frac{\beta\pi}{2} \right)} \right] \gamma \right\}}{\left[ 1 + 2(\omega\tau)^\beta \cos \left( \frac{\beta\pi}{2} \right) + (\omega\tau)^{2\beta} \right]^{\frac{\gamma}{2}}} \quad (3.4b)$$

where  $G_\infty = \lim_{\omega \rightarrow \infty} G^*(\omega)$ ,  $G_s = \lim_{\omega \rightarrow 0} G^*(\omega)$ ,  $\tau$  is the relaxation time,  $\beta$  is Cole-Cole shape parameter that contributes to the broadness of the peak and  $\gamma$  is the Davidson-Cole shape parameter that corresponds to the asymmetry of the peak [132,133]. It should be noted that the data were fitted only to obtain an approximate value of the relaxation strength,  $G_\infty - G_s$ , of each relaxation process, since a frequency-dependent model is applied to temperature-dependent experimental data [157]. Hence, considering the principle of *time-temperature superposition*, the  $G_\infty$  corresponds to the low temperature edge and the  $G_s$  to the high

temperature edge of the relaxation, while the relaxation times for all relaxations were set as  $\tau = 0.004 \text{ s} = (2 \cdot \pi \cdot 39.8)^{-1}$ , not corresponding to the actual relaxation times of the observed processes. The fitting parameters are presented in Table 3.2.



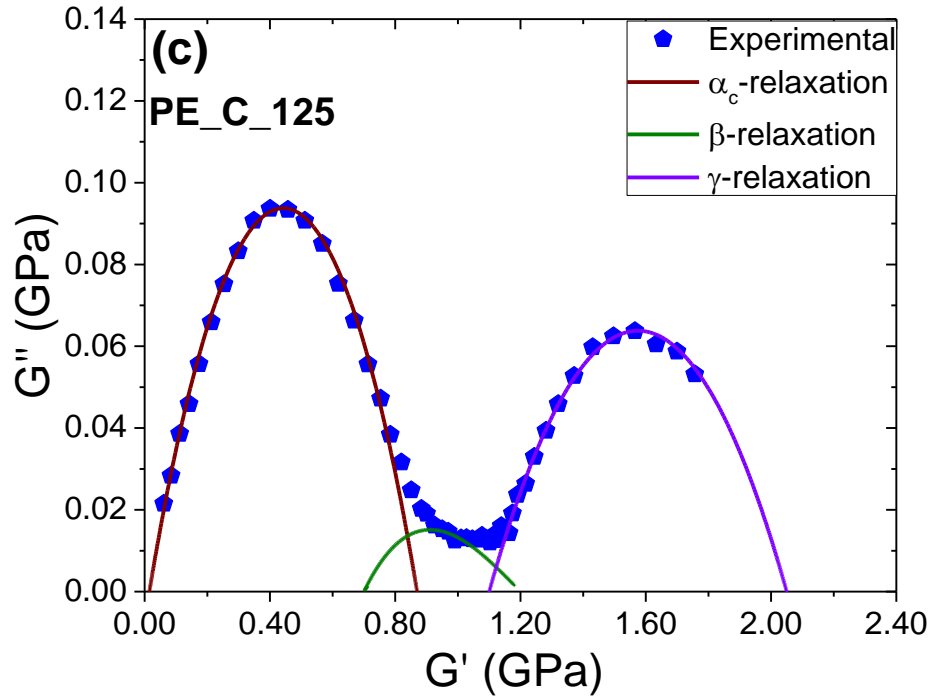


Figure 3.4. Cole-Cole representation of the data at 39.8 Hz for the (a) PE\_C\_160, (b) PE\_D\_160 and (c) PE\_D\_125 samples. The lines follow Equation (3.4) and the corresponding parameters can be found in Table 3.2.

Table 3.2. The  $G_\infty$ ,  $G_\infty - G_s$ ,  $G_N$ ,  $\beta$  and  $\gamma$  Havriliak-Negami parameters for the fittings at 39.8 Hz.

Sample	Process	$G_\infty$ (GPa)	$G_\infty - G_s$ (GPa)	$G_N$ (a.u.)	$\beta$	$\gamma$
PE_C_160	$\alpha_c$ -relaxation	1.000	0.990	0.202	0.135	0.300
	$\beta$ -relaxation	1.750	1.150	0.235	0.080	1.000
	$\gamma$ -relaxation	4.900	3.250	0.663	0.340	0.340
PE_D_160	$\alpha_c$ -relaxation	0.170	0.160	0.120	0.080	1.000
	$\beta$ -relaxation	0.400	0.270	0.203	0.125	0.600
	$\gamma$ -relaxation	1.330	0.950	0.714	0.340	0.340
PE_D_125	$\alpha_c$ -relaxation	0.870	0.855	0.417	0.275	1.000
	$\beta$ -relaxation	1.200	0.500	0.244	0.100	0.500
	$\gamma$ -relaxation	2.050	0.950	0.463	0.170	1.000



As it can be observed for all samples, the  $\alpha_c$ -relaxations start from the (0,0) of the Cole-Cole graph, indicating that there is no other relaxation at higher temperatures. For comparison reasons, all the relaxation strengths  $G_\infty - G_s$  are normalized with the  $\gamma$ -relaxation's  $G_\infty$  value (as the value in its glassy state corresponding to the  $G'$  value at T approaching 0 K) and shown as a normalized relaxation strength parameter  $G_N$ , as seen below [259]:

$$G_N = \frac{G_\infty - G_s}{G_\infty|_{\gamma-rel.}} \quad (3.5)$$

In Figure 3.5, the normalized relaxation strength parameter,  $G_N$ , is presented as a function of crystallinity, obtained by the DSC first heating cycle. A strong linear dependence is observed, only for the  $\alpha_c$ - and  $\gamma$ -relaxations, with the  $\beta$ -relaxation being almost independent of crystallinity. As expected, the  $\alpha_c$ -relaxation  $G_N$  increases with crystallinity, while the  $\gamma$ -relaxation decreases. The values of the relaxation strength (and thus its normalized value here) are a measure of the number of molecules that participate in the corresponding relaxation [157]. In the literature, in the case of branched polyethylene, a similar trend was observed with increasing the branching density but for the  $\beta$ -relaxation [160].

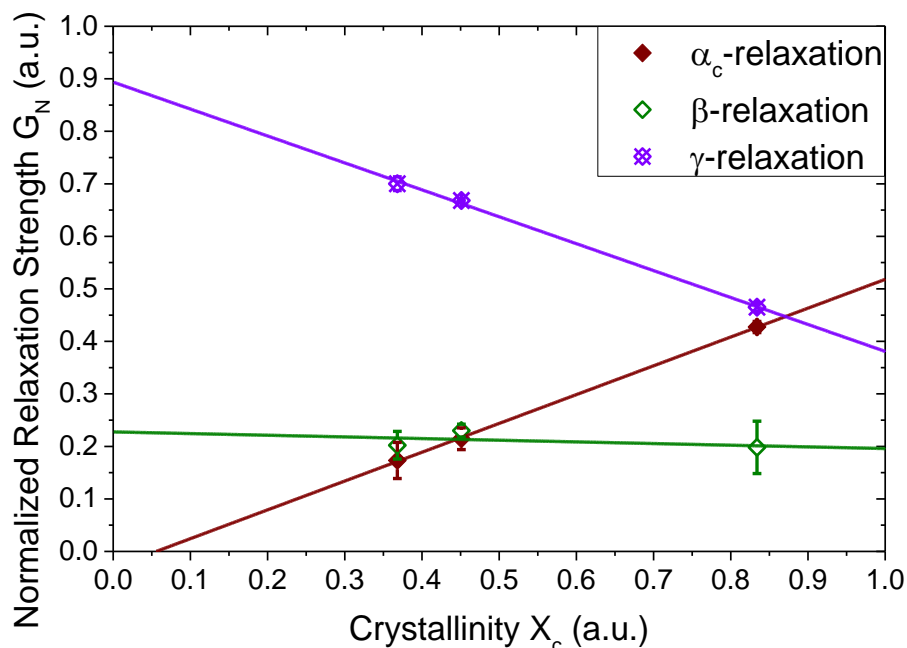


Figure 3.5. The normalized relaxation strength,  $G_N$ , of the recorded relaxations as a function of crystallinity fraction,  $X_c$ , for the samples under study. The values presented are the average of the  $G_N$  as calculated for each relaxation from the  $10^{-2}$  Hz,  $10^{-1}$  Hz,  $10^0$  Hz,  $10^1$  Hz and  $10^2$  Hz Cole-Cole plots and the errors correspond to the uncertainty calculations. (The lines serve as guide for the eye only.)

The temperature dependence of each recorded relaxation was determined by fitting the loss modulus versus the temperature with Lorentzian curves, thus obtaining the temperature loss peak position varying with frequency [127]. The  $\alpha_c$ - and  $\beta$ -relaxations as observed for all the samples under study were found to follow an Arrhenius temperature trend alongside the  $\gamma$ -relaxation of the melt processed samples, as follows below:

$$f = f_0 e^{-\frac{E_A}{k_B T}} \quad (3.6)$$

where  $f_0$  is a pre-exponential factor,  $E_A$  is the activation energy,  $k_B$  the Boltzmann constant and  $T$  the absolute temperature. An Arrhenius temperature dependency is expected for the  $\alpha_c$ -relaxation of semi-crystalline polymers and secondary processes [260].

The temperature dependence of  $\gamma$ -relaxation originating from the solid-state processed sample, however, exhibits a non-Arrhenius behaviour, typical of the dynamic glass-to-rubber transition process [261,262]. This deviation from the Arrhenius behaviour is attributed to a decrease in the unoccupied volume with temperature decreasing, as approaching the glass transition in isobaric conditions, where the relaxation dynamics slow down dramatically (the relaxation time increases faster than the Arrhenius dependence allows) [263,264]. The non-Arrhenius behaviour can also be translated as the cooperative rearrangement of the amorphous segments to reach an energetic minimum approaching the glass transition temperature [265–268]. The cooperativity of the relaxation refers to the cooperative relaxation motion of the neighbouring molecules of any given molecule as they are approaching the glass transition temperature [55]. This process was found to follow the Vogel-Fulcher-Tammann-Hess (VFTH) equation which obeys the expression below:

$$f = f_0 e^{-\frac{DT_V}{T-T_V}} \quad (3.7)$$

where  $f_0$  is again a pre-exponential factor,  $D$  is a dimensionless parameter that can be related with the steepness (fragility) of the relaxation process and how much it deviates from the Arrhenius behaviour,  $T_V$  the Vogel temperature which corresponds to an ideal glass-to-rubber transition and  $T$  is the absolute temperature [136,137]. The relaxation dynamics are presented for all the samples at Figure 3.6 and the calculated fitting parameters are listed in Table 3.3.

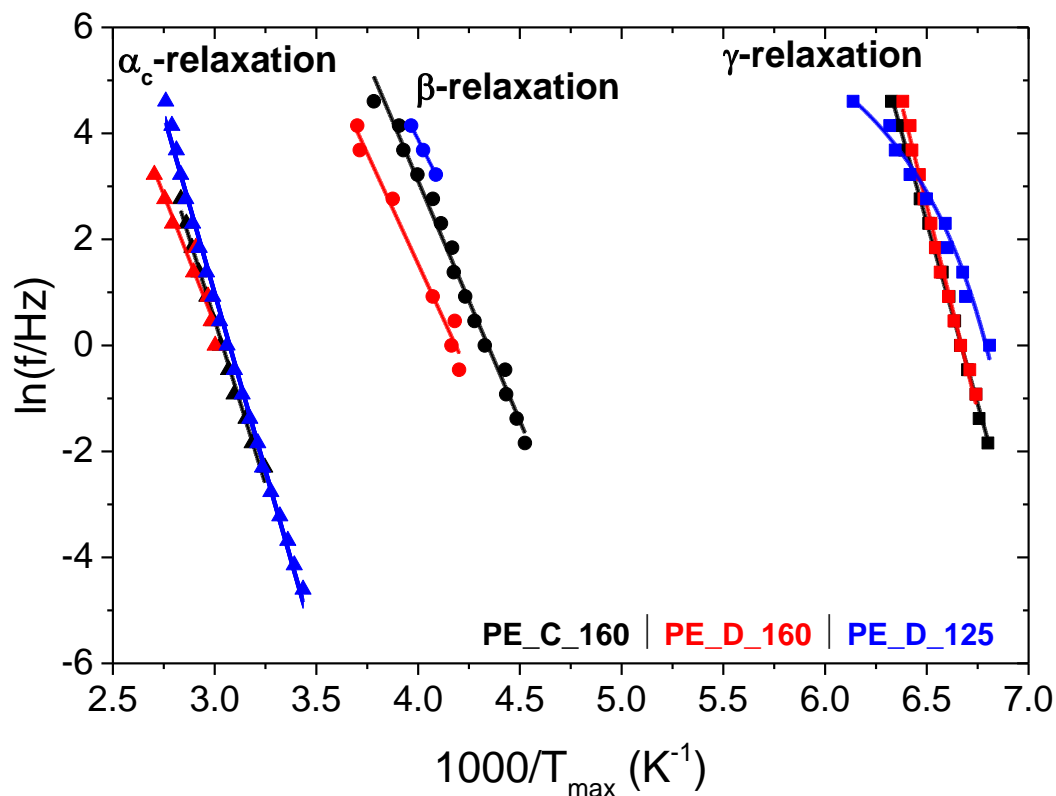


Figure 3.6. Arrhenius plot of the recorded relaxations for all the samples under study.

Table 3.3. Arrhenius and VFTH fitting parameters of the corresponding relaxations.

Sample	Process	Arrhenius	VFTH	
		$E_A$ (eV   kJ/mol)	$T_V$ ( $^{\circ}\text{C}$   K)	D (a.u.)
PE_C_160	$\alpha_c$ -relaxation	1.070   103.24		
	$\beta$ -relaxation	0.780   75.26		
	$\gamma$ -relaxation	1.180   113.85		
PE_D_160	$\alpha_c$ -relaxation	0.839   80.95		
	$\beta$ -relaxation	0.719   69.37		
	$\gamma$ -relaxation	1.334   128.71		
PE_D_125	$\alpha_c$ -relaxation	1.156   111.54		
	$\beta$ -relaxation	0.653   63.00		
	$\gamma$ -relaxation	-	-135.10   138.05	0.740

The calculated activation energy of the  $\alpha_c$ -relaxation for each sample shows a crystallinity dependency, with the more crystalline sample (PE\_D\_125) exhibiting the highest activation energy. The  $\beta$ -relaxation activation energies were found to vary between 0.653 eV for sample

PE\_D\_125 to 0.780 eV for sample PE\_C\_160, showing a strong discrepancy from reported values of 2.280 eV for lower molecular weight polyethylene samples, indicating a different molecular mechanism [143]. The samples reported in the literature exhibit either VFTH trends [143], or Arrhenius trends with calculated values ranging between 2.073 eV to 3.309 eV indicating a cooperative segmental motion [142,147,269], both assigned to the dynamic glass-to-rubber transition process. However, the polyethylene grades discussed in the literature are not linear, like in the case of UHMWPE, highlighting thus, that linear polyethylene's dynamic glass-to-rubber transition process is not the  $\beta$ -relaxation. The  $\gamma$ -relaxation of the melt-processed samples PE\_C\_160 and PE\_D\_160 exhibited activation energies of 1.180 eV and 1.334 eV respectively. The relatively high values indicate a cooperative segmental motion similar to what is observed in the literature ( $\sim 1.5$  eV) for the dynamic glass-to-rubber transition process [142]. The  $\gamma$ -relaxation of polyethylene have been attributed to crankshaft motions involving up to 4 carbon atoms (Schatzki crankshaft motion [270]) and considered to take place in the glassy state (below the glass-to-rubber transition temperature) [271]. However, the corresponding activation energies generally observed, range between 0.477 eV to 0.650 eV [271], which are considerably lower than those we report here and therefore we would exclude the crankshaft motions as the molecular origin for this relaxation process, but attribute the relaxation to the dynamic glass-to-rubber transition process as mentioned previously.

The notable exception is the  $\gamma$ -relaxation temperature dynamics of the disentangled sample (PE\_D\_125) that follows a non-Arrhenius behaviour. The data are fitted with a VFTH equation, indicative of the dynamic glass-to-rubber transition, reinforcing the notion that this should be the physical mechanism behind the  $\gamma$ -relaxation, as discussed earlier.

It is very interesting to note that only the  $\gamma$ -relaxation originating from the disentangled highly crystalline sample follows this trend. The significant relaxation variation between the melt and solid-state processed samples arises from the different size and concentration of the crystalline domains, supported also by DSC. The melting temperature of the first heating cycle observed for the solid-state processed sample is  $\sim 6^\circ\text{C}$  higher comparing to the melt processed samples, indicating larger crystals as discussed elsewhere from our group [89,91]. Considering that the entanglements work as physical constrains hindering the movement due to the application of the mechanical strain, the lower entanglement density in the amorphous parts of the chains contribute into more mobile amorphous regions [48]. Hence, the combination of bigger crystals and less entangled amorphous fractions result into more mobile amorphous regions, exhibiting thus a non-Arrhenius temperature dependence for the

$\gamma$ -relaxation. In general, the Vogel temperature,  $T_V$ , is expected to be around 40 K below the calorimetric glass-to-rubber transition [108], placing the  $T_g$  of dis-UHMWPE from the present analysis to about 178 K (-95°C).

Since the dynamic glass-to-rubber transition process is attributed to the  $\gamma$ -relaxation and the  $\alpha_c$ -relaxation to the crystalline domains, it is possible that the  $\beta$ -relaxation originates from fluctuations of amorphous segments of larger length scales than the dynamic glass-to-rubber transition or amorphous segments close to the lamella as already suggested by others [272,273].

To summarize the results presented in this section of Chapter 3, three different relaxation processes were observed, namely  $\alpha_c$ -,  $\beta$ - and  $\gamma$ -relaxations as expected for polyethylene. The relaxation strengths of the  $\alpha_c$ - and  $\gamma$ -relaxations were found to be dependent of the crystallinity content, verified by means of differential scanning calorimetry. The temperature loss peak positions of the recorded relaxation processes were analysed at different frequencies and all were found to follow the Arrhenius equation apart from the  $\gamma$ -relaxation of the solid-state processed disentangled sample, which followed a VFTH trend. This sample is characterized by bigger crystalline structures and less entangled amorphous fractions, resulting into more mobile amorphous segments. On the contrary, the amorphous segments of the melt-state processed samples are more confined within the crystalline domains and hindered by the entanglements, following thus an Arrhenius behaviour. Since the VFTH trend is indicative of the dynamic glass-to-rubber transition process, it is proposed that the crystalline polydispersity and entanglement density are affecting the free volume and thus the relaxation chain dynamics of the  $\gamma$ -relaxation.

### 3.1.2. Broadband dielectric spectroscopy

Following the chain dynamics of solid-state processed dis-UHMWPE obtained by torsional rheology and presented previously in Chapter 3 section 1.1, dielectric spectroscopy is employed in the present chapter to identify the relaxation properties. Since polyethylene has a very small dipole moment, the  $\text{Al}_2\text{O}_3$  catalytic ashes were used as dielectric probes to enhance the dielectric response and thus the obtained signal [30]. When the presence of dielectric probes is kept to a minimum concentration (1-10% w/w), it does not affect significantly the polymer chain dynamics but it significantly increases the relaxation strength and the  $\tan\delta$  values, according to an older study of polyethylene –  $\text{TiO}_2$  dielectric probes systems [143].

The dielectric response of all dis-UHMWPE samples is shown in Figure 3.7, where the real and imaginary parts of dielectric permittivity at 160°C are presented in Figure 3.7a and Figure 3.7b respectively. The complex dielectric permittivity  $\varepsilon^*$  is defined as:

$$\varepsilon^* = \varepsilon' - i\varepsilon'' \quad (3.8)$$

where,  $\varepsilon'$  and  $\varepsilon''$  are the real and imaginary parts of dielectric permittivity respectively. Figure 3.7a shows how the relaxation strength increases with increasing Al<sub>2</sub>O<sub>3</sub> content. This can be better appreciated in Figure 3.7b, where the imaginary part of the dielectric permittivity is presented. The PE\_5.6 sample (no Al<sub>2</sub>O<sub>3</sub> content) exhibits a close to zero dielectric loss behaviour in the middle and high frequency range where all the relaxation processes are located, thus confirming that the presence of dielectric probes is paramount to obtain a dielectric response from UHMWPE, as discussed elsewhere for the case of PE [30,143,274]. However, this sample exhibits relatively higher values of losses combined with an increase in the real part of dielectric permittivity in the low frequency edge which could be ascribed to interfacial polarization between the crystalline and the amorphous phases of polyethylene and also some contribution from the dc conduction. This effect seems to be less intense in the rest of the samples in the window of observation, since the whole process has moved to lower frequencies due to the increased heterogeneity from the presence of Al<sub>2</sub>O<sub>3</sub> catalytic ashes. As the concentration of catalytic ashes increases, the dielectric loss values increase as well. It is interesting to note that the loss peak maximum tends to shift to lower frequencies with the increase of molecular weight, as bigger chains require more time to react to the applied electric field. To follow the formation of entanglements, we have decided to focus on sample with an Al<sub>2</sub>O<sub>3</sub> concentration of 2.6% w/w (sample PE\_4.2\_AIO). This sample balances a strong enough relaxation strength to perform dielectric studies with a concentration of catalytic ashes that is not expected to affect strongly the entanglement topology in the melt.

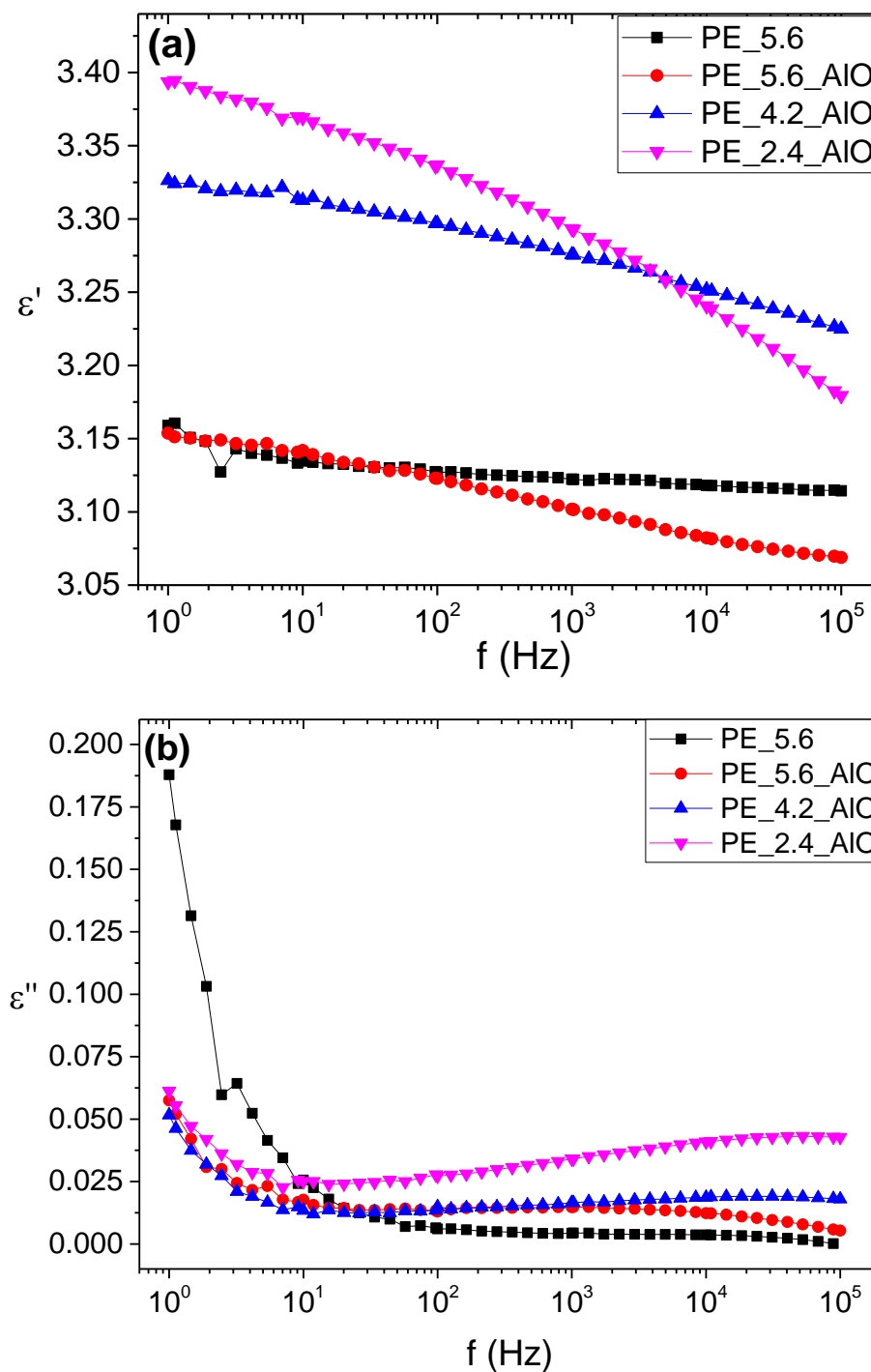


Figure 3.7. (a) The real and (b) imaginary parts of dielectric permittivity as a function of frequency at 160°C for the studied samples.

In Figure 3.8, we report the comparison between the imaginary part of dielectric permittivity (Figure 3.8a) and electric modulus (Figure 3.8b) as a function of frequency and temperature for the PE\_4.2\_AIO specimen. The complex electric modulus  $M^*$  is defined according to Equation (3.9):

$$M^* = \frac{1}{\varepsilon^*} = \frac{1}{\varepsilon' - i\varepsilon''} = \frac{\varepsilon'}{\varepsilon'^2 + \varepsilon''^2} + i \frac{\varepsilon''}{\varepsilon'^2 + \varepsilon''^2} = M' + iM'' \quad (3.9)$$

where  $M'$ , and  $M''$  are the real and the imaginary parts of the electric modulus respectively, in analogy to the complex modulus defined for other types of dynamic measurements, like torsional rheology discussed earlier. The processes that can be found using the complex permittivity formalism are present at very similar frequencies and temperatures range in the electric modulus formalism. For a single process, the relationship between the peak frequencies in both formalisms can be written as:

$$f_{M,max} = \frac{\varepsilon_s}{\varepsilon_\infty} f_{\varepsilon,max} \quad (3.10)$$

where  $f_{M,max}$  and  $f_{\varepsilon,max}$  are the relaxation peak frequencies in the modulus and permittivity formalisms respectively while  $\lim_{f \rightarrow 0} \varepsilon^* = \varepsilon_s$  and  $\lim_{f \rightarrow \infty} \varepsilon^* = \varepsilon_\infty$ . When the ratio of  $\varepsilon_s/\varepsilon_\infty$  is relatively close to 1, the loss peak positions of dielectric permittivity and electric modulus are very similar. For this reason, using the dielectric permittivity or electric modulus formalisms for the analysis in our systems is equivalent.



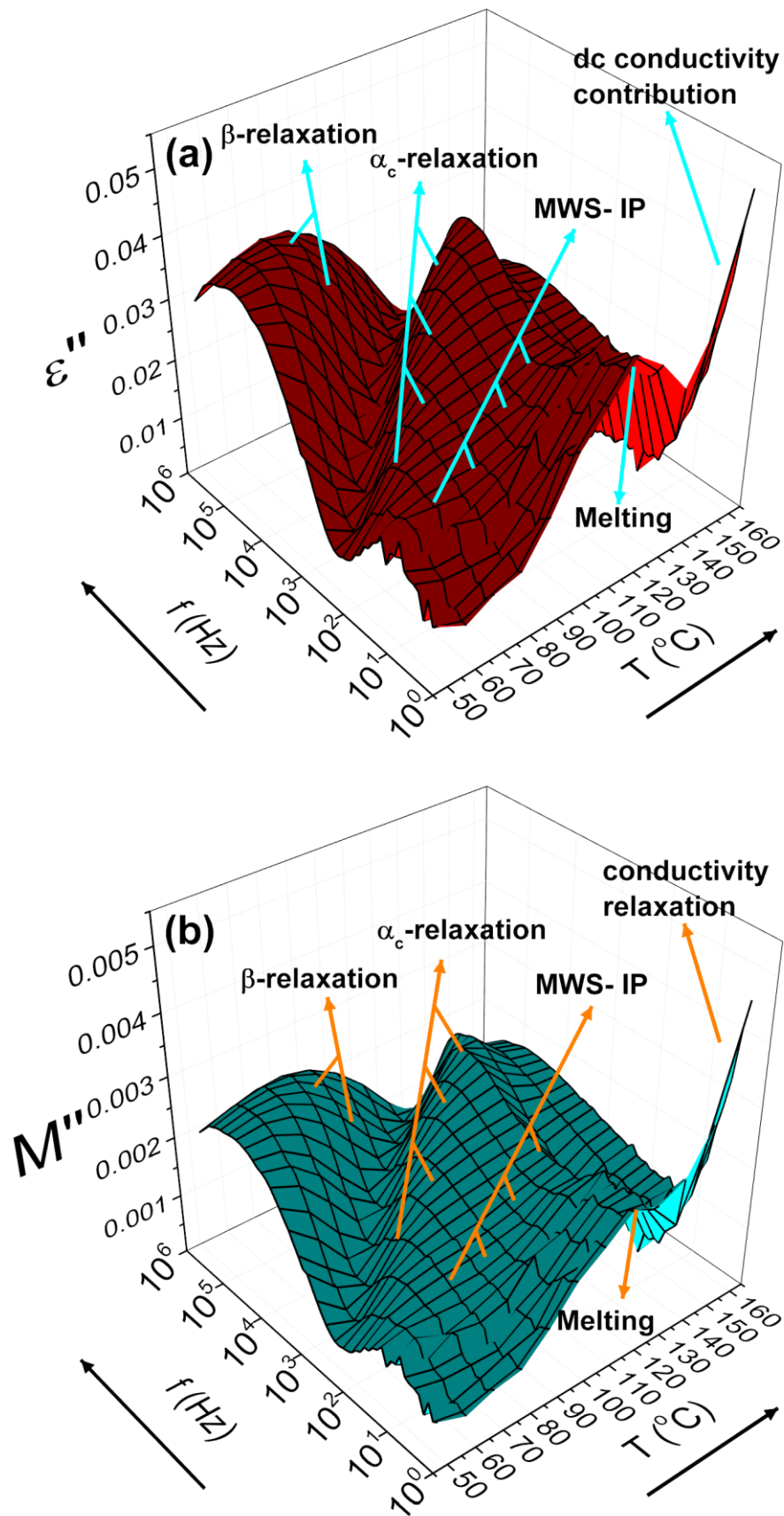


Figure 3.8. The imaginary parts of (a) dielectric permittivity and (b) electric modulus both as a function of frequency and temperature for the PE\_4.2\_AIO sample.

To better discern sub-relaxation processes, the electric modulus formalism will be adopted from now on in this analysis. To analyse the different processes present in the PE\_4.2\_AIO sample a deconvolution technique that employs frequency-dependent model functions, namely the Havriliak-Negami model function, in its electric modulus formalism as developed by Tsangaris *et al.* [114], was used. Equations (3.11) provide the expressions for the real and imaginary part of electric modulus:

$$M' = \frac{M_\infty M_s [M_s A^\gamma + (M_\infty - M_s) \cos \gamma \varphi] A^\gamma}{M_s^2 A^{2\gamma} + 2A^\gamma (M_\infty - M_s) M_s \cos \gamma \varphi + (M_\infty - M_s)^2} \quad (3.11a)$$

$$M'' = \frac{M_\infty M_s [(M_\infty - M_s) \sin \gamma \varphi] A^\gamma}{M_s^2 A^{2\gamma} + 2A^\gamma (M_\infty - M_s) M_s \cos \gamma \varphi + (M_\infty - M_s)^2} \quad (3.11b)$$

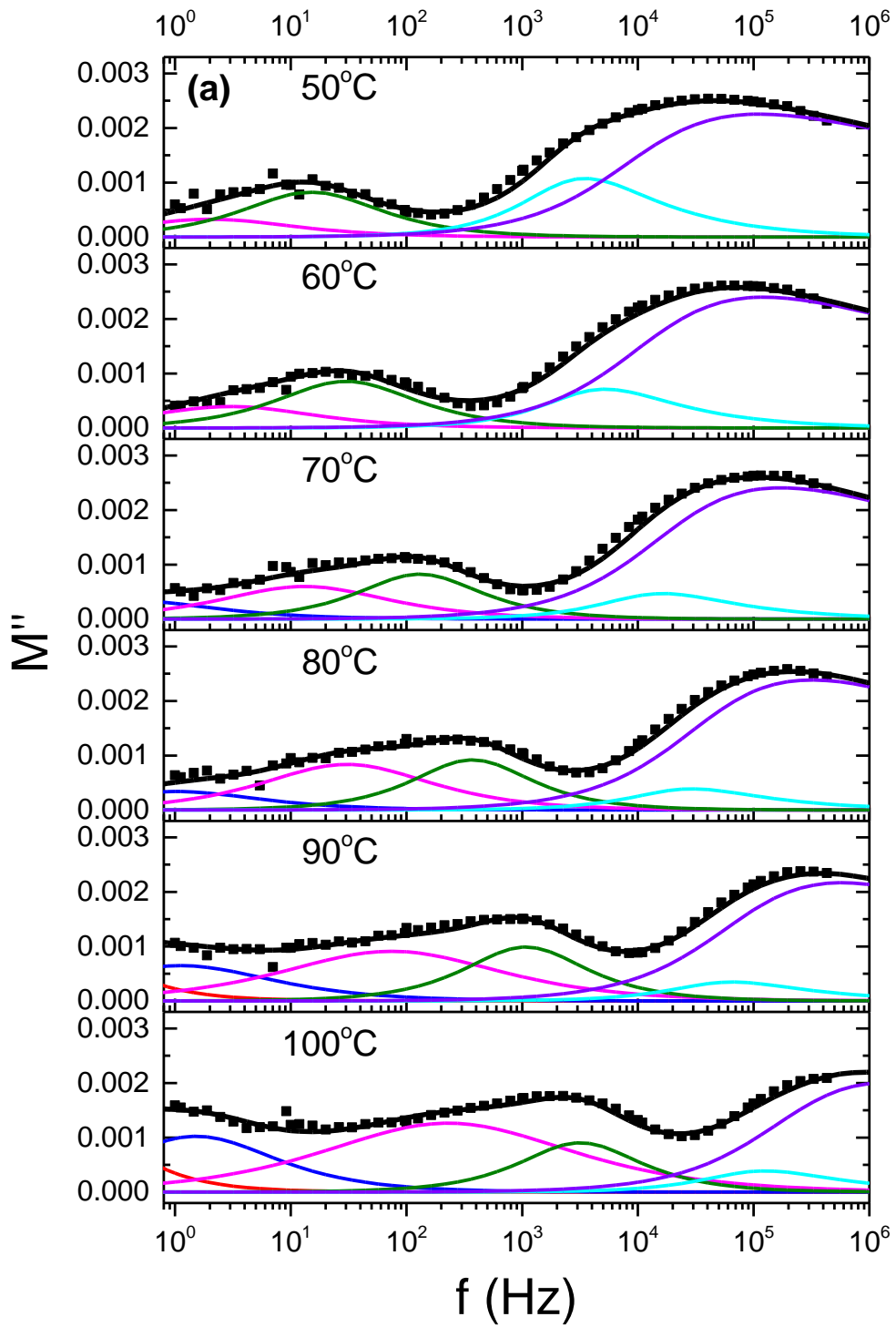
where:

$$A = \left[ 1 + 2(\omega\tau)^\beta \sin\left(\frac{\pi(1-\beta)}{2}\right) + (\omega\tau)^{2\beta} \right]^{1/2} \quad (3.11c)$$

$$\varphi = \arctan \left[ \frac{(\omega\tau)^\beta \cos\left(\frac{\pi(1-\beta)}{2}\right)}{1 + (\omega\tau)^\beta \sin\left(\frac{\pi(1-\beta)}{2}\right)} \right] \quad (3.11d)$$

For  $\beta = \gamma = 1$  the above relations reduce to the Debye function model for a single relaxation time, while for  $\beta < 1$ ,  $\gamma = 1$  and  $\beta = 1$ ,  $\gamma < 1$  the symmetrical Cole-Cole and asymmetrical Davidson-Cole model functions apply respectively.  $M_\infty$  and  $M_s$  are the reciprocal values of  $\epsilon_\infty$  and  $\epsilon_s$  respectively. To fit the experimental data in the entire temperature range, a total of six processes were required.

In Figure 3.9 the imaginary part of electric modulus as a function of frequency for PE\_4.2\_AIO is presented, in a range of temperatures that goes from 50 – 100°C (Fig 3.9a) and 110 – 160°C (Fig 3.9b). The points represent the experimental data while the lines are the Havriliak-Negami fits, reproducing with good agreement the experimental data.



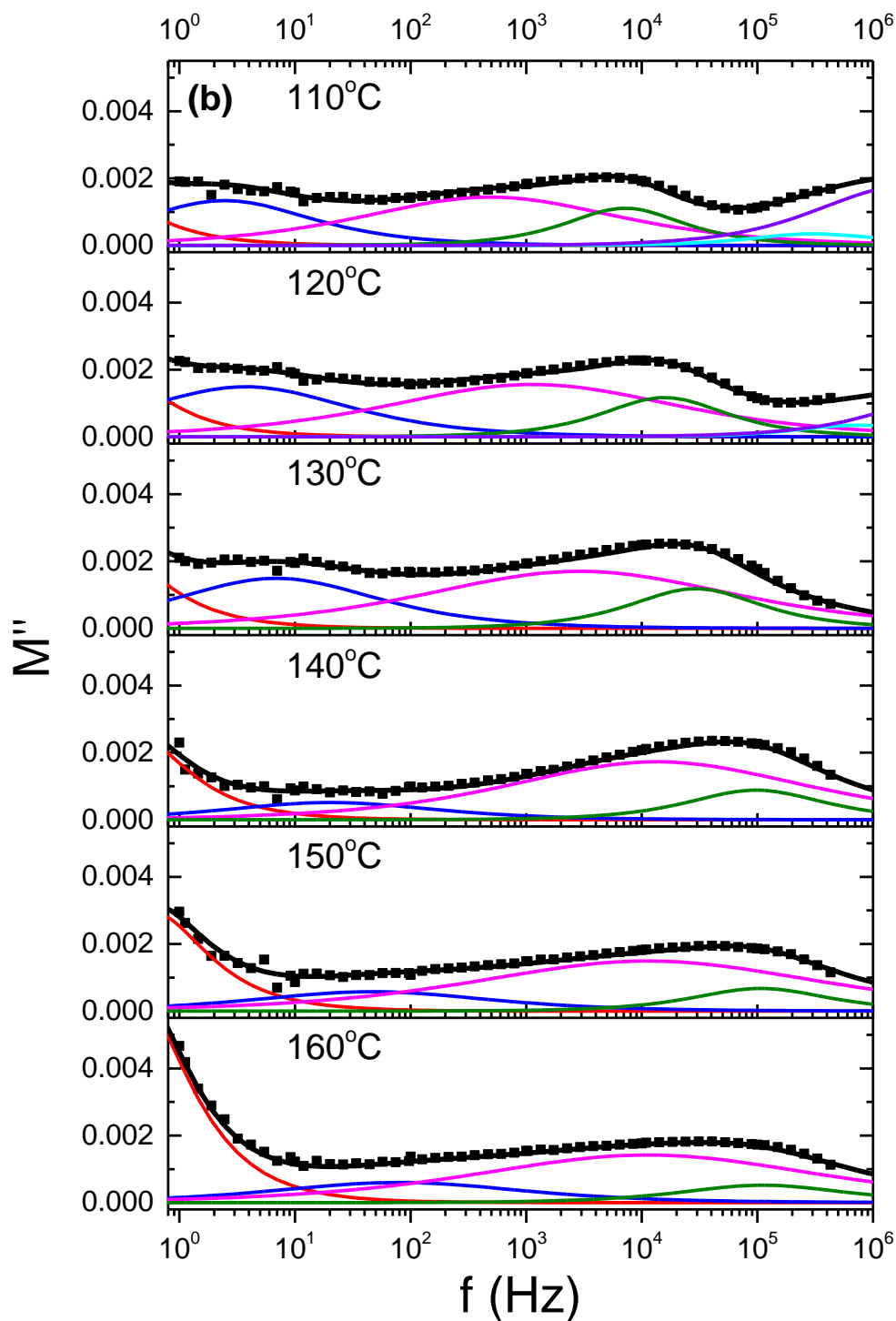


Figure 3.9. The imaginary part of electric modulus as a function of frequency for PE\_4.2\_AIO at Top to bottom: (a) 50 – 100°C and (b) 110 – 160°C with a step of 10°C. The points represent the experimental data while the interpolating lines are obtained from the computational model. The lines are: —  $\beta_1$ -relaxation, —  $\beta_2$ -relaxation, —  $\alpha_c$ -relaxation, — MWS-IP<sub>1</sub>, — MWS-IP<sub>2</sub> and — conductivity relaxation.

The conductivity relaxation is found in the lower end of the frequency window appears from 90°C and is enhanced especially above 130°C. This process is attributed to the contribution of dc conductivity ascribed to the movement of charges from impurities and Al<sub>2</sub>O<sub>3</sub> catalytic ashes within the material. This is presented in a clearer way in Figure 3.10 where the slope of the line in the low frequencies in a log-log graph of loss permittivity and angular frequency is given to be -1. In the electric modulus formalism, this relaxation process is better described employing a Debye function model, as discussed in Chapter 1 section 1.

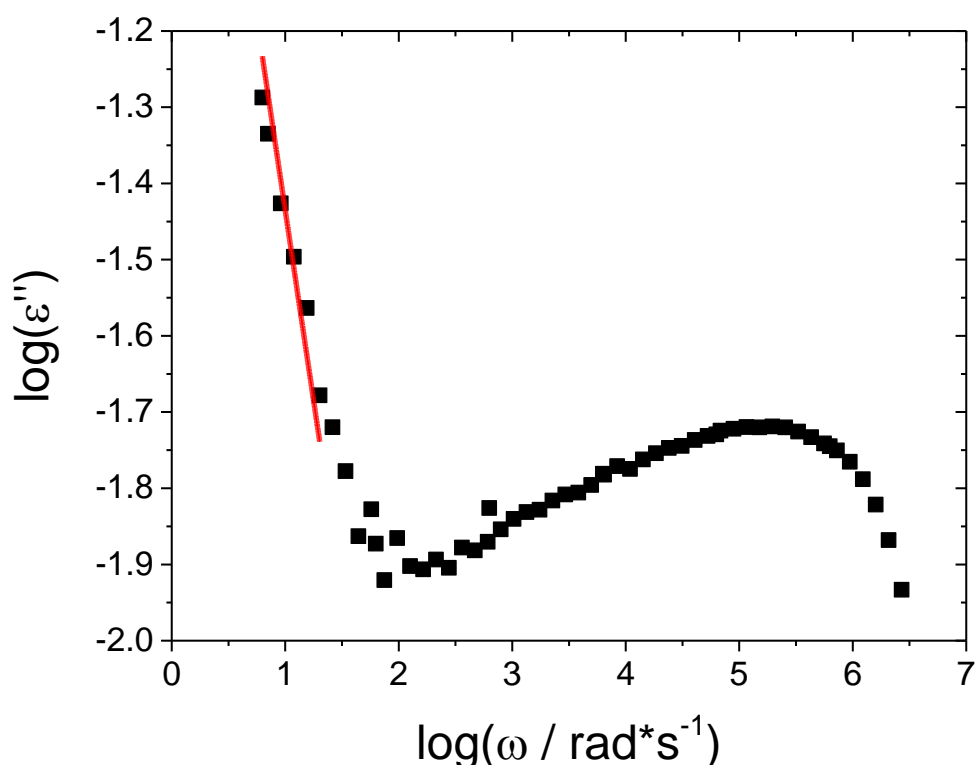


Figure 3.10. The log-log representation of the imaginary part of dielectric permittivity as a function of angular frequency at 160°C for sample PE\_4.2\_AIO. The fitting line has a slope equal to -1 and from the intercept the dc conduction can be approximately calculated as  $\sim 3.3 \cdot 10^{-12}$  S/m, following the relation:  $\log \varepsilon''_{dc} = \log \left( \frac{\sigma_{dc}}{\varepsilon_0} \right) - \log \omega$ .

The MWS-IP, observed in higher frequencies than the conductivity relaxation, is attributed to polarization at the interface between the polymer chains and the ceramic catalytic ashes. Interfacial polarization arises due to the electrical heterogeneity between a material's constituents. It is possible a contributing interfacial polarization between the crystalline and amorphous regions to exist, however its contribution could not be significant comparing to the Al<sub>2</sub>O<sub>3</sub> – polymer contribution, because of the small difference in dielectric

permittivity and conductivity of the amorphous and crystalline parts of UHMWPE. A pronounced interfacial polarization effect should result in high values of the real and imaginary part of permittivity, leading to low values of electric modulus because of Equation (3.9). The MWS-IP is found to have two sub-processes, MWS-IP<sub>1</sub>- and MWS-IP<sub>2</sub> referring to two distinct processes characterized with different entanglement densities. The two regions are expected to react differently to the electric field, as chains in the entangled amorphous will have longer relaxation times compared to the disentangled regions, where the chains can move more easily.

The  $\alpha_c$ -relaxation involves the polarization of the crystalline phase because of the application of the electric field. The intensity of the process was observed to diminish with the increase of temperature, due to the progressive disappearance of the crystals, although it does not vanish completely, even at 160°C.

Finally, the  $\beta$ -relaxation is attributed to the molecular fluctuations of amorphous chain segments. In the case of dis-UHMWPE, we have observed two distinct processes that might be attributed to two distinct amorphous regions present in this material, described with different entanglement densities, in parallel with the interfacial polarization dynamics that we discussed previously. Both sub-relaxations are strongly asymmetrical (the asymmetrical  $\gamma$  parameter in  $\beta_1$ -process varied from 0.190 to 0.260, while in the case of the  $\beta_2$ -process was found to be 0.658 in the considered temperature range), with  $\beta_2$  showing slightly higher relaxation times than  $\beta_1$ .

In Figure 3.11 are reported the loss peak positions versus the reciprocal temperature for the processes described above, except for the conductivity relaxation. All five processes' frequency loss peak positions follow the Arrhenius equation expressed by Equation (3.6) as seen previously. Calculated values of the activation energy are given in Figure 3.11. These results are going to be discussed in comparison with torsional rheology relaxation data in Chapter 3 section 1.3.

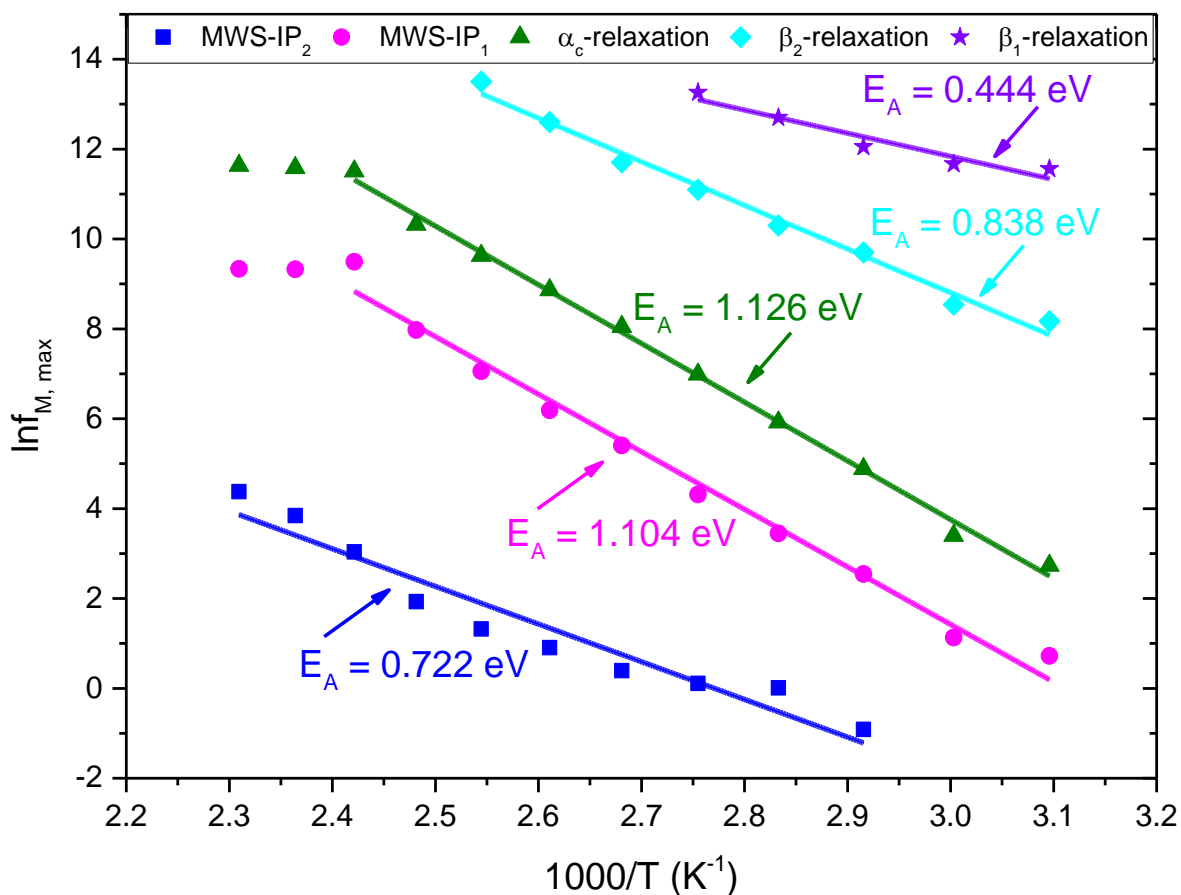


Figure 3.11. Arrhenius plot for the maximum loss positions as a function of the reciprocal temperature for all observed relaxation processes in PE<sub>4.2</sub>A10. The activation energy for each process is given as well.

When simulating  $M''$  as a function of frequency, it was observed that the relaxation times for the  $\alpha_c$ -relaxation appear to remain constant between 140 and 160°C, instead of decreasing, which is expressed via shifting the frequency loss peak position to higher frequencies, as would be expected from the increased kinetic energy. According to the literature, this behaviour is due to gradual melting of crystals of different dimensions [274].

Interestingly, in the case of the MWS-IP<sub>1</sub>, the relaxation times appear to remain constant when entering the melt state similarly to what happens to the  $\alpha_c$ -relaxation: we ascribe this effect to the progressive formation of entanglements in both the initial disentangled amorphous and disentangled molten crystals. In the case of the MWS-IP<sub>2</sub> instead, the frequency maximum increases with temperature even during the melting, as no further entanglement formation is expected to happen in these regions. Both processes are described

by the symmetrical Cole-Cole function model, in analogy with the  $\alpha_c$ -relaxation described above.

The activation energy of the  $\alpha_c$ -relaxation is in very good agreement with the literature values, as we estimated to be  $E_A = 1.126$  eV ( $R^2 = 0.99634$ ) against a reported value of 1.036 eV [147]. According to previous studies, the  $\beta$ -process temperature dependency also follows the Arrhenius equation (although a non-linear relation modelled by the Vogel-Fulcher-Tammann-Hesse equation may be found for low molecular weight samples and amorphous polymers) with an estimated activation energy of  $E_A = 2.280$  eV [143,147]. In our case, it was found that the temperature dependency of the two processes were  $E_A = 0.444$  eV ( $R^2 = 0.90763$ ) for the  $\beta_1$ -process and  $E_A = 0.838$  eV ( $R^2 = 0.98660$ ) for the  $\beta_2$ -process. It is expected from the disentangled amorphous phase to exhibit a lower activation energy and be characterized by a lower relaxation time due to the increased mobility of the less entangled segments, thus attributed to the  $\beta_1$ -process. The two interfacial polarization sub-processes exhibited activation energies of 1.104 eV ( $R^2 = 0.98589$ ) and 0.722 eV ( $R^2 = 0.93035$ ) for the MWS-IP<sub>1</sub> and MWS-IP<sub>2</sub> respectively.

In this section of Chapter 3, the dielectric relaxations of dis-UHMWPE in the presence of Al<sub>2</sub>O<sub>3</sub> catalytic ashes are presented. Two relaxation processes were observed attributed to polyethylene itself, an  $\alpha_c$  process and  $\beta$ -process consisting of two sub-relaxations. Due to the presence of Al<sub>2</sub>O<sub>3</sub> catalytic ashes within the polyethylene matrix, also interfacial polarization was observed which also consisted of two sub-processes, attributed to different dynamics due to the disentangled and entangled amorphous phases.

### 3.1.3. Comparison

Comparing the rheological data to the dielectric via the relaxation map presented in Figure 3.12 below, it is evident that the dielectric  $\beta$ - and  $\alpha_c$ -relaxations corresponds to the one observed with torsional rheology respectively. Especially regarding the  $\alpha_c$ -relaxation, the mechanical dispersion is usually broader compared to the dielectric dispersion which is attributed to the participation of amorphous segments that transfer the mechanical strain to the crystalline domains [156]. The contribution of this amorphous segments to the mechanical  $\alpha_c$ -relaxation is also responsible for the difference of 20 to 30°C ( $T_{\text{dielectric}} < T_{\text{mechanical}}$ ) in the temperature loss peak position at the same frequency of similar polyethylene samples, compared by the two techniques [144]. In the dielectric case, the application of the electric field is responsible for the electric displacement, thus the dielectric response related



to the  $\alpha_c$ -relaxation comes solely from the polymer crystals via a rotational-translation of chain segments [147]. This temperature difference is observable in Figure 3.12 for the dielectric (solid blue symbols) and the rheological (open blue symbols) data of similar dis-UHMWPE polymers, according to the Table 2.1.

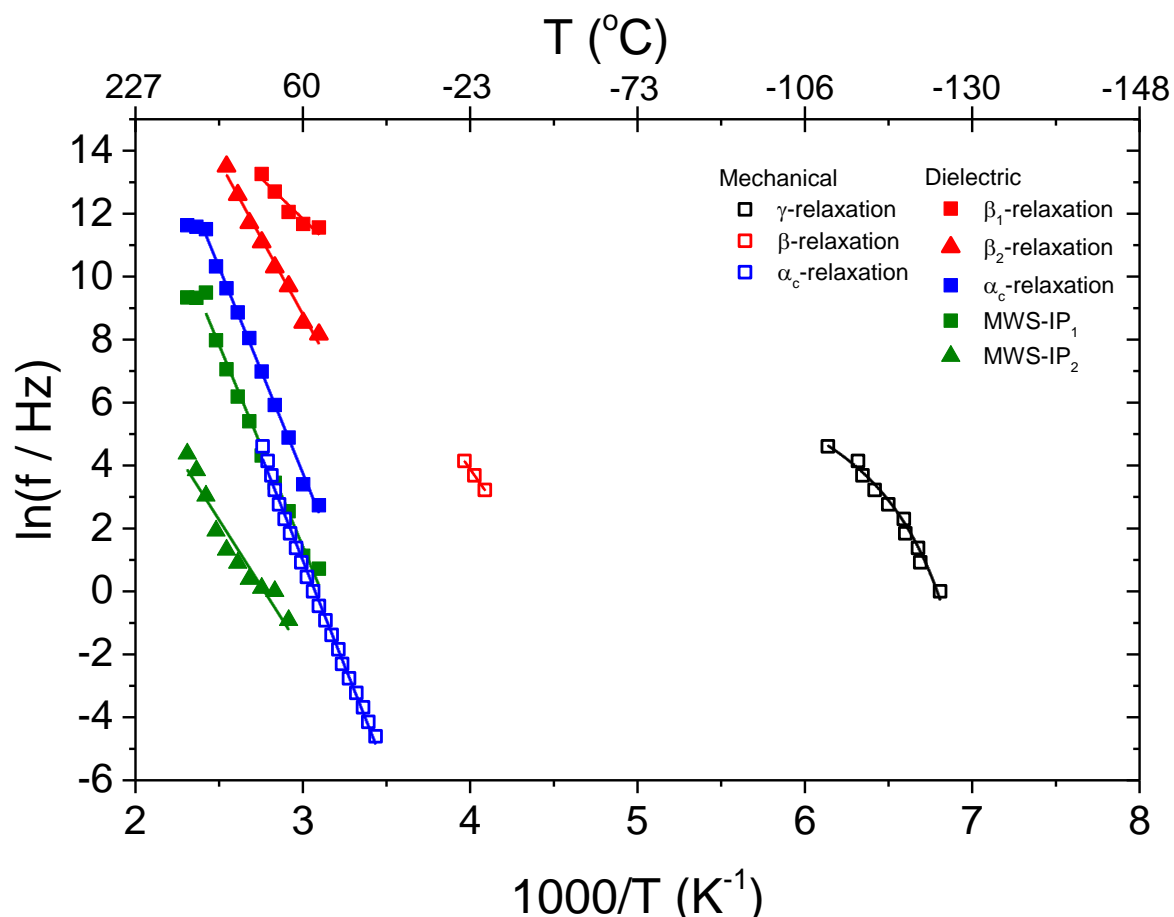


Figure 3.12. Arrhenius plot comparing the dielectric data (solid symbols) as obtained from the PE\_4.2\_AIO sample and the rheological (mechanical) data (open symbols) of the PE\_D\_125 sample.

### 3.2. Entanglement dynamics

#### 3.2.1. Connection between electric modulus & mechanical shear modulus

In the present chapter, a connection via the modulus formalism is drawn between the well-established analysis with melt plate-plate rheology to monitor the formation of entanglements, and dielectric spectroscopy. As soon as this connection is achieved, more information can be deduced from the dielectric spectra regarding the formation of entanglements, with the most prominent to be the experimental verification of the formation

of entanglements in the disentangled amorphous area at temperatures below the melting (solid state).

In Figure 3.13, the real part of electric modulus as a function of time at 160°C for PE\_4.2\_AIO at 10 and 100 Hz is presented. For comparison, the real part of mechanical shear modulus  $G'$  for the same sample at the same temperature at 1 and 10 Hz is presented in the inset of Figure 3.13. An increase in elastic shear modulus  $G'$  is observed as time proceeds due to the progressive increase of entanglements, according to Equation (1.2) [105]. This increase is in agreement with other studies in the literature [49–51]. As it can be appreciated, the same behaviour is observed in the electrical modulus as well, due to the formation of entanglements, although the timescales involved appear to be faster. The formed entanglements restrict the motion of polar parts hindering their ability to be aligned with the field. Consequently, polarization and permittivity diminish approaching a constant value. Electric modulus, being the inverse quantity of permittivity, increases with time reaching a plateau. The different timescale reflects the disparity of the excited substances in the two techniques, i.e. masses and dipoles respectively as previously discussed by Pakula [60].

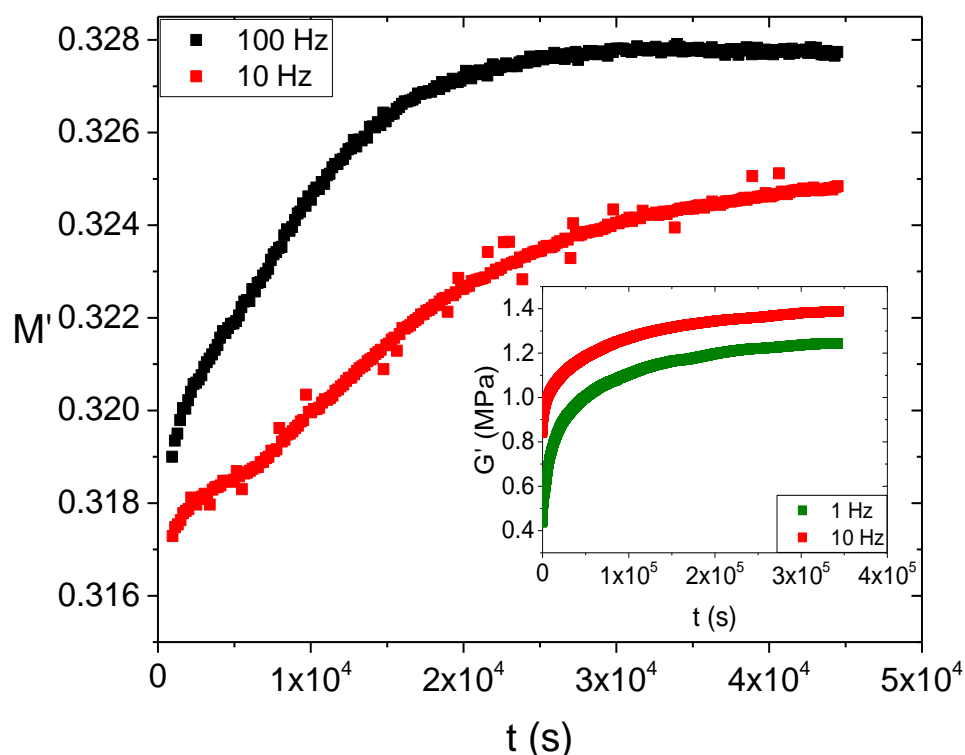


Figure 3.13. The real part of electric modulus as a function of time at 100 and 10 Hz. Inset the real part of mechanical shear modulus as a function of time at 1 and 10 Hz. All for the PE\_4.2\_AIO sample at 160°C.

To gain a better insight on the mechanism of entanglement formation, isothermal runs at various temperatures of dis-UHMWPE were measured as a function of time. In Figure 3.14 the imaginary part of electric modulus as a function of frequency varying the number of frequency sweep cycles at 160°C for the PE\_4.2\_AIO sample analysed before is presented. The points represent the experimental data, while the continuous lines are obtained from the superposition of the processes described before. The experiment clearly shows that with the evolution of time (number of frequency sweep cycles) at constant temperature, the spectra move to lower frequencies, as expected from a system that is becoming more entangled (and less mobile) [275]. From the simulations, it was found out that the process that is most heavily influenced by the evolution of time, in terms of frequency loss peak position, is the MWS-IP<sub>1</sub>, as expected from the entanglement formation. This shift agrees with the fact that entanglements hinder the relaxation of the polymer chains. It should be taken into account that at 160°C the two β-processes will also be affected by the melting transition but having moved to higher frequencies outside the window of observation, they cannot be observed. Therefore, the change that we observe in time as a result of the formation of entanglements is related to the MWS-IP<sub>1</sub> alone, as supported by relaxation simulations.

This study proves that it is possible to follow the dynamics of chain relaxation through either dielectric or mechanical techniques, as already suggested in previous literature [146,149], with the advantage of extending the range of accessible frequencies and temperatures. In addition, the inherent rapidity of dipole movements when compared to masses allows a faster timescale to be accessed and to explore the initial stages of the entanglement formation.

To study the dynamics of entanglement formation a new model based on two equations is hereby proposed. The natural logarithmic loss peak position  $\ln f_{M,max}$  of the MWS-IP<sub>1</sub> versus time, is presented as an inset in Figure 3.14 and it is linear. Therefore, we propose a new model called *linear model of isothermal entanglement formation*. From this equation, the amount of energy that is spent at constant temperature to trigger the transition can be calculated according to:

$$f_{max} = f_0 e^{-\left(\frac{E_D n}{k_B T_M}\right)} \quad (3.12a)$$

where  $f_0$  is an exponential factor indicating the frequency loss peak position for zero-time,  $T_M$  is the temperature during the isothermal measurement,  $E_D$  is the entanglement formation energy,  $n$  is the number of frequency sweeps and  $k_B$  is the Boltzmann constant. Equation (3.12a) should not be confused with the Arrhenius equation (Equation (3.6)), as  $E_D$  is the

energy spent by the polymer to entangle at the temperature  $T_M$  and not an activation energy. In this equation, the number of frequency sweep cycles,  $n$ , has no units although it is an indirect measure of time. When the frequency sweep time duration is kept constant then Equation (3.12b) holds:

$$E_D n \equiv P_D t_0 n \equiv P_D t \quad (3.12b)$$

where  $P_D$  is the entanglement formation power and  $t_0$  is the duration of one frequency sweep cycle;  $t$  is the absolute time. The higher the value of  $P_D$ , the higher the number of entanglements forming at a constant temperature with the evolution of time.

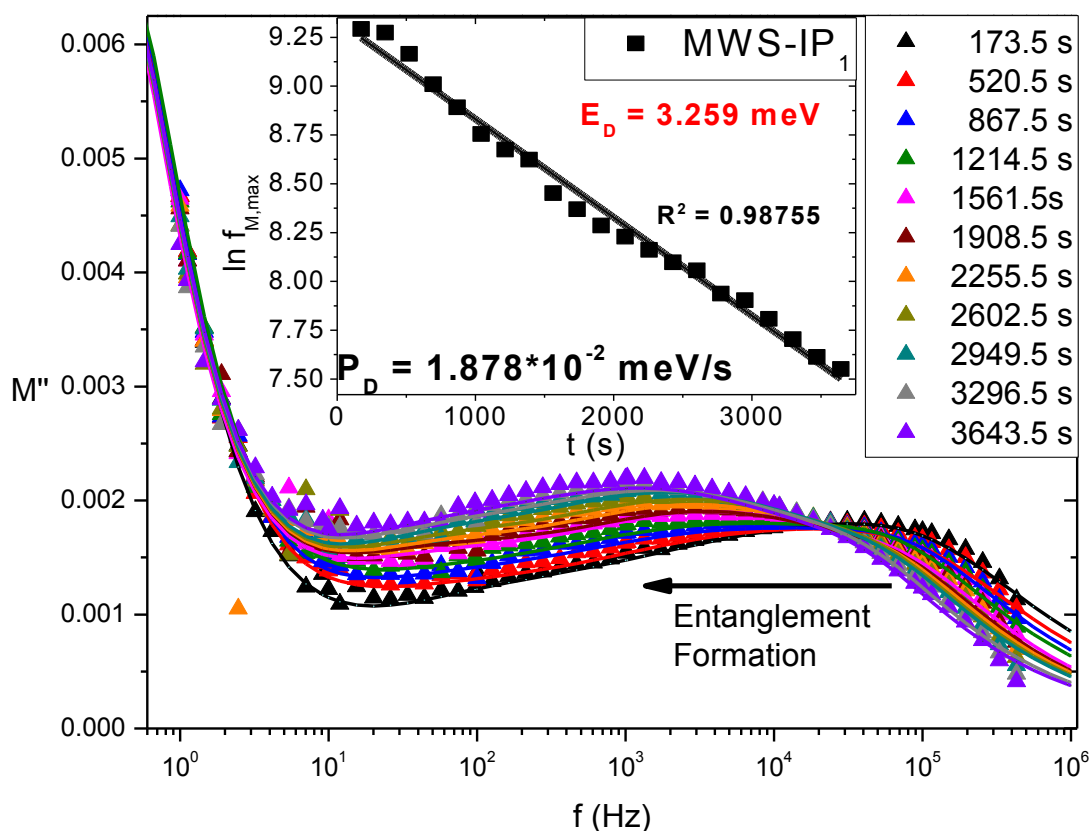


Figure 3.14. The imaginary part of electric modulus as a function of frequency varying time at 160°C for PE\_4.2\_AIO. The arrow shows the shift towards lower frequencies caused by the progressive entanglement formation. The points represent the experimental data while the lines represent the superposition of the computational models. Inset shows the loss peak position of the MWS-IP<sub>1</sub> with the progression of time where the values of the entanglement formation power and energy are indicated.

In Figure 3.15a the evolution of the frequency loss peak position of the computed MWS-IP<sub>1</sub> as a function of time at 80, 100, 120, 140 and 160°C is presented and the values of the

entanglement formation energy ( $E_D$ ) are calculated. A newly prepared specimen from the same sample was employed for each temperature, to ensure the same starting point was present in all measurements (minimum number of entanglements). By increasing the measurement temperature ( $T_M$ ) we observed that the entanglement formation energy ( $E_D$ ) is linearly increasing since there is more available energy for entanglements to form. Only in the case of 140°C the value is deviating from the linear increase, but this should be expected since the crystalline parts are melting and most of the energy is spent for this transition.

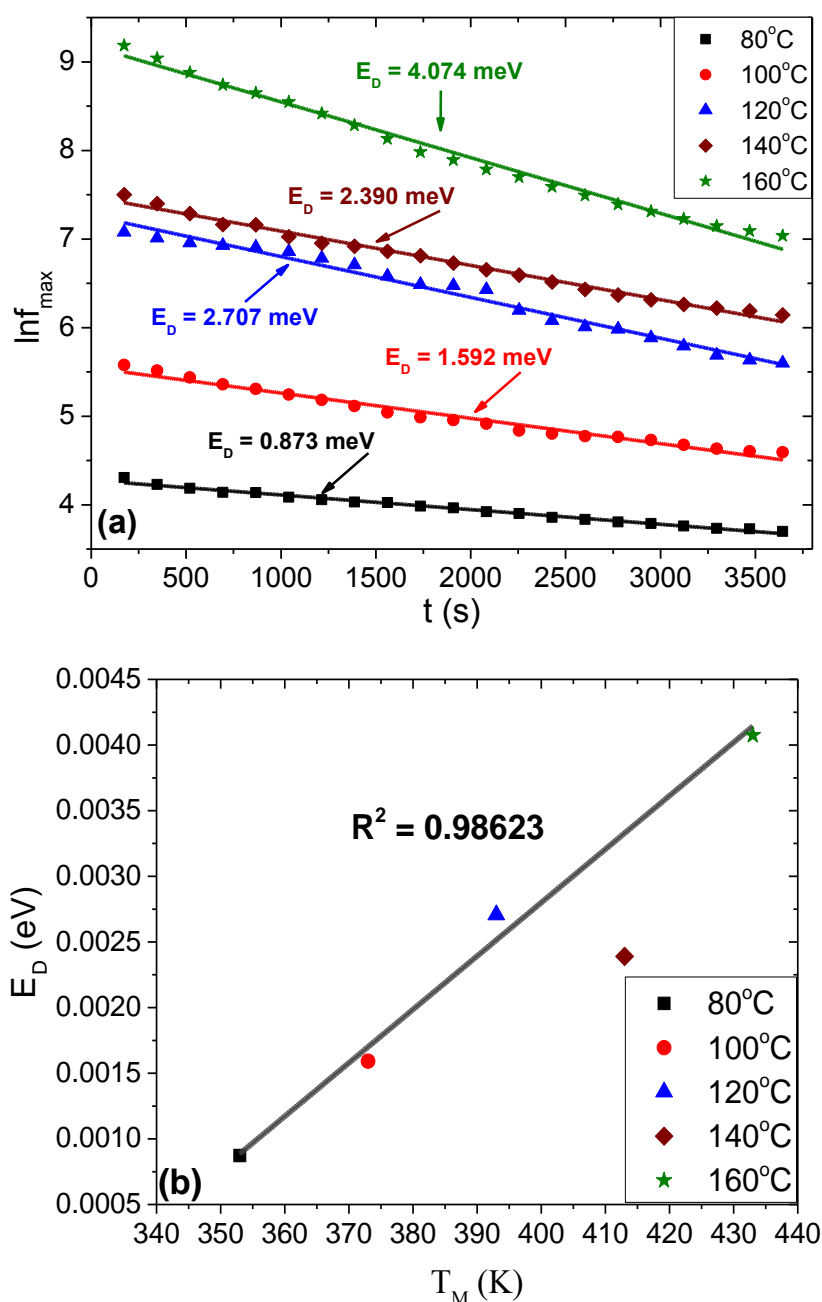


Figure 3.15. (a) The maximum loss positions as a function of time for the MWS-IP<sub>1</sub> in PE\_4.2\_AIO at different temperatures where the entanglement formation energy ( $E_D$ ) is

indicated for each temperature ( $R^2 > 0.98$  in all cases); (b) the values of the entanglement formation energy ( $E_D$ ) as a function of temperature, as calculated by Equation (3.12). The point at 140°C deviates from the linear behaviour, due to the melting of crystals, and it has not been included in the fitting line.

In Figure 3.15b the values of the entanglement formation energy ( $E_D$ ) are plotted as a function of the measurement temperature. The entanglement formation energy ( $E_D$ ) exhibits a linear behaviour with temperature (the value at 140°C was excluded from the fitting for the reasons explained above). The linear relationship between the entanglement formation energy ( $E_D$ ) and temperature can be described by:

$$E_D(T_M) = ST_M - E_A \quad (3.12c)$$

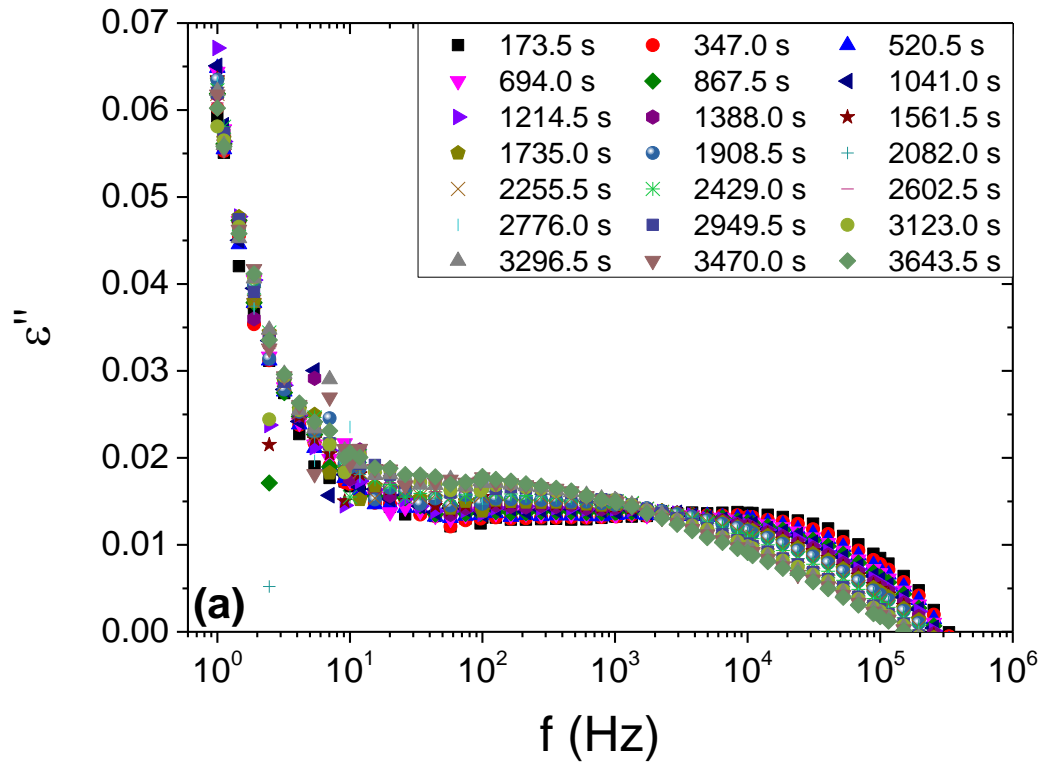
where  $S$  is the slope in Fig. 7b. The minus symbol in front of the activation energy describes the energetic barrier. The intercept of the line is the energy barrier of the entanglement formation, calculated to be  $E_A = 13.480$  meV. The limit temperature at which  $E_D \geq 0$  where the formation of entanglements is energetically favourable, was found to be  $T_{A(E_D=0)} = 331$  K (58°C) which according to previous studies from our group is close to the temperature where the thermal conductivity of a uni-axially stretched UHMWPE sample starts to decrease [276]. In addition, the slope ( $S$ ) of the line was calculated to be  $4.069 \cdot 10^{-2}$  meV/K.

The temperature dependency of the entanglements formation as presented from our model would also explain the challenges that melt processing of dis-UHMWPE presents, which usually occurs at temperatures as high as 260°C (533 K) [63]. According to Equation (3.12b), at 260°C the entanglement formation energy equals  $E_D \sim 9.5$  meV which is over twice the amount at 160°C (Figure 3.15b). In addition, the mechanical stirring coming from extrusion techniques would feed the melt with extra energy resulting to even faster entanglement formation. Thus, contrary to rheological experiments, in real-life processing conditions, the formation of entanglements occurs significantly faster. This is why a short residence time (30 minutes) in the melt processing of dis-UHMWPE is suggested even at those temperatures where re-entanglement according to rheology should take place in the range of hours [277].

### 3.2.2. The molecular weight effect

Figure 3.16 presents the imaginary part of dielectric permittivity as a function of frequency at 160°C, varying time for the three molecular weights explored in Chapter 3 section 1.2. As the concentration of catalytic ashes increases, the observable loss permittivity values increase as well. In addition, the metastable character due to the formation of entanglements is evident with the evolution of time in all the samples. As we have previously

observed, the formation of entanglements affects mostly the frequency loss peak position of the MWS-IP<sub>1</sub> which shifts to lower frequencies. This is exhibited by all samples, irrespective of their molecular weights. As shown by the data presented, for higher molecular weight we can observe that the formation of entanglements is slightly slower compared to lower molecular weight, thus supporting previous studies done through rheology [49,249]. However, the observable difference is not significant with dielectric spectroscopy.



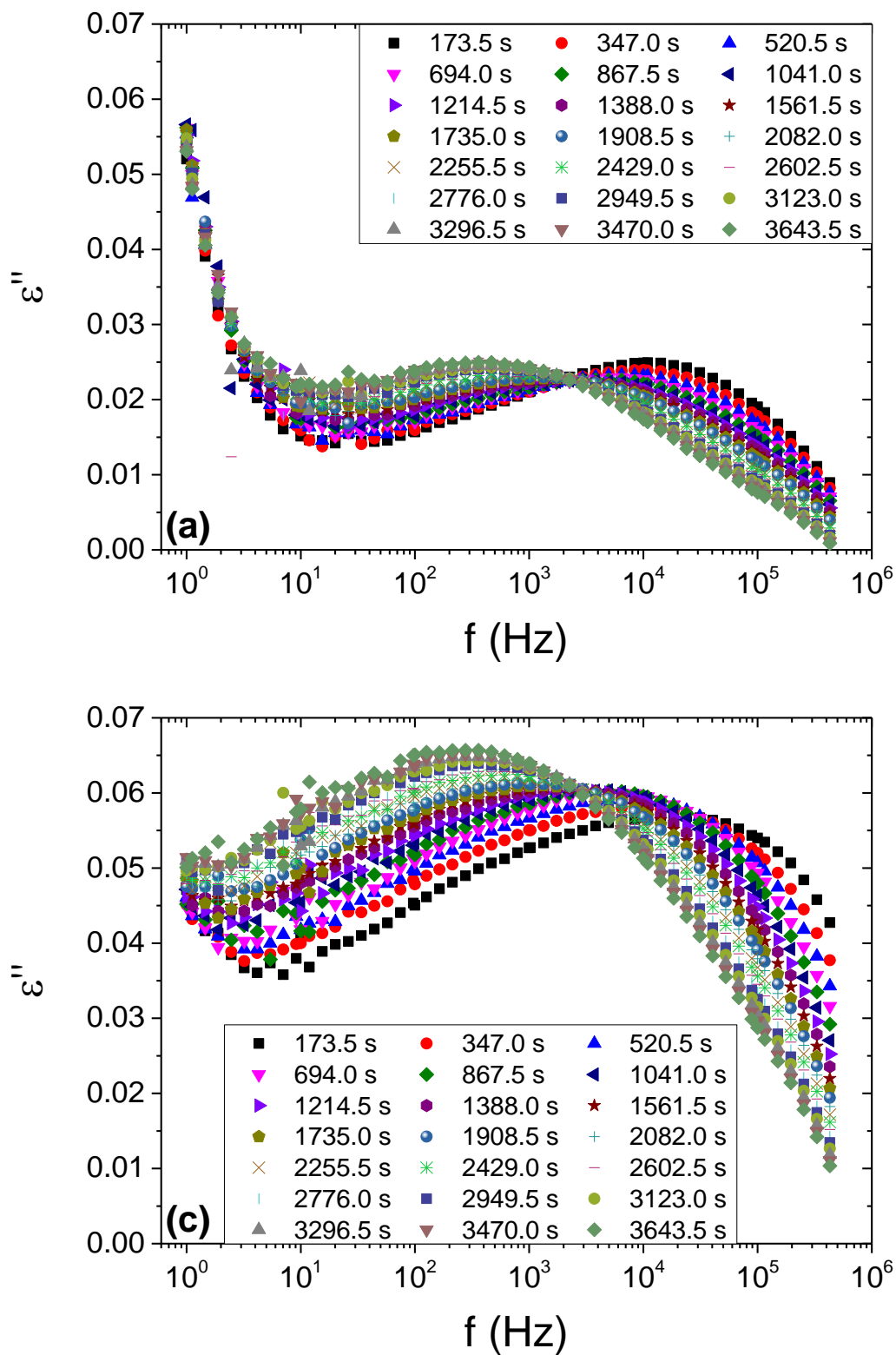


Figure 3.16. The imaginary part of dielectric permittivity as a function of frequency varying time at 160°C for samples with different molecular weight: (a) PE\_5.6\_AIO, (b) PE\_4.2\_AIO and (c) PE\_2.4\_AIO.



### 3.3. Conclusions

The goal of this chapter was to understand how the disentangled amorphous phase is affecting the relaxation and entanglement dynamics.

The disentangled specimens were subject to two different processing temperatures, solid-state (125°C) and melt-state (160°C) while the latter was also compared with a commercial melt-state processed sample to be measured with torsional rheology. Three different relaxation processes were observed, namely  $\alpha_c$ -,  $\beta$ - and  $\gamma$ -relaxations as expected for polyethylene. The relaxation strengths of the  $\alpha_c$ - and  $\gamma$ -relaxations were found to be dependent of the crystallinity content, verified by means of differential scanning calorimetry. The temperature loss peak positions of the recorded relaxation processes were analysed at different frequencies and all were found to follow the Arrhenius equation apart from the  $\gamma$ -relaxation of the solid-state processed disentangled sample which followed a VFTH trend. This sample is characterized by bigger crystalline structures and less entangled amorphous fractions, resulting into more mobile amorphous segments. On the contrary, the amorphous segments of the melt-state processed samples are more confined within the crystalline domains and hindered by the entanglements, following thus an Arrhenius behaviour. Since the VFTH trend is indicative of the dynamic glass-to-rubber transition process, based on the presented experiments here, it can be concluded that the crystalline polydispersity and entanglement density are affecting the free volume and thus the relaxation chain dynamics of UHMWPE. As a consequence of the  $\gamma$ -relaxation's VFTH temperature dependence, it is reasonable to consider it as the dynamic glass-to-rubber relaxation process of linear polyethylene and estimate its glass transition temperature from the Vogel temperature to be -95°C.

On the other hand, the application of broadband dielectric relaxation spectroscopy to dis-UHMWPE has allowed us to further expand our understanding of both its solid and metastable melt states. We have identified three main relaxation processes, two of which are composed of two sub-relaxations. One is attributed to interfacial polarization due to the presence of the Al<sub>2</sub>O<sub>3</sub> particles and the polymer chains with two sub-relaxations attributed to different dynamics due to the disentangled and entangled amorphous phase. The second is the crystalline part ( $\alpha_c$  process), and the third is the amorphous  $\beta$ -process which also exhibited two sub-processes, again due to the differences in the entanglement density. By following the evolution of the disentangled interfacial polarization process as a function of both time and temperature, we have been able to formulate a model to estimate the activation energy related

to the entanglement formation process in UHMWPE ( $E_A = 13.480$  meV), as well as the minimum temperature at which this process will start appearing ( $58^\circ\text{C}$ ). The entanglement formation energy ( $E_D$ ) which is the remaining thermal energy after the subtraction of the activation energy, is introduced in this chapter as a measure of the entanglements amount forming in a given temperature. The work presented here is providing with further understanding on the effect that entanglements have on the processability of dis-UHMWPE.

## **4. Uniaxial plastic deformation in the presence of fillers**

In this chapter, the physical properties of oriented dis-UHMWPE composites in the presence of fillers are studied. Three types of fillers are investigated, (i) metallic, (ii) ceramic and (iii) organic, with the metallic being the most interesting and therefore most thoroughly analysed. A dual target is upon this chapter, to explore both the effect that uniaxial orientation brings and also the reinforcing effects that the fillers provide.

### **4.1. Metallic filler: Au nanoparticles at low draw ratios**

In this chapter, uniaxially stretched dis-UHMWPE/gold nanocomposites at low drawing ratios are studied. A thorough structural study on the crystallinity and orientation induced by stretching is performed by means of wide and small angle x-ray scattering (WAXS/SAXS), Raman spectroscopy and visible and near infrared spectrophotometry. The effect of stretching upon the thermal management of the composites through the measurement of their thermal conductivities at varying angles with respect of the chain orientation is also presented. Finally, the potential of such composite materials to be used as dielectric material in electrical energy storage devices, placing an emphasis on how to optimize the energy recovery from the charged system, is investigated via BDS and DC measurements. The research presented here aims to provide a pathway towards thinner, lighter, more efficient and thermally stable capacitors for energy storage applications, by employing oriented dis-UHMWPE/gold nanocomposites. Additionally, the formation of entanglements followed by broadband dielectric spectroscopy in uniaxially oriented nanocomposites of dis-UHMWPE/gold is also provided within this chapter and their effect upon the dc conduction are discussed.

#### **4.1.1. Structural information & optical absorption**

In order to appreciate the effect that stretching has on the crystalline structure of UHMWPE, wide-angle X-ray scattering (WAXS) experiments were performed. In Figure 4.1 the contributions arising from the amorphous halos and the crystalline peaks are given for the DR1 (unoriented) dis-UHMWPE/gold nanocomposite. The deconvolution of the amorphous and crystalline curves is useful to approximate the crystallinity, which is calculated by dividing the area below the crystalline peaks, fitted by Lorentzian curves, by the total area of crystalline and amorphous halos.

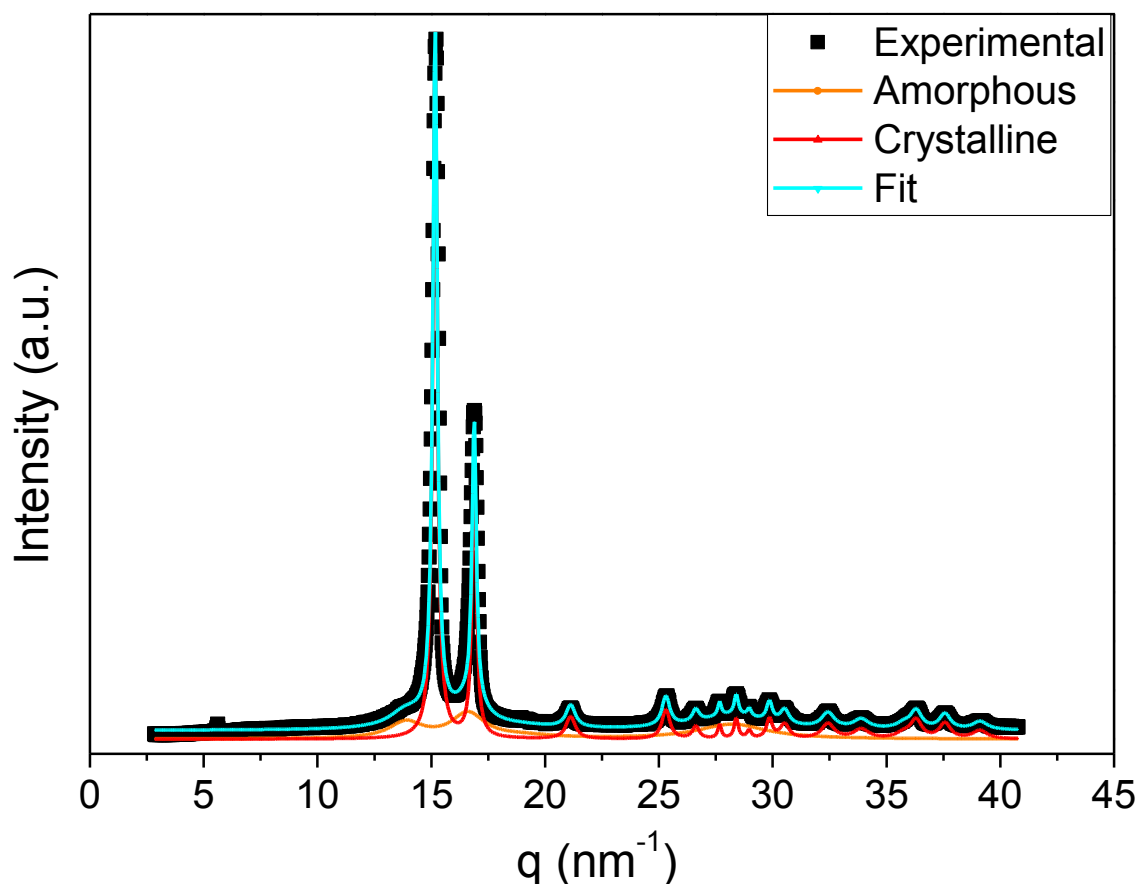


Figure 4.1. The WAXS profile of DR1 (unoriented) dis-UHMWPE/gold nanocomposite indicating the amorphous halos and the crystalline peaks.

Figure 4.2 shows the scattered intensity of the composites as a function of the angle between the incident beam and the detector ( $2\theta$ ), with the peaks indexed according to the reported orthorhombic crystal structure of PE with the (110) and (200) characteristic reflections, as also presented in Chapter 1 section 5 [278]. As shown in Figure 4.2b, uniaxial stretching results in a moderate increase in crystallinity because of the enhanced chain orientation, however limited due to the low drawing ratios used. Another prominent feature of the WAXS profile (Figure 4.2a) is that as samples are stretched further, there is an inversion in the ratio between the (110) and (200) reflections (Figure 4.2a). This inversion can be better visualized in Figure 4.2b, where the ratio switches from below to above 1 between DR2 and DR3. The prevalence of the (200) reflection at higher drawing ratios, associated with planes perpendicular to the stretching direction, is a clear indication of an increase in chain orientation.

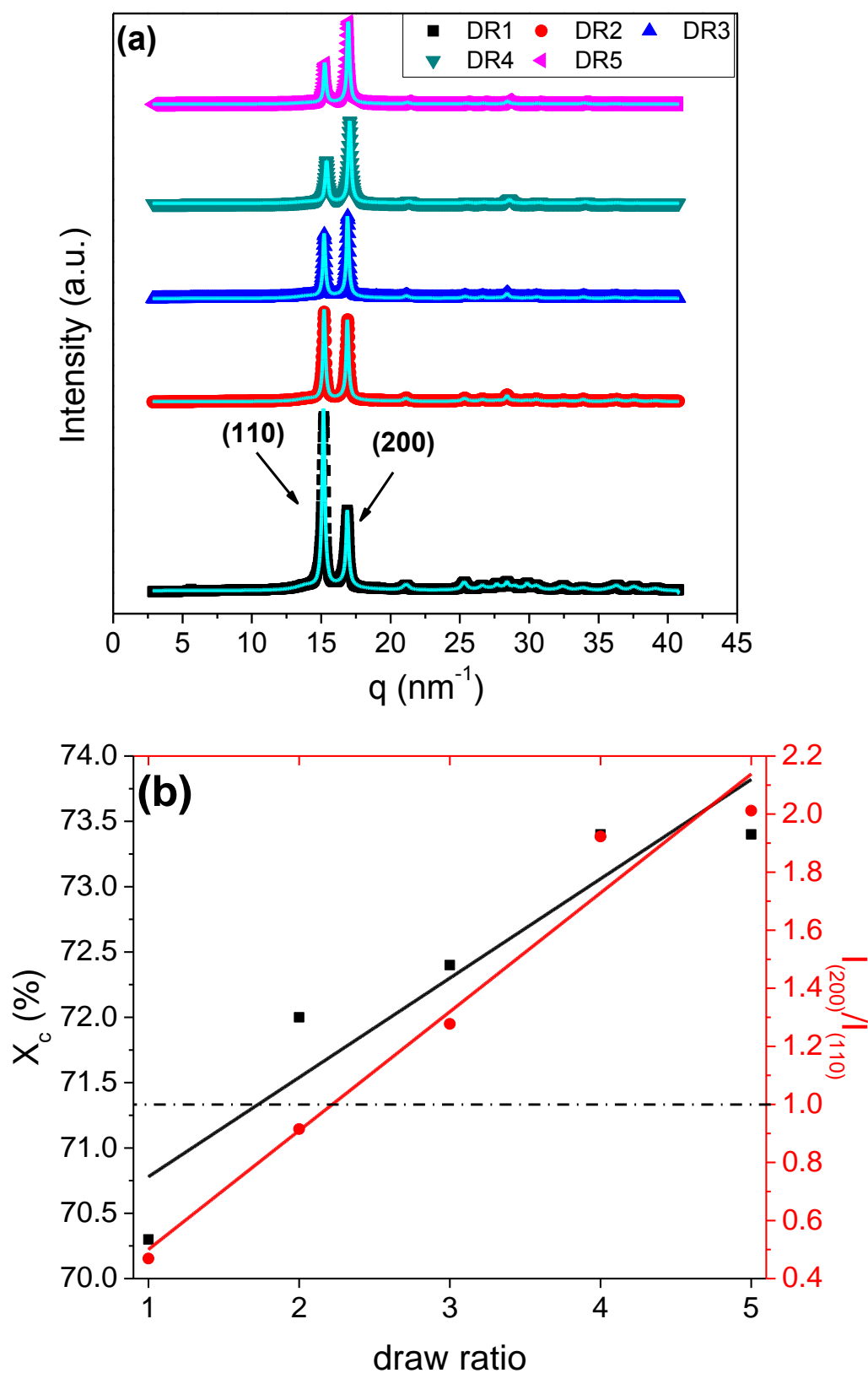


Figure 4.2. (a) WAXS profiles of gold/UHMWPE nanocomposite films where the intensity is normalized with the (200) reflection. (b) Crystallinity as calculated by WAXS (left axis) and

intensity ratio of the (200) and (110) reflections (right axis) versus draw ratio. The dotted line is a guide for the eye to show when the peak inversion of the reflections takes place.

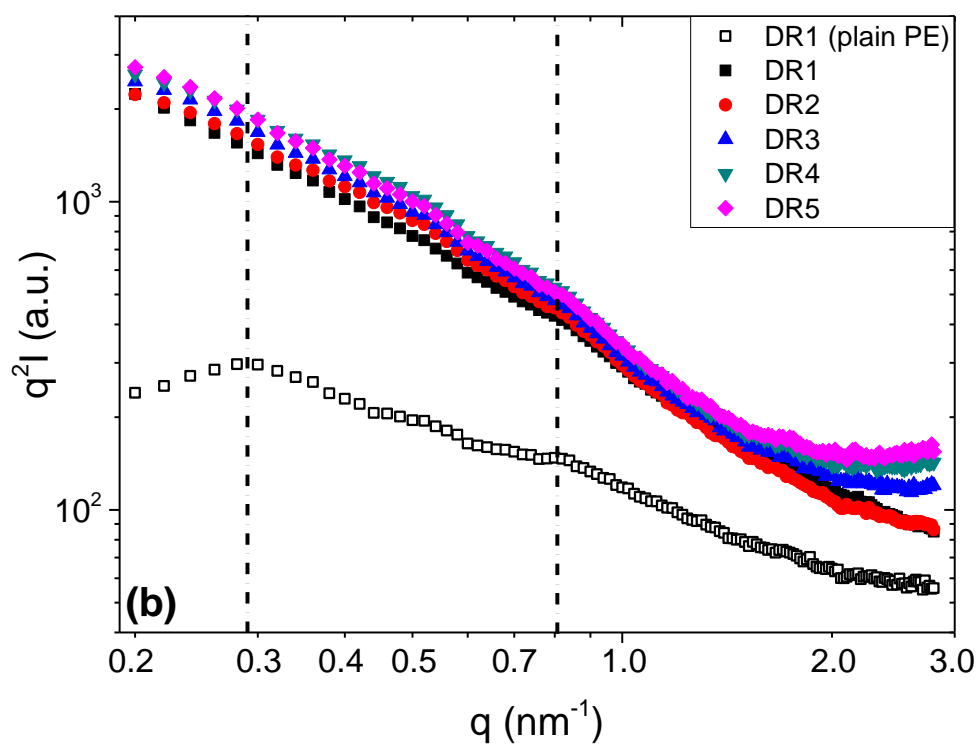
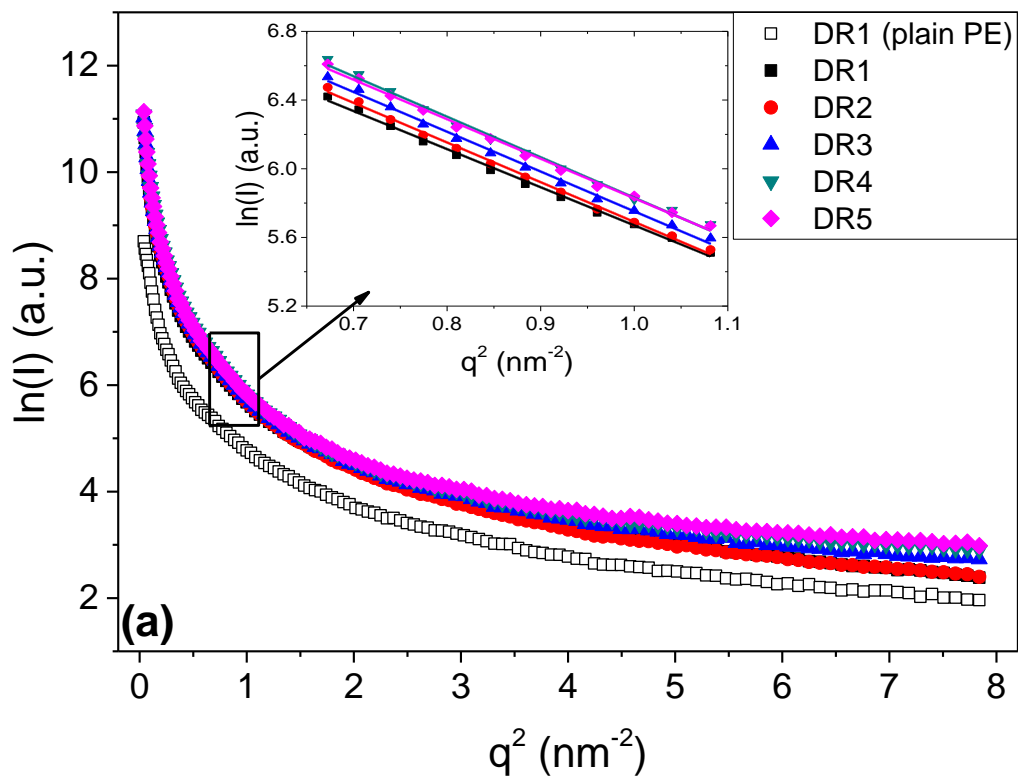
Small-angle X-ray scattering (SAXS) experiments were carried out to elucidate the crystalline structure of the composite and the gold nanoparticle distribution. Figure 4.3 shows the corresponding 1D profiles, normalized by the thickness of the specimens. For comparison purposes, an unstretched (DR1) sample without Au nanoparticles has been included in the analysis. In the log-log representation shown in Figure 4.3c, in the absence of Au nanoparticles, two bumps are visible. The first bump is at  $q = 0.29 \text{ nm}^{-1}$  ( $L = 2\pi/q = 22 \text{ nm}$ ) and the second bump is at around  $q = 0.80 \text{ nm}^{-1}$ , both corresponding to the long spacing of polyethylene crystalline lamellae and the second order maximum of the same long spacing respectively.

To calculate the average nanoparticle size, the Guinier law was used:

$$I(q) \sim e^{-\frac{q^2 R_g^2}{3}} \quad (4.1a)$$

$$d = 2 \sqrt{\frac{5}{3}} R_g \quad (4.1b)$$

where the  $R_g$  and  $d$  are the radius of gyration and the diameter of the nanoparticle respectively. From this analysis it can be deduced that the average nanoparticle diameter is around  $6.8 \pm 0.1 \text{ nm}$  as presented in the inset of the Figure 4.3a.



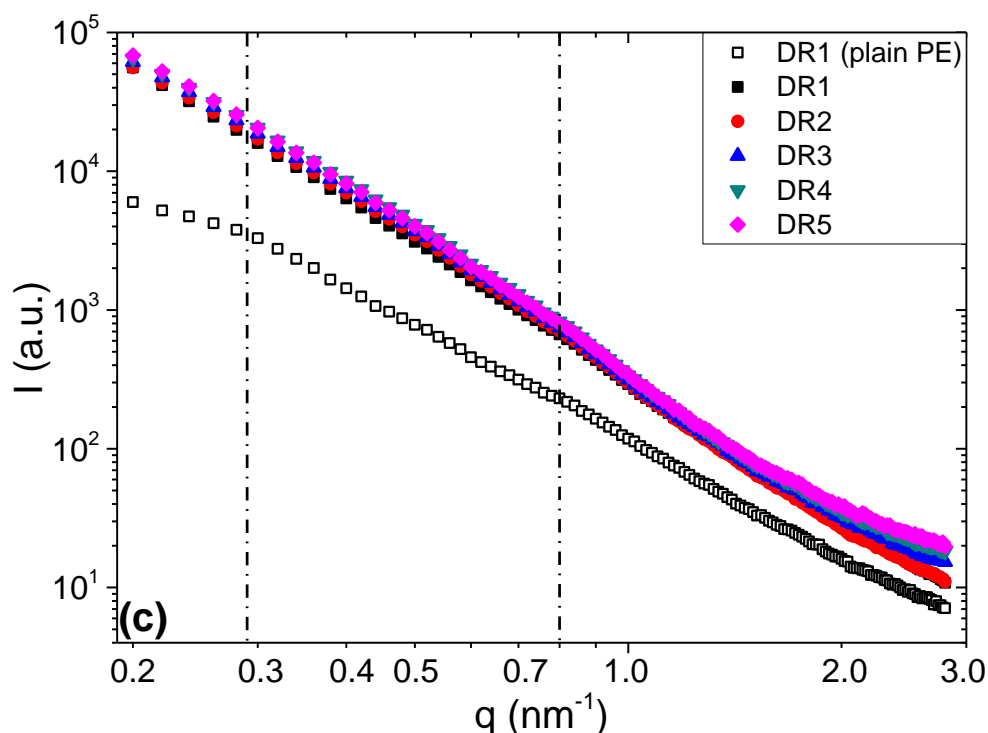


Figure 4.3. SAXS profile of gold/UHMWPE nanocomposite films normalized by the thickness for all samples under study including the DR1 in the absence of Au nanoparticles. In (a) the Guinier plot fitted with the Guinier law according to Equation (4.1) as an inset, (b) Lorentz-correction and (c) the log-log representations of the data.

In Figure 4.3b, the Lorentz-corrected scattering curves normalized with the thickness of all samples under study are presented. In the absence of Au nanoparticles, two peaks are visible. The first peak at  $q = 0.29 \text{ nm}^{-1}$ , 22 nm in real space, corresponds to the long spacing of polyethylene crystalline lamellae [279]. The second peak which is in the form of a shoulder, is at around  $q = 0.80 \text{ nm}^{-1}$  is attributed to a second order maximum of the same long spacing [280,281]. The peak at  $q = 0.80 \text{ nm}^{-1}$  is still visible when gold nanoparticles are added, while the peak at  $q = 0.29 \text{ nm}^{-1}$  is vanished completely. A strong slope of  $I(q)$  at low  $q$  is widely attributed to the presence of aggregates with dimensions on a length scale larger than that probed by SAXS. The low  $q$  range of the nanocomposites is fitted with Equation (4.2) as shown below:

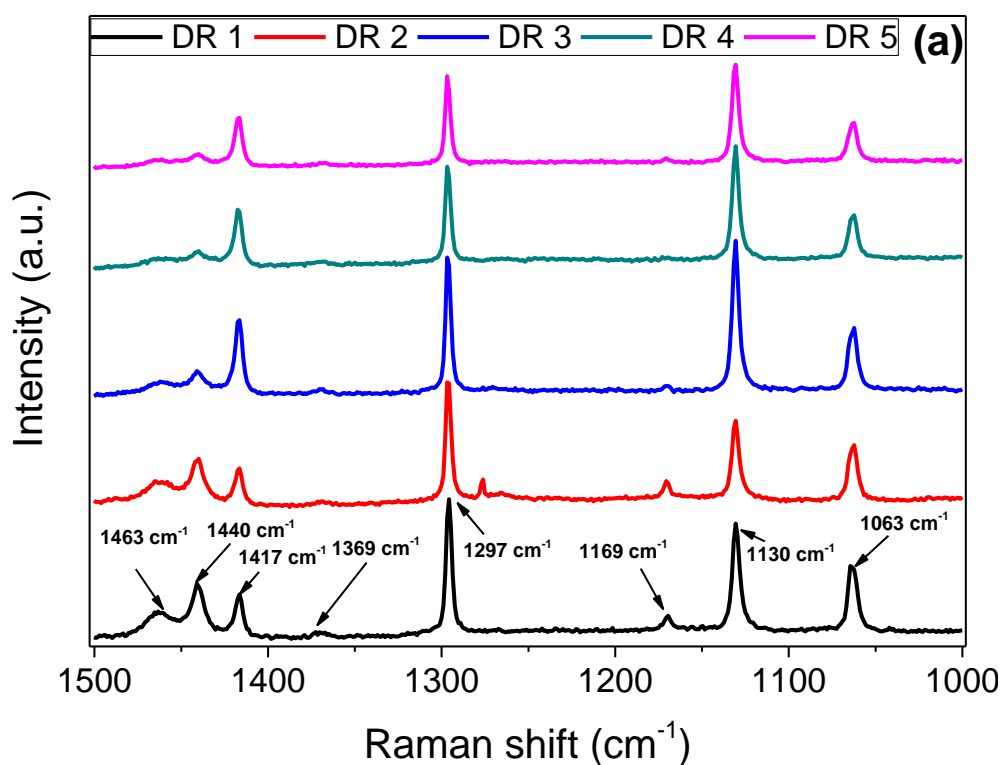
$$q^2 I(q) = q^{-x} \quad (4.2)$$

where  $x$  is the power of  $q$  after the Lorentz-correction.

The slope of  $I(q)$  can be fitted as  $q^{-3.09 \pm 0.07}$  indicating that the aggregates are compact and scatter in a similar way as surface fractals [282,283].



The Raman spectra of the composites is presented in Figure 4.4a. The main features, observed in the 1500 to 1000  $\text{cm}^{-1}$  region, correspond with those reported in the literature for polyethylene [284–286], i.e. skeletal C-C stretching vibrations (1130 and 1063  $\text{cm}^{-1}$ ) [285] and the twisting vibration of  $\text{CH}_2$  (1297  $\text{cm}^{-1}$ ). For highly crystalline samples, a contribution from the amorphous component at 1303  $\text{cm}^{-1}$  is not observed [94]. The  $\text{CH}_2$  bending vibrational mode is split into two components at 1440 and 1417  $\text{cm}^{-1}$  which is indicative of an orthorhombic crystal structure, also in accordance to the WAXS analysis presented previously in Figures 4.1 and 4.2 [287]. In the 1400 to 1500  $\text{cm}^{-1}$  range, the intensities of the peaks vary as a function of uniaxial stretching plastic deformation. For the case of the two amorphous peaks, 1463 and 1440  $\text{cm}^{-1}$ , the intensity decreases, while for the 1417  $\text{cm}^{-1}$  crystalline peak, the intensity increases as a function of stretching.



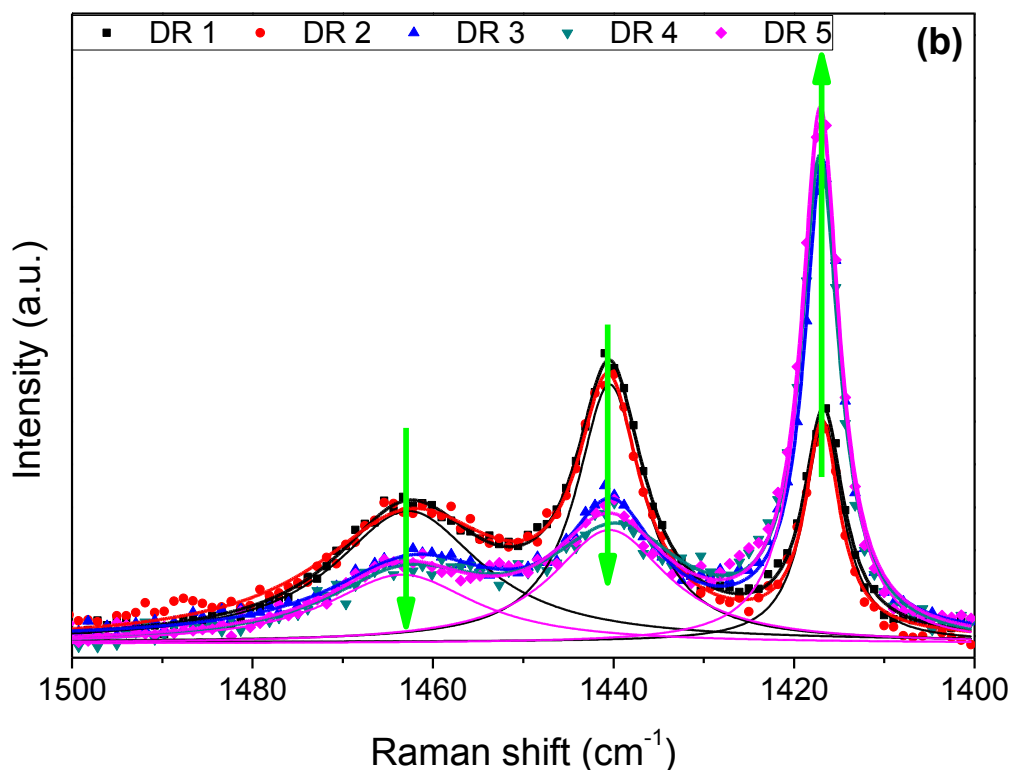


Figure 4.4. Raman spectra as a function of wavenumber at room temperature varying the draw ratio for dis-UHMWPE/gold nanocomposite films at (a) 1500 to 1000  $\text{cm}^{-1}$  and (b) 1500 to 1400  $\text{cm}^{-1}$  including the Lorentzian fitting (only for DR1 and DR5 to avoid confusion). The green arrows indicate the variation in intensity of each peak with orientation.

The trend of the peaks is an indirect way to show that the crystallinity increases upon stretching, in agreement with the WAXS experiments. The normalized intensity values of each peak with respect to the 1063  $\text{cm}^{-1}$  peak are given in Table 4.1. The intensity,  $I$ , of the peaks varying the Raman shift,  $RS$ , in Figure 4.4 are fitted with Lorentzian functions and their superposition follows the experimental data, as presented according to Equation (4.3):

$$I(RS) = y_0 + \frac{2A}{\pi} \frac{w}{4(RS - p)^2 + w^2} \quad (4.3)$$

where  $w$  is the full-width at half maximum (FWHM),  $p$  is the peak position,  $A$  the area below the curve and  $y_0$  a fitting parameter. The parameters are given in Table 4.2.

Table 4.1. Relative Raman intensities as a function of uniaxial plastic deformation with respect to the 1063 cm<sup>-1</sup> peak.

Sample	Raman shift (cm <sup>-1</sup> )							
	1063	1130	1169	1297	1369	1417	1440	1463
	Relative Raman Intensities							
DR1	<b>1.000</b>	1.467	0.453	1.736	0.272	0.689	0.806	0.501
DR2	<b>1.000</b>	1.307	0.545	1.793	0.289	0.706	0.826	0.543
DR3	<b>1.000</b>	2.108	0.263	1.895	0.224	1.099	0.451	0.299
DR4	<b>1.000</b>	1.956	0.414	1.671	0.357	1.075	0.503	0.405
DR5	<b>1.000</b>	1.984	0.405	1.789	0.327	1.088	0.474	0.376

Table 4.2. Fitting parameters from the Raman spectra according to Equation (4.3).

Sample	Raman shift (cm <sup>-1</sup> )						
	y <sub>0</sub>	1417		1440		1463	
		A	w	A	w	A	w
DR1	-132.53	42483.48	5.29	84714.87	8.99	95229.18	19.87
DR2	-152.26	34513.18	4.56	71917.15	8.30	115385.66	25.13
DR3	-60.30	83984.68	4.91	53260.80	12.17	62278.60	22.90
DR4	-254.58	88580.43	5.11	72335.46	18.63	53014.22	21.86
DR5	-170.14	96236.37	5.04	65456.58	15.76	50289.38	19.94

To further elucidate the structure of the composites, visible and near infrared (Vis/NIR) spectra were acquired and presented in Figure 4.5. In the visible part of the spectrum, the peak at 539 nm is associated with the transverse plasmon resonance of the Au nanoparticles [288]. For the DR1 (unstretched) and DR2 samples, the peak is broad, indicating gold nanoparticles of different sizes or aggregates. At the highest drawing ratios investigated (DR4 and DR5) the peak is more intense and narrower, an indication that the clusters are breaking apart due to the progressive orientation of the chains.

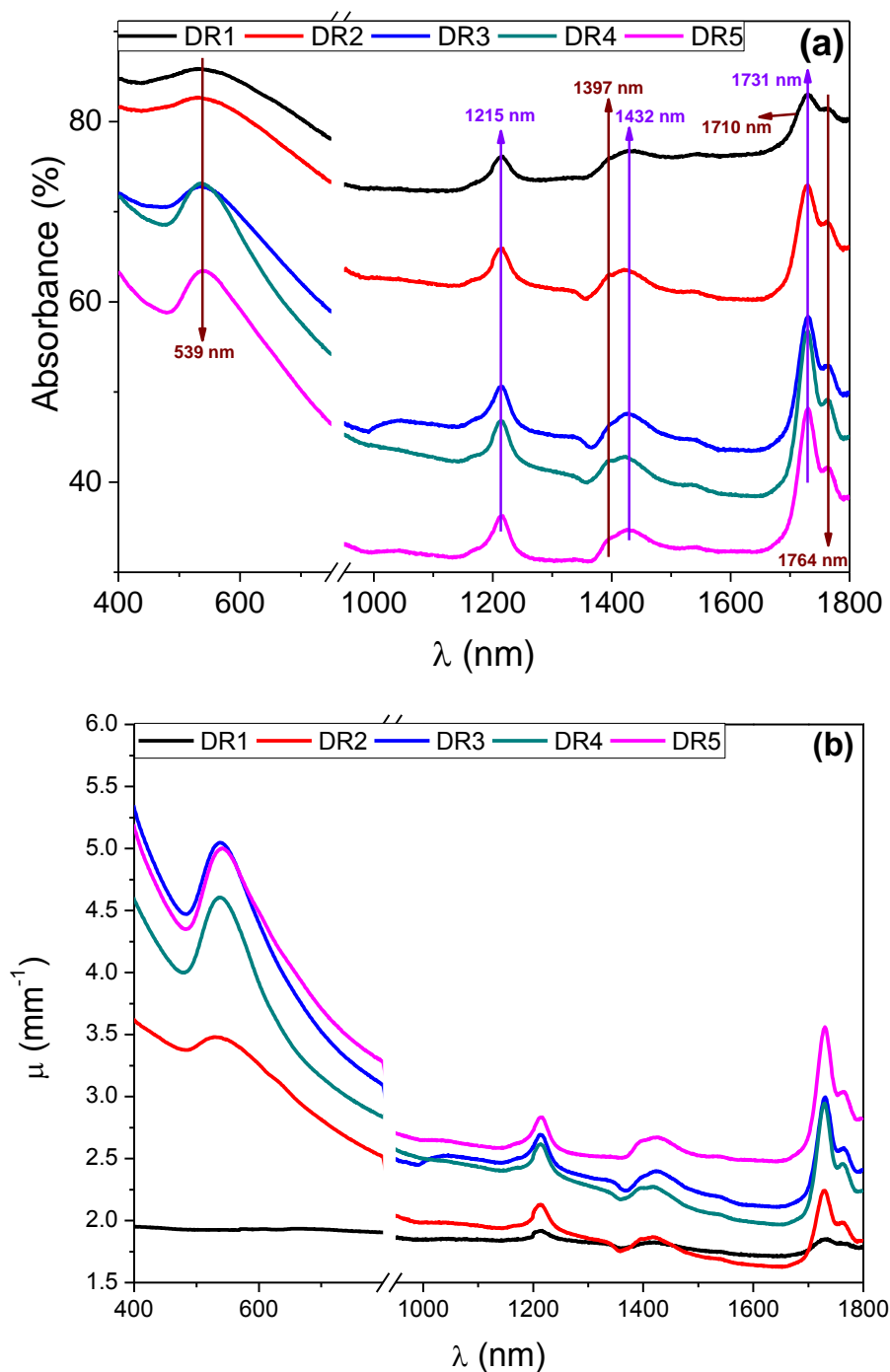


Figure 4.5. (a) Vis/NIR absorbance and (b) linear absorption coefficient both as a function of wavelength at room temperature varying the draw ratio for ds-UHMWPE/gold nanocomposite films.

In the near infrared region the main contribution to the absorbance is expected to come from the polymer matrix, as no absorption is expected from the gold nanoparticles [288,289]. The peak at 1731 nm, associated with the antisymmetric stretching mode of  $\text{CH}_2$  group in crystals, becomes more intense as stretching proceeds. This is a clear signature of orientation,

as this mode has its electric dipole-transition moment perpendicular to the polymer backbone [290,291]. The peaks at 1215, 1432 and 1764 nm are slightly affected by orientation as well; the latter is also related with the crystalline phase, while the peak at 1215 nm has been reported to increase with the increase in density [292]. In our experiments, density is expected to increase with the increase of order (either higher crystalline percentage or induced order in the amorphous regions) and it can be associated with this slight increase that we observed over stretching deformation. A very small shoulder at 1710 nm is indicating a peak which is present only in the unstretched sample. This peak is associated with the amorphous component and its disappearance only strengthens the notion that the crystallinity and oriented amorphous components increase with stretching [290,291].

Since the thickness of the samples decreases with orientation, the linear absorption coefficient,  $\mu$ , is also presented in Figure 4.5b, according to the Equation (4.4) below [293]:

$$\mu = -\frac{\ln(T)}{l} \quad (4.4)$$

where  $T$  is the fractional intensity of light transmission and  $l$  the thickness of the sample. It is evident that with tensile stretching, the absorption coefficient values increase in addition to a change in the peak morphology.

#### 4.1.2. Thermal conductivity

One of the key issues of electrical storage devices is thermal management. Enhanced thermal conductivity is desired in these systems, to avoid overheating and minimize safety concerns [294]. To assess the influence of stretching on thermal management, and to study how the oriented chains improve the thermal transport along the chain direction ( $\theta = 0^\circ$ ) compared to that along the perpendicular direction ( $\theta = 90^\circ$ ), we studied the in-plane thermal conductivity as a function of the rotation angle. DR4 and DR5 were the only samples that could be measured with Transient Grating Spectroscopy, as the lower draw ratio specimens would scatter too strongly. A pair of pump pulses was focused onto the sample to create a spatially periodic heating profile that yields transient thermal grating that was later optically monitored by lasers. Figure 4.6 shows their angle-dependent thermal conductivity, which peaks at  $\theta = 0^\circ$ :  $4.2 \pm 0.4 \text{ Wm}^{-1}\text{K}^{-1}$  for DR4, and  $4.6 \pm 0.4 \text{ Wm}^{-1}\text{K}^{-1}$  for DR5. These are significantly higher thermal conductivities than those reported in the literature for unstretched UHMWPE, namely  $\sim 0.3 \text{ Wm}^{-1}\text{K}^{-1}$  [187]. The fitted anisotropy ratio of the thermal transport along the chain direction to perpendicular direction for the DR4 and DR5 samples is 4, and 7, respectively. We note the peak of the thermal conductivity increases with the draw ratio

while its minimum decreases, indicating an increase in thermal anisotropy with draw ratio and therefore an improved thermal management.

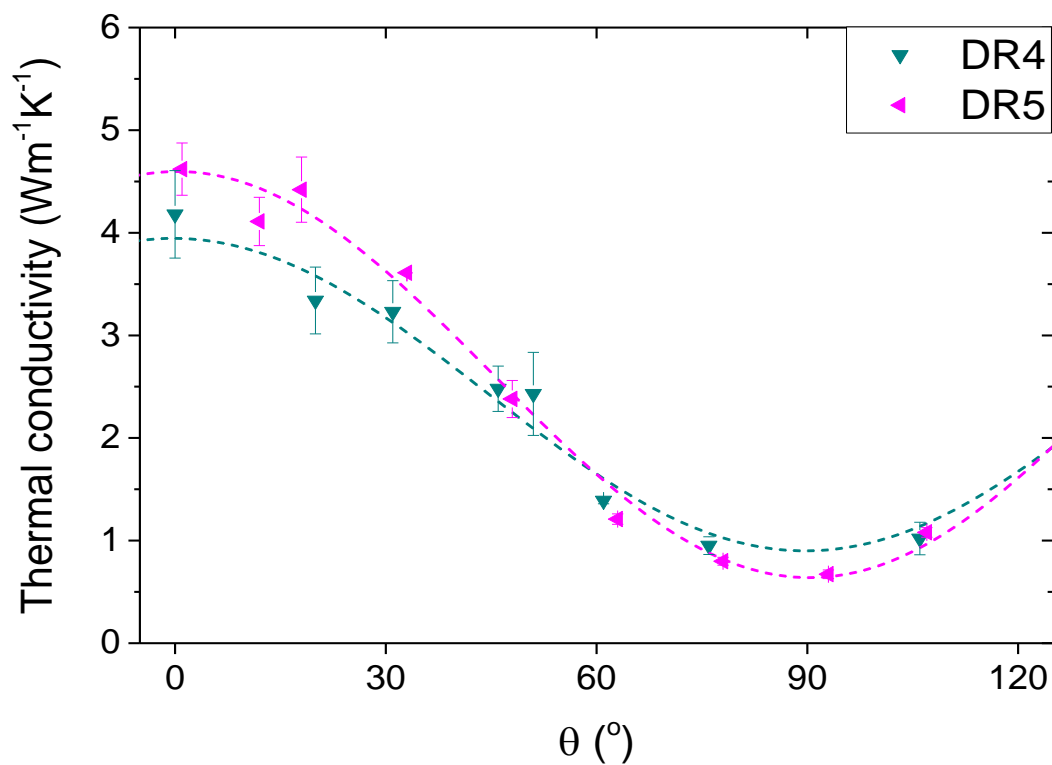


Figure 4.6. Measured thermal conductivity for partially drawn gold/UHMWPE nanocomposite films (DR4 and DR5) versus the angle with respect to the stretching direction at 30°C. The presented data were provided from our collaborators in CalTech.

#### 4.1.3. Electrical energy storage & recovery

The analysis was limited to frequencies up to  $10^2$  Hz because at higher frequencies, the values of  $\tan\delta = \epsilon''/\epsilon'$  are very close to the limits of detection of the frequency analyser, resulting in increased measurement error as discussed also in the Chapter 2 section 3. To test the application of uniaxially oriented dis-UHMWPE/gold nanocomposites as dielectric capacitors, first the dielectric behaviour of the samples was measured as a function of the external electric field frequency at 30°C, as presented in Figure 4.7. The dielectric formalism employed in this work is the complex dielectric permittivity which follows the Equation (3.8) presented previously. As it can be appreciated in Figure 4.7a, the real part of the dielectric permittivity exhibits a behaviour that does not depend strongly on frequency, with no significant increase approaching the lower frequency edge. This corresponds to the low-loss character of plain polyethylene, which is a desirable property in efficient energy storage

materials. Additionally, it is evident that the dielectric permittivity decreases for increasing drawing ratios, a phenomenon that can be correlated to the higher orientation and the increase in crystallinity proven by WAXS, Raman, and NIR spectroscopy measurements shown previously in Chapter 4 section 1.1. With the orientation of the crystalline and amorphous regions, the ability of the corresponding polymer phases to be polarized is hindered, hence the permittivity decreases.

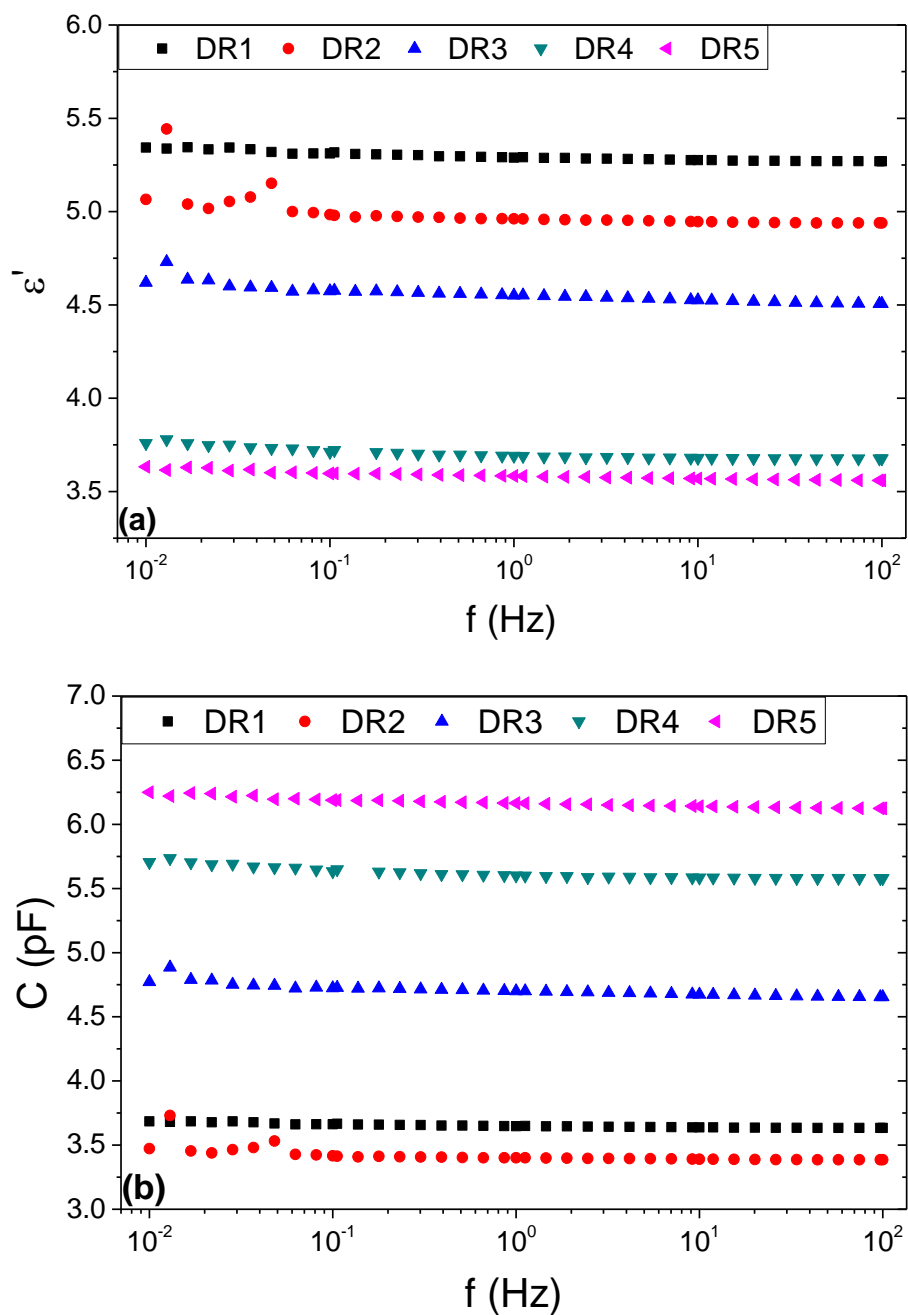


Figure 4.7. (a) The real part of dielectric permittivity and (b) capacitance of gold/UHMWPE nanocomposite films as a function of frequency at 30°C varying the stretching draw ratio.

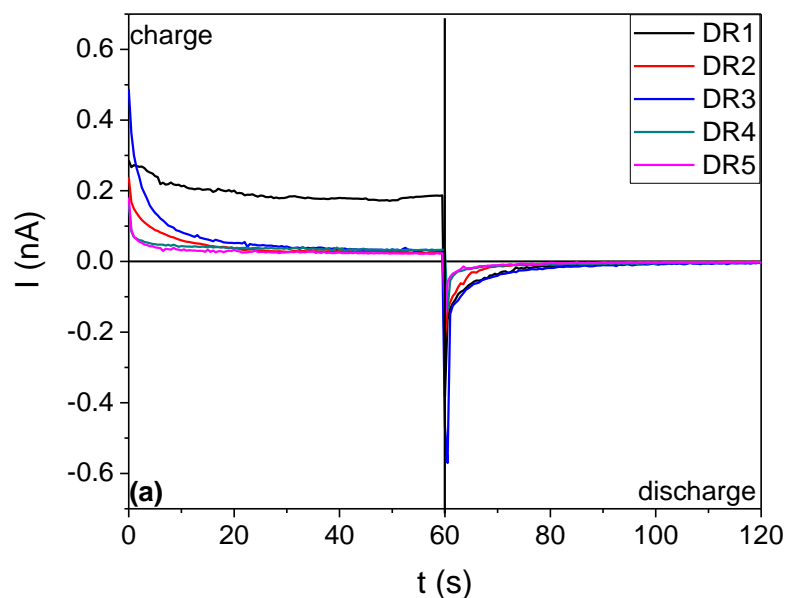
The capacitance,  $C$ , and energy,  $E$ , of the capacitor relate to the dielectric material and the capacitor's geometry and can be calculated as follows:

$$C = \varepsilon \varepsilon_0 \frac{A}{d} \quad (4.5)$$

$$E = \int_0^Q V dq = \frac{1}{2} \frac{Q^2}{C} \quad (4.6)$$

where  $\varepsilon$  is the dielectric permittivity of the material,  $\varepsilon_0$  the dielectric constant of free space,  $A$  and  $d$  are the electrodes' surface and distance and  $Q$  is the accumulated charge. Figure 4.7b shows how the reduction in thickness as a result of stretching (lowering the  $d$  value in Equation (4.5)) has a greater impact on the capacitance of the system than the decrease in permittivity (Figure 4.7a), resulting in higher capacitance values for the oriented samples. Since the thickness of the DR1 and DR2 samples is very close, the capacitance is only affected by their permittivity difference resulting in a slightly decreased value, as presented in Figure 4.7b.

The next step was evaluating the performance of the composites during a charge-discharge cycle. In Figure 4.8 the charge and discharge currents under a dc electrical field are presented for all the samples as a function of time at 100 V, 300 V, and 500 V. First, the intensity drops as the capacitor is charging until it reaches a constant value. After stopping the application of the external field, the discharging process begins with an initially sharp discharge that plateaus close to zero intensity after most of the energy has been recovered. With increasing voltage, both the charge and discharge currents values increase.





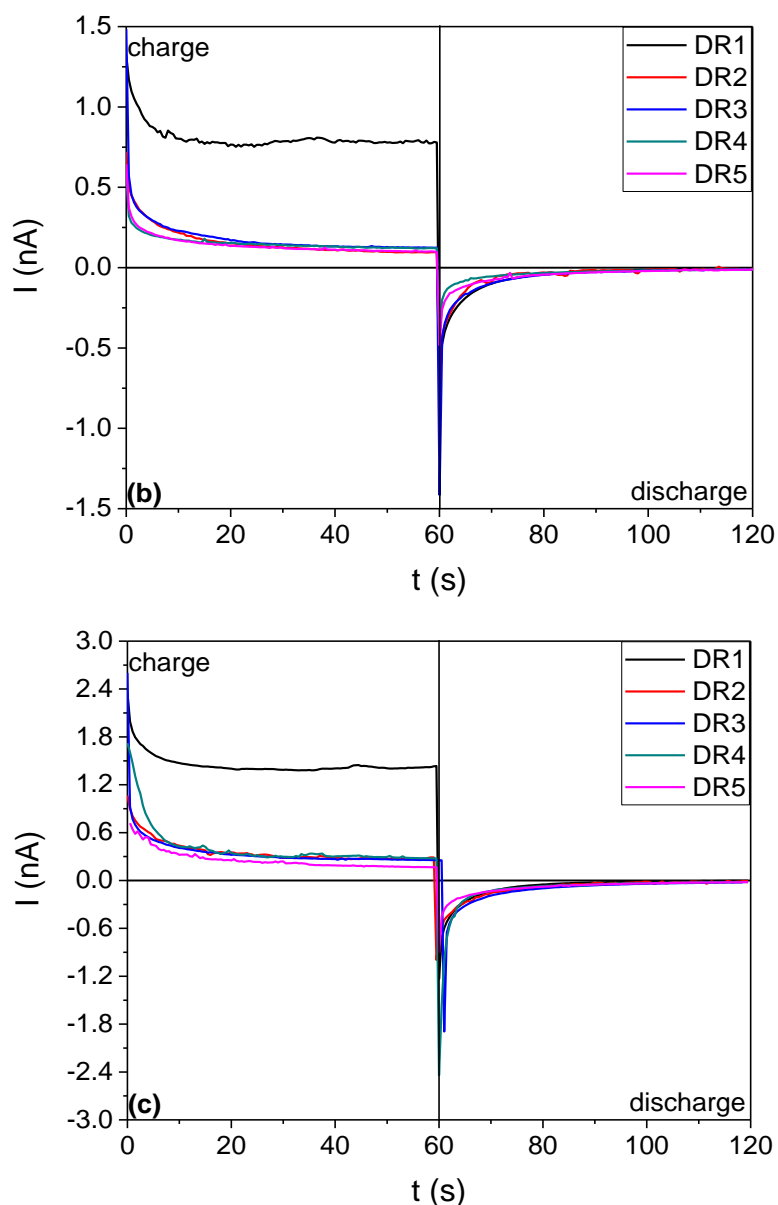


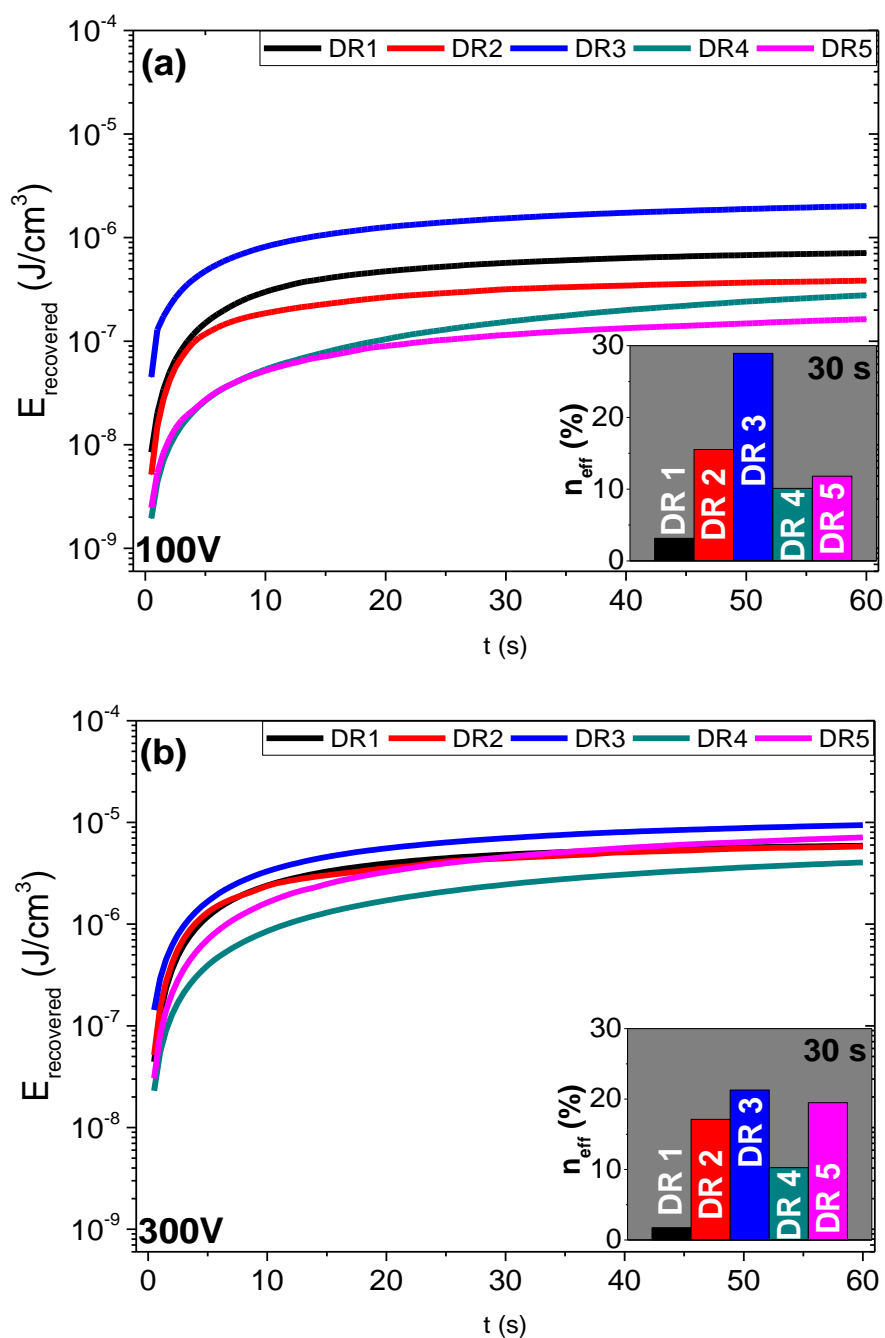
Figure 4.8. The charge-discharge dc currents gold/UHMWPE nanocomposite films as a function of time for different drawing ratios at: (a) 100V, (b) 300V and (c) 500V.

Stored ( $E_s$ ) and recovered ( $E_r$ ) energies were calculated by integrating the charge ( $I_c$ ) and discharge ( $I_d$ ) currents respectively:

$$E_s = \frac{1}{2} \frac{[\int I_c(t) dt]^2}{C} \quad \text{and} \quad E_r = \frac{1}{2} \frac{[\int I_d(t) dt]^2}{C} \quad (4.7)$$

Figure 4.9 presents the recovered energy density as a function of time for different drawing ratios during the discharge period. As the applied voltage increases (field intensity), the energy density values enhance significantly for the samples under study as the number of charge carriers injected by the electrodes also increases, facilitating the transportation of the charges within the material by lowering the local potential barrier. This has a more

pronounced effect in the higher plastic deformations (DR4 and DR5). At 500V, the energy density generally increases with stretching and all the oriented samples exhibit energy density values which are at least double when compared to the unstretched one. It should be noted that the calculated energies are a slight overestimation since the dielectric permittivity at the lowest measured frequency is slightly lower than the expected dielectric constant. However, the relaxation strength of polyethylene is very low in the absence of dielectric probes as discussed earlier, and so no significant changes are expected in the static permittivity values at this temperature.



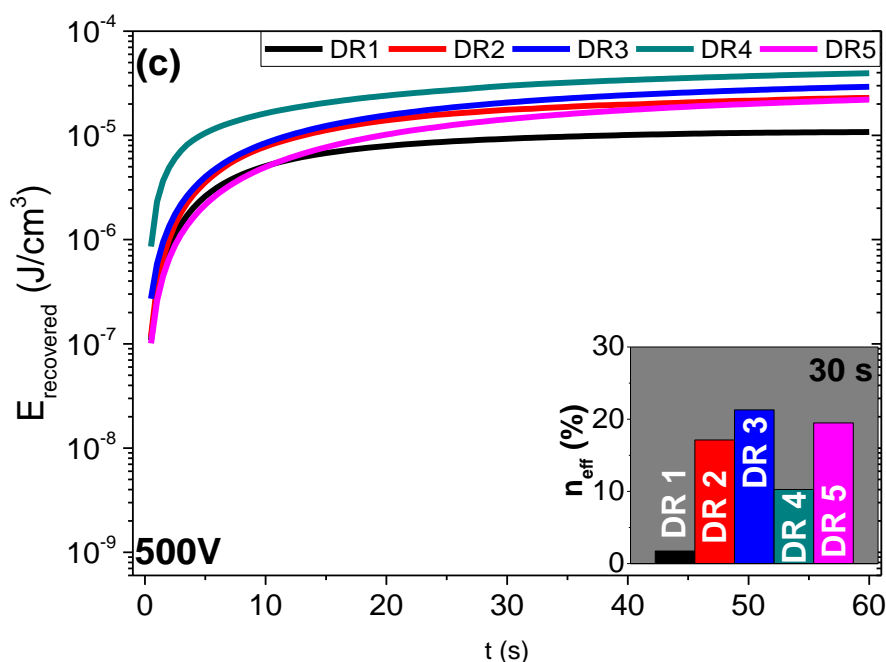


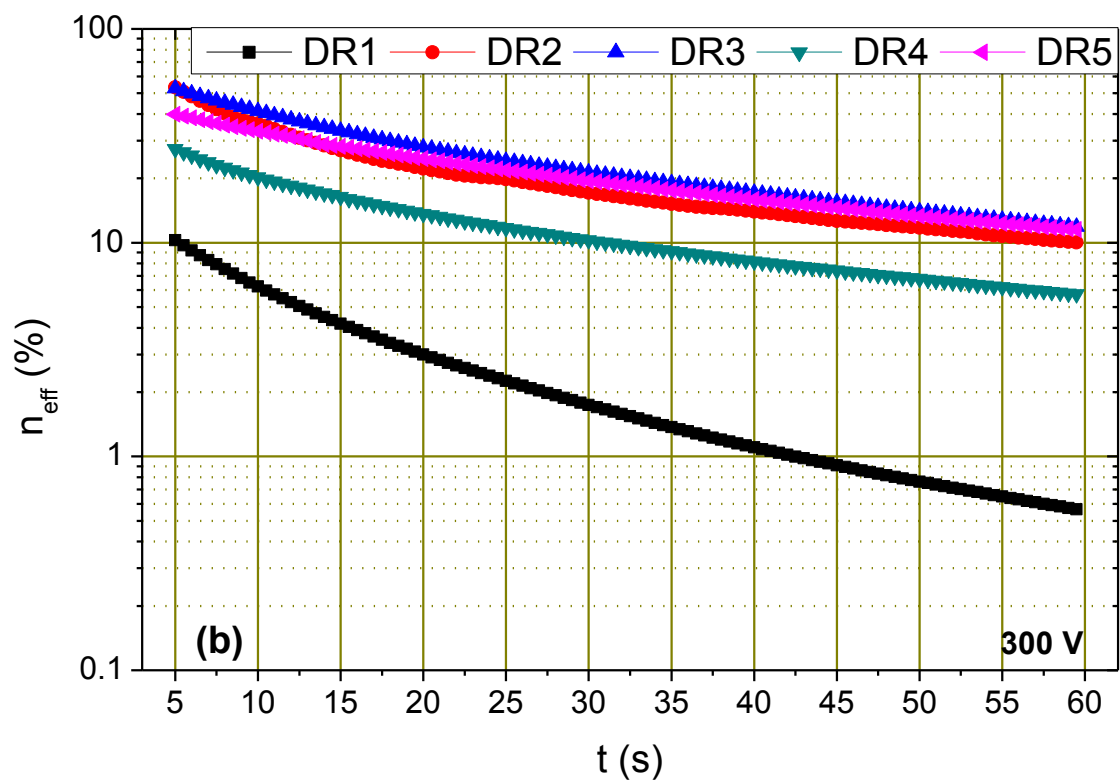
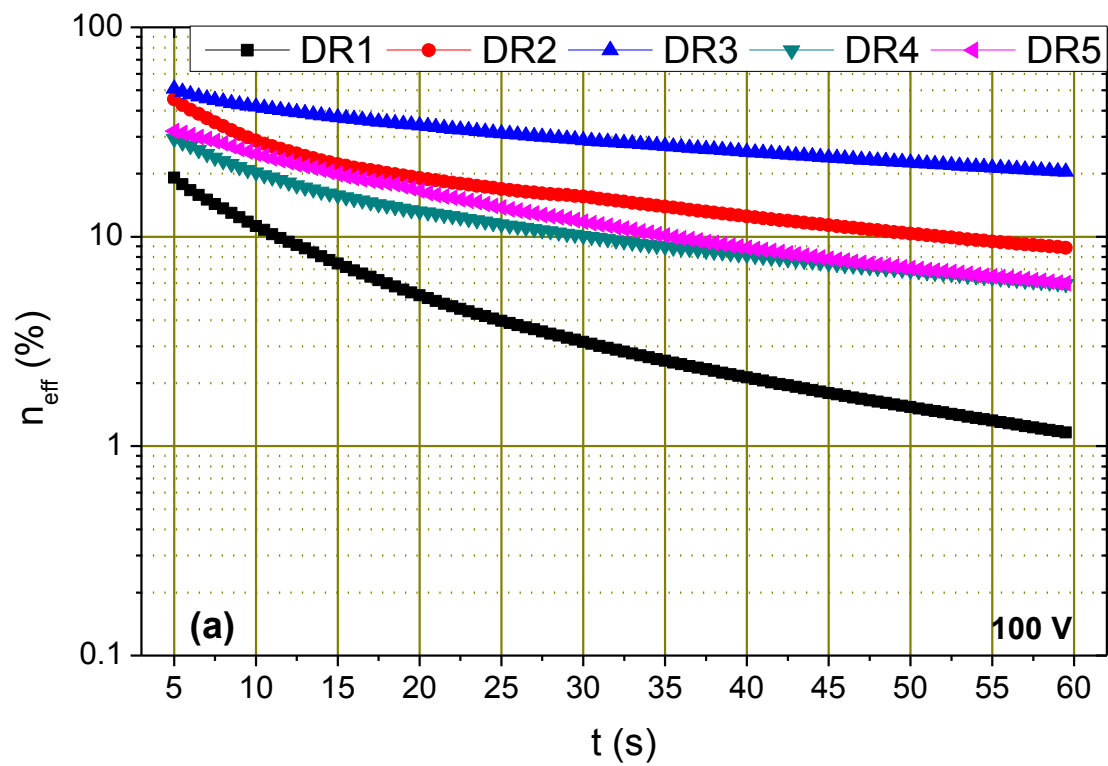
Figure 4.9. Recovered energy density values of gold/UHMWPE nanocomposite films as a function of time varying the draw ratio for: (a) 100V, (b) 300V and (c) 500V. The inset represents the coefficient of energy recovery efficiency after 30 seconds of discharge.

To quantify the electrical energy efficiency of the specimens under different voltages, the coefficient of recovery efficiency was calculated according to the literature [193,251,295] as:

$$n_{eff} = \frac{E_r}{E_s} \times 100\% \quad (4.8)$$

The coefficient of recovery efficiency of the oriented samples, presented in Figure 4.10 and as an inset at 30 s in Figure 4.9 and in Table 4.3, is dramatically enhanced when compared to the unstretched composites. The fact that orientation obstructs the ability of the chains to be polarized is translated into less degrees of freedom in the movement of the dipoles. Considering this, when the electric field is switched off to monitor the discharge effect, the dipoles' new equilibrium state is similar to the one prior to the experiment. Since there are less degrees of freedom in the dipoles' movement, reduced influence of the internal electric fields from re-orientation of dipoles would be present which could potentially decrease the recovered energy. From the plasmon resonance of the gold nanoparticles at the visible wavelength spectrum (Figure 4.5) we observed that as stretching plastic deformation increases, the peak gets more intense due to the breaking of the clusters/aggregates. This effect should increase the contribution of interfacial phenomena between the polymer chains and the nanoparticles and possibly enhance the accumulation of charges at the interface of an

insulator/conductor system due to Maxwell-Wagner-Sillars interfacial polarization phenomena [222,296].



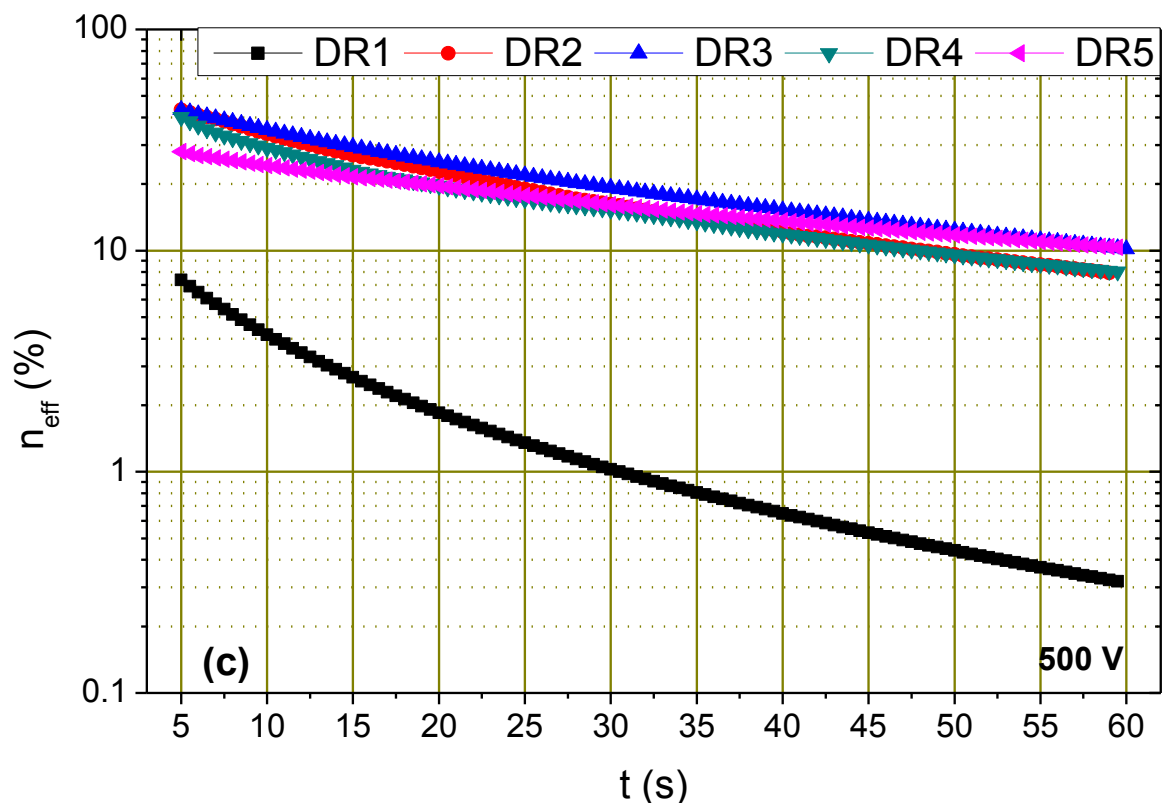


Figure 4.10. Coefficient of recovery efficiency as a function of time for the samples under study at: (a) 100 V, (b) 300 V and (c) 500 V.

Table 4.3. Coefficient of recovery efficiency at 30 seconds varying the voltage for the samples under study.

Sample	$n_{\text{eff}}$ (%)		
	100V	300V	500V
DR 1	3.15	1.74	1.03
DR 2	15.53	17.12	16.22
DR 3	28.93	21.28	19.25
DR 4	10.11	10.27	15.31
DR 5	11.81	19.48	16.10

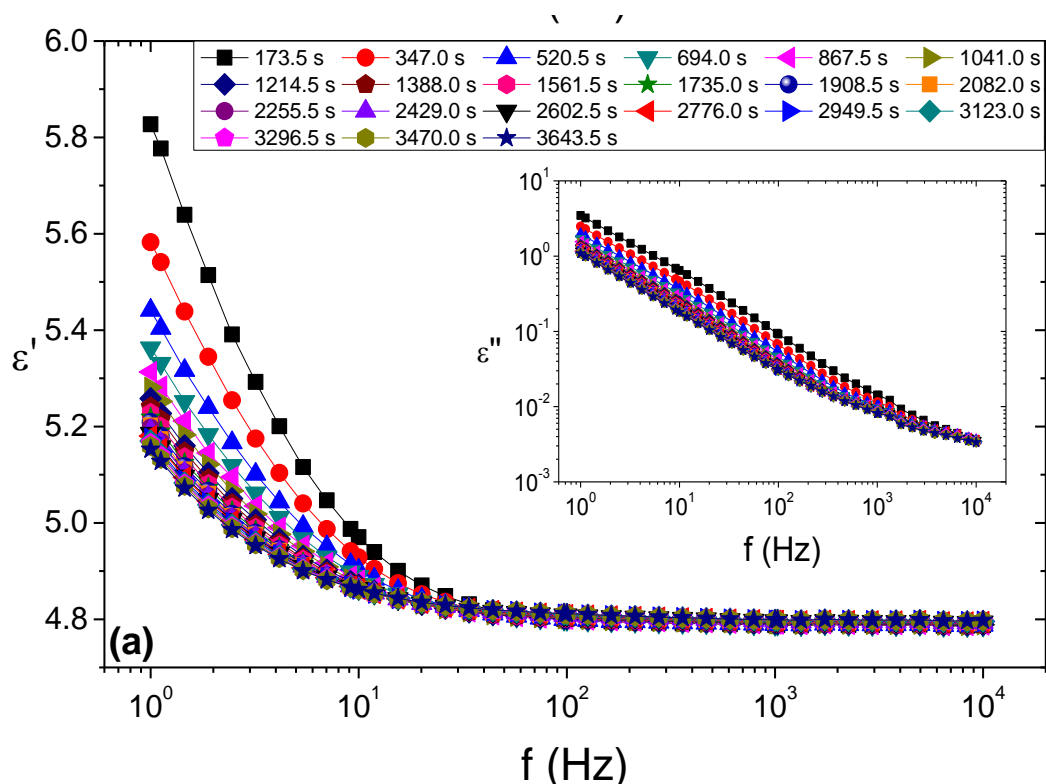
According to Figure 4.10a, the 100 V coefficient of recovery efficiency at 10 seconds of the best performing sample DR3 is 41.76% which is comparable to BaTiO<sub>3</sub>/epoxy nanocomposites of similar filler concentration and same measurement conditions (43.80%) according to Manika and Psarras (2019) [295]. BaTiO<sub>3</sub> and epoxy resin possess considerably better polarizability than polyethylene but also higher dc conductivities, limiting thus their

performance at higher electric fields due to destructive percolation effects (dielectric breakdown). Hence, further investigations in uniaxially oriented polyethylene nanocomposites could result into more attractive dielectric materials for capacitor applications [247]. More ideas on the topic are discussed in Chapter 5.

#### 4.1.4. Entanglements formation

In the present section of Chapter 4, the investigation of the formation of entanglements in uniaxially oriented dis-UHMWPE/gold nanocomposites employing broadband dielectric spectroscopy is presented. In Chapter 3 section 2 of the present dissertation, the advantages of this technique over rheology to study the formation of entanglements in the solid state were discussed. Here, uniaxially oriented dis-UHMWPE/gold nanocomposites are investigated, giving for the first time information on how entanglements affect entanglements.

The dielectric response of the uniaxially oriented dis-UHMWPE composites is presented in Figure 4.11, where the real part of dielectric permittivity as a function of frequency is shown at 160°C. The draw ratios DR1, DR2 and DR3 are given at Figure 4.11a, 4.11b and 4.11c respectively. As an inset, the imaginary part of dielectric permittivity is also presented. The complex dielectric permittivity  $\epsilon^*$  is defined according to Equation (3.8) as shown previously.



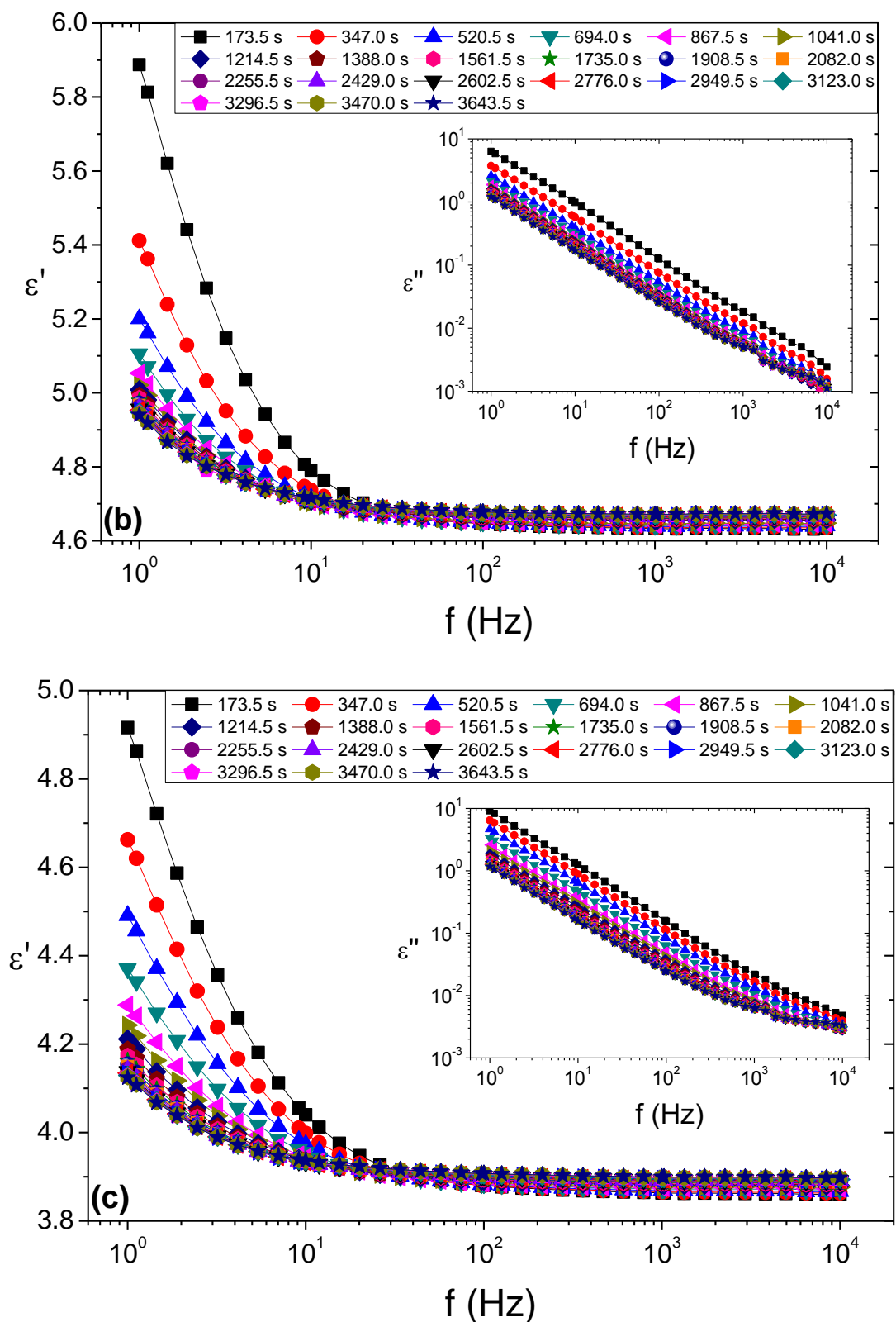


Figure 4.11. The real part of dielectric permittivity as a function of frequency varying the time for the samples under study: (a) DR1, (b) DR2 and (c) DR3. As an inset the corresponding imaginary part of dielectric permittivity is presented.

It is observed that the real part of dielectric permittivity increases significantly with decreasing frequency, indicating a strong dipolar polarization, as observed for all samples in Figure 4.11. With the evolution of time, the relaxation tends to lower frequencies, as it can also be evaluated by the imaginary part of dielectric permittivity, presented as an inset. The loss permittivity versus frequency in the log-log representation shows a linear behaviour, attributed to the contribution of dc conduction, masking the dipolar polarization peak. An effort is made to remove the conductivity term in order to appreciate the dipolar contribution alone, as seen below.

The Maxwell-Wagner-Sillars (*MWS*) interfacial polarization consists of a Debye dispersion model and the dc conduction contribution and is given by Equation (4.9) below:

$$\varepsilon^*(\omega) = \varepsilon_\infty + \frac{\varepsilon_s - \varepsilon_\infty}{1 + i\omega\tau} + \frac{i\sigma_{dc}}{\varepsilon_0\omega^s} \quad (4.9)$$

where  $\tau$  is the Debye relaxation time,  $\lim_{f \rightarrow 0} \varepsilon^* = \varepsilon_s$ ,  $\lim_{f \rightarrow \infty} \varepsilon^* = \varepsilon_\infty$ ,  $\sigma_{dc}$  is the dc conduction and  $s$  a parameter depending on the examined material ( $0.5 \leq s \leq 1.0$  and it is Ohmic when  $s = 1$  [297]) and  $\varepsilon_0$  is the dielectric constant of vacuum ( $8.854 \cdot 10^{-12}$  F/m). In the analysis below, the assumption that the dc conduction is Ohmic ( $s = 1$ ) is followed, based on the experimental conditions (homogenous low intensity external electric field) and the absence of ionic charges. After implementing Equation (3.7) in Equation (4.9), the *MWS* interfacial polarization can be split in a real and an imaginary part as shown below:

$$\varepsilon'(\omega) = \varepsilon_\infty + \frac{\varepsilon_s - \varepsilon_\infty}{1 + \omega^2\tau^2} \quad (4.10a)$$

$$\varepsilon''(\omega) = \frac{(\varepsilon_s - \varepsilon_\infty)\omega\tau}{1 + \omega^2\tau^2} + \frac{\sigma_{dc}}{\varepsilon_0\omega} \quad (4.10b)$$

In the case of the imaginary part of dielectric permittivity the first part of the equation corresponds to the dipolar contribution and the second part to the Ohmic conduction contribution. In materials with relatively high values of electrical conductivity or weak dipolar response, the presence of charge carriers can mask the dielectric response and obscure the dielectric analysis, especially at low frequencies because the contribution of dc conductivity to loss permittivity follows a power law. Since the Ohmic conduction is present only in the loss permittivity part, following Equations (4.9 and 4.10), a way to remove the conductivity term is by applying the logarithmic derivative on the real part of dielectric permittivity as shown in Equation (4.11) [117]:

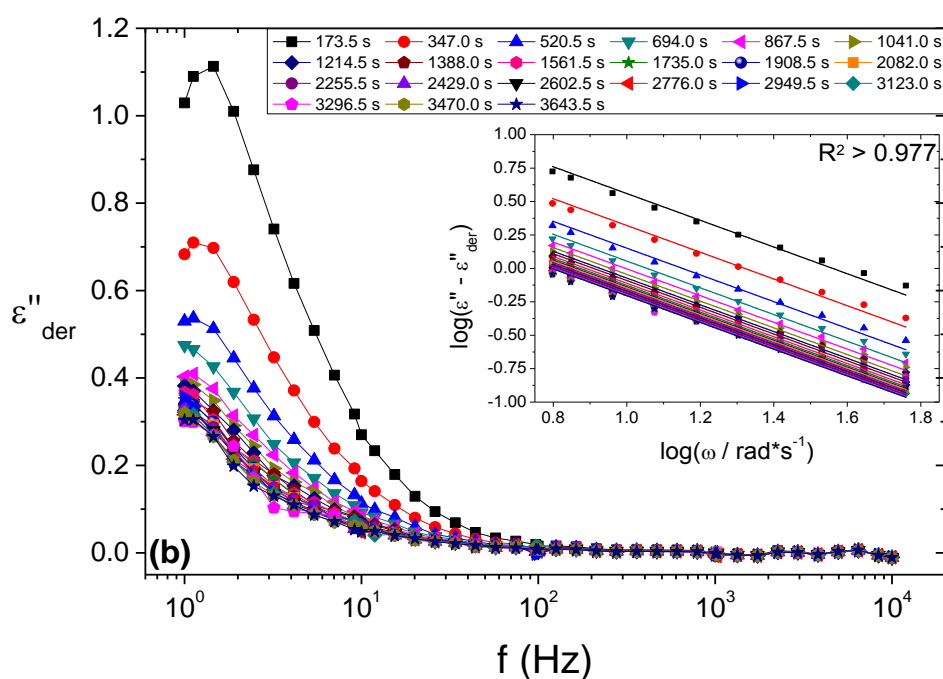
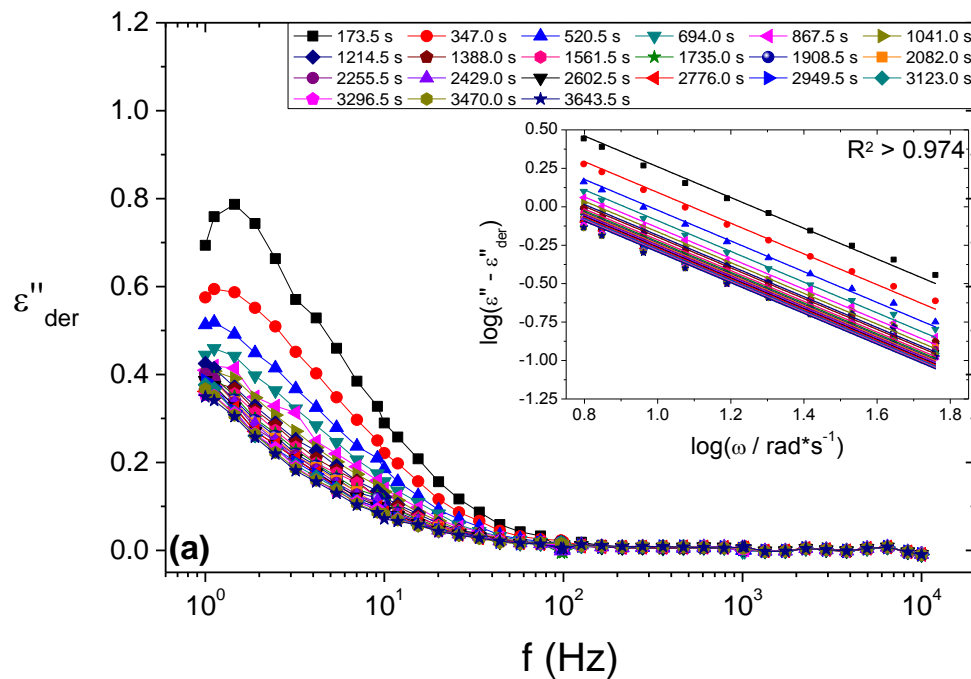


$$\varepsilon''_{der} = -\frac{\pi}{2} \frac{\partial \varepsilon'(\omega)}{\partial \ln \omega} \quad (4.11)$$

thus, making the  $\varepsilon''_{der}$  is approximately equal only to the dipolar contribution of the imaginary part of dielectric permittivity. To approximately calculate the dc conduction, the  $\varepsilon''_{der}$  can be subtracted from the  $\varepsilon''$  as seen in Equation (4.12):

$$\varepsilon'' - \varepsilon''_{der} \approx \frac{\sigma_{dc}}{\varepsilon_0 \omega} \Leftrightarrow \log(\varepsilon'' - \varepsilon''_{der}) = \log\left(\frac{\sigma_{dc}}{\varepsilon_0}\right) - \log(\omega) \quad (4.12)$$

Equation (4.12) is a line with a slope equal to -1 and an intercept equal to  $\log(\sigma_{dc}/\varepsilon_0)$ .



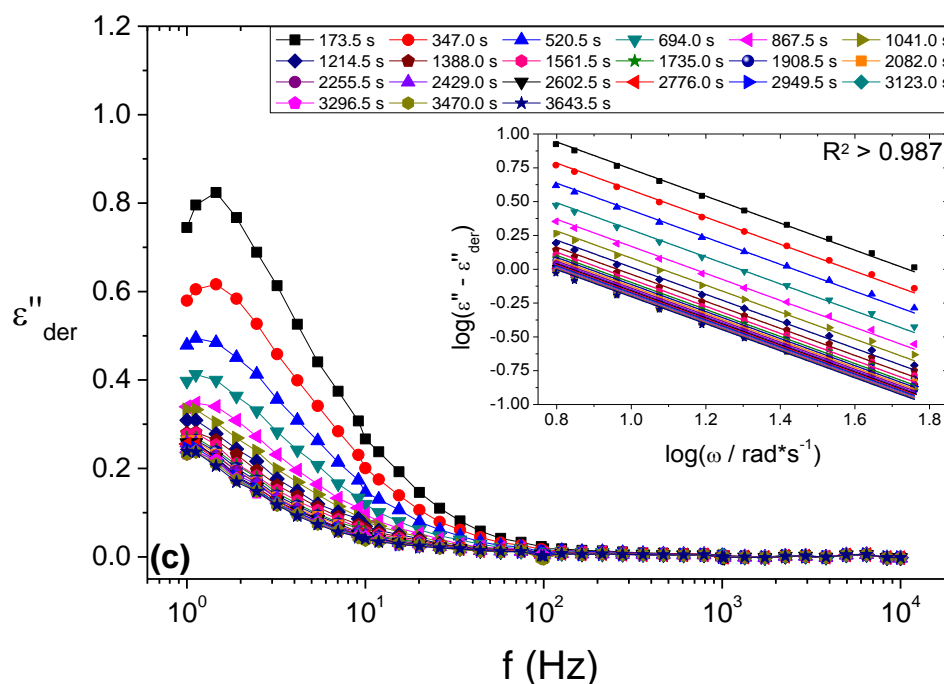


Figure 4.12. The logarithmic derivative of dielectric permittivity as a function of frequency (following Equation (4.11)) varying time for the samples under study: (a) DR1, (b) DR2 and (c) DR3. As an inset the log-log fittings of the imaginary part minus the logarithmic derivative of dielectric permittivity as a function of frequency (following Equation (4.12)) are presented with a fixed slope of -1.

In Figure 4.12, the logarithmic derivative of dielectric permittivity as a function of frequency varying the time is presented. A peak is clearly shown for all the samples and is attributed to the dipolar contribution of the Maxwell-Wagner-Sillars (*MWS*) interfacial polarization that forms due to the accumulation of charges at the interface of the insulator/conductor system [114,296]. However, since the *MWS* interfacial polarization enhances when materials of different electrical characteristics are in contact (dielectric permittivity, electrical conductivity) no significant dielectric effect is expected in the interface between crystalline and amorphous polyethylene, which can be more intense in the case of more polar or conductive semi-crystalline polymers [119,120]. This fact can be easily understood if a comparison is made between the sample PE\_5.6 presented in Figure 3.7a and the DR1 sample presented in Figure 4.11a which both are tested at 160°C. Small molecular differences exist between the samples as given in Table 2.1, but the presence of 1% w/w of gold nanoparticles increased the variation in the real part of dielectric permittivity in the frequency range of 10<sup>0</sup> Hz to 10<sup>4</sup> Hz, from approximately 3.16 – 3.12 = 0.04 to approximately 5.80 – 4.80 = 1.00 i.e. around 25 times more. In addition, the testing

temperature is above the melting temperature, thus most crystalline structures should be considered molten. Dielectric evidence of some residual larger crystallites is given in Chapter 3 section 1.2. As it can be appreciated from Figure 4.12, the peak moves to lower frequencies with the evolution of time for all the draw ratios. This comes in accordance with Chapter 3 section 2 where at temperatures above 58°C, entanglements are energetically favoured and therefore are associated with the entanglements formation that hinders the polarization and thus increase the relaxation time of the process [107]. In addition, it seems that the relaxation strength is decreasing (peak intensity), although, since it is shifting towards the lower frequency edge outside the observational window of the experiment, is not possible to analyse the effect for the overall time frame.

According to Equation (4.12) presented previously, the dc conduction contribution can be approximately calculated by subtracting the  $\varepsilon''_{der}$  from the  $\varepsilon''$  by fitting  $\log(\varepsilon'' - \varepsilon''_{der})$  versus  $\log\omega$ . The corresponding fittings are given as an inset within Figure 4.12 varying time with  $R^2$  over 0.974 in any case, indicating the linearity of the obtained data. The fittings were performed only in the frequency range of  $10^0$  Hz to  $10^1$  Hz in order to exclude any mathematical artefacts at higher frequencies where the contribution of the dc conduction to the loss permittivity is less prominent.

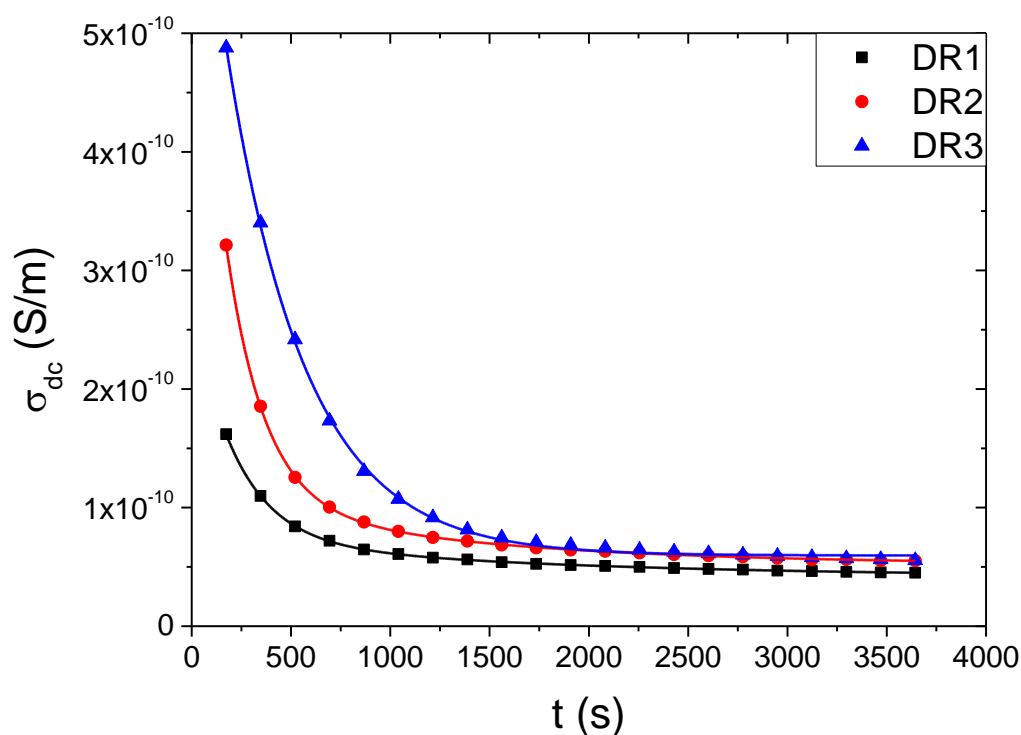


Figure 4.13. The calculated estimation of the dc conductivity for the samples under study as a function of time. The lines serve as guides for the eye only.

In Figure 4.13, the obtained dc conduction from Equation (4.12) is presented as a function of time for all the draw ratios under study. It is shown that the electrical conductivity is affected by the formation of entanglements mainly in the first 20 minutes of experiments then reaching a plateau value. According to Chapter 3 section 2, the real part of electric modulus as a function of time shows a similar increase (build-up) with the real part of mechanical modulus as obtained from melt plate-plate rheological measurement of dis-UHMWPE. Therefore, the equation that was first proposed by Yamazaki et al., [298] and Teng et al., [299] to follow chain entanglement and relaxation in rheological build up data or crystallization experiments and employed by Liu et al., [49] for dis-UHMWPE, can be employed here to fit the electric modulus build-up. The fitted values are presented in Figure 4.14 and the expression can be seen below:

$$M'(t) = M'_0 - \sum_{i=1}^N M'_i e^{\left(\frac{-t}{\tau_i}\right)} \quad (4.13)$$

where  $M'(t)$  here is the variation of the real part of electric modulus with time,  $M'_0$  is the plateau value of the real part of electric modulus,  $M'_i$  is an electric modulus increment corresponding to a characteristic time  $\tau_i$ . The reported findings in Figure 4.13 agree with the literature on the two time-regions of the entanglements formation, as explained in more detail in Chapter 1 section 2 [49]. However, the timescales involved in the rheological build-up experiments are significantly higher than the dielectric experiments presented here (i.e. in the range of an order of magnitude).

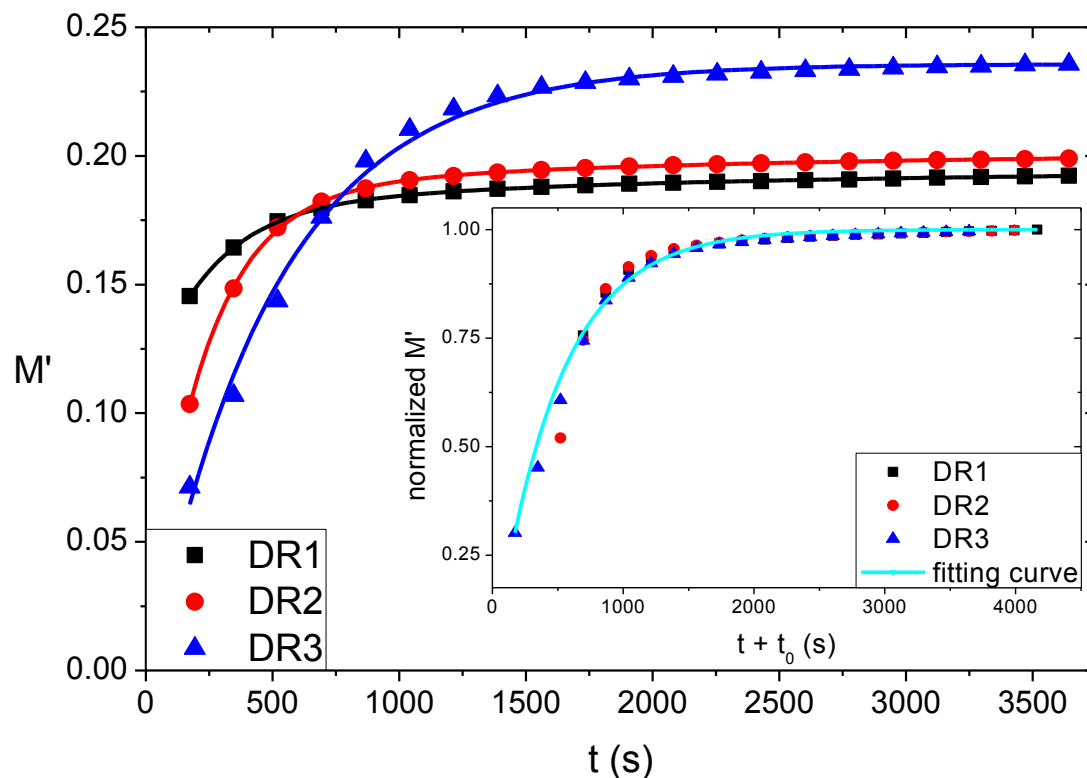


Figure 4.14. The real part of electric modulus for the samples under study as a function of time. As an inset, a normalized representation of the same data is provided with a common fitting as a superposition of extended time ( $t + t_0$ ) and draw ratio with DR3 being the reference sample ( $t_0 = 0$  s). The  $t_0$  parameter for samples DR1 and DR2 was calculated to be 520.5 s and 347.0 s respectively. The lines correspond to fittings follow Equation (4.13) and the parameters are presented at Table 4.4.

Interestingly, if the values of electric modulus presented in Figure 4.14 were subject to normalization, then a similar concept as the time-temperature-superposition principle could be applied, but instead of temperature, draw ratio can be employed. The specific analysis presented in Figure 4.14 also gives another dimension to the analysis of dis-UHMWPE; that orientation hinders the formation of entanglements over time, even at the melt state, resembling thus what is expected from unoriented dis-UHMWPE sample of higher molecular weights, as discussed in Chapter 1 section 2. This could be an interesting tool to predict the properties of oriented samples at different draw ratios and maybe it could be combined with similar testing in different temperatures; combining thus the ideas presented in this chapter with Chapter 3 section 2. The aforementioned potential is going to be discussed more in Chapter 5.

Table 4.4. Fitting parameters for the real part of electric modulus as a function of time, according to Equation (4.13) employing two modes. The fitted superimposed data in the inset of Figure 4.14 are also included.

Sample	$M'_0$ (a.u.)	$M'_1$ (a.u.)	$\tau_1$ (s)	$M'_2$ (a.u.)	$\tau_2$ (s)	$R^2$ (a.u.)
DR1	0.194	0.071	250.0	0.015	1783.1	0.99992
DR2	0.201	0.179	227.8	0.015	1680.6	0.99979
DR3	0.236	0.242	496.9	-	-	0.99391
Superimposed	1.000	1.000	483.1	-	-	0.97149

Comparing the characteristic times,  $\tau$ , as obtained from fittings of the rate at which the low temperature endothermic peak increases with the annealing time of a similar dis-UHMWPE sample in the literature [49] and our data in Table 4.4, it is visible that the chain explosion corresponds to our 2<sup>nd</sup> mode ( $\tau_2$ ). Considering that the real part of electric modulus ‘‘carries’’ both information from the dipolar response and the Ohmic conduction (combination of Equations (3.8) and (4.10)) variation in either affects its values. The effect of time in the formation of entanglements has been indeed observed in both the dipolar (Figure 4.12) and the Ohmic (Figure 4.13) response as discussed earlier. The 1<sup>st</sup> mode corresponds to the first 3 to 5 minutes of experiments and is attributed to the more intense decrease in Ohmic conduction, as it can be appreciated from Figure 4.13. It might be associated with entanglements forming in the unentangled areas that previously were part of the extended nascent crystals. This notion also agrees with the evidence presented in Figure 4.13 where a stronger decrease in dc conductivity is observed as the draw ratio increases.

#### 4.2. Metallic filler: Au nanoparticles at high draw ratios

In the present section of Chapter 4, the dis-UHMWPE/gold nanocomposites previously discussed, are oriented at high draw ratios. The effect of orientation upon the structural characteristics of the samples was investigated by means of wide-angle and small-angle X-ray scattering, Raman spectroscopy and near-infrared spectrophotometry. The presence of the gold nanoparticles and orientation affected the optical properties as observed via visible spectrophotometry.

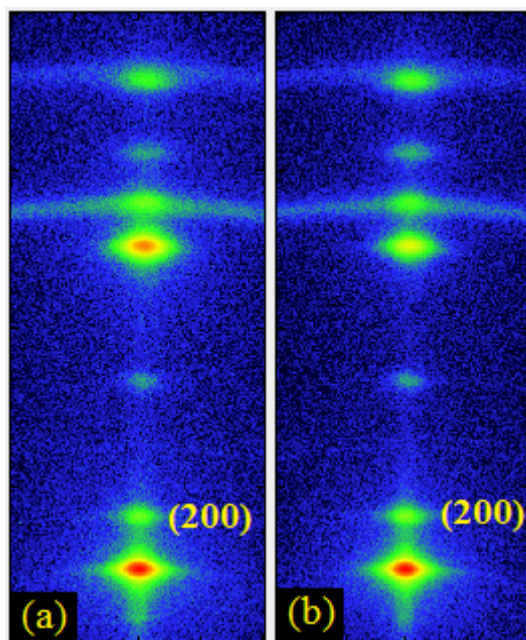


Figure 4.15. 2D WAXS patterns of oriented UHMWPE/gold nanocomposites at (a) DR72.5 and (b) DR150 with corresponding crystallinities  $X_c$  to be 84.8% and 86.3% respectively.

In order to understand the effect of tensile stretching upon the crystalline structure of UHMWPE, wide-angle X-ray scattering (WAXS) was employed. In Figure 4.15, the 2D WAXS patterns are presented, where the anisotropy can be appreciated since higher intensity concentrated in the central region of the scattering arcs. Comparing with lower draw ratios of the same composites presented in Chapter 4 section 1.1, the increase in crystallinity at higher draw ratios is almost independent of orientation with corresponding crystallinities  $X_c$  to be 84.8% and 86.3% for DR72.5 and DR150 respectively since the present of entanglements does not allow further crystallization with orientation. Hence, it evident that crystallinity is particularly sensitive to draw ratio only at the initial stages of orientation in respect to the disentangled amorphous chains that facilitate spherulitic deformation and then fibril transformation, as discussed in Chapter 1 section 4.

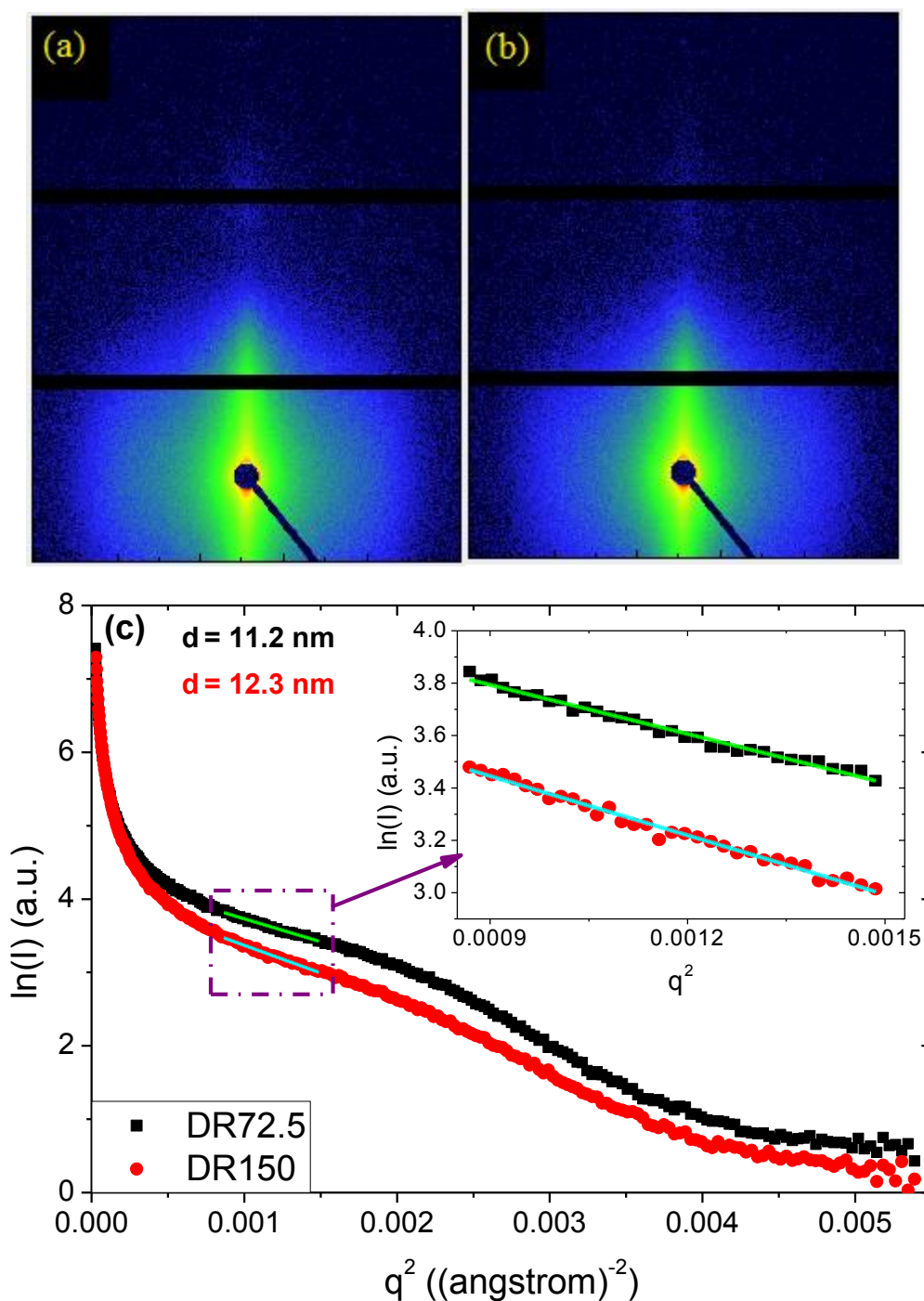


Figure 4.16. 2D SAXS patterns of UHMWPE/gold nanocomposites at (a) DR72.5 and (b) DR150. After integration, the (c) Guinier plot of the SAXS patterns are also given, fitted with the Guinier law. The diameters of the gold nanoparticles as obtained by the Guinier law for spherical nanoparticles are presented within the graph.

The 2D SAXS patterns are presented in Figure 4.16a and 4.16b and show a similar picture as the WAXS patterns in respect to anisotropy at the investigated high drawing ratios. Orientation brings an increase in intensity close to the meridian, as analyzed extensively in



the past [300]. Due to the highly anisotropic nature of the samples, a Lorentz-correction of the integrated spectra is not representative of the structures' size and distribution [301]. For unoriented samples of HDPE and UHMWPE, the lamellar spacing is expected to be in the range 20 nm, as calculated by means of SAXS and presented in Chapter 4 section 1.1 previously [279]. However, due to the presence of the gold nanoparticles and their corresponding scattering, this observation is not possible for the nanocomposites. In order to calculate the average diameter of the gold nanoparticles, the Guinier law was employed following Equation (4.1) introduced previously.

From this analysis the average size of the nanoparticles (aggregates) is presented within Figure 4.16c, and was found to be 11.2 and 12.3 nm corresponding to DR72.5 and DR150 respectively, indicating that at high draw ratios, aggregation is favored, contradicting the observed phenomenon at low draw ratios discussed previously in section 1.1 of the same chapter, where the average diameter of the aggregated nanoparticles were observed to decrease as a function of drawing ratio. Here, the increase of the aggregates' diameter is attributed to the decrease of the amorphous fractions with orientation (crystallinity increasing significantly) resulting into less available space for the nanoparticles to be relatively far away from each other. It should be taken into consideration that the nanoparticles lie in the amorphous regions of the hosting polyethylene matrix. If the crystallinity was not affected by orientation, we would expect the average size of the particles to decrease due to the breaking of aggregates; that is the case with very low drawing ratios ( $\leq$  DR 5) where the crystallinity slightly increases as discussed previously.

Uniaxial orientation also induces structural changes in the molecular vibrations for draw ratios up to 5, as previously discussed in section 1.1 of the present chapter. In Figure 4.17 the Raman shift of the highly oriented samples is presented. Evidently, no changes have been observed in the range of 1350 to 1000  $\text{cm}^{-1}$  comparing with the samples previously presented. In the 1500 to 1400  $\text{cm}^{-1}$  range, a complete diminish of the 1440 and 1463  $\text{cm}^{-1}$  peaks was observed with only the peak at 1417  $\text{cm}^{-1}$  be present indicating a strong increase of crystallinity, in agreement with WAXS presented in Figure 4.15. Instead of the 1463  $\text{cm}^{-1}$  peak, a very broad and weak halo at 1461  $\text{cm}^{-1}$  is observed and is attributed to the amorphous segments.

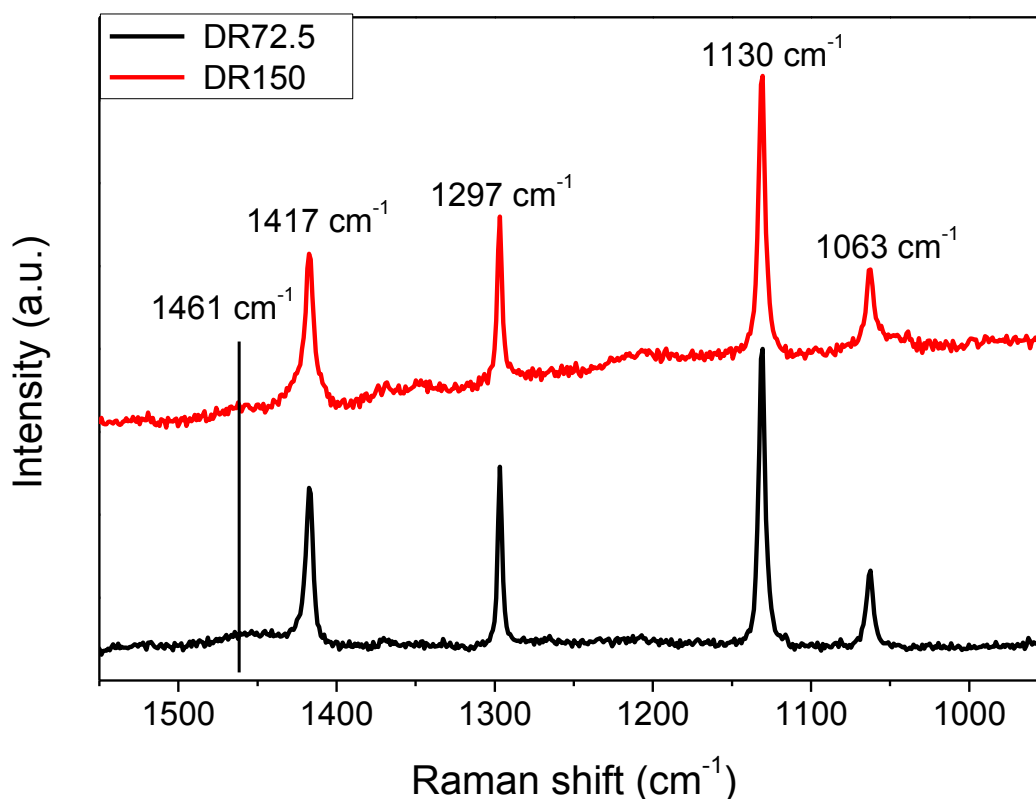


Figure 4.17. Raman spectra as a function of wavenumber for UHMWPE/gold composites at high drawing ratios.

The visible and near infrared (Vis/NIR) absorption spectra of the composites are presented in Figure 4.18. In order to effectively compare the samples besides their thickness differences, the linear absorption coefficient,  $\mu$ , is employed as presented in Equation (4.4). At the wavelength range between 1000 and 1800 nm (NIR) the absorption at high draw ratios exhibits three main peaks, all related to polyethylene alone indicating that high orientation is diminishing the 1392 nm and 1432 nm (2CH stretching) peaks to the point that they are no longer visible. It is also evident that with tensile stretching, the absorption coefficient values increase in addition to a change in the peak morphology. In the visible part of the spectrum, only one peak at 540 nm is visible and is due to the transverse plasmon resonance of the gold nanoparticles that are present in the amorphous regions of the polymer, as expected also from Figure 4.5 presented previously [288]. It is apparent that the plasmon peak is becoming broader with tensile orientation, indicating an increase in the average size of the nanoparticles (aggregates), in agreement with the experimental findings of SAXS discussed in Figure 4.16.

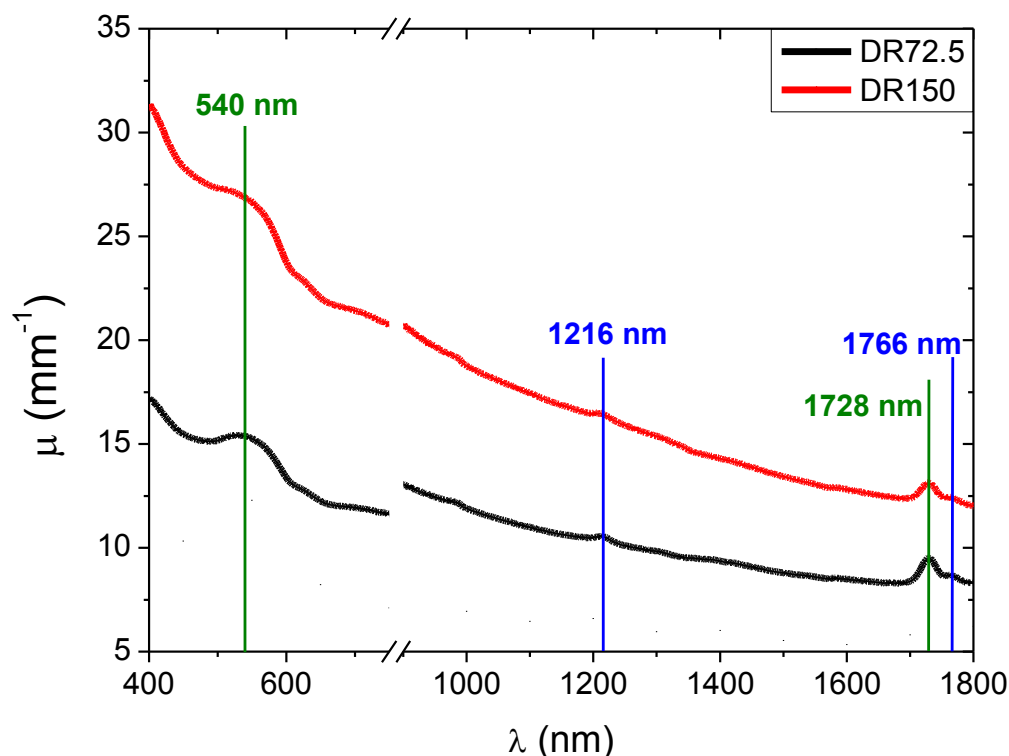


Figure 4.18. Vis/NIR absorbance of the UHMWPE/gold nanocomposites as a function of wavelength. For clarity, blue and green lines are employed to show the corresponding peaks.

The experimental data obtained by WAXS, SAXS and optical absorbance in the visible spectrum indicate that due to a decrease of the amorphous fractions, the gold nanoparticle aggregates increase in size with orientation, attributed to the decrease of amorphous fractions where the nanoparticles lie.

#### 4.3. Ceramic or organic filler: ZnO nanoparticles or $\beta$ -carotene

Structural analysis on the effect of uniaxial orientation upon the crystalline structure of UHMWPE in the presence of either ZnO nanocomposites or  $\beta$ -carotene, was conducted by means of wide-angle X-ray scattering (WAXS). In Figure 4.19, the 2D WAXS patterns are presented, where it can be appreciated that the anisotropy of the patterns increases with increasing orientation. The three lower draw ratio samples (only twin-roll calendering employed) already show signs of orientation, with more intensity concentrating in the central region of the scattering arcs. As the drawing ratio increases, more intensity is accumulated in the area surrounding the meridian, indicating an enhanced orientation, as also observed for the case of gold nanoparticle containing dis-UHMWPE samples and discussed in Chapter 4 section 1.1 and 2 for low and high draw ratios respectively. With the application of tensile

stretching, no new crystallographic peaks were observed, thus no transition from the orthorhombic to the monoclinic crystal structures was observed, due to the application of mechanical stress.

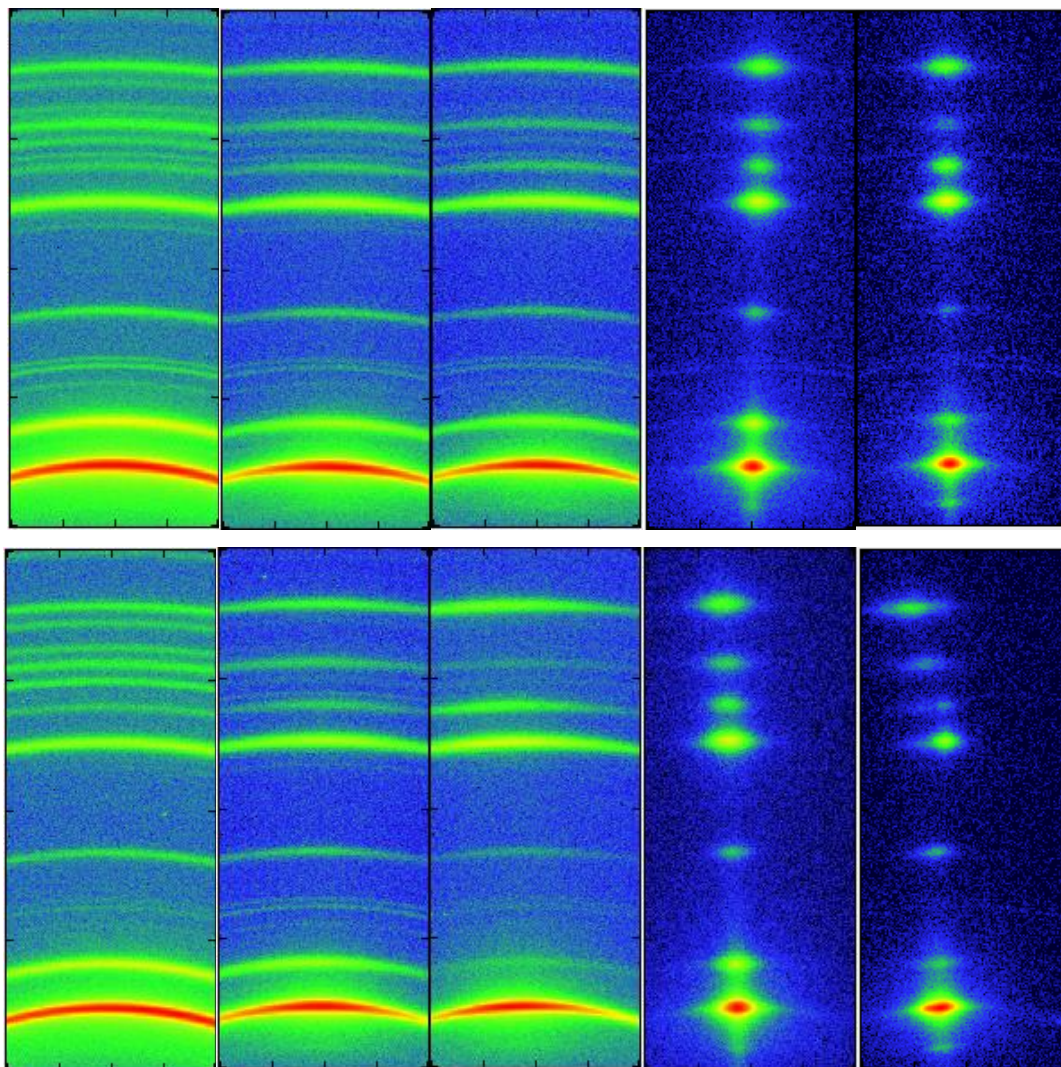


Figure 4.19. 2D WAXS patterns. (L – R): DR2.5, DR5.0, DR7.5, DR72.5 and DR150 draw ratios of dis-UHMWPE containing: (top) ZnO nanoparticles and (bottom)  $\beta$ -carotene.

In Figure 4.20, the crystallinity as a function of draw ratio is presented and was calculated by dividing the area below the crystalline peaks by the total area of crystalline and amorphous halos. Both samples exhibit an increase in crystallinity, from around 70% (DR = 2.5) to values exceeding 82% (DR = 150). A small but still detectable variation was observed between the samples containing ZnO nanoparticles and  $\beta$ -carotene, ranging from 2% to 4% higher for ZnO. Since the concentrations of the fillers is extremely low (0.035% w/w), the crystalline structure of ZnO is not expected to affect significantly the overall crystallinity

values of the nanocomposites. On the contrary, the cause of this variation it is possible to lie on the size difference between the ZnO nanoparticles (< 100 nm in diameter) and the  $\beta$ -carotene molecules ( $\sim 2.5$  nm in length). Since the  $\beta$ -carotene molecules are comparable in size with crystal defects, they might hinder cold-crystallization through stretching. However, this claim would require further testing to be proven. Comparing the crystallinity values obtained for the ZnO and  $\beta$ -carotene dis-UHMWPE samples with the aforementioned gold containing samples, no significant deviations were observed. At low draw ratios, the gold containing sample exhibit crystallinities in between the other two composites, while at high draw ratios, slightly higher values were observed.

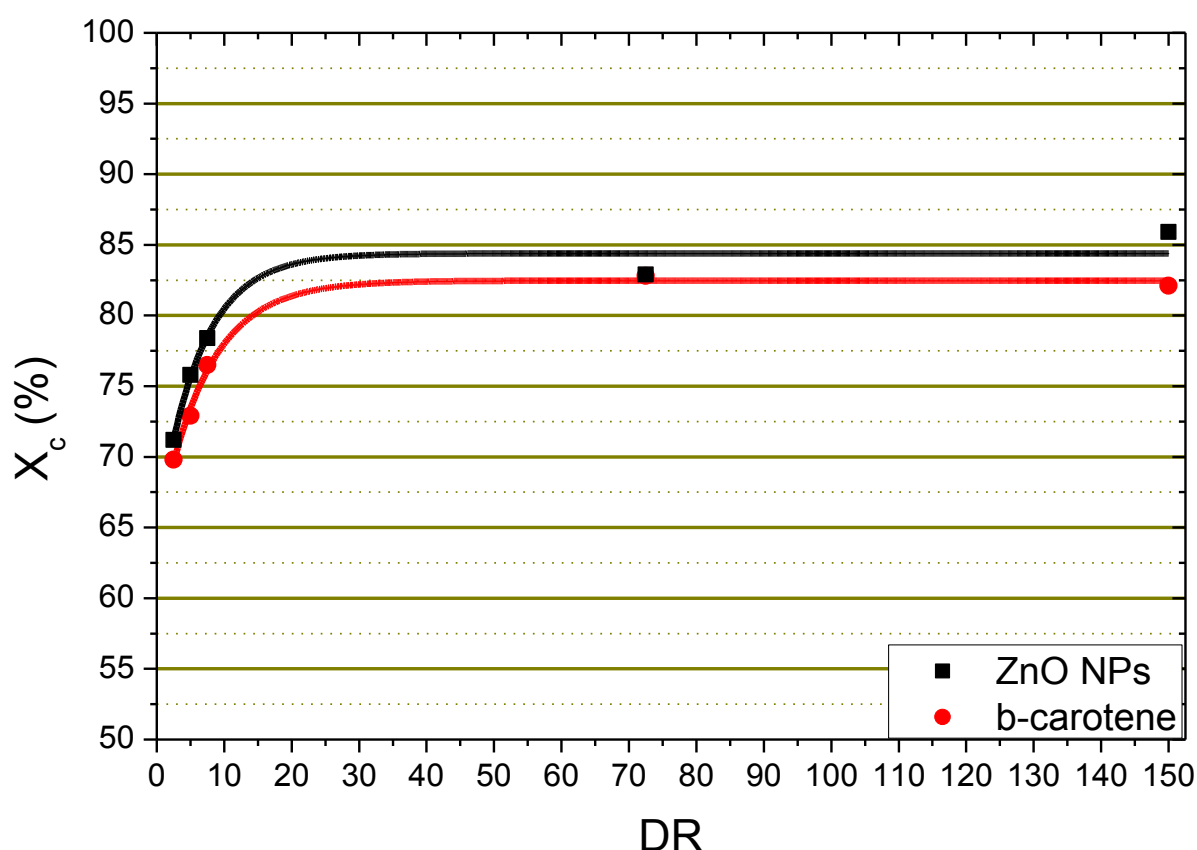


Figure 4.20. Calculated crystallinities as obtained from the integrated WAXS patterns for the different fillers as a function of draw ratio, indicating an increase with uniaxial orientation.

This very low filler concentration (0.035% w/w) was chosen in order to minimize the effect of the fillers towards the thermal properties, intended for experiments employing transient grating spectroscopy, in order to measure the thermal conductivity varying the orientation. Since polyethylene is almost entirely transparent at the visible range, and the transient grating spectroscopy requires light absorption at such wavelengths, this trace

amount of fillers was required. Experimentation with the rolled samples (DR up to 7.5) showed that ballistic phonons travel distances as far as 200 nm by traversing crystalline domains, despite the relatively low draw ratio [248].

#### 4.4. Conclusions

In the present chapter, the effect of uniaxial orientation of dis-UHMWPE in the presence of fillers was investigated. Three types of fillers were studied, metallic (gold nanoparticles), ceramic (ZnO nanoparticles) and organic ( $\beta$ -carotene). From these three types, the physical properties of the uniaxially oriented dis-UHMWPE/gold nanocomposites were studied while the other two types were only investigated with WAXS, showing an increase in crystallinity with orientation but not any change to monoclinic crystal structure because of the mechanical stress.

The structural characteristics of the dis-UHMWPE/gold nanocomposites at low drawing ratios were analysed by means of Raman spectroscopy, Vis/NIR spectrophotometry, small-angle and wide-angle X-ray scattering, revealing an increase in crystallinity with increasing orientation, as well as a decrease in gold nanoparticle aggregation. Uniaxial plastic deformation significantly affected the thermal conductivity in a beneficial way increasing from the reported  $\sim 0.3 \text{ Wm}^{-1}\text{K}^{-1}$  of unstretched polyethylene to up to  $4.6 \text{ Wm}^{-1}\text{K}^{-1}$ , enabling faster cooling and favouring thermal management. The dielectric materials under study were subjected to experimentation as electrical energy storage devices for capacitor application, by testing their performance during charge and discharge cycles and found that the recovery efficiency increased dramatically in oriented samples. This phenomenon was attributed to interfacial polarization induced by the presence of gold nanoparticles in the dis-UHMWPE matrix, enhanced by the breaking down of the aggregates that resulted in higher surface area between the conducting nanoparticles and the polymer matrix. However, with orientation comes higher crystallinity, which hinders the polymer chains mobility and their ability to be polarized, reducing the permittivity of the composites. Therefore, a balance between orientation and recovery efficiency was observed, which in these systems was embodied by the nanocomposite stretched to drawing ratio 3, that yielded the optimum configuration. Therefore, the results presented in the present chapter are key for the design and fabrication of composites for electrical energy storage applications, providing valuable guidance on which crystallinity and orientation values should be chosen depending on the final properties that are sought. More generally, this study paves the way towards lighter, more efficient and thermally stable dielectric capacitors based on polymer nanocomposites.

When subject to tensile orientation to achieve higher drawing ratios, it was observed that crystallinity reached a maximum value close to  $X_c \sim 85\%$  and was then almost independent of orientation. After the SAXS analysis, it was observed that the increase of crystallinity had a negative effect upon the gold nanoparticles by favouring aggregation. Therefore, a decrease and an increase of the average size of gold aggregates were observed for low and high drawing ratios respectively, in association with crystallinity. The almost independent effect of orientation upon crystallinity, was also observed in other composites containing traces of ZnO nanoparticles and  $\beta$ -carotene respectively.

## 5. Conclusions & future work

### 5.1. Concluding remarks

In the present doctoral thesis, the molecular origin of the chain relaxations as observed in linear disentangled ultra-high molecular weight polyethylene (both pure and as the matrix in composite systems) was investigated and discussed. Due to its disentangled character, more light was shed towards the formation of entanglements and how this affects the relaxation dynamics. In addition, the effect of uniaxial orientation upon the physical properties of the samples in the presence of fillers was another aspect that was investigated. The observations and conclusion are summarized below in a way to answer the initial five questions that were asked in the Introduction of the present doctoral dissertation:

- (1) What is the role of the disentangled amorphous phase upon the mechanical and dielectric relaxation dynamics in a broad range of temperatures and frequencies?

To determine the disentangled amorphous phase, two basic dynamic techniques were employed; torsional rheology and broadband dielectric spectroscopy. Torsional rheology was employed to analyse the relaxation mechanisms in ultra-high molecular weight polyethylene in the temperature and frequency range of  $-130^{\circ}\text{C}$  to  $130^{\circ}\text{C}$  and  $10^{-2}$  Hz to  $10^2$  Hz respectively with a step of  $5^{\circ}\text{C}$ . To examine the disentangled character of our samples we applied two processing conditions: (a) solid-state compression moulding ( $125^{\circ}\text{C}$ ) and (b) melt-state compression moulding ( $160^{\circ}\text{C}$ ). To identify possible variations between our in-house prepared sample and other types of linear ultra-high molecular weight polyethylene, we compared it with a melt-state processed, fully entangled commercial sample. As expected according to the literature, three basic processes were observed, namely  $\alpha_c$ -,  $\beta$ - and  $\gamma$ -relaxations, with the first being attributed to motions in the crystalline phase and the other two being related to the amorphous phase. It was determined that the melt-state processed samples (both in-house and commercial) exhibited a very similar rheological behaviour. That is attributed to the disruption of the initial (pristine) crystalline structure of the disentangled sample (where the crystallinity decreases from  $X_c \sim 79\%$  prior to melting to  $\sim 37\%$  after melting and re-crystallisation) reaching very similar crystallite concentrations with the commercial, and also to the formation of entanglements during the melt processing. The solid-state disentangled sample, however, showed a significantly different rheological behaviour, affecting all the relaxation processes. It was found from our analysis that after



plotting the normalized relaxation strength of each process with the crystallinity obtained from DSC, the  $\alpha_c$ - and  $\gamma$ -relaxations showed a strong crystallinity dependence, where the first increased and the second decreased with the crystallite content respectively; the  $\beta$ - relaxation exhibited an independent relation to crystallinity. The observation that the  $\gamma$ -relaxation is increasing in intensity with the amorphous increase is the first indication that we have that this relaxation might be the dynamic glass-to-rubber transition process. The second and strongest indication can be drawn by the non-Arrhenius temperature dependence that this process exhibits. It is very interesting to see that the non-Arrhenius dependence is observed only in the case of the solid-state processed disentangled sample. The non-Arrhenius temperature dependence is indicative of the dynamic glass-to-rubber transition process and thus the rheological experiments presented in this doctoral research are a direct indication of the  $T_g$  in linear UHMWPE. Following the interesting relaxation dynamics obtained by torsional rheology, dis-UHMWPE was examined by means of broadband dielectric spectroscopy in the temperature and frequency range of 50°C to 160°C and 10<sup>0</sup> Hz to 0.429\*10<sup>6</sup> Hz respectively with a step of 10°C. Because of the highly insulating character of polyethylene, Al<sub>2</sub>O<sub>3</sub> catalytic ashes were employed as dielectric probes at a low concentration. The  $\alpha_c$ - and  $\beta$ -relaxations were identified with the latter consisting of two sub-relaxations. An additional contribution to interfacial polarization was identified and attributed to the presence of Al<sub>2</sub>O<sub>3</sub> particles: also, in this case we could identify the presence of two sub-processes in this relaxation. Since entanglements work as spatial constrictions in the movement of the chains, the fast sub-process (high frequency) was attributed to the disentangled amorphous phase while the slow sub-process (low frequency) to the entangled amorphous phase.

(2) Is the solid state metastable like the melt state?

Considering the metastable character of dis-UHMWPE in the melt state, a comparison between melt plate-plate rheology and dielectric spectroscopy was conducted via the modulus formalism. It is well-established in the literature that the real part of mechanical modulus increases over time due to the progressive formation of entanglements; the same effect was identified and presented in this doctoral thesis, employing dielectric spectroscopy via the real part of electric modulus. With the use of dielectric spectroscopy however, it was possible to monitor the formation of entanglements also in the solid state. By running different dis-UHMWPE specimens each at a different temperature, it was experimentally observable that entanglements form at a temperature as low as 80°C. By constructing a model as a part of the

present doctoral research, the critical temperature for the formation of entanglements was calculated to be 58°C. This is a direct experimental observation that indeed entanglements can form in the solid state, given that enough energy is provided.

(3) How does uniaxial orientation affect the physical properties?

Although no experiments were conducted in plain dis-UHMWPE with orientation, constant filler concentrations were employed to determine the effect of uniaxial stretching. By means of wide-angle X-ray scattering and Raman spectroscopy, it was determined that crystallinity increased with orientation from 70% up to 86% in the unoriented (DR1) and highly oriented (DR150) state respectively. The thermal conductivity was also found to increase significantly even at lower draw ratios ( $\leq$  DR5) over 15 times, from  $\sim 0.3 \text{ Wm}^{-1}\text{K}^{-1}$  of unstretched polyethylene up to  $4.6 \text{ Wm}^{-1}\text{K}^{-1}$ . Due to the increase of crystallinity and thus the restriction upon the mobility of the dipoles, the dielectric permittivity was reduced from 5.6 to 3.6 at DR1 and DR5 respectively.

(4) How does uniaxial orientation affect the formation of entanglements?

Considering the applicability of dielectric spectroscopy to investigate the formation of entanglements as shown previously, similar experiments in oriented samples were firstly examined in the present doctoral thesis. The formation of entanglements was found to affect the interfacial polarization, as with the unoriented sample containing  $\text{Al}_2\text{O}_3$  (discussed earlier and also the dc conductivity). As expected from the formation of entanglements, the real part of electric modulus was found to increase with time and a master curve was designed to combine the data as a time and draw ratio superposition. From this analysis, the effect of orientation was found to hinder the formation of entanglements, therefore, a parallel can be drawn between uniaxial orientation and the increase of molecular weight in an unoriented dis-UHMWPE sample.

(5) What is the role of nanofillers in the resulting physical properties with or without uniaxial orientation?

The presence of fillers inside a dis-UHMWPE matrix was identified by means of several techniques. Gold nanoparticles were employed for their very high electrical conductivity to induce significant interfacial polarization phenomena in the highly insulating polyethylene matrix. Hence, dis-UHMWPE/gold samples were prepared as dielectric materials for capacitor applications. The dielectric properties were tested at room temperature in ac and dc

conditions. The ac capacitance was found to increase with orientation and very low dielectric losses were observed, both beneficial for capacitive energy storing systems. By testing the electrical response during charge and discharge cycles in dc conditions, the recovery efficiency was observed to increase up to 30 times with orientation. This impressive performance was attributed to the breaking of large gold nanoparticle aggregates, as identified via Vis/NIR spectrophotometry. This resulted in higher surface area between the conducting nanoparticles and the polymer matrix, enhancing thus interfacial polarization. Considering the importance of crystallinity as a measure to increase dielectric breakdown strength and thermal conductance in order to effectively dissipate heat, the crystallinity and the thermal conductivity were both investigated and were found to increase with orientation as discussed previously. Since orientation induced crystallization, the chain mobility and polarization were hindered so the sample with draw ratio 3 exhibited the optimum performance.

## 5.2. Future work

In this section, experiments under study or untested ideas that arose from the present doctoral research are briefly discussed.

1. Neutron scattering experiments to determine the reptation characteristics of dis-UHMWPE samples with graphene oxide are going to take place in the ILL institute in Grenoble in France. In the literature, evidence that graphene oxide hinders the formation of entanglements have been given via melt plate-plate rheology. This evidence will be further analysed with the proposed technique.
2. The structural information of highly oriented dis-UHMWPE/gold nanocomposites by means of Raman spectroscopy, Vis/NIR spectrophotometry, SAXS/WAXS including the application of such composite as a polarizer are under preparation.
3. It would be very interesting to investigate the formation of entanglements as a function of uniaxial orientation by means of dielectric spectroscopy in the presence of a ceramic nanofiller. It would be possible to obtain time-temperature-orientation superposition and predict the formation of entanglements in other disentangled polymers varying the temperature and the degree of orientation.
4. Highly oriented dis-UHMWPE in the presence or not of nanofillers could be used for dielectric capacitor applications due to the highly insulating character of polyethylene and the significant increase in crystallinity with orientation. These two parameters are important to increase the dielectric breakdown strength and thus increase the electrical

energy storage. The presence of nanofillers could potentially increase the dielectric permittivity and increase even more the energy storage.

## 6. Acknowledgements

Mr Stavros X. Drakopoulos would like to thank (in institution order):

- Loughborough University: My main supervisor Dr. **Sara Ronca** for her valuable contribution throughout my whole doctoral research and for being a tutor to me during the scientific and writing process. Most importantly for giving me the chance to join her group in the first place and trusting my ideas, curiosities and research intuition throughout the PhD process. My co-supervisor Dr. **Ignacio Martin-Fabiani** for his valuable and determinant input on dielectric and light scattering data and for giving me guidance and supervision throughout my doctoral research and teaching me an introduction to SAXS/WAXS analysis. Dr. **Giuseppe Forte** for the chemical synthesis of the dis-UHMWPE samples and performing the melt plate-plate and torsional rheology experiments. Dr. **Gianfranco Claudio** for giving me access to the Vis/NIR spectrophotometer apparatus.
- University of Patras: Professor Dr. **Georgios C. Psarras** for providing the BDS and DC apparatuses to perform the measurements and his valuable opinion during the analysis of the dielectric data. Dr. **Georgia C. Manika** for providing experimental guidance during the DC measurements.
- California Institute of Technology: Professor Dr. **Austin J. Minnich** for his interest to our work and for offering his TGS technique to obtain the thermal conductivity of oriented dis-UHMWPE composites. Dr. **Andrew B. Robbins** and Mr. **Taeyong Kim** for performing the above experiments.
- Instituto de Estructura de la Materia: Professors Dr. **Aurora Nogales** and Dr. **Tiberio A. Ezquerro** for performing the experiments on our oriented dis-UHMWPE/gold nanocomposites by means of SAXS/WAXS and giving me the opportunity to participate in a polyolefin dielectric relaxation book chapter.
- University of Ioannina: Professor Dr. **Georgios A. Floudas** for the very fruitful and enlightening discussions on dielectric relaxation analysis that we had during the *10<sup>th</sup> Conference on Broadband Dielectric Spectroscopy and its Applications* that took place in Brussels (Belgium) from 26/8 to 31/8 2018.

I would also like to thank Dr. Elisa Mele (Loughborough University) and Dr. Chaoying Wan (University of Warwick) for their constructive comments and corrections during my doctoral defence (PhD viva) on 25<sup>th</sup> of November 2019 as they served as my internal and external examiners respectively.

In a more personal note, I would like to thank from the bottom of my heart my family and most importantly my mother Lila for her endless love and support since my first breath. Many thanks for their support to my stepfather Ntinou and also my grandmother Fofi who passed away during the completion of this doctoral work (9/5/2019). Many thanks to my best friends Iordanis, Fani, Costas and Apostolis for supporting me, especially during my time in Greece and my brother-by-choice Ilias who always makes me to try my best with his own great example. To my good friends and colleagues Orestis and Vaggelis, with whom we became friends through our common love for dielectrics in Patras and continued our friendships as PhD students in the UK. To my mates in Loughborough, Davide, Vasilis, Jing and Giuseppe for making my days better and all the great fun we had during lab work. To my partner in crime Yannis, with whom I shared an office from the first day until the last of this doctoral work and for the great friendship we built around it. I am also grateful to my good friend and mentor, Giorgos, for his advice, trust and friendship the past 8 years. My love and appreciation to my wonderful partner Lena who supported me throughout the whole process of my doctoral work, from the application stage until the end, and making my life easier and more beautiful with her presence in the UK pursuing her own PhD in Bioscience in the University of Birmingham.

Finally, I want to dedicate all the intellectual effort I put for this research work to the memory of my grandfather Stavros A. Drakopoulos, who provided me with the right tools and advice from the beginning of my life until the end of his.

## 7. Publications and Conferences

### 7.1. Published articles in peer-review journals

1. D. Nocita, G. Forte, **S. X. Drakopoulos**, A. Visco, A. Gianporcaro, S. Ronca (2017) Processing and characterization of bio-polyester reactive blends: From thermoplastic blends to cross-linked networks. *Polymer* 132:252-263.
2. **S. X. Drakopoulos**, G. C. Psarras, G. Forte, I. Martin-Fabiani, S. Ronca (2018) Entanglement dynamics in ultra-high molecular weight polyethylene as revealed by dielectric spectroscopy. *Polymer* 150:35-43.
3. **S. X. Drakopoulos**, J. Karger-Kocsis, G. C. Psarras (2019) In situ thermodielectric analysis of the gelatinization mechanism of raw maize starch: An experimental and theoretical approach. *Journal of Polymers and the Environment* 27(2):333-342.
4. A. B. Robbins, **S. X. Drakopoulos**, I. Martin-Fabiani, S. Ronca, and A. J. Minnich (2019) Ballistic thermal phonons traversing nanocrystalline domains in oriented polyethylene. *Proceedings of the National Academy of Sciences* 116:17163-17168.

### 7.2. Submitted or under preparation manuscripts

1. **S. X. Drakopoulos**, G. C. Psarras, A. Nogales, T. A. Ezquerra, T. Kim, A. B. Robbins, A. J. Minnich, G. C. Manika, G. Claudio, I. Martin-Fabiani, S. Ronca (2019) Gold/ultra-high molecular weight polyethylene nanocomposites for electrical energy storage: Enhanced recovery efficiency upon uniaxial deformation. (Submitted.)
2. **S. X. Drakopoulos**, G. Forte, S. Ronca (2019) Relaxation dynamics in disentangled ultra-high molecular weight polyethylene via torsional rheology. (Submitted.)
3. **S. X. Drakopoulos**, I. Martin-Fabiani, L. Guan, S. Ronca (2019) Oriented disentangled UHMWPE/gold nanocomposites: An optical and structural study\*. (Manuscript under preparation.)
4. **S. X. Drakopoulos**, G. C. Psarras, S. Ronca (2019) Oriented ultra-high molecular weight polyethylene/gold nanocomposites: Electrical conductivity and chain entanglement dynamics\*. (Manuscript under preparation.)

\*Working title.

### 7.3. Chapters in Books

1. **Drakopoulos S. X.**, Ronca S., Martin-Fabiani I. (2020) Dielectric spectroscopy of nonpolar polymers: The case of semicrystalline polyolefins. In T. A. Ezquerra & A. Nogales (Eds.), *Dielectrics and Crystallization*. Part of the Advances in Dielectrics series, F. Kremer (Ed.). Springer International Publishing.

### 7.4. International conference participation

1. **S. X. Drakopoulos\***, G. C. Psarras, S. Ronca (August 26-31, 2018, Brussels, Belgium) Understanding the Evolution of Entanglements upon the Dielectric Relaxations in dis-UHMWPE in the Presence of Al<sub>2</sub>O<sub>3</sub> Catalytic Ashes. Oral Presentation in the *10<sup>th</sup> Conference on Broadband Dielectric Spectroscopy and its Applications*.
2. **S. X. Drakopoulos\***, G. C. Manika, G. C. Psarras, S. Ronca (May 5-8, 2019, Budapest, Hungary) Au/ultra-high molecular weight polyethylene nanodielectrics: the effect of calendering on the electrical energy storage potential. Oral Presentation in the *6<sup>th</sup> International Symposium Frontiers in Polymer Science*.
3. **S. X. Drakopoulos\***, I. Martin-Fabiani, A. Nogales, T. A. Ezquerra, G. Claudio, S. Ronca (May 5-8, 2019, Budapest, Hungary) Au/ultra-high molecular weight polyethylene nanocomposites: the effect of calendering on structural and thermal properties. Poster Presentation in the *6<sup>th</sup> International Symposium Frontiers in Polymer Science*.
4. **S. X. Drakopoulos\***, G. Forte, G. C. Psarras, S. Ronca (June 24-28, 2019, Naples & Sorrento, Italy) Relaxation dynamics of disentangled UHMWPE as revealed by broadband dielectric spectroscopy and torsional rheology. Poster Presentation in the *5<sup>th</sup> Blue Sky Conference on Catalytic Olefin Polymerization*.
5. **S. X. Drakopoulos\***, I. Martin-Fabiani, S. Ronca (June 24-28, 2019, Naples & Sorrento, Italy) Uniaxially oriented UHMWPE in the presence of ZnO nanoparticles or  $\beta$ -carotene: A small/wide-angle X ray scattering study. Poster Presentation in the *5<sup>th</sup> Blue Sky Conference on Catalytic Olefin Polymerization*.

### **7.5. Invited talks**

1. From Thermoplastic Starch Biocomposites to Disentangled Ultra-High Molecular Weight Polyethylene: A Dielectric Journey (December 21, 2017, Patras, Greece) 40-minute talk, Department of Materials Science, University of Patras.
2. Broadband Dielectric Relaxation Spectroscopy: Applications to Polymer Science (September 11, 2018, Maastricht, Netherlands) 50-minute talk, Department of Biobased Materials, Faculty of Sciences and Engineering, Maastricht University.



## 8. Short Curriculum Vitae

### Education

---

**Ph.D. in Materials Engineering** (October 2016 – September 2019), Department of Materials, School of Aeronautical, Automotive, Chemical and Materials Engineering, Loughborough University, Leicestershire, England, UK.

**Funding:** *Full University Research Studentship* for 3 years.

**Thesis:** "Disentangled ultra-high molecular weight polyethylene and its nanocomposites: Relaxation dynamics, entanglement formation and anisotropic properties due to orientation".

**Supervisors:** Dr. Sara Ronca, Dr. Ignacio Martin-Fabiani, Dr. Simon J. Martin.

**B.Sc. in Materials Science** (October 2011 – August 2016), Department of Materials Science, School of Natural Sciences, University of Patras, Greece.

**Greek Academic Grading:** 7.29/10 (Very Good, ECTS B)

**Thesis:** "Chemical composition, thermomechanical behaviour and electrical response of biocomposite thermoplastic starch matrix materials, reinforced with latex and cellulose particles".

**Supervisor:** Professor Dr. Georgios C. Psarras.

### Research Interests

---

- ✓ Polymers, biopolymers and polymer nano/micro-composite materials.
- ✓ Dielectric properties, electrical energy storage and recovery.
- ✓ Frequency and temperature dependence of relaxation dynamics.
- ✓ Orientation phenomena, anisotropic properties.
- ✓ Smart and multifunctional materials, applications of piezoelectric materials.



### Publications

---

✓ Published/Accepted Articles	7	
Submitted Articles	2	2015 – present
Manuscripts under Preparation	3	
Citations	71	
Independent Citations (excluding self-citations)	62	source: Scopus, Mendeley
h-index	5	
✓ Issued Patents	2	Hellenic Industrial Property Organization
Pending Patents	-	
✓ International Conferences	8	6 Poster + 2 Oral Presentations
National Conferences (Greek)	4	3 Poster + 1 Oral Presentations
National Conferences (United Kingdom)	2	2 Poster Presentations

### Memberships in Societies

---

- ✓ Associate Member of the Royal Society of Chemistry since April 2018.
  -  Polymer Physics Group.
  -  Macro Group UK.
- ✓ Junior Member of the European Society for Biomaterials (ESB) since May 2018.
- ✓ Student Member of the International Dielectric Society (IDS) since August 2018.
- ✓ Member of the Greek MENSA since August 2016.

## 9. References

- [1] A.J. Peacock, Handbook of Polyethylene, Marcel Dekker Inc., New York, Basel, 2000.
- [2] S. Dadbin, M. Frounchi, M. Haji Saeid, F. Gangi, Molecular structure and physical properties of E-beam crosslinked low-density polyethylene for wire and cable insulation applications, *J. Appl. Polym. Sci.* 86 (2002) 1959–1969. doi:10.1002/app.11111.
- [3] S.J. Dodd, Y. Zhao, A.S. Vaughan, S.J. Sutton, The effect of voltage, temperature and morphology on electrical treeing in polyethylene blends, in: Eighth Int. Conf. Dielectr. Mater. Meas. Appl., 2000: pp. 35–40. doi:10.1049/ip-rmt.
- [4] Y.L. Chong, G. Chen, I.L. Hosier, A.S. Vaughan, Y.F.F. Ho, Heat treatment of cross-linked polyethylene and its effect on morphology and space charge evolution, *IEEE Trans. Dielectr. Electr. Insul.* 12 (2005) 1209–1221. doi:10.1109/TDEI.2005.1561801.
- [5] I.L. Hosier, M. Praeger, A.S. Vaughan, S.G. Swingler, The effects of hydration on the DC breakdown strength of polyethylene composites employing oxide and nitride fillers, *IEEE Trans. Dielectr. Electr. Insul.* 24 (2017) 3073–3082. doi:10.1109/TDEI.2017.006579.
- [6] C.D. Green, A.S. Vaughan, G. Stevens, S.J. Sutton, T. Geussens, M. Fairhurst, Recyclable power cable comprising a blend of slow-crystallized polyethylenes, *IEEE Trans. Dielectr. Electr. Insul.* 20 (2013) 1–9. doi:10.1109/TDEI.2013.6451335.
- [7] H.A. Khonakdar, S.H. Jafari, U. Wagenknecht, D. Jehnichen, Effect of electron-irradiation on cross-link density and crystalline structure of low- and high-density polyethylene, *Radiat. Phys. Chem.* 75 (2006) 78–86. doi:10.1016/j.radphyschem.2005.05.014.
- [8] J.M. Kelly, Ultra-High Molecular Weight Polyethylene\*, *J. Macromol. Sci. Part C Polym. Rev.* 42 (2002) 355–371. doi:10.1081/MC-120006452.
- [9] S. Ronca, G. Forte, H. Tjaden, Y. Yao, S. Rastogi, Tailoring molecular structure via nanoparticles for solvent-free processing of ultra-high molecular weight polyethylene composites, *Polym. (United Kingdom)*. 53 (2012) 2897–2907. doi:10.1016/j.polymer.2012.04.051.
- [10] A. Niemczyk, K. Dziubek, B. Sacher-Majewska, K. Czaja, M. Dutkiewicz, B. Marciniak, Study of thermal properties of polyethylene and polypropylene nanocomposites with long alkyl chain-substituted POSS fillers, *J. Therm. Anal.*

- Calorim. 125 (2016) 1287–1299. doi:10.1007/s10973-016-5497-4.
- [11] Q. Chen, Y. Xi, Y. Bin, M. Matsuo, Electrical and dielectric properties in carbon fiber-filled LMWPE/UHMWPE composites with different blend ratios, *J. Polym. Sci. Part B Polym. Phys.* 46 (2008) 359–369. doi:10.1002/polb.21371.
- [12] R.J. Volungis, R.S. Stein, Temperature dependency of the statistical segment size of polyethylene, *J. Chem. Phys.* 23 (1955) 1179. doi:10.1063/1.1742231.
- [13] R.S. Stein, M.B. Rhodes, Photographic light scattering by polyethylene films, *J. Appl. Phys.* 31 (1960) 1873–1884. doi:10.1063/1.1735468.
- [14] M.B. Rhodes, R.S. Stein, Light scattering study of the annealing of drawn polyethylene, *J. Appl. Phys.* 32 (1961) 2344–2352. doi:10.1063/1.1777072.
- [15] J.T. Judge, R.S. Stein, Growth of crystals from molten crosslinked oriented polyethylene, *J. Appl. Phys.* 32 (1961) 2357–2363. doi:10.1063/1.1777074.
- [16] P.D. Griswold, A.E. Zachariades, R.S. Porter, Solid state coextrusion: A new technique for ultradrawing thermoplastics illustrated with high density polyethylene, *Polym. Eng. Sci.* 18 (1978) 861–863. doi:10.1002/pen.760181106.
- [17] A.E. Zachariades, R. Ball, R.S. Porter, Extrusion of self-reinforced thermoplastic composites illustrated by high density polyethylene, *J. Mater. Sci.* 13 (1978) 2671–2675. doi:10.1007/BF02402754.
- [18] A.E. Zachariades, T. Kanamoto, R.S. Porter, Solid-State coextrusion of high-density polyethylene. II. Effect of molecular weight and molecular weight distribution, *J. Polym. Sci. Polym. Phys. Ed.* 18 (1980) 575–585. doi:10.1002/pol.1980.180180316.
- [19] T. Kanamoto, A.E. Zachariades, R.S. Porter, Deformation Profiles in Solid State Extrusion of High Density Polyethylene, *Polym. J.* 11 (1979) 307–313.
- [20] A.E. Zachariades, P.D. Griswold, R.S. Porter, Ultradrawing of Thermoplastics by Solid State Coextrusion Illustrated with High Density Polyethylene, *Polym. Eng. Sci.* 19 (1979) 441–449.
- [21] A.E. Zachariades, W.T. Mead, R.S. Porter, Recent Developments in Ultraorientation of Polyethylene by Solid State Extrusion, *Chem. Rev.* 80 (1980) 351–364. doi:10.1021/cr60326a005.
- [22] H. Schonhorn, F.W. Ryan, Surface Crosslinking of Polyethylene and Adhesive Joint Strength, *J. Appl. Polym. Sci.* 18 (1974) 235–243. doi:10.1039/F29827801451.
- [23] E. Sclipa, K. Piekarski, Carbon fiber reinforced polyethylene for possible orthopedic uses, *J. Biomed. Mater. Res.* 7 (1973) 59–70. doi:10.1002/jbm.820070105.
- [24] R.D. Tetik, J.O. Galante, W. Rostoker, A wear resistant material for total joint

- replacement-tissue biocompatibility of an ultra-high molecular weight (UHMW) polyethylene-graphite composite, *J. Biomed. Mater. Res.* 8 (1974) 231–250. doi:10.1002/jbm.820080506.
- [25] S. Yousef, A. Visco, G. Galtieri, D. Nocita, C. Espro, Wear behaviour of UHMWPE reinforced by carbon nanofiller and paraffin oil for joint replacement, *Mater. Sci. Eng. C.* 73 (2017) 234–244. doi:10.1016/j.msec.2016.11.088.
- [26] M. Wang, W. Bonfield, Chemically coupled hydroxyapatite-polyethylene composites: Structure and properties, *Biomaterials.* 22 (2001) 1311–1320. doi:10.1016/S0142-9612(00)00283-0.
- [27] M. Brahmakumar, C. Pavithran, R.M. Pillai, Coconut fibre reinforced polyethylene composites: Effect of natural waxy surface layer of the fibre on fibre/matrix interfacial bonding and strength of composites, *Compos. Sci. Technol.* 65 (2005) 563–569. doi:10.1016/j.compscitech.2004.09.020.
- [28] N. Boonthanom, M. White, Polymer-metal composite films, *Thin Solid Films.* 24 (1974) 295–306.
- [29] D. Kumlutaş, I.H. Tavman, M. Turhan Çoban, Thermal conductivity of particle filled polyethylene composite materials, *Compos. Sci. Technol.* 63 (2003) 113–117. doi:10.1016/S0266-3538(02)00194-X.
- [30] O. van den Berg, W.G.F. Sengers, W.F. Jager, S.J. Picken, M. Wübbenhorst, Dielectric and Fluorescent Probes To Investigate Glass Transition, Melt, and Crystallization in Polyolefins, *Macromolecules.* 37 (2004) 2460–2470. doi:10.1021/ma0305333.
- [31] C.D. Green, A.S. Vaughan, G.R. Mitchell, T. Liu, Structure property relationships in polyethylene/montmorillonite nanodielectrics, *IEEE Trans. Dielectr. Electr. Insul.* 15 (2008) 134–143. doi:10.1109/T-DEI.2008.4446744.
- [32] A. Schönhals, H. Goering, F.R. Costa, U. Wagenknecht, G. Heinrich, Dielectric properties of nanocomposites based on polyethylene and layered double hydroxide, *Macromolecules.* 42 (2009) 4165–4174. doi:10.1021/ma900077w.
- [33] P.J. Purohit, D.-Y. Wang, F. Emmerling, A.F. Thünemann, G. Heinrich, A. Schönhals, Arrangement of layered double hydroxide in a polyethylene matrix studied by a combination of complementary methods, *Polymer (Guildf).* 53 (2012) 2245–2254. doi:10.1016/j.polymer.2012.03.041.
- [34] D.J. Cole-Hamilton, Nature’s Polyethylene, *Angew. Chemie Int. Ed.* 49 (2010) 8564–8566. doi:10.1002/anie.201002593.
- [35] S. Ramakrishna, J. Mayer, E. Wintermantel, K.W. Leong, Biomedical applications of

- polymer-composite materials: a review, *Compos. Sci. Technol.* 61 (2001) 1189–1224. doi:10.1016/S0266-3538(00)00241-4.
- [36] C.K. Henry, G.R. Palmese, N.J. Alvarez, The evolution of crystalline structures during gel spinning of ultra-high molecular weight polyethylene fibers, *Soft Matter*. 14 (2018) 8974–8985. doi:10.1039/C8SM01597J.
- [37] R.W. Rendell, K.L. Ngai, G.B. McKenna, Molecular Weight and Concentration Dependences of the Terminal Relaxation Time and Viscosity of Entangled Polymer Solutions, *Macromolecules*. 20 (1987) 2250–2256. doi:10.1021/ma00175a033.
- [38] S. Padmanabhan, K.R. Sarma, S. Sharma, Synthesis of Ultrahigh Molecular Weight Polyethylene Using Traditional Heterogeneous Ziegler–Natta Catalyst Systems, *Ind. Eng. Chem. Res.* 48 (2009) 4866–4871. doi:10.1021/ie802000n.
- [39] J. Meissner, Basic parameters, melt rheology, processing and end-use properties of three similar low density polyethylene samples, *Pure Appl. Chem.* 42 (1975) 551–612. doi:10.1351/pac197542040551.
- [40] Z. Bashir, J.A. Odell, A. Keller, High modulus filaments of polyethylene with lamellar structure by melt processing; the role of the high molecular weight component, *J. Mater. Sci.* 19 (1984) 3713–3725. doi:10.1007/BF00552284.
- [41] Q. Zhang, S. Rastogi, D. Chen, D. Lippits, P.J. Lemstra, Low percolation threshold in single-walled carbon nanotube/high density polyethylene composites prepared by melt processing technique, *Carbon N. Y.* 44 (2006) 778–785. doi:10.1016/j.carbon.2005.09.039.
- [42] S. Ruan, P. Gao, T.X. Yu, Ultra-strong gel-spun UHMWPE fibers reinforced using multiwalled carbon nanotubes, *Polymer (Guildf)*. 47 (2006) 1604–1611. doi:10.1016/j.polymer.2006.01.020.
- [43] A.J. Pennings, R.J. van der Hooft, A.R. Postema, W. Hoogsteen, G. ten Brinke, High-speed gel-spinning of ultra-high molecular weight polyethylene, *Polym. Bull.* 16 (1986) 167–174. doi:10.1007/BF00955487.
- [44] P. Selg, H.H. Brintzinger, R.A. Andersen, I.T. Horváth, Coordination of CO to the Alkaline Earth Metallocene [(Me<sub>5</sub>C<sub>5</sub>)<sub>2</sub>Ca], *Angew. Chemie Int. Ed. English*. 34 (1995) 791–793. doi:10.1002/anie.199507911.
- [45] V.C. Gibson, S.K. Spitzmesser, Advances in non-metallocene olefin polymerization catalysis, *Chem. Rev.* 103 (2003) 283–315. doi:10.1021/cr980461r.
- [46] S. Rastogi, D.R. Lippits, G.W.M. Peters, R. Graf, Y. Yao, H.W. Spiess, Heterogeneity in polymer melts from melting of polymer crystals, *Nat. Mater.* 4 (2005) 635–641.

- doi:10.1038/nmat1437.
- [47] D. Romano, E. Andablo-Reyes, S. Ronca, S. Rastogi, Aluminoxane co-catalysts for the activation of a bis phenoxyimine titanium (IV) catalyst in the synthesis of disentangled ultra-high molecular weight polyethylene, *Polym. (United Kingdom)*. 74 (2015) 76–85. doi:10.1016/j.polymer.2015.07.039.
- [48] S. Rastogi, Y. Yao, S. Ronca, J. Bos, J. Van Der Eem, Unprecedented high-modulus high-strength tapes and films of ultrahigh molecular weight polyethylene via solvent-free route, *Macromolecules*. 44 (2011) 5558–5568. doi:10.1021/ma200667m.
- [49] K. Liu, E.L. De Boer, Y. Yao, D. Romano, S. Ronca, S. Rastogi, Heterogeneous distribution of entanglements in a nonequilibrium polymer melt of UHMWPE: Influence on crystallization without and with graphene oxide, *Macromolecules*. 49 (2016) 7497–7509. doi:10.1021/acs.macromol.6b01173.
- [50] K. Liu, S. Ronca, E. Andablo-Reyes, G. Forte, S. Rastogi, Unique rheological response of ultrahigh molecular weight polyethylenes in the presence of reduced graphene oxide, *Macromolecules*. 48 (2015) 131–139. doi:10.1021/ma501729y.
- [51] D. Romano, N. Tops, J. Bos, S. Rastogi, Correlation between Thermal and Mechanical Response of Nascent Semicrystalline UHMWPEs, *Macromolecules*. 50 (2017) 2033–2042. doi:10.1021/acs.macromol.6b02339.
- [52] K. Liu, E. Andablo-Reyes, N. Patil, D.H. Merino, S. Ronca, S. Rastogi, Influence of reduced graphene oxide on the rheological response and chain orientation on shear deformation of high density polyethylene, *Polymer (Guildf)*. 87 (2016) 8–16. doi:https://doi.org/10.1016/j.polymer.2016.01.056.
- [53] L. Szántó, R. Vogt, J. Meier, D. Auhl, E. Van Ruymbeke, C. Friedrich, Entanglement relaxation time of polyethylene melts from high-frequency rheometry in the megahertz range, *J. Rheol. (N. Y. N. Y)*. 61 (2017) 1023–1033. doi:10.1122/1.4998174.
- [54] A. Schönhals, F. Kremer, Analysis of Dielectric Spectra, in: F. Kremer, A. Schönhals (Eds.), *Broadband Dielectr. Spectrosc.*, Springer Berlin Heidelberg, Berlin, Heidelberg, 2003: pp. 59–98. doi:10.1007/978-3-642-56120-7.
- [55] G.C. Psarras, Conductivity and dielectric characterization of polymer nanocomposites, in: S.C. Tjong, Y.-W. Mai (Eds.), *Phys. Prop. Appl. Polym. Nanocomposites*, 1st ed., Elsevier, 2010: pp. 31–69. doi:10.1533/9780857090249.1.31.
- [56] J. Gu, Y. Guo, Z. Lv, W. Geng, Q. Zhang, Highly thermally conductive POSS-g-SiCp/UHMWPE composites with excellent dielectric properties and thermal stabilities, *Compos. Part A Appl. Sci. Manuf*. 78 (2015) 95–101.

- doi:10.1016/j.compositesa.2015.08.004.
- [57] L. Vaisman, M. Fernanda González, G. Marom, Transcrystallinity in brominated UHMWPE fiber reinforced HDPE composites: morphology and dielectric properties, *Polymer (Guildf)*. 44 (2003) 1229–1235. doi:10.1016/S0032-3861(02)00848-0.
- [58] M.H. Al-Saleh, S.A. Jawad, H.M. El Ghanem, Electrical and dielectric behaviors of dry-mixed CNT/UHMWPE nanocomposites, *High Perform. Polym.* 26 (2014) 205–211. doi:10.1177/0954008313507590.
- [59] S.A. Maqbool, M.S. Mehmood, S.S. Mukhtar, M.A. Baluch, S. Khan, T. Yasin, Y. Khan, Dielectric relaxation and ac conduction in  $\gamma$ -irradiated UHMWPE/MWCNTs nano composites: Impedance spectroscopy analysis, *Radiat. Phys. Chem.* 134 (2017) 40–46. doi:10.1016/j.radphyschem.2017.01.020.
- [60] T. Pakula, Dielectric and Mechanical Spectroscopy — a Comparison, in: F. Kremer, A. Schönhals (Eds.), *Broadband Dielectr. Spectrosc.*, Springer Berlin Heidelberg, Berlin, Heidelberg, 2003: pp. 597–623. doi:10.1007/978-3-642-56120-7.
- [61] T. Deplancke, O. Lame, F. Rousset, R. Seguela, G. Vigier, Mechanisms of Chain Reentanglement during the Sintering of UHMWPE Nascent Powder: Effect of Molecular Weight, *Macromolecules*. 48 (2015) 5328–5338. doi:10.1021/acs.macromol.5b00618.
- [62] T. Deplancke, O. Lame, F. Rousset, I. Aguilí, R. Seguela, G. Vigier, Diffusion versus Cococrystallization of Very Long Polymer Chains at Interfaces: Experimental Study of Sintering of UHMWPE Nascent Powder, *Macromolecules*. 47 (2014) 197–207. doi:10.1021/ma402012f.
- [63] Y.-F.F. Huang, J.-Z.Z. Xu, Z.-C.C. Zhang, L. Xu, L.-B. Bin Li, J.-F.F. Li, Z.-M.M. Li, Melt processing and structural manipulation of highly linear disentangled ultrahigh molecular weight polyethylene, *Chem. Eng. J.* 315 (2017) 132–141. doi:10.1016/j.cej.2016.12.133.
- [64] K. Chaudhuri, S. Poddar, H. Pol, A. Lele, A. Mathur, G.S. Srinivasa Rao, R. Jasra, The effect of processing conditions on the rheological properties of blends of ultra high molecular weight polyethylene with high-density polyethylene, *Polym. Eng. Sci.* 59 (2019) 821–829. doi:10.1002/pen.25016.
- [65] K. Chaudhuri, A.K. Lele, Rheological quantification of the extent of dissolution of ultrahigh molecular weight polyethylene in melt-compounded blends with high density polyethylene, *J. Rheol. (N. Y. N. Y.)*. 64 (2020) 1–12. doi:10.1122/1.5113705.
- [66] H. Yang, L. Hui, J. Zhang, P. Chen, W. Li, Effect of entangled state of nascent

- UHMWPE on structural and mechanical properties of HDPE/UHMWPE blends, *J. Appl. Polym. Sci.* 134 (2017). doi:10.1002/app.44728.
- [67] A.E. Ferreira, M.L. Cerrada, E. Perez, V. Lorenzo, E. Valles, J. Ressia, H. Cramail, J.P. Lourenco, M.R. Ribeiro, UHMWPE/HDPE in-reactor blends, prepared by in situ polymerization: Synthetic aspects and characterization, *Express Polym. Lett.* 11 (2017) 344–361. doi:10.3144/expresspolymlett.2017.34.
- [68] W. Li, C. Guan, J. Xu, J. Mu, D. Gong, Z. Chen, Q. Zhou, Disentangled UHMWPE/POSS nanocomposites prepared by ethylene in situ polymerization, *Polymer (Guildf)*. 55 (2014) 1792–1798. doi:10.1016/j.polymer.2014.02.023.
- [69] W. Li, T. Chen, C. Guan, D. Gong, J. Mu, Z. Chen, Q. Zhou, Influence of Polyhedral Oligomeric Silsesquioxane Structure on the Disentangled State of Ultrahigh Molecular Weight Polyethylene Nanocomposites during Ethylene in Situ Polymerization, *Ind. Eng. Chem. Res.* 54 (2015) 1478–1486. doi:10.1021/ie504273r.
- [70] A. Heidari, S. Talebi, M. Rezaei, H. Keshavarz-Mirzamohamadi, E. Jafariyeh-Yazdi, In Situ Synthesis of Ultrahigh Molecular Weight Polyethylene/Graphene Oxide Nanocomposite Using the Immobilized Single-site Catalyst, *Polym. Plast. Technol. Eng.* 57 (2018) 1313–1324. doi:10.1080/03602559.2017.1381246.
- [71] A. Keller, The spherulitic structure of crystalline polymers. Part I. Investigations with the polarizing microscope, *J. Polym. Sci.* 17 (1955) 291–308. doi:10.1002/pol.1955.120178414.
- [72] P.J. Flory, On the Morphology of the Crystalline State in Polymers, *J. Am. Chem. Soc.* 84 (1962) 2857–2867. doi:10.1021/ja00874a004.
- [73] C.W. Bunn, The crystal structure of long-chain normal paraffin hydrocarbons. The “shape” of the <CH<sub>2</sub> group, *Trans. Faraday Soc.* 35 (1939) 482–491. doi:10.1039/TF9393500482.
- [74] A. Muller, A Further X-Ray Investigation of Long Chain Compounds (n-Hydrocarbon), *Proc. R. Soc. A Math. Phys. Eng. Sci.* 120 (1928) 437–459. doi:10.1098/rspa.1928.0158.
- [75] W.R. Busing, X-ray diffraction study of disorder in Allied Spectra-1000 polyethylene fibers, *Macromolecules*. 23 (1990) 4608–4610. doi:10.1021/ma00223a018.
- [76] A.A. Alsaygh, J. Al-hamidi, F.D. Alsewailem, I.M. Al-Najjar, V.L. Kuznetsov, Characterization of polyethylene synthesized by zirconium single site catalysts, *Appl. Petrochemical Res.* 4 (2014) 79–84. doi:10.1007/s13203-014-0053-2.
- [77] I. Sakurada, K. Keisuke, K. Nakamae, S. Wadano, Experimental Determination of the



- Elastic Moduli of Polymer Crystals in the Direction Perpendicular to the Chain Axis, *Bull. Inst. Chem. Res. Kyoto Univ.* 44 (1966) 168–182.
- [78] M. Matsuo, C. Sawatari, Elastic modulus of polyethylene in the crystal chain direction as measured by x-ray diffraction, *Macromolecules.* 19 (1986) 2036–2040. doi:10.1021/ma00161a042.
- [79] K. Tashiro, M. Kobayashi, H. Tadokoro, Calculation of Three-Dimensional Elastic Constants of Polymer Crystals. 2. Application to Orthorhombic Polyethylene and Poly(vinyl alcohol), *Macromolecules.* 11 (1978) 914–918. doi:10.1021/ma60065a014.
- [80] L. Lozano-Sánchez, I. Bagudanch, A. Sustaita, J. Iturbe-Ek, L. Elizalde, M. Garcia-Romeu, A. Elías-Zúñiga, Single-Point Incremental Forming of Two Biocompatible Polymers: An Insight into Their Thermal and Structural Properties, *Polymers (Basel).* 10 (2018) 391. doi:10.3390/polym10040391.
- [81] D.C. Bassett, S. Block, G.J. Piermarini, A high-pressure phase of polyethylene and chain-extended growth, *J. Appl. Phys.* 45 (1974) 4146–4150. doi:10.1063/1.1663028.
- [82] G. Ungar, A. Keller, Effect of radiation on the crystals of polyethylene and paraffins: 1. Formation of the hexagonal lattice and the destruction of crystallinity in polyethylene, *Polymer (Guildf).* 21 (1980) 1273–1277. doi:10.1016/0032-3861(80)90192-5.
- [83] S. Tsubakihara, A. Nakamura, M. Yasuniwa, Hexagonal Phase of Polyethylene Fibers under High Pressure, *Polym. J.* 23 (1991) 1317–1324. doi:10.1295/polymj.23.1317.
- [84] S. Rastogi, M. Hikosaka, H. Kawabata, A. Keller, Role of mobile phases in the crystallization of polyethylene. Part 1. Metastability and lateral growth, *Macromolecules.* 24 (1991) 6384–6391. doi:10.1021/ma00024a003.
- [85] M. Hikosaka, K. Tsukijima, S. Rastogi, A. Keller, Equilibrium triple point pressure and pressure-temperature phase diagram of polyethylene, *Polymer (Guildf).* 33 (1992) 2502–2507. doi:10.1016/0032-3861(92)91130-T.
- [86] G.-R. Nejabat, A theoretical reasoning on why coordination catalysts supported on mesoporous supports produce HDPE crystalline nanofibers but not iPP crystalline nanofibers, *Polyolefins J.* 5 (2018) 153–156. doi:10.22063/poj.2018.2122.1111.
- [87] L. Brambilla, G. Zerbi, F. Piemontesi, S. Nascetti, G. Morini, Structure of MgCl<sub>2</sub>–TiCl<sub>4</sub> complex in co-milled Ziegler–Natta catalyst precursors with different TiCl<sub>4</sub> content: Experimental and theoretical vibrational spectra, *J. Mol. Catal. A Chem.* 263 (2007) 103–111. doi:10.1016/j.molcata.2006.08.001.
- [88] V. Busico, M. Causà, R. Cipullo, R. Credendino, F. Cutillo, N. Friederichs, R.

- Lamanna, A. Segre, V. Van Axel Castelli, Periodic DFT and High-Resolution Magic-Angle-Spinning (HR-MAS)  $^1\text{H}$  NMR Investigation of the Active Surfaces of  $\text{MgCl}_2$ -Supported Ziegler–Natta Catalysts. The  $\text{MgCl}_2$  Matrix, *J. Phys. Chem. C.* 112 (2008) 1081–1089. doi:10.1021/jp076679b.
- [89] S. Ronca, D. Romano, G. Forte, E. Andablo-Reyes, S. Rastogi, Improving the performance of a catalytic system for the synthesis of ultra high molecular weight polyethylene with a reduced number of entanglements, *Adv. Polym. Technol.* 31 (2012) 193–204. doi:10.1002/adv.21265.
- [90] A. Pandey, A. Toda, S. Rastogi, Influence of Amorphous Component on Melting of Semicrystalline Polymers, *Macromolecules.* 44 (2011) 8042–8055. doi:10.1021/ma201797k.
- [91] S. Rastogi, Y. Yao, D.R. Lippits, G.W.H.H. Höhne, R. Graf, H.W. Spiess, P.J. Lemstra, Segmental Mobility in the Non-crystalline Regions of Semicrystalline Polymers and its Implications on Melting, *Macromol. Rapid Commun.* 30 (2009) 826–839. doi:10.1002/marc.200900025.
- [92] D. Romano, N. Tops, E. Andablo-Reyes, S. Ronca, S. Rastogi, Influence of Polymerization Conditions on Melting Kinetics of Low Entangled UHMWPE and Its Implications on Mechanical Properties, *Macromolecules.* 47 (2014) 4750–4760. doi:10.1021/ma5008122.
- [93] G. Avitabile, R. Napolitano, B. Pirozzi, K.D. Rouse, M.W. Thomas, B.T.M. Willis, Low temperature crystal structure of polyethylene: Results from a neutron diffraction study and from potential energy calculations, *J. Polym. Sci. Polym. Lett. Ed.* 13 (1975) 351–355. doi:10.1002/pol.1975.130130607.
- [94] G.R. Strobl, W. Hagedorn, Raman Spectroscopic Method for Determining the Crystallinity of Polyethylene., *J. Polym. Sci. Polym. Phys. Ed.* 16 (1978) 1181–1193. doi:10.1002/pol.1978.180160704.
- [95] B. Wunderlich, *Thermal Analysis of Polymeric Materials*, Springer-Verlag, Berlin/Heidelberg, 2005. doi:10.1007/b137476.
- [96] J. Klein, Evidence for reptation in an entangled polymer melt, *Nature.* 271 (1978) 143–145. doi:10.1038/271143a0.
- [97] J.F. Vega, S. Rastogi, G.W.M. Peters, H.E.H. Meijer, Rheology and reptation of linear polymers. Ultrahigh molecular weight chain dynamics in the melt, *J. Rheol. (N. Y. N. Y.)* 48 (2004) 663–678. doi:10.1122/1.1718367.
- [98] W.F. Busse, Mechanical structures in polymer melts. II. Roles of entanglements in

- viscosity and elastic turbulence, *J. Polym. Sci. Part A-2 Polym. Phys.* 5 (1967) 1261–1281. doi:10.1002/pol.1967.160050621.
- [99] T. Nicolai, F. Prochazka, D. Durand, Comparison of Polymer Dynamics between Entanglements and Covalent Cross-Links, *Phys. Rev. Lett.* 82 (1999) 863–866. doi:10.1103/PhysRevLett.82.863.
- [100] D.T. Turner, Glass transition elevation by polymer entanglements, *Polymer (Guildf)*. 19 (1978) 789–796. doi:10.1016/0032-3861(78)90006-X.
- [101] R.S. Porter, J.F. Johnson, The Entanglement Concept in Polymer Systems, *Chem. Rev.* 66 (1966) 1–27. doi:10.1021/cr60239a001.
- [102] P.G. De Gennes, Dynamics of Entangled Polymer Solutions. I. The Rouse Model, *Macromolecules*. 9 (1976) 587–593. doi:10.1021/ma60052a011.
- [103] J.T. Padding, W.J. Briels, Time and length scales of polymer melts studied by coarse-grained molecular dynamics simulations, *J. Chem. Phys.* 117 (2002) 925–943. doi:10.1063/1.1481859.
- [104] S. Talebi, R. Duchateau, S. Rastogi, J. Kaschta, G.W.M. Peters, P.J. Lemstra, Molar Mass and Molecular Weight Distribution Determination Of UHMWPE Synthesized Using a Living Homogeneous Catalyst, *Macromolecules*. 43 (2010) 2780–2788. doi:10.1021/ma902297b.
- [105] J.D. Ferry, *Viscoelastic Properties of Polymers*, 3rd ed., Wiley, New York, 1980.
- [106] A. Pandey, Y. Champouret, S. Rastogi, Heterogeneity in the distribution of entanglement density during polymerization in disentangled ultrahigh molecular weight polyethylene, *Macromolecules*. 44 (2011) 4952–4960. doi:10.1021/ma2003689.
- [107] S.X. Drakopoulos, G.C. Psarras, G. Forte, I. Martin-Fabiani, S. Ronca, Entanglement dynamics in ultra-high molecular weight polyethylene as revealed by dielectric spectroscopy, *Polymer (Guildf)*. 150 (2018) 35–43. doi:10.1016/j.polymer.2018.07.021.
- [108] F. Kremer, A. Schönhals, eds., *Broadband Dielectric Spectroscopy*, Springer Berlin Heidelberg, Berlin, Heidelberg, 2003. doi:10.1007/978-3-642-56120-7.
- [109] P. Debye, Introductory paper—Part I: Mobilities of ions. Report on conductivity of strong electrolytes in dilute solutions, *Trans. Faraday Soc.* 23 (1927) 334–340. doi:10.1039/TF9272300334.
- [110] P. Debye, Part I. Dielectric constant. Energy absorption in dielectrics with polar molecules, *Trans. Faraday Soc.* 30 (1934) 679. doi:10.1039/tf9343000679.

- [111] P. Debye, Dielectric Properties of Pure Liquids., *Chem. Rev.* 19 (1936) 171–182. doi:10.1021/cr60064a002.
- [112] J.C. Dyre, The random free-energy barrier model for ac conduction in disordered solids, *J. Appl. Phys.* 64 (1988) 2456–2468. doi:10.1063/1.341681.
- [113] R. Gerhardt, Impedance and dielectric spectroscopy revisited: Distinguishing localized relaxation from long-range conductivity, *J. Phys. Chem. Solids.* 55 (1994) 1491–1506. doi:10.1016/0022-3697(94)90575-4.
- [114] G.M. Tsangaris, G.C. Psarras, N. Kouloumbi, Electric modulus and interfacial polarization in composite polymeric systems, *J. Mater. Sci.* 33 (1998) 2027–2037. doi:10.1023/A:1004398514901.
- [115] S.X. Drakopoulos, J. Karger-Kocsis, Á. Kmetty, L. Lendvai, G.C. Psarras, Thermoplastic starch modified with microfibrillated cellulose and natural rubber latex: A broadband dielectric spectroscopy study, *Carbohydr. Polym.* 157 (2017). doi:10.1016/j.carbpol.2016.10.036.
- [116] M. Hernández, J. Carretero-González, R. Verdejo, T.A. Ezquerra, M.A. López-Manchado, Molecular dynamics of natural rubber/layered silicate nanocomposites as studied by dielectric relaxation spectroscopy, *Macromolecules.* 43 (2010) 643–651. doi:10.1021/ma902379t.
- [117] M. Wübbenhorst, J. van Turnhout, J. Van Turnhout, W. Michael, Analysis of complex dielectric spectra. I. One-dimensional derivative techniques and three-dimensional modelling, *J. Non. Cryst. Solids.* 305 (2002) 40–49. doi:10.1016/S0022-3093(02)01086-4.
- [118] T. Hanai, Theory of the dielectric dispersion due to the interfacial polarization and its application to emulsions, *Kolloid-Zeitschrift.* 171 (1960) 23–31. doi:10.1007/BF01520320.
- [119] I. Martín-Fabiani, A. Linares, A. Nogales, T.A. Ezquerra, Dielectric relaxation of poly (trimethylene terephthalate) in a broad range of crystallinity, *Polymer (Guildf).* 54 (2013) 5892–5898. doi:10.1016/j.polymer.2013.08.048.
- [120] T.A. Ezquerra, J. Majszczyk, F.J. Baltà-Calleja, E. López-Cabarcos, K.H. Gardner, B.S. Hsiao, Molecular dynamics of the  $\alpha$  relaxation during crystallization of a glassy polymer: A real-time dielectric spectroscopy study, *Phys. Rev. B.* 50 (1994) 6023–6031. doi:10.1103/PhysRevB.50.6023.
- [121] G.C. Psarras, E. Manolakaki, G.M. Tsangaris, Dielectric dispersion and ac conductivity in - Iron particles loaded: Polymer composites, *Compos. Part A Appl. Sci.*

- Manuf. 34 (2003) 1187–1198. doi:10.1016/j.compositesa.2003.08.002.
- [122] G.C. Psarras, E. Manolakaki, G.M. Tsangaris, Electrical relaxations in polymeric particulate composites of epoxy resin and metal particles, *Compos. - Part A Appl. Sci. Manuf.* 33 (2002) 375–384. doi:10.1016/S1359-835X(01)00117-8.
- [123] S. Paszkiewicz, I. Taraghi, A. Szymczyk, A. Huczko, M. Kurcz, B. Przybyszewski, R. Stanik, A. Linares, T.A. Ezquerro, Z. Rosłaniec, Electrically and thermally conductive thin elastic polymer foils containing SiC nanofibers, *Compos. Sci. Technol.* 146 (2017) 20–25. doi:10.1016/j.compscitech.2017.04.016.
- [124] G.C. Psarras, Hopping conductivity in polymer matrix–metal particles composites, *Compos. Part A Appl. Sci. Manuf.* 37 (2006) 1545–1553. doi:10.1016/j.compositesa.2005.11.004.
- [125] G.C. Psarras, Charge transport properties in carbon black/polymer composites, *J. Polym. Sci. Part B Polym. Phys.* 45 (2007) 2535–2545. doi:10.1002/polb.21278.
- [126] N. González, M. dels À. Custal, G.N. Tomara, G.C. Psarras, J.R. Riba, E. Armelin, Dielectric response of vulcanized natural rubber containing BaTiO<sub>3</sub> filler: The role of particle functionalization, *Eur. Polym. J.* 97 (2017) 57–67. doi:10.1016/j.eurpolymj.2017.10.001.
- [127] O. Vryonis, D.L. Anastassopoulos, A.A. Vradis, G.C. Psarras, Dielectric response and molecular dynamics in epoxy-BaSrTiO<sub>3</sub> nanocomposites: Effect of nanofiller loading, *Polym. (United Kingdom)*. 95 (2016) 82–90. doi:10.1016/j.polymer.2016.04.050.
- [128] N. Bouropoulos, G.C. Psarras, N. Moustakas, A. Chrissanthopoulos, S. Baskoutas, Optical and dielectric properties of ZnO-PVA nanocomposites, *Phys. Status Solidi Appl. Mater. Sci.* 205 (2008) 2033–2037. doi:10.1002/pssa.200778863.
- [129] G.C. Psarras, K.G. Gatos, P.K. Karahaliou, S.N. Georga, C.A. Krontiras, J. Karger-Kocsis, Relaxation phenomena in rubber/layered silicate nanocomposites, *Express Polym. Lett.* 1 (2007) 837–845. doi:10.3144/expresspolymlett.2007.116.
- [130] G.C. Psarras, Nanodielectrics: an emerging sector of polymer nanocomposites, *Express Polym. Lett.* 2 (2008) 460–460. doi:10.3144/expresspolymlett.2008.55.
- [131] G.C. Psarras, Fundamentals of Dielectric Theories, in: *Dielectr. Polym. Mater. High-Density Energy Storage*, Elsevier, 2018: pp. 11–57. doi:10.1016/B978-0-12-813215-9.00002-6.
- [132] K.S. Cole, R.H. Cole, Dispersion and Absorption in Dielectrics I. Alternating Current Characteristics, *J. Chem. Phys.* 9 (1941) 341–351. doi:10.1063/1.1750906.
- [133] D.W. Davidson, R.H. Cole, Dielectric Relaxation in Glycerine, *J. Chem. Phys.* 18

- (1950) 1417–1417. doi:10.1063/1.1747496.
- [134] S. Havriliak, S. Negami, A complex plane representation of dielectric and mechanical relaxation processes in some polymers, *Polymer (Guildf)*. 8 (1967) 161–210. doi:10.1016/0032-3861(67)90021-3.
- [135] S.X. Drakopoulos, J. Karger-Kocsis, G.C. Psarras, In Situ Thermodielectric Analysis of the Gelatinization Mechanism of Raw Maize Starch: An Experimental and Theoretical Approach, *J. Polym. Environ.* 27 (2019) 333–342. doi:10.1007/s10924-018-1348-7.
- [136] K.N. Raftopoulos, B. Janowski, L. Apekis, K. Pielichowski, P. Pissis, Molecular mobility and crystallinity in polytetramethylene ether glycol in the bulk and as soft component in polyurethanes, *Eur. Polym. J.* 47 (2011) 2120–2133. doi:10.1016/j.eurpolymj.2011.07.020.
- [137] J.C. Martinez-Garcia, S.J. Rzoska, A. Drozd-Rzoska, S. Starzonek, J.C. Mauro, Fragility and basic process energies in vitrifying systems, *Sci. Rep.* 5 (2015) 8314. doi:10.1038/srep08314.
- [138] G. Floudas, T. Reisinger, Pressure dependence of the local and global dynamics of polyisoprene, *J. Chem. Phys.* 111 (1999) 5201–5204. doi:10.1063/1.479774.
- [139] G. Floudas, C. Gravalides, T. Reisinger, G. Wegner, Effect of pressure on the segmental and chain dynamics of polyisoprene. Molecular weight dependence, *J. Chem. Phys.* 111 (1999) 9847–9852. doi:10.1063/1.480327.
- [140] G. Floudas, Effects of pressure on systems with intrinsic orientational order, *Prog. Polym. Sci.* 29 (2004) 1143–1171. doi:10.1016/j.progpolymsci.2004.08.004.
- [141] M. Mierzwa, G. Floudas, P. Štěpánek, G. Wegner, Effect of pressure on the side-chain crystallization of poly(*n*-octadecyl methacrylate) studied by dielectric spectroscopy, *Phys. Rev. B - Condens. Matter Mater. Phys.* 62 (2000) 14012–14019. doi:10.1103/PhysRevB.62.14012.
- [142] N. Alberola, J.Y. Cavaille, J. Perez, Mechanical  $\gamma$  and  $\beta$  relaxations in polyethylene—I. Glass transitions of polyethylene, *Eur. Polym. J.* 28 (1992) 935–948. doi:10.1016/0014-3057(92)90322-S.
- [143] P. Fröbing, D. Blischke, R. Gerhard-Multhaupt, M. Salah Khalil, Complete relaxation map of polyethylene: filler-induced chemical modifications as dielectric probes, *J. Phys. D. Appl. Phys.* 34 (2001) 3051–3057. doi:10.1088/0022-3727/34/20/308.
- [144] M. Mansfield, R.H. Boyd, Molecular motions, the  $\alpha$  relaxation, and chain transport in polyethylene crystals, *J. Polym. Sci. Polym. Phys. Ed.* 16 (1978) 1227–1252.

- doi:10.1002/pol.1978.180160707.
- [145] K. Schmidt-Rohr, H.W. Spiess, Chain Diffusion between Crystalline and Amorphous Regions in Polyethylene Detected by 2D Exchange  $^{13}\text{C}$  NMR, *Macromolecules*. 24 (1991) 5288–5293. doi:10.1021/ma00019a011.
- [146] M. Kakizaki, T. Kakudate, T. Hideshima, Comparative study of dielectric, mechanical, and nuclear magnetic relaxations in linear polyethylene. II. relaxation spectroscopy of the  $\alpha$ ,  $\beta$ , and  $\gamma$  loss bands with special emphasis on fine structure, *J. Polym. Sci. B Polym. Phys. Ed.* 23 (1985) 809–824.
- [147] A. Schönhals, Molecular Dynamics in Polymer Model Systems, in: F. Kremer, A. Schönhals (Eds.), *Broadband Dielectr. Spectrosc.*, Springer Berlin Heidelberg, Berlin, Heidelberg, 2003: pp. 225–293. doi:10.1007/978-3-642-56120-7.
- [148] P. Audren, D. Ronarc'h, Determination of the chain segment lengths involved in  $\gamma$  relaxation of low-density polyethylene by thermostimulated depolarization measurements, *J. Appl. Phys.* 60 (1986) 946–954.
- [149] T. Kakudate, M. Kakizaki, T. Hideshima, Comparative study of dielectric, mechanical, and nuclear magnetic relaxations of linear polyethylene. I. Broad-line NMR investigation of the fine structure of the  $\alpha$  and  $\gamma$  loss bands observed by dielectric and mechanical measurements, *J. Polym. Sci. B Polym. Phys. Ed.* 23 (1985) 787–808.
- [150] Y. Ohta, H. Yasuda, The influence of short branches on the  $\alpha$ ,  $\beta$  and  $\gamma$ -relaxation processes of ultra-high strength polyethylene fibers, *J. Polym. Sci. Part B Polym. Phys.* 32 (1994) 2241–2249. doi:10.1002/polb.1994.090321311.
- [151] R. Böhmer, F. Kremer, *Dielectric Spectroscopy and Multidimensional NMR – a Comparison*, Springer Berlin Heidelberg, Berlin, Heidelberg, 2003. doi:10.1007/978-3-642-56120-7.
- [152] M. Rubinstein, R.H. Colby, *Polymer Physics*, 1st ed., Oxford University Press, 2003.
- [153] M. Matsuo, Y. Bin, C. Xu, L. Ma, T. Nakaoki, T. Suzuki, Relaxation mechanism in several kinds of polyethylene estimated by dynamic mechanical measurements, positron annihilation, X-ray and  $^{13}\text{C}$  solid-state NMR, *Polymer (Guildf)*. 44 (2003) 4325–4340. doi:10.1016/S0032-3861(03)00352-5.
- [154] A. Gemant, The conception of a complex viscosity and its application to dielectrics, *Trans. Faraday Soc.* 31 (1935) 1582–1590.
- [155] R. Popli, M. Glotin, L. Mandelkern, R.S. Benson, Dynamic mechanical studies of  $\alpha$  and  $\beta$  relaxations of polyethylenes, *J. Polym. Sci. Polym. Phys. Ed.* 22 (1984) 407–448. doi:10.1002/pol.1984.180220306.

- [156] H. Nakayasu, H. Markovitz, D.J. Plazek, The Frequency and Temperature Dependence of the Dynamic Mechanical Properties of a High Density Polyethylene, *Trans. Soc. Rheol.* 5 (1961) 261–283. doi:10.1122/1.548899.
- [157] R.H. Boyd, Relaxation processes in crystalline polymers: experimental behaviour — a review, *Polymer (Guildf)*. 26 (1985) 323–347. doi:10.1016/0032-3861(85)90192-2.
- [158] B. Wunderlich, Reversible crystallization and the rigid–amorphous phase in semicrystalline macromolecules, *Prog. Polym. Sci.* 28 (2003) 383–450. doi:10.1016/S0079-6700(02)00085-0.
- [159] F.C. Stehling, L. Mandelkern, The Glass Temperature of Linear Polyethylene, *Macromolecules*. 3 (1970) 242–252. doi:10.1021/ma60014a023.
- [160] H. Lee, K. Cho, T. Ahn, S. Choe, I. Kim, I. Park, B.H. Lee, Solid-state relaxations in linear low-density (1-octene comonomer), low-density, and high-density polyethylene blends, *J. Polym. Sci. Part B Polym. Phys.* 35 (1997) 1633–1642. doi:10.1002/(SICI)1099-0488(19970730)35:10<1633::AID-POLB15>3.0.CO;2-B.
- [161] D. Vlassopoulos, Commentary on the observations of solid-like rheological response in unentangled polymer melts by H. Mendil, P. Baroni, L. Noirez, D. Collin, P. Martinoty, *Eur. Phys. J. E.* 19 (2006) 113–117. doi:10.1140/epje/e2006-00008-5.
- [162] N. Alberola, J.Y. Cavaille, J. Perez, Mechanical  $\gamma$  and  $\beta$  relaxations in polyethylene—II. Physical models of the mechanical  $\gamma$  relaxation in polyethylene, *Eur. Polym. J.* 28 (1992) 949–953. doi:10.1016/0014-3057(92)90323-T.
- [163] A. V. Tobolsky, Stress relaxation studies of the viscoelastic properties of polymers, *J. Appl. Phys.* 27 (1956) 673–685. doi:10.1063/1.1722465.
- [164] A.P. Sokolov, Y. Hayashi, Breakdown of time-temperature superposition: From experiment to the coupling model and beyond, *J. Non. Cryst. Solids*. 353 (2007) 3838–3844. doi:10.1016/j.jnoncrysol.2007.02.063.
- [165] M. Lei, K. Yu, H. Lu, H.J. Qi, Influence of structural relaxation on thermomechanical and shape memory performances of amorphous polymers, *Polymer (Guildf)*. 109 (2017) 216–228. doi:10.1016/j.polymer.2016.12.047.
- [166] R.S. Stein, F.H. Norris, The X-ray diffraction, birefringence, and infrared dichroism of stretched polyethylene, *J. Polym. Sci.* 21 (1956) 381–396. doi:10.1002/pol.1958.1203112310.
- [167] A. Ziabicki, K. Kedzierska, Studies on the orientation phenomena by fiber formation from polymer melts. III. Effect of structure on orientation. Condensation polymers, *J. Appl. Polym. Sci.* 6 (1962) 111–119. doi:10.1002/app.1962.070061913.



- [168] C.M. Wu, M. Chen, J. Karger-Kocsis, Effect of micromorphologic features on the interfacial strength of iPP/Kevlar fiber microcomposites, *Polymer (Guildf)*. 42 (2001) 199–208. doi:10.1016/S0032-3861(00)00312-8.
- [169] J. Karger-Kocsis, H. Mahmood, A. Pegoretti, Recent advances in fiber/matrix interphase engineering for polymer composites, *Prog. Mater. Sci.* 73 (2015) 1–43. doi:10.1016/j.pmatsci.2015.02.003.
- [170] G. Romhány, J. Karger-Kocsis, T. Czigány, Tensile fracture and failure behavior of thermoplastic starch with unidirectional and cross-ply flax fiber reinforcements, *Macromol. Mater. Eng.* 288 (2003) 699–707. doi:10.1002/mame.200300040.
- [171] Z.W. Wilchinsky, Orientation in crystalline polymers related to deformation, *Polymer (Guildf)*. 5 (1964) 271–281. doi:10.1016/0032-3861(64)90144-2.
- [172] J.L. White, J.E. Spruiell, Specification of biaxial orientation in amorphous and crystalline polymers, *Polym. Eng. Sci.* 21 (1981) 859–868. doi:10.1002/pen.760211309.
- [173] P.D. Wu, E. Van Der Giessen, On improved network models for rubber elasticity and their applications to orientation hardening in glassy polymers, *J. Mech. Phys. Solids*. 41 (1993) 427–456. doi:10.1016/0022-5096(93)90043-F.
- [174] A. Peterlin, Molecular model of drawing polyethylene and polypropylene, *J. Mater. Sci.* 6 (1971) 490–508. doi:10.1007/BF00550305.
- [175] C.L. Choy, Thermal Conductivity of Polymers, *Polymer (Guildf)*. 18 (1977) 984–1004. doi:10.1149/2.090404jes.
- [176] C. Bastiaansen, H.W. Schmidt, T. Nishino, P. Smith, Transparency and dichroism of ultra-drawn UHMW-PE films in the visible wavelength range, *Polymer (Guildf)*. 34 (1993) 3951–3954. doi:10.1016/0032-3861(93)90526-G.
- [177] C. Weder, C. Sarwa, C. Bastiaansen, P. Smith, Highly polarized luminescence from oriented conjugated polymer/polyethylene blend films, *Adv. Mater.* 9 (1997) 1035–1039. doi:10.1002/adma.19970091308.
- [178] A.R.A. Palmans, M. Eglin, A. Montali, C. Weder, P. Smith, Tensile orientation behavior of alkoxy-substituted bis(phenylethynyl)benzene derivatives in polyolefin blend films, *Chem. Mater.* 12 (2000) 472–480. doi:10.1021/cm990558+.
- [179] A. Pucci, C. Cappelli, S. Bronco, G. Ruggeri, Dichroic Properties of Bis(benzoxazolyl)stilbene and Bis(benzoxazolyl)thiophene Dispersed into Oriented Polyethylene Films: A Combined Experimental and Density Functional Theory Approach, *J. Phys. Chem. B*. 110 (2006) 3127–3134. doi:10.1021/jp056325p.

- [180] Y. Dirix, C. Bastiaansen, W. Caseri, P. Smith, Preparation, structure and properties of uniaxially oriented polyethylene-silver nanocomposites, *J. Mater. Sci.* 34 (1999) 3859–3866. doi:10.1023/A:1004614604641.
- [181] W. Heffels, C. Bastiaansen, W. Caseri, P. Smith, W. Heffels, C. Bastiaansen, W. Caseri, P. Smith, Oriented Nanocomposites of Ultrahigh-Molecular-Weight Polyethylene and Gold, *Mol. Cryst. Liq. Cryst. Sci. Technol. Sect. A. Mol. Cryst. Liq. Cryst.* 353 (2000) 191–201. doi:10.1080/10587250008025659.
- [182] Y. Dirix, C. Darribe, W. Heffels, C. Bastiaansen, W. Caseri, Optically anisotropic polyethylene – gold nanocomposites, *Appl. Opt.* 38 (1999) 6581–6586.
- [183] Y. Dirix, C. Bastiaansen, W. Caseri, P. Smith, Oriented Pearl-Necklace Arrays of Metallic Nanoparticles in Polymers : A New Route Toward Polarization-Dependent Color Filters \*\*, *Adv. Mater.* 11 (1999) 223–227.
- [184] R. Berman, The thermal conductivity of dielectric solids at low temperatures (Theoretical), *Proc. R. Soc. London. Ser. A. Math. Phys. Sci.* 208 (1951) 108–133. doi:10.1098/rspa.1951.0147.
- [185] I. Pomeranchuk, On the Thermal Conductivity of Dielectrics, *Phys. Rev.* 60 (1941) 820–821. doi:10.1103/PhysRev.60.820.
- [186] C.L. Choy, D. Greig, The low-temperature thermal conductivity of a semi-crystalline polymer, polyethylene terephthalate, *J. Phys. C Solid State Phys.* 8 (1975) 3121–3130. doi:10.1088/0022-3719/8/19/012.
- [187] S. Ronca, T. Igarashi, G. Forte, S. Rastogi, Metallic-like thermal conductivity in a lightweight insulator: Solid-state processed Ultra High Molecular Weight Polyethylene tapes and films, *Polym. (United Kingdom)*. 123 (2017) 203–210. doi:10.1016/j.polymer.2017.07.027.
- [188] S. Shen, A. Henry, J. Tong, R. Zheng, G. Chen, Polyethylene nanofibres with very high thermal conductivities, *Nat. Nanotechnol.* 5 (2010) 251–255. doi:10.1038/nnano.2010.27.
- [189] D. Larcher, J.M. Tarascon, Towards greener and more sustainable batteries for electrical energy storage, *Nat. Chem.* 7 (2015) 19–29. doi:10.1038/nchem.2085.
- [190] M.R. Lukatskaya, B. Dunn, Y. Gogotsi, Multidimensional materials and device architectures for future hybrid energy storage, *Nat. Commun.* 7 (2016) 1–13. doi:10.1038/ncomms12647.
- [191] X. Huang, P. Jiang, Core-shell structured high- k polymer nanocomposites for energy storage and dielectric applications, *Adv. Mater.* 27 (2015) 546–554.

- doi:10.1002/adma.201401310.
- [192] J.W. Choi, D. Aurbach, Promise and reality of post-lithium-ion batteries with high energy densities, *Nat. Rev. Mater.* 1 (2016) 2019. doi:10.1038/natrevmats.2016.13.
- [193] V. Presser, C.R. Dennison, J. Campos, K.W. Knehr, E.C. Kumbur, Y. Gogotsi, The electrochemical flow capacitor: A new concept for rapid energy storage and recovery, *Adv. Energy Mater.* 2 (2012) 895–902. doi:10.1002/aenm.201100768.
- [194] J. Kim, J.H. Lee, J. Lee, Y. Yamauchi, C.H. Choi, J.H. Kim, Research Update: Hybrid energy devices combining nanogenerators and energy storage systems for self-charging capability, *APL Mater.* 5 (2017). doi:10.1063/1.4979718.
- [195] Q. Wang, L. Zhu, Polymer nanocomposites for electrical energy storage, *J. Polym. Sci. Part B Polym. Phys.* 49 (2011) 1421–1429. doi:10.1002/polb.22337.
- [196] X. Zhang, Y. Shen, B. Xu, Q. Zhang, L. Gu, J. Jiang, J. Ma, Y. Lin, C.W. Nan, Giant Energy Density and Improved Discharge Efficiency of Solution-Processed Polymer Nanocomposites for Dielectric Energy Storage, *Adv. Mater.* 28 (2016) 2055–2061. doi:10.1002/adma.201503881.
- [197] G.C. Psarras, Editorial corner – A personal view ‘energy materials’ ... the role of polymers, *Express Polym. Lett.* 10 (2016) 721. doi:10.3144/expresspolymlett.2016.65.
- [198] L. Wen, J. Chen, J. Liang, F. Li, H.M. Cheng, Flexible batteries ahead, *Natl. Sci. Rev.* 4 (2017) 20–23. doi:10.1093/nsr/nww041.
- [199] J. Jiang, X. Zhang, Z. Dan, J. Ma, Y. Lin, M. Li, C.-W. Nan, Y. Shen, Tuning Phase Composition of Polymer Nanocomposites toward High Energy Density and High Discharge Efficiency by Nonequilibrium Processing, *ACS Appl. Mater. Interfaces.* 9 (2017) 29717–29731. doi:10.1021/acsami.7b07963.
- [200] P. Jiang, X. Huang, Editorial: Dielectric materials for electrical energy storage, *IEEE Trans. Dielectr. Electr. Insul.* 24 (2017) 6619. doi:10.1109/TDEI.2017.006619.
- [201] X. Hao, A review on the dielectric materials for high energy-storage application, *J. Adv. Dielectr.* 03 (2013) 1330001. doi:10.1142/S2010135X13300016.
- [202] Q. Chen, Y. Shen, S. Zhang, Q.M. Zhang, Polymer-Based Dielectrics with High Energy Storage Density, *Annu. Rev. Mater. Res.* 45 (2015) 433–458. doi:10.1146/annurev-matsci-070214-021017.
- [203] V. Tomer, G. Polizos, C.A. Randall, E. Manias, Polyethylene nanocomposite dielectrics: Implications of nanofiller orientation on high field properties and energy storage, *J. Appl. Phys.* 109 (2011) 074113. doi:10.1063/1.3569696.
- [204] A. Mannodi-Kanakkithodi, G.M. Treich, T.D. Huan, R. Ma, M. Tefferi, Y. Cao, G.A.

- Sotzing, R. Ramprasad, Rational Co-Design of Polymer Dielectrics for Energy Storage, *Adv. Mater.* (2016) 6277–6291. doi:10.1002/adma.201600377.
- [205] W.A. Izzati, Y.Z. Arief, Z. Adzis, M. Shafanizam, Partial discharge characteristics of polymer nanocomposite materials in electrical insulation: A review of sample preparation techniques, analysis methods, potential applications, and future trends, *Sci. World J.* 2014 (2014). doi:10.1155/2014/735070.
- [206] Z. Yao, Z. Song, H. Hao, Z. Yu, M. Cao, S. Zhang, M.T. Lanagan, H. Liu, Homogeneous/Inhomogeneous-Structured Dielectrics and their Energy-Storage Performances, *Adv. Mater.* 29 (2017). doi:10.1002/adma.201601727.
- [207] Y. Zhang, C. Zhang, Y. Feng, T. Zhang, Q. Chen, Q. Chi, L. Liu, G. Li, Y. Cui, X. Wang, Z. Dang, Q. Lei, Excellent energy storage performance and thermal property of polymer-based composite induced by multifunctional one-dimensional nanofibers oriented in-plane direction, *Nano Energy.* 56 (2019) 138–150. doi:10.1016/j.nanoen.2018.11.044.
- [208] T. Brezesinski, J. Wang, S.H. Tolbert, B. Dunn, Ordered mesoporous  $\alpha$ -MoO<sub>3</sub> with iso-oriented nanocrystalline walls for thin-film pseudocapacitors, *Nat. Mater.* 9 (2010) 146–151. doi:10.1038/nmat2612.
- [209] D. Kang, G. Wang, Y. Huang, P. Jiang, X. Huang, Decorating TiO<sub>2</sub> Nanowires with BaTiO<sub>3</sub> Nanoparticles: A New Approach Leading to Substantially Enhanced Energy Storage Capability of High-k Polymer Nanocomposites, *ACS Appl. Mater. Interfaces.* 10 (2018) 4077–4085. doi:10.1021/acsami.7b16409.
- [210] Z. Pan, L. Yao, J. Zhai, D. Fu, B. Shen, H. Wang, High-energy-density polymer nanocomposites composed of newly structured one-dimensional BaTiO<sub>3</sub>@Al<sub>2</sub>O<sub>3</sub> nanofibers, *ACS Appl. Mater. Interfaces.* 9 (2017) 4024–4033. doi:10.1021/acsami.6b13663.
- [211] B. Li, E. Manias, Increased Dielectric Breakdown Strength of Polyolefin Nanocomposites via Nanofiller Alignment, *MRS Adv.* 2 (2017) 357–362. doi:10.1557/adv.2016.621.
- [212] S.N. and S.I. Hasyiya K. Adli, Takashi Harada, Seigo Ito, MRS, Effects of TiO<sub>2</sub> Properties on Performance of CH<sub>3</sub>NH<sub>3</sub>PbI<sub>3</sub> Perovskite Photovoltaic Cells, *MRS Adv.* (2016) 1. doi:10.1557/adv.2016.
- [213] G. Wang, X. Huang, P. Jiang, Bio-Inspired Fluoro-polydopamine Meets Barium Titanate Nanowires: A Perfect Combination to Enhance Energy Storage Capability of Polymer Nanocomposites, *ACS Appl. Mater. Interfaces.* 9 (2017) 7547–7555.

- doi:10.1021/acsami.6b14454.
- [214] B. Li, F. Salcedo-Galan, P.I. Xidas, E. Manias, Improving Electrical Breakdown Strength of Polymer Nanocomposites by Tailoring Hybrid-Filler Structure for High-Voltage Dielectric Applications, *ACS Appl. Nano Mater.* 1 (2018) 4401–4407. doi:10.1021/acsanm.8b01127.
- [215] M. Roy, J.K. Nelson, R.K. MacCrone, L.S. Schadler, C.W. Reed, R. Keefe, W. Zenger, Polymer nanocomposite dielectrics - the role of the interface, *IEEE Trans. Dielectr. Electr. Insul.* 12 (2005) 629–643. doi:10.1109/TDEI.2005.1511089.
- [216] T. Tanaka, M. Kozako, N. Fuse, Y. Ohki, Proposal of a multi-core model for polymer nanocomposite dielectrics, *IEEE Trans. Dielectr. Electr. Insul.* 12 (2005) 669–681. doi:10.1109/TDEI.2005.1511092.
- [217] M. Arous, I. Ben Amor, A. Kallel, Z. Fakhfakh, G. Perrier, Crystallinity and dielectric relaxations in semi-crystalline poly(ether ether ketone), *J. Phys. Chem. Solids.* 68 (2007) 1405–1414. doi:10.1016/j.jpcs.2007.02.046.
- [218] N. Hozumi, M. Ishida, T. Okamoto, H. Fukagawa, The influence of morphology on electrical tree initiation in polyethylene under AC and impulse voltages, *IEEE Trans. Electr. Insul.* 25 (1990) 707–714. doi:10.1109/14.57094.
- [219] K. Yahagi, Dielectric Properties and Morphology in Polyethylene, *IEEE Trans. Electr. Insul.* EI-15 (1980) 241–250. doi:10.1109/TEI.1980.298316.
- [220] I. Rytöluoto, A. Gitsas, S. Pasanen, K. Lahti, Effect of film structure and morphology on the dielectric breakdown characteristics of cast and biaxially oriented polypropylene films, *Eur. Polym. J.* 95 (2017) 606–624. doi:10.1016/j.eurpolymj.2017.08.051.
- [221] A. Kahouli, O. Gallot-Lavallée, P. Rain, O. Lesaint, L. Heux, C. Guillermin, J.-M. Lupin, Structure effect of thin film polypropylene view by dielectric spectroscopy and X-ray diffraction: Application to dry type power capacitors, *J. Appl. Polym. Sci.* 132 (2015) n/a-n/a. doi:10.1002/app.42602.
- [222] I. Tantis, G.C. Psarras, D. Tasis, Functionalized graphene - poly(vinyl alcohol) nanocomposites: Physical and dielectric properties, *Express Polym. Lett.* 6 (2012) 283–292. doi:10.3144/expresspolymlett.2012.31.
- [223] O. Vryonis, S.T.H. Virtanen, T. Andritsch, A.S. Vaughan, P.L. Lewin, Understanding the cross-linking reactions in highly oxidized graphene/epoxy nanocomposite systems, *J. Mater. Sci.* (2018). doi:10.1007/s10853-018-3076-8.
- [224] A.A. Bakhtiary Davijani, H.C. Liu, K. Gupta, S. Kumar, High Surface Area Electrodes

- Derived from Polymer Wrapped Carbon Nanotubes for Enhanced Energy Storage Devices, *ACS Appl. Mater. Interfaces*. 8 (2016) 24918–24923.  
doi:10.1021/acsami.6b08845.
- [225] Z.-M. Dang, J.-K. Yuan, S.-H. Yao, R.-J. Liao, Flexible Nanodielectric Materials with High Permittivity for Power Energy Storage, *Adv. Mater.* 25 (2013) 6334–6365.  
doi:10.1002/adma.201301752.
- [226] T. Hanemann, D.V. Szabó, Polymer-Nanoparticle Composites: From Synthesis to Modern Applications, *Materials (Basel)*. 3 (2010) 3468–3517.  
doi:10.3390/ma3063468.
- [227] Z.M. Dang, M.S. Zheng, J.W. Zha, 1D/2D Carbon Nanomaterial-Polymer Dielectric Composites with High Permittivity for Power Energy Storage Applications, *Small*. 12 (2016) 1688–1701. doi:10.1002/smll.201503193.
- [228] P. Kim, S.C. Jones, P.J. Hotchkiss, J.N. Haddock, B. Kippelen, S.R. Marder, J.W. Perry, Phosphonic acid-modified barium titanate polymer nanocomposites with high permittivity and dielectric strength, *Adv. Mater.* 19 (2007) 1001–1005.  
doi:10.1002/adma.200602422.
- [229] P. Kim, N.M. Doss, J.P. Tillotson, P.J. Hotchkiss, M. Pan, S.R. Marder, J. Li, J.P. Calame, J.W. Perry, High Energy Density Nanocomposites Based on Surface-Modified BaTiO<sub>3</sub> and a Ferroelectric Polymer, *ACS Nano*. 3 (2009) 2581–2592.  
doi:10.1021/nn9006412.
- [230] L.E. Norena-Franco, S. Il Seok, Q. Wang, J. Li, J. Claude, Electrical Energy Storage in Ferroelectric Polymer Nanocomposites Containing Surface-Functionalized BaTiO<sub>3</sub> Nanoparticles, *Chem. Mater.* 20 (2008) 6304–6306. doi:10.1021/cm8021648.
- [231] Q. Li, L. Chen, M.R. Gadinski, S. Zhang, G. Zhang, H. Li, A. Haque, L.Q. Chen, T. Jackson, Q. Wang, Flexible higher temperature dielectric materials from polymer nanocomposites, *Nature*. 523 (2015) 576–579. doi:10.1038/nature14647.
- [232] Q. Li, G. Zhang, F. Liu, K. Han, M.R. Gadinski, C. Xiong, Q. Wang, Solution-processed ferroelectric terpolymer nanocomposites with high breakdown strength and energy density utilizing boron nitride nanosheets, *Energy Environ. Sci.* 8 (2015) 922–931. doi:10.1039/c4ee02962c.
- [233] V. Georgakilas, J.N. Tiwari, K.C. Kemp, J.A. Perman, A.B. Bourlinos, K.S. Kim, R. Zboril, Noncovalent Functionalization of Graphene and Graphene Oxide for Energy Materials, Biosensing, Catalytic, and Biomedical Applications, *Chem. Rev.* 116 (2016) 5464–5519. doi:10.1021/acs.chemrev.5b00620.

- [234] I. Kovalenko, D.G. Bucknall, G. Yushin, Detonation nanodiamond and onion-like-carbon-embedded polyaniline for supercapacitors, *Adv. Funct. Mater.* 20 (2010) 3979–3986. doi:10.1002/adfm.201000906.
- [235] V. Tomer, G. Polizos, E. Manias, C.A. Randall, Epoxy-based nanocomposites for electrical energy storage. I: Effects of montmorillonite and barium titanate nanofillers, *J. Appl. Phys.* 108 (2010). doi:10.1063/1.3487275.
- [236] V. Tomer, E. Manias, C.A. Randall, High field properties and energy storage in nanocomposite dielectrics of poly(vinylidene fluoride-hexafluoropropylene), *J. Appl. Phys.* 110 (2011). doi:10.1063/1.3609082.
- [237] A.L.M. Reddy, S.R. Gowda, M.M. Shaijumon, P.M. Ajayan, Hybrid nanostructures for energy storage applications, *Adv. Mater.* 24 (2012) 5045–5064. doi:10.1002/adma.201104502.
- [238] B. Park, K.J. Im, K. Cho, S. Kim, Electrical characteristics of gold nanoparticle-embedded MIS capacitors with parylene gate dielectric, *Org. Electron. Physics, Mater. Appl.* 9 (2008) 878–882. doi:10.1016/j.orgel.2008.06.010.
- [239] X. Luo, D.D. Chung, Electromagnetic interference shielding using continuous carbon-fiber carbon-matrix and polymer-matrix composites, *Compos. Part B Eng.* 30 (1999) 227–231. doi:10.1016/S1359-8368(98)00065-1.
- [240] F. Lux, Models proposed to explain the electrical conductivity of mixtures made of conductive and insulating materials, *J. Mater. Sci.* 28 (1993) 285–301. doi:10.1007/BF00357799.
- [241] M.T. Connor, S. Roy, T.A. Ezquerra, F.J. Baltá Calleja, Broadband ac conductivity of conductor-polymer composites, *Phys. Rev. B.* 57 (1998) 2286–2294. doi:10.1103/PhysRevB.57.2286.
- [242] A.M. Pourrahimi, R.T. Olsson, M.S. Hedenqvist, The Role of Interfaces in Polyethylene/Metal-Oxide Nanocomposites for Ultrahigh-Voltage Insulating Materials, *Adv. Mater.* 30 (2018) 1703624. doi:10.1002/adma.201703624.
- [243] R. Ayoob, F. Alhabill, T. Andritsch, A. Vaughan, Enhanced dielectric properties of polyethylene/hexagonal boron nitride nanocomposites, *J. Mater. Sci.* 53 (2018) 3427–3442. doi:10.1007/s10853-017-1786-y.
- [244] K.P. Pipe, M.S. Kwon, D. Lee, D. Gidley, G.-H. Kim, A. Shanker, J. Kim, L. Shao, High thermal conductivity in amorphous polymer blends by engineered interchain interactions, *Nat. Mater.* 14 (2014) 295–300. doi:10.1038/nmat4141.
- [245] W. Santos, J. Sousa, R. Jr, Thermal conductivity behaviour of polymers around glass

- transition and crystalline melting temperatures, *Polym. Test.* 32 (2013) 987–994. doi:10.1016/j.polymertesting.2013.05.007.
- [246] E.C. Senis, I.O. Golosnoy, J.M. Dulieu-Barton, O.T. Thomsen, Enhancement of the electrical and thermal properties of unidirectional carbon fibre/epoxy laminates through the addition of graphene oxide, *J. Mater. Sci.* 54 (2019) 8955–8970. doi:10.1007/s10853-019-03522-8.
- [247] B. Li, P.I. Xidas, E. Manias, High Breakdown Strength Polymer Nanocomposites Based on the Synergy of Nanofiller Orientation and Crystal Orientation for Insulation and Dielectric Applications, *ACS Appl. Nano Mater.* 1 (2018) 3520–3530. doi:10.1021/acsanm.8b00671.
- [248] A.B. Robbins, S.X. Drakopoulos, I. Martin-Fabiani, S. Ronca, A.J. Minnich, Ballistic thermal phonons traversing nanocrystalline domains in oriented polyethylene, *Proc. Natl. Acad. Sci.* 116 (2019) 17163–17168. doi:10.1073/pnas.1905492116.
- [249] S. Ronca, G. Forte, H. Tjaden, S. Rastogi, Solvent-Free Solid-State-Processed Tapes of Ultrahigh-Molecular-Weight Polyethylene: Influence of Molar Mass and Molar Mass Distribution on the Tensile Properties, *Ind. Eng. Chem. Res.* 54 (2015) 7373–7381. doi:10.1021/acs.iecr.5b01469.
- [250] G. Forte, S. Ronca, Synthesis of Disentangled Ultra-High Molecular Weight Polyethylene: Influence of Reaction Medium on Material Properties, *Int. J. Polym. Sci.* 2017 (2017). doi:10.1155/2017/7431419.
- [251] G.C. Manika, G.C. Psarras, Energy storage and harvesting in BaTiO<sub>3</sub>/epoxy nanodielectrics, *High Volt.* 1 (2016) 151–157. doi:10.1049/hve.2016.0063.
- [252] C. Dessi, G.D. Tsibidis, D. Vlassopoulos, M. De Corato, M. Trofa, G. D’Avino, P.L. Maffettone, S. Coppola, Analysis of dynamic mechanical response in torsion, *J. Rheol.* (N. Y. N. Y). 60 (2016) 275–287. doi:10.1122/1.4941603.
- [253] J.A. Johnson, A.A. Maznev, J. Cuffe, J.K. Eliason, A.J. Minnich, T. Kehoe, C.M.S. Torres, G. Chen, K.A. Nelson, Direct measurement of room-temperature nondiffusive thermal transport over micron distances in a silicon membrane, *Phys. Rev. Lett.* 110 (2013) 1–5. doi:10.1103/PhysRevLett.110.025901.
- [254] N.K. Ravichandran, H. Zhang, A.J. Minnich, Spectrally Resolved Specular Reflections of Thermal Phonons from Atomically Rough Surfaces, *Phys. Rev. X.* 8 (2018) 41004. doi:10.1103/PhysRevX.8.041004.
- [255] X.-Y. Wang, R. Salovey, Melting of ultrahigh molecular weight polyethylene, *J. Appl. Polym. Sci.* 34 (1987) 593–599. doi:10.1002/app.1987.070340214.



- [256] B. Wunderlich, G. Czornyj, A Study of Equilibrium Melting of Polyethylene, *Macromolecules*. 10 (1977) 906–913. doi:10.1021/ma60059a006.
- [257] G.W.H. Höhne, Another approach to the Gibbs–Thomson equation and the melting point of polymers and oligomers, *Polymer (Guildf)*. 43 (2002) 4689–4698. doi:10.1016/S0032-3861(02)00305-1.
- [258] S. Rastogi, D.R. Lippits, G.W.H. Höhne, B. Mezari, P.C.M.M. Magusin, The role of the amorphous phase in melting of linear UHMW-PE; implications for chain dynamics, *J. Phys. Condens. Matter*. 19 (2007) 205122. doi:10.1088/0953-8984/19/20/205122.
- [259] L. Lendvai, J. Karger-Kocsis, Á. Kmetty, S.X. Drakopoulos, Production and characterization of microfibrillated cellulose-reinforced thermoplastic starch composites, *J. Appl. Polym. Sci.* 133 (2016) n/a-n/a. doi:10.1002/app.42397.
- [260] R.H. Boyd, Relaxation processes in crystalline polymers: molecular interpretation — a review, *Polymer (Guildf)*. 26 (1985) 1123–1133. doi:10.1016/0032-3861(85)90240-X.
- [261] W. Kauzmann, The Nature of the Glassy State and the Behavior of Liquids at Low Temperatures., *Chem. Rev.* 43 (1948) 219–256. doi:10.1021/cr60135a002.
- [262] F.H. Stillinger, Relaxation and flow mechanisms in ““fragile”” glass-forming liquids, *J. Chem. Phys.* 89 (1988) 6461–6469. doi:10.1063/1.455365.
- [263] M. Paluch, Effect of temperature, pressure and volume on long time relaxation dynamics in fragile glass-forming liquid, *J. Chem. Phys.* 115 (2001) 10029–10035. doi:10.1063/1.1415442.
- [264] K.L. Ngai, R. Casalini, S. Capaccioli, M. Paluch, C.M. Roland, Do Theories of the Glass Transition, in which the Structural Relaxation Time Does Not Define the Dispersion of the Structural Relaxation, Need Revision?, *J. Phys. Chem. B*. 109 (2005) 17356–17360. doi:10.1021/jp053439s.
- [265] G. Adam, J.H. Gibbs, On the Temperature Dependence of Cooperative Relaxation Properties in Glass-Forming Liquids, *J. Chem. Phys.* 43 (1965) 139–146. doi:10.1063/1.1696442.
- [266] L. Berthier, G. Biroli, J.-P. Bouchaud, L. Cipelletti, D. El Masri, D. L’Hôte, F. Ladieu, M. Pierno, Direct Experimental Evidence of a Growing Length Scale Accompanying the Glass Transition, *Science (80-. )*. 310 (2005) 1797–1800. doi:10.1126/science.1120714.
- [267] T. Bauer, P. Lunkenheimer, A. Loidl, Cooperativity and the Freezing of Molecular Motion at the Glass Transition, *Phys. Rev. Lett.* 111 (2013) 225702.

- doi:10.1103/PhysRevLett.111.225702.
- [268] A. Schönhal, B. Frick, R. Zorn, The Scaling of the Molecular Dynamics of Liquid Crystals as Revealed by Broadband Dielectric, Specific Heat, and Neutron Spectroscopy, in: F. Kremer, A. Loidl (Eds.), *Scaling Relax. Process.*, Springer International Publishing AG, Cham, Switzerland, 2018: pp. 279–306. doi:10.1007/978-3-319-72706-6\_9.
- [269] Y.T. Jang, D. Parikh, P.J. Phillips, The influence of morphology on the dielectric and dynamic mechanical behavior of a linear low-density polyethylene, *J. Polym. Sci. Polym. Phys. Ed.* 23 (1985) 2483–2498. doi:10.1002/pol.1985.180231207.
- [270] T.F. Schatzki, Molecular interpretation of the  $\gamma$ -transition in polyethylene and related compounds, *J. Polym. Sci. Part C Polym. Symp.* 14 (2007) 139–140. doi:10.1002/polc.5070140114.
- [271] R.H. Boyd, S.M. Breitling, The Conformational Analysis of Crankshaft Motions in Polyethylene, *Macromolecules.* 7 (1974) 855–862. doi:10.1021/ma60042a032.
- [272] E. Laredo, N. Suarez, A. Bello, B. Rojas de Gáscue, M.A. Gomez, J.M.G. Fatou,  $\alpha$ ,  $\beta$  and  $\gamma$  relaxations of functionalized HD polyethylene: a TSDC and a mechanical study, *Polymer (Guildf).* 40 (1999) 6405–6416. doi:10.1016/S0032-3861(99)00049-X.
- [273] N.G. McCrum, B.E. Read, G. Williams, *Anelastic and Dielectric Effects in Polymer Solids*, John Wiley & Sons, Inc., London, 1967.
- [274] C.R. Ashcraft, R.H. Boyd, A Dielectric Study of Molecular Relaxation in Oxidized and Chlorinated Polyethylenes., *J. Polym. Sci. Polym. Phys. Ed.* 14 (1976) 2153–2193. doi:10.1002/pol.1976.180141204.
- [275] K. Adachi, T. Kotaka, Effect of entanglement on the dielectric normal mode process in solutions of cis-polyisoprene, *J. Mol. Liq.* 36 (1987) 75–90.
- [276] G. Forte, S. Ronca, Laser-flash in-plane thermal analysis: The case of oriented UHMWPE, in: *AIP Conf. Proc.*, AIP Publishing, 2016. doi:10.1063/1.4949746.
- [277] A.V. Pandey, S. Rastogi, G.W.M. Peters, S. Ramandeep, Process for the melt extrusion of ultra high molecular weight polyethylene, WO/2013/034582, 2013. <https://patentscope.wipo.int/search/en/detail.jsf?docId=WO2013034582>.
- [278] J.-T. Yeh, S.-C. Lin, C.-W. Tu, K.-H. Hsie, F.-C. Chang, Investigation of the drawing mechanism of UHMWPE fibers, *J. Mater. Sci.* 43 (2008) 4892–4900. doi:10.1007/s10853-008-2711-1.
- [279] A. Linares, J.C. Canalda, M.E. Cagiao, M.C. Garcia-Gutiérrez, A. Nogales, I. Martín-Gullón, J. Vera, T.A. Ezquerro, Broad-band electrical conductivity of high density

- polyethylene nanocomposites with carbon nanoadditives: Multiwall carbon nanotubes and carbon nanofibers, *Macromolecules*. 41 (2008) 7090–7097.  
doi:10.1021/ma801410j.
- [280] H.H. Song, D.Q. Wu, B. Chu, M. Satkowski, M. Ree, R.S. Stein, J.C. Phillips, Time-resolved small-angle x-ray scattering of a high-density polyethylene/low-density polyethylene blend, *Macromolecules*. 23 (1990) 2380–2384.  
doi:10.1021/ma00210a040.
- [281] M. Azuma, L. Ma, C. He, T. Suzuki, Y. Bin, H. Kurosu, M. Matsuo, Ultradrawing of blend films of ethylene-dimethyl-aminoethyl methacrylate copolymer and ultra-high molecular weight polyethylene prepared by gelation/crystallization from solutions, *Polymer (Guildf)*. 45 (2004) 409–421. doi:10.1016/j.polymer.2003.09.031.
- [282] R. Mangal, S. Srivastava, L.A. Archer, Phase stability and dynamics of entangled polymer-nanoparticle composites, *Nat. Commun*. 6 (2015) 1–9.  
doi:10.1038/ncomms8198.
- [283] Y. Li, J. Moll, L.S. Schadler, H. Liu, S.K. Kumar, A.Z. Panagiotopoulos, J. Ilavsky, B.C. Benicewicz, V. Pryamitsyn, V. Ganesan, J.F. Douglas, R.H. Colby, D. Acehan, P. Thiyagarajan, P. Akcora, Anisotropic self-assembly of spherical polymer-grafted nanoparticles, *Nat. Mater*. 8 (2009) 354–359. doi:10.1038/nmat2404.
- [284] M.J. Gall, P.J. Hendra, O.J. Peacock, M.E.A. Cudby, H.A. Willis, The laser-Raman spectrum of polyethylene. The assignment of the spectrum to fundamental modes of vibration, *Spectrochim. Acta Part A Mol. Spectrosc*. 28 (1972) 1485–1496.  
doi:10.1016/0584-8539(72)80118-1.
- [285] M. Pigeon, R.E. Prud'homme, M. Pezolet, Characterization of Molecular Orientation in Polyethylene by Raman Spectroscopy, *Macromolecules*. 24 (1991) 5687–5694.  
doi:10.1021/ma00020a032.
- [286] S. Abbate, M. Gussoni, G. Zerbi, Raman intensities of stretch oriented polyethylene and perdeuteropolyethylene. II. Electro-optical parameters for solid N-hydrocarbons, *J. Chem. Phys*. 73 (1980) 4680–4687. doi:10.1063/1.440661.
- [287] F.J. Boerio, J.L. Koenig, Raman scattering in crystalline polyethylene, *J. Chem. Phys*. 52 (1970) 3425–3431. doi:10.1063/1.1673506.
- [288] T.J. Norman, C.D. Grant, D. Magana, J.Z. Zhang, J. Liu, D. Cao, F. Bridges, A. Van Buuren, Near Infrared Optical Absorption of Gold Nanoparticle Aggregates, *J. Phys. Chem. B*. 106 (2002) 7005–7012. doi:10.1021/jp0204197.
- [289] M. Hu, J. Chen, Z.Y. Li, L. Au, G. V. Hartland, X. Li, M. Marquez, Y. Xia, Gold

- nanostructures: Engineering their plasmonic properties for biomedical applications, *Chem. Soc. Rev.* 35 (2006) 1084–1094. doi:10.1039/b517615h.
- [290] H. Shinzawa, W. Kanematsu, I. Noda, Rheo-optical near-infrared (NIR) spectroscopy study of low-density polyethylene (LDPE) in conjunction with projection two-dimensional (2D) correlation analysis, *Vib. Spectrosc.* 70 (2014) 53–57. doi:10.1016/j.vibspec.2013.11.005.
- [291] S. Watanabe, J. Dybal, K. Tashiro, Y. Ozaki, A near-infrared study of thermally induced structural changes in polyethylene crystal, *Polymer (Guildf)*. 47 (2006) 2010–2017. doi:10.1016/j.polymer.2006.01.067.
- [292] M. Watari, H. Higashiyama, N. Mitsui, M. Tomo, Y. Ozaki, On-Line Monitoring of the Density of Linear Low-Density Polyethylene in a Real Plant by Near-Infrared Spectroscopy and Chemometrics, *Appl. Spectrosc.* 58 (2004) 248–255. doi:10.1366/000370204322843011.
- [293] I. Martín-Fabiani, M.L. Koh, F. Dalmas, K.L. Elidottir, S.J. Hinder, I. Jurewicz, M. Lansalot, E. Bourgeat-Lami, J.L. Keddie, Design of Waterborne Nanoceria/Polymer Nanocomposite UV-Absorbing Coatings: Pickering versus Blended Particles, *ACS Appl. Nano Mater.* 1 (2018) 3956–3968. doi:10.1021/acsanm.8b00736.
- [294] B. Koo, P. Goli, A. V. Sumant, P.C. dos Santos Claro, T. Rajh, C.S. Johnson, A.A. Balandin, E. V. Shevchenko, Toward Lithium Ion Batteries with Enhanced Thermal Conductivity, *ACS Nano*. 8 (2014) 7202–7207. doi:10.1021/nn502212b.
- [295] G.C. Manika, G.C. Psarras, Barium titanate/epoxy resin composite nanodielectrics as compact capacitive energy storing systems, *Express Polym. Lett.* 13 (2019) 749–758. doi:10.3144/expresspolymlett.2019.63.
- [296] T.A. Ezquerro, J.C. Canalda, A. Sanz, A. Linares, On the electrical conductivity of PVDF composites with different carbon-based nanoadditives, *Colloid Polym. Sci.* 292 (2014) 1989–1998. doi:10.1007/s00396-014-3252-6.
- [297] L. Hartmann, K. Fukao, F. Kremer, Molecular Dynamics in Thin Polymer Films, in: F. Kremer, A. Schönhals (Eds.), *Broadband Dielectr. Spectrosc.*, Springer Berlin Heidelberg, Berlin, Heidelberg, 2003: pp. 433–473.
- [298] S. Yamazaki, F. Gu, K. Watanabe, K. Okada, A. Toda, M. Hikosaka, Two-step formation of entanglement from disentangled polymer melt detected by using nucleation rate, *Polymer (Guildf)*. 47 (2006) 6422–6428. doi:10.1016/j.polymer.2006.07.010.
- [299] C. Teng, Y. Gao, X. Wang, W. Jiang, C. Zhang, R. Wang, D. Zhou, G. Xue,

- Reentanglement Kinetics of Freeze-Dried Polymers above the Glass Transition Temperature, *Macromolecules*. 45 (2012) 6648–6651. doi:10.1021/ma300885w.
- [300] M. Nakae, H. Uehara, T. Kanamoto, A.E. Zachariades, R.S. Porter, Structure development upon melt drawing of ultrahigh molecular weight polyethylene: Effect of prior thermal history, *Macromolecules*. 33 (2000) 2632–2641. doi:10.1021/ma991330a.
- [301] F. Cser, About the Lorentz correction used in the interpretation of small angle X-ray scattering data of semicrystalline polymers, *J. Appl. Polym. Sci.* 80 (2001) 2300–2308. doi:10.1002/app.1335.